

**JOÃO DUARTE NEVES CRUZ**

**EXPERIMENTAL STUDY OF PROTON  
INDUCED NUCLEAR REACTIONS IN  $^{6,7}\text{Li}$**

**LISBOA**

**2006**

- nº de arquivo

- "copyright"

**JOÃO DUARTE NEVES CRUZ**

**EXPERIMENTAL STUDY OF PROTON  
INDUCED NUCLEAR REACTIONS IN  ${}^{6,7}\text{Li}$**

Dissertação apresentada para  
obtenção do grau de Doutor em Física,  
especialidade de Física Nuclear,  
pela Universidade Nova de Lisboa,  
Faculdade de Ciências e Tecnologia.

**LISBOA**

**2006**

# Acknowledgments

This work has been done in a framework of an international collaboration and, in spite of the long list of people, I wish to thank all of them for their help. My special thanks go to:

Professor Adelaide Pedro de Jesus, who gave me the opportunity to join the Lisboa group, introducing me to the exciting field of nuclear astrophysics. Her constant support during all the phases of my work is gratefully acknowledged.

Professor Claus Rolfs, for his guidance and constant support during my stays at Bochum.

Prof. Dr. João Pires Ribeiro, for his support during data taking, and electronics and physics teachings.

Prof. Dr. Rui Coelho da Silva, who contributed to this work with very interesting discussions about physics.

Dr. Rodrigo Mateus, Eng. Micaela Fonseca and Eng. Hélio Luís, for their friendship and constant support during the long runs of data taking.

Dr. Francesco Raiola, for his friendship and fruitful discussions about electron screening (and airplanes).

Dr. Karl Kettner, for his big help in spectra analysis.

Dr. Eduardo Alves, for his teachings in physics and on the Van de Graaff accelerator operation techniques.

Manuel Cabaça for converting on the lathe, my blueprints into pieces for the target chamber, and for his valuable help in mechanical issues.

Jorge Rocha for doing the lithium implantations and for helping with his expertise in vacuum technology.

Eng. Hugo Marques and Prof. Dr. Orlando Teodoro for taking the SIMS and XPS spectra and helping me in the analysis.

I wish to thank the Faculdade de Ciências e Tecnologia da Universidade Nova de Lisboa and

the Centro de Física Nuclear da Universidade de Lisboa for financial support to do my Ph.D..

To my family, who constantly supported me with their love and allowed me to complete this work. This thesis is dedicated to them.

# Resumo

Este trabalho apresenta os resultados do estudo experimental das reacções nucleares induzidas por protões em lítio, nomeadamente as reacções  ${}^7\text{Li}(p,\alpha){}^4\text{He}$ ,  ${}^6\text{Li}(p,\alpha){}^3\text{He}$  e  ${}^7\text{Li}(p,p){}^7\text{Li}$ .

As abundâncias de  ${}^7\text{Li}$  e  ${}^6\text{Li}$  identificadas como primordiais e observadas em estrelas muito antigas do halo da Via Láctea diferem consideravelmente dos valores previstos por modelos de nucleossíntese primordial e evolução estelar que dependem, entre outros factores, das secções eficazes de reacções nucleares como a  ${}^7\text{Li}(p,\alpha){}^4\text{He}$  e a  ${}^6\text{Li}(p,\alpha){}^3\text{He}$ . A procura da resposta para estas discrepâncias desencadeou nestes últimos anos investigação intensa nos campos da evolução estelar, da cosmologia, da evolução pré-galáctica e das reacções nucleares a baixa energia.

Focando-se nas reacções nucleares, este trabalho determinou com maior precisão experimental as secções eficazes (expressas em termos do factor astrofísico) das reacções  ${}^7\text{Li}(p,\alpha){}^4\text{He}$  e  ${}^6\text{Li}(p,\alpha){}^3\text{He}$  e os efeitos de blindagem electrónica nestas reacções para diferentes ambientes (alvos isolantes e metálicos). Foram igualmente medidas as distribuições angulares da reacção do  ${}^7\text{Li}$ . Estas medições foram realizadas em dois laboratórios, no âmbito da colaboração internacional LUNA (Laboratory for Underground Nuclear Astrophysics), nomeadamente o Laboratório de Feixe de Iões do ITN (Instituto Tecnológico e Nuclear) em Sacavém, Portugal e o Dynamitron-Tandem-Laboratorium na Ruhr-Universität em Bochum, Alemanha. No ITN, a câmara dos alvos foi modificada de forma a otimizar a medição destas reacções com o desenho e construção de novas peças, a inclusão de mais uma bomba turbomolecular no sistema e de um dedo frio. As reacções  ${}^7\text{Li}(p,\alpha){}^4\text{He}$  e  ${}^6\text{Li}(p,\alpha){}^3\text{He}$  foram medidas em simultâneo com sete e quatro alvos, respectivamente. Os alvos foram produzidos de forma a obter perfis de lítio em profundidade adequados e estáveis.

Os valores obtidos para a energia potencial de blindagem electrónica em ambientes metálicos estão muito acima dos limites dos modelos de física atómica. O modelo de blindagem electrónica

de Debye aplicado aos electrões de condução dos metais consegue reproduzir estes valores constituindo um modelo simples, mas que parametriza com robustez os dados experimentais. Ao nível dos modelos estelares e de nucleossíntese primordial, estes resultados são muito importantes porque mostram que as medições em laboratório estão bem compreendidas e, portanto, os parâmetros de entrada destes modelos correspondentes às secções eficazes estão correctos.

Neste trabalho também foi medida a secção eficaz diferencial da reacção de dispersão elástica dos protões por  ${}^7\text{Li}$ , útil para descrever o canal de entrada da reacção  ${}^7\text{Li}(p,\alpha){}^4\text{He}$ .

## Palavras chave

Lítio primordial, reacções nucleares induzidas por partículas carregadas, secção eficaz, factor astrofísico  $S$ , distribuições angulares, blindagem electrónica, modelo de Debye.

# Abstract

This work presents the results of the experimental study of proton induced nuclear reactions in lithium, namely the  ${}^7\text{Li}(p,\alpha){}^4\text{He}$ ,  ${}^6\text{Li}(p,\alpha){}^3\text{He}$  and  ${}^7\text{Li}(p,p){}^7\text{Li}$  reactions.

The amount of  ${}^7\text{Li}$  and  ${}^6\text{Li}$  identified as primordial and observed in very old stars of the Milky Way galactic halo strongly deviates from the predictions of primordial nucleosynthesis and stellar evolution models which depend, among other factors, on the cross sections of reactions like  ${}^7\text{Li}(p,\alpha){}^4\text{He}$  and  ${}^6\text{Li}(p,\alpha){}^3\text{He}$ . These discrepancies have triggered a large amount of research in the fields of stellar evolution, cosmology, pre-galactic evolution and low energy nuclear reactions.

Focusing on nuclear reactions, this work has measured the  ${}^7\text{Li}(p,\alpha){}^4\text{He}$  and  ${}^6\text{Li}(p,\alpha){}^3\text{He}$  reactions cross sections (expressed in terms of the astrophysical  $S$ -factor) with higher accuracy, and the electron screening effects in these reactions for different environments (insulators and metallic targets). The  ${}^7\text{Li}(p,\alpha){}^4\text{He}$  angular distributions were also measured. These measurements took place in two laboratory facilities, in the framework of the LUNA (Laboratory for Underground Nuclear Astrophysics) international collaboration, namely the Laboratório de Feixe de Iões in ITN (Instituto Tecnológico e Nuclear) Sacavém, Portugal, and the Dynamitron-Tandem-Laboratorium in Ruhr-Universität Bochum, Germany. The ITN target chamber was modified to measure these nuclear reactions, with the design and construction of new components, the addition of one turbomolecular pump and a cold finger. The  ${}^7\text{Li}(p,\alpha){}^4\text{He}$  and  ${}^6\text{Li}(p,\alpha){}^3\text{He}$  reactions were measured concurrently with seven and four targets, respectively. These targets were produced in order to obtain adequate and stable lithium depth profiles.

In metallic environments, the measured electron screening potential energies are much higher than the predictions of atomic-physics models. The Debye screening model applied to the metallic conduction electrons is able to explain these high values. It is a simple model, but also very robust. Concerning primordial nucleosynthesis and stellar evolution models, these

results are very important as they show that laboratory measurements are well controlled, and the model inputs from these cross sections are therefore correct.

In this work the  ${}^7\text{Li}(p,p){}^7\text{Li}$  differential cross section was also measured, which is useful to describe the  ${}^7\text{Li}(p,\alpha){}^4\text{He}$  entrance channel.

## **Keywords**

Primordial lithium, charged-particle-induced nuclear reactions, cross section, Astrophysical  $S$ -factor, angular distributions, electron screening, Debye model.

# List of symbols

$A$	Abundance
$A$	Mass number
$A_\ell$	Angular distribution coefficient
$B$	Magnetic induction
$c$	Speed of light
$d\sigma/d\Omega$	Differential cross section
$D_N$	Nominal fluence
$D_I$	Retained fluence
$E$	Center-of-mass reference frame energy
$E_{\text{lab}}$	Laboratory reference frame energy
$E_C$	Coulomb barrier
$E_G$	Gamow energy
$E_0$	Gamow peak maximum
$E_0$	Incident energy
$E_r$	Resonance energy
$f$	Screening factor
$f_p$	Screening factor in a plasma
$F$	Effective area for collision
$g$	Surface gravity
$H$	Hubble constant
$h$	Planck constant
$\hbar$	Reduced Planck constant
$I$	Electric current

$\vec{j}$	Particle spin
$\vec{J}$	Total angular momentum
$J$	Bessel function
$J$	Flux of incident particles
$k$	Thermal conductivity
$k$	Wavenumber
$k_B$	Boltzmann constant
$K_\Omega$	Solid angle transformation between the laboratory and center-of-mass frame
$\vec{\ell}$	Orbital angular momentum
$m$	Mass
$N$	Number of particles
$N$	Areal density (number of particles per square centimeter)
$N_A$	Avogadro number
$N_p$	Number of incident protons
$n$	Atomic density (number of particles per cubic centimeter)
$n_e$	Conduction electrons density
$n_{e0}$	Conduction electrons average density
$n_{eff}$	Number of conduction electrons per metallic atom
$\vec{p}$	Linear momentum
$P$	Pressure
$P$	Power
$P_\ell$	Legendre polynomial
$q_e$	Electron electric charge
$Q$	Reaction $Q$ -value
$Q$	Electric charge
$Q_\ell$	Solid angle correction factor
$r$	Stoichiometric ratio
$r$	Total reaction rate
$\vec{r}$	Position
$R_a$	Atomic radius

$R_c$	Classical turning point
$R_D$	Debye-Hückel radius / Debye radius
$R_H$	Bohr radius
$R_n$	Nuclear radius
$R_{\text{Hall}}$	Hall coefficient
$R_p$	Projected range
$S$	Sputtering yield
$S$	Astrophysical $S$ -factor
$S_{\text{eff}}$	Effective astrophysical $S$ -factor
$T$	Absolute temperature
$T_6$	Absolute temperature in millions of K
$T_9$	Absolute temperature in billions of K
$T_{\text{eff}}$	Star's effective absolute temperature
$U_D$	Debye energy
$U_e$	Electron screening potential energy
$U_e^{\text{exp}}$	Experimental electron screening potential energy
$U_e^{\text{th}}$	Theoretical electron screening potential energy
$U_e^{\text{sud}}$	$U_e$ sudden limit
$U_e^{\text{ad}}$	$U_e$ adiabatic limit
$U_e^{\text{bound}}$	Bound electron screening potential energy
$\vec{v}$	Velocity
$V$	Potential energy
$W$	Angular distribution
$x$	Depth
$X$	Mass fraction
$V_c$	Coulomb potential energy
$y$	Solubility
$Y$	Reaction yield per incident particle
$Y_p$	$^4\text{He}$ primordial abundance
$z$	Cosmological redshift

$Z$	Atomic number
$\Gamma$	Resonance width
$\delta$	Kronecker delta
$\delta$	Uncertainty
$\Delta$	Target thickness
$\Delta$	Energy step
$\Delta R_p$	Straggling
$\epsilon$	Stopping power cross section
$\epsilon_0$	Permittivity of free space
$\epsilon_{\text{eff}}$	Effective stopping power cross section
$\eta$	Baryon-to-photon ratio
$\eta$	Sommerfeld parameter
$\eta$	Si detector efficiency
$\theta$	Scattering angle in center-of-mass frame
$\theta_{\text{lab}}$	Scattering angle in laboratory frame
$\lambda$	Reduced de Broglie wavelength
$\mu$	Reduced mass
$\xi$	Microturbulence
$\phi$	Probability function
$\phi$	Coulomb potential
$\rho$	Density
$\rho_a$	Atomic density
$\pi$	Parity
$\sigma$	Cross section
$\sigma$	Depletion
$\sigma$	Standard deviation
$\sigma_b$	Bare nucleus cross section
$\sigma_s$	Screened nucleus cross section
$\sigma_p$	Screened nucleus cross section in a plasma
$\sigma_t$	Transfer cross section

- $\langle \sigma v \rangle$  reaction rate per particle pair
- $\Omega_{\text{lab}}$  Solid angle in laboratory frame
- $\Omega_{\text{B}}$  Baryon density parameter



# List of acronyms

ADC	Analog-to-Digital Converter
AMRSFs	Average Matrix Sensitive Factors
BBN	Big Bang Nucleosynthesis
CAB	Cores and Bonds
CeFITec	Centro de Física e Investigação Tecnológica
CMB	Cosmic Microwave Background
DTL	Dynamitron-Tandem-Laboratorium
FWHM	Full Width at Half Maximum
GIDS	Grupo de I & D em Superfícies
GCR	Galactic Cosmic Rays
GUI	Graphics User Interface
ISM	Interstellar Medium
ITN	Instituto Tecnológico e Nuclear
LTE	Local Thermodynamic Equilibrium
LUNA	Laboratory for Underground Nuclear Astrophysics
MB	Maxwell-Boltzmann
NASA	National Aeronautics and Space Administration
ndf	number of degrees of freedom
PIGE	Proton Induced Gamma-ray Emission
PIPS	Passivated Implanted Planar Silicon
RBS	Rutherford Backscattering Spectroscopy
RGB	Red Giant Branch
SBBN	Standard Big Bang Nucleosynthesis

SIMS	Secondary Ion Mass Spectrometry
SN	Supernovae
THM	Trojan-Horse Method
WMAP	Wilkinson Microwave Anisotropy Probe
XPS	X-ray Photoelectron Spectroscopy

# Contents

<b>Introduction</b>	<b>1</b>
<b>1 Primordial lithium in the universe</b>	<b>5</b>
1.1 Big Bang Nucleosynthesis . . . . .	6
1.1.1 SBBN primordial abundances compared to observations . . . . .	8
1.2 Search for solutions to the lithium discrepancies . . . . .	18
1.2.1 Stellar . . . . .	19
1.2.2 Pre-galactic evolution . . . . .	23
1.2.3 Cosmology . . . . .	26
1.2.4 Nuclear . . . . .	27
<b>2 Determination of nuclear reaction rates</b>	<b>31</b>
2.1 Nuclear reaction rate . . . . .	31
2.2 Coulomb barrier and Gamow peak . . . . .	33
2.3 Electron screening . . . . .	36
2.3.1 Theoretical models . . . . .	39
2.3.2 Electron screening in D(d,p)T . . . . .	41
<b>3 Available data on the <math>{}^7\text{Li}(p,\alpha){}^4\text{He}</math> and <math>{}^6\text{Li}(p,\alpha){}^3\text{He}</math> reactions</b>	<b>45</b>
3.1 Methods for fitting data . . . . .	45
3.1.1 $S$ -factor . . . . .	45
3.1.2 Angular distributions . . . . .	47
3.2 Fits to ${}^7\text{Li}(p,\alpha){}^4\text{He}$ data . . . . .	50
3.2.1 $S$ -factor . . . . .	50

3.2.2	Angular distributions . . . . .	56
3.3	Fits to ${}^6\text{Li}(p,\alpha){}^3\text{He}$ data . . . . .	56
3.3.1	$S$ -factor . . . . .	56
3.3.2	Angular distributions . . . . .	60
<b>4</b>	<b>Experimental details</b>	<b>61</b>
4.1	Experimental setup . . . . .	61
4.1.1	ITN setup . . . . .	62
4.1.2	DTL setup . . . . .	69
4.2	Target preparation and analysis . . . . .	72
4.2.1	LiF targets . . . . .	72
4.2.2	${}^7\text{Li}$ implanted into Al target . . . . .	79
4.2.3	$\text{PdLi}_x$ targets . . . . .	91
4.2.4	Li metal target . . . . .	92
4.2.5	$\text{Li}_2\text{WO}_4$ target . . . . .	93
4.2.6	Targets stability . . . . .	94
<b>5</b>	<b>Analysis and results</b>	<b>97</b>
5.1	$S$ -factor determination . . . . .	97
5.1.1	Integral method . . . . .	97
5.1.2	Differential method . . . . .	98
5.1.3	Effective stopping cross section . . . . .	100
5.1.4	Solid angle transformation between the laboratory and center of mass systems . . . . .	102
5.1.5	Angular distributions . . . . .	103
5.1.6	Error analysis . . . . .	108
5.2	Results for $S_b(E)$ and $U_e$ . . . . .	114
5.2.1	Integral method – $S_b(E)$ . . . . .	114
5.2.2	Differential method – $U_e$ . . . . .	130
5.3	Debye shielding . . . . .	134
5.3.1	Electron screening in the $\text{Li}_2\text{WO}_4$ insulator . . . . .	136
5.3.2	Electron screening in the Li metal . . . . .	137

5.3.3	Electron screening in the PdLi <sub>x</sub> alloys . . . . .	138
<b>6</b>	<b>The <sup>7</sup>Li(p,p)<sup>7</sup>Li reaction</b>	<b>143</b>
6.1	Experimental setup . . . . .	143
6.2	Analysis and results . . . . .	144
<b>7</b>	<b>Conclusions</b>	<b>151</b>
<b>A</b>	<b>ITN target chamber blueprints</b>	<b>153</b>
<b>B</b>	<b><sup>7</sup>Li(p,α)<sup>4</sup>He angular distributions tables</b>	<b>165</b>
<b>C</b>	<b>FORTTRAN programs</b>	<b>171</b>
<b>D</b>	<b>Tables for <sup>7</sup>Li(p,α)<sup>4</sup>He and <sup>6</sup>Li(p,α)<sup>3</sup>He S-factor values calculated by the integral method</b>	<b>183</b>
	<b>Bibliography</b>	<b>189</b>



# List of Figures

1.1	The 12 most important reactions affecting the predictions of the light element abundances ( $^4\text{He}$ , D, $^3\text{He}$ , $^7\text{Li}$ ). . . . .	7
1.2	CMB full-sky map taken by NASA probe WMAP [1]. Colors indicate 'warmer' (red) and 'cooler' (blue) spots. . . . .	8
1.3	Abundance predictions for standard BBN [5]; the width of the curves give the $1\sigma$ uncertainty range. The WMAP $\eta_{10}$ range ( $\eta_{10} = 6.14 \pm 0.25$ ) is shown in the vertical (grey) band. . . . .	10
1.4	Left panel: D/H measurements as a function of $\log N(\text{H I})$ [ $N(\text{H I})$ is the column density in units of $\text{cm}^{-2}$ ] in the absorber where the measurement was made. The hashed region is the WMAP+SBBN prediction for D/H from Coc <i>et al.</i> 2004 [5]. Right panel: Ratio D/H as a function of $\eta_{10}$ . The horizontal stripe represent the average primordial D abundance deduced from observational data, $(2.40 \pm 0.3) \times 10^{-5}$ – see text. The vertical stripe represent the ( $1\sigma$ uncertainty range) $\eta_{10}$ limits of WMAP. . . . .	12
1.5	Top panel: $A(\text{Li})$ on $[\text{Fe}/\text{H}]$ for halo stars with $T_{\text{eff}} > 5600$ K. Bottom panel: As for the top panel, but restricting the halo sample to $T_{\text{eff}} > 6000$ K to avoid the $T_{\text{eff}}$ dependence. Plot taken from [16]. . . . .	15
1.6	Abundance of $^7\text{Li}$ as a function of the baryon over photon ratio. The horizontal stripe represents the primordial $^7\text{Li}$ abundance deduced from observational data, and the vertical stripe represents the ( $1\sigma$ uncertainty) $\eta_{10}$ limits provided by WMAP. . . . .	16
1.7	Derived $^6\text{Li}/^7\text{Li}$ as a function of $[\text{Fe}/\text{H}]$ . The stars considered to have a significant detection ( $\geq 2\sigma$ ) of $^6\text{Li}$ are shown as solid circles while non-detections are plotted as open circles. Plot taken from [20]. . . . .	18

- 1.8 Grotrian diagram for the 21-level Li atom model. All levels are connected with the Li II ground state by photo-ionization transitions. The astrophysically relevant 670.8 and 610.4 nm lines correspond to the  $2s-2p$  and  $2p-3d$  transitions, respectively. Diagram taken from [27]. . . . . 19
- 1.9 Left panel: Sample spectra around the Li I 670.8 nm line for three metal-poor halo stars. Plot taken from [20]. Right panel: The region around the Li I 610.4 nm for three metal-poor stars. The Fe I 610.22 nm, Ca I 610.27 nm, and Fe I 610.32 nm lines are also present in this region. These lines have a different strength in each star. In contrast, the Li I line has a very similar strength in the three stars – an illustration of the Spite plateau. Plot taken from [28]. . . . . 21
- 1.10 Evolution of  ${}^7\text{Li}$ ,  ${}^6\text{Li}$ , and Be in the Milky Way. The  ${}^7\text{Li}$  abundance corresponding to the baryonic density of the universe derived by WMAP is indicated as *dashed horizontal line*. The other curves correspond to a simple chemical evolution model where the metallicity dependent stellar yields component comes from production of  ${}^7\text{Li}$  and  ${}^6\text{Li}$  by GCR. The GCR composition is assumed primary in order to reproduce the Be observations. The contribution of the GCR component of  ${}^6\text{Li}$  is indicated by a *dashed curve*. Plot taken from [39]. . . . . 26
- 2.1 Schematic representation of the combined square nuclear and Coulomb potentials. A projectile incident with energy  $E < E_c$  has to penetrate the Coulomb barrier in order to reach the nuclear domain. . . . . 34
- 2.2 Dominant energy dependencies for fusion reactions. While both the Maxwell-Boltzmann function and the tunneling probability function, are small in the overlapping region, the convolution of both functions leads to a peak, the Gamow peak (shaded area), at energy  $E_0$  and width  $\Delta E_0$ . . . . . 36
- 2.3 Effect of the atomic electron cloud on the Coulomb potential of a bare nucleus (shown in an exaggerated and idealized way). This potential is reduced at all distances and goes essentially to zero beyond the atomic radius  $R_a$ . . . . . 37

2.4 Left panel:  $S(E)$  factor of  $D(d,p)T$  for Hf at  $T = 200^\circ\text{C}$  and  $T = 20^\circ\text{C}$ , with the deduced solubilities  $y$  and  $U_e$  given at each temperature. The curve for  $T = 20^\circ\text{C}$  represents well the bare  $S(E)$  factor, while the curve for  $T = 200^\circ\text{C}$  includes the electron screening with the given  $U_e$  value. Right panel:  $S(E)$  factor of  $D(d,p)T$  for Pt at  $T = 20^\circ\text{C}$  and  $300^\circ\text{C}$ , with the deduced solubilities  $y$  and  $U_e$  given at each temperature. In both figures, the curves through the data points are the  $S(E)$  fits to these points. Both plots were taken from [55]. . . . . 42

2.5 Periodic table showing the elements studied, where those with low  $U_e$  values ( $U_e < 70$  eV) are colored yellow and those with high  $U_e$  values ( $U_e > 150$  eV) are colored green. 43

3.1  $S$ -factor for the  ${}^7\text{Li}(p,\alpha){}^4\text{He}$  as a function of  ${}^7\text{Li} + p$  c.m. energy. The experimental points are from Engstler *et al.* [50] (atomic target: pluses; molecular target: crosses), Spinka *et al.* [59] (solid squares), and Rolfs and Kavanagh [60] (circles). The solid curve is an  $R$ -matrix best fit to the data from Engstler *et al.* , together with angular-distribution data also from Engstler *et al.* , and  $\alpha+\alpha$   $d$ -wave phase shifts values. The dashed curve is the best fit when the  $S$ -factor data for  $E \geq 100$  keV are from Refs.[59, 60] rather than from Ref.[50]. The dotted curves give the corresponding bare  $S$ -factor. Plot taken from [62]. . . . . 51

3.2  ${}^8\text{Be}$  level scheme. . . . . 53

3.3  ${}^7\text{Li}(p,\alpha){}^4\text{He}$   $S$ -factor as a function of  ${}^7\text{Li} + p$  c.m. energy. The data are taken from Ref. [63] (Cassagnou 62), Ref. [64] (Fiedler 67), Ref. [59] (Spinka 71), Ref. [60] (Rolfs 86), Ref. [50] (Engstler 92), and Ref. [61] (Lattuada 01). The solid curve represents the  $R$ -matrix fit done by Descouvemont *et al.* [58], and the dotted curves represent the lower and upper  $1\sigma$  limits. Plot taken from [58]. . . . . 54

3.4 Left panel: Angular distribution  $W(E,\theta)$  at representative c.m. energies for the  ${}^7\text{Li}(p,\alpha){}^4\text{He}$  reaction. Data taken from [50]. Right panel: Energy dependence of the dominant coefficient,  $A_2$ , in the angular distribution for the  ${}^7\text{Li}(p,\alpha){}^4\text{He}$  reaction. Data taken from [50] and [60]. . . . . 57

3.5	$S$ -factor for the ${}^6\text{Li}(p,\alpha){}^3\text{He}$ as a function of ${}^6\text{Li} + p$ c.m. energy. The experimental points are from Engstler <i>et al.</i> [50] (atomic target: pluses; molecular target: crosses); Marion <i>et al.</i> [66] (solid squares); Shinozuka <i>et al.</i> [69] (triangles); Elwyn <i>et al.</i> [68] (circles). The solid curve is a best fit, based on a cubic form for the bare $S$ -factor, which is shown by the dotted curve. Plot taken from [62]. . . . .	58
3.6	Energy dependence of the dominant coefficient, $A_1$ , in the angular distribution for the ${}^6\text{Li}(p,\alpha){}^3\text{He}$ reaction. Data taken from [50]. . . . .	60
4.1	The excitation function of the ${}^{27}\text{Al}(p,\gamma){}^{28}\text{Si}$ reaction at $E_{r,\text{lab}} = 992$ keV using an Al target 99.999% pure ( $E_\gamma = 1.779$ MeV). The curve through the data points is to guide the eye only. $E_{r,\text{lab}}$ corresponds to the mid-point on the excitation function curve halfway between the 12% and 88% height of the net yield. The energy difference between these points is the energy spread of the beam, 1.1 keV in our case. . . . .	62
4.2	Schematic diagram of the beam line vacuum system. . . . .	63
4.3	Top view drawing of target chamber used at ITN. Colour legend: green – steel AISI 304; orange – other metals; blue – insulator; red – o’rings. . . . .	64
4.4	Left panel: Photo of collimating system - view from inside the target chamber. Right panel: drawing of the collimating system and insulating supports. . . . .	65
4.5	Left panel: Photo of beam stopper - view from inside the target chamber. Right panel: beam stopper drawing. . . . .	66
4.6	Number of $\alpha$ 's detected by each Si detector as a function of its angular position. The full lines represents the results of the linear fits to the data, as reported in the text. . . .	66
4.7	Left panel: Particle spectrum obtained with the Si detector at an angle of $124^\circ$ by bombarding the LiF-Ag target with protons of incident energy $E_p = 1404.5$ keV. Right panel: $\gamma$ -ray spectrum obtained with the HPGe detector at an angle of $130^\circ$ by bombarding the ${}^7\text{Li}$ implanted in Al target with protons of incident energy $E_p = 894$ keV. . . . .	67
4.8	Left panel: The excitation function of the ${}^{11}\text{B}(p,\gamma){}^{12}\text{C}$ reaction at $E_{r,\text{lab}} = 163.0$ keV using a thick boron foil. The blue line connecting the data points are an interpolation curve and is to guide the eye only. Right panel: The excitation function of the ${}^{19}\text{F}(p,\alpha\gamma){}^{16}\text{O}$ reaction at $E_{r,\text{lab}} = 340.5$ keV using a thin LiF film. The blue line corresponds to a gaussian function fitted to the data points (see text for details). . . . .	69

4.9	Schematic diagram of the main components of the 100 kV accelerator at DTL, Bochum. Figure taken from [54]. . . . .	70
4.10	Schematic view of the target chamber at DTL, Bochum. Figure taken from [54]. . . . .	71
4.11	Particle spectra obtained with a Si detector at an angle of $130^\circ$ by bombarding the $\text{Li}_2\text{WO}_4$ target with protons of incident energy $E_p = 100$ keV (left panel) and 30 keV (right panel). . . . .	72
4.12	The 1.574 MeV $^4\text{He}^+$ backscattering spectra of the LiF-Ag target, measured simultaneously at two different angles, $\theta_{lab} = 94^\circ$ and $115^\circ$ . . . . .	73
4.13	The 1.574 MeV $^4\text{He}^+$ backscattering spectra of the LiF-Ag target, measured at $\theta_{lab} = 115^\circ$ . Ag plural scattering events (background) subtraction under the $^7\text{Li}$ , C, O and F peaks. The background events are fitted with exponentials and then subtracted from the spectrum. . . . .	74
4.14	The 1.574 MeV $^4\text{He}^+$ backscattering spectra of the LiF-Ag target, measured at $\theta_{lab} = 115^\circ$ . Ag plural scattering events (background) subtraction under the $^7\text{Li}$ , C, F and O peaks. The background events are fitted with an $E^{-\alpha}$ dependence under the $^7\text{Li}$ peak and by two exponentials under the C, O and F peaks. The fitted functions are then subtracted from the spectrum. . . . .	75
4.15	The 1.574 MeV $^4\text{He}^+$ backscattering spectrum of the LiF-Ag target measured at $\theta_{lab} = 115^\circ$ (after background subtraction), and the XRUMP simulated spectrum (red curve). . . . .	76
4.16	Left panel: $\gamma$ -ray spectrum taken from the LiF-Cu target at $E_{lab} = 1134$ keV. Right panel: Same spectrum zoomed over the $\gamma$ window from the $^{19}\text{F}(p,\alpha\gamma)^{16}\text{O}$ reaction. The SE and DE peaks correspond, respectively, to the single escape and double escape peaks of the 6125 keV photo peak. . . . .	78
4.17	The excitation function of the $^{19}\text{F}(p,\alpha\gamma)^{16}\text{O}$ reaction at $E_{r,lab} = 483.6$ keV using the LiF-Cu target. The curve through the data points is to guide the eye only. . . . .	78
4.18	The Sn-Li alloy phase diagram. Plot taken from [76]. . . . .	79
4.19	Implanted profile evolution with increasing fluence as predicted by eq. 4.10, for $^7\text{Li}$ implantation into aluminium at 10 keV. The red horizontal line indicates the atomic density of pure Al. . . . .	82

- 4.20 The excitation function of the  ${}^7\text{Li}(p,\gamma){}^8\text{Be}$  reaction at  $E_{r,\text{lab}} = 441.4$  keV using the two implanted targets and a vacuum evaporated LiF thin target. The quoted uncertainties are only of statistical nature and the lines through the data points are to guide the eye only. . . . . 84
- 4.21 The 2.0 MeV  ${}^4\text{He}^+$  backscattering spectra of the  ${}^7\text{Li}$  implanted target, measured at  $\theta_{\text{lab}} = 140^\circ$ . The left panel shows the  $\chi^2$  fit to the Al barrier with two exponentials (red curve). The right panel shows the RBS spectrum after subtracting the Al barrier with the fitted exponentials. . . . . 85
- 4.22 Left panel: The 2.0 MeV  ${}^4\text{He}^+$  backscattering spectrum of the  ${}^7\text{Li}$  implanted in Al target measured at  $\theta_{\text{lab}} = 140^\circ$  (with the Al barrier partially subtracted), and the XRUMP simulated spectrum (red curve). Right panel: Original RBS spectrum, superimposed on the XRUMP fit (red curve). . . . . 85
- 4.23 Depth profile of  ${}^7\text{Li}$ , Al, O and C predicted by the XRUMP fit to the RBS spectrum of the  ${}^7\text{Li}$  implanted in Al target. The lines through the data points are to guide the eye only. 86
- 4.24 Left panel: The excitation function of the  ${}^{27}\text{Al}(p,\gamma){}^{28}\text{Si}$  reaction at  $E_{r,\text{lab}} = 992$  keV using the Al target before (gray triangles) and after  ${}^7\text{Li}$  implantation (blue squares). Right panel: Comparison of Al depth profiles obtained by the  ${}^{27}\text{Al}(p,\gamma){}^{28}\text{Si}$  excitation function measurement (blue squares) and RBS measurements (orange circles) – see text for details. . . . . 88
- 4.25 The normalized sputtered  ${}^7\text{Li}_2^+$  and  $\text{Al}_2^+$  yield as a function of sputtering time (in arbitrary units) for the  ${}^7\text{Li}$  implanted target obtained with a 4 keV  $\text{Ar}^+$  primary beam in an  $\text{O}_2$  atmosphere ( $P = 1.0 \times 10^{-6}$  mbar). The lines through the data points are to guide the eye only. . . . . 89
- 4.26 Left panel: The normalized sputtered  $\text{H}^+$ ,  ${}^7\text{Li}^+$ ,  $\text{Na}^+$ ,  $\text{Al}^+$  and  $\text{K}^+$  yield as a function of sputtering time (in arbitrary units) for the  ${}^7\text{Li}$  implanted target obtained with a 4 keV  $\text{Ar}^+$  primary beam. Right panel: The normalized sputtered  $\text{C}^-$ ,  $\text{O}^-$ ,  $\text{C}_2^+$  and  $\text{Cl}^-$  yield as a function of sputtering time (in arbitrary units) for the  ${}^7\text{Li}$  implanted target obtained with a 4 keV  $\text{Ar}^+$  primary beam. The lines through the data points are to guide the eye only. . . . . 89
- 4.27 Mg  $\text{K}_\alpha$  X-rays XPS spectrum that shows the detected photo-emitted electrons as a function of the binding energy for the  ${}^7\text{Li}$  implanted in Al target surface. . . . . 90

4.28	The excitation function of the ${}^7\text{Li}(\alpha,\gamma){}^{11}\text{B}$ reaction at $E_{r,\text{lab}} = 953$ keV using a $\text{Pd}_{94.1\%}\text{Li}_{5.9\%}$ target. The line through the data points is to guide the eye only. . . . .	91
4.29	${}^7\text{Li}(\text{p},\alpha){}^4\text{He}$ yield $[\text{N}({}^4\text{He})/\text{Q}]$ evolution with accumulated charge for the LiF-Cu target, at different energies. The white and orange data points correspond to the Si detectors at $124^\circ$ and $145^\circ$ , respectively. The error bars come from the statistical error on $\text{N}({}^4\text{He})$ counts. . . . .	94
4.30	${}^7\text{Li}(\text{p},\alpha){}^4\text{He}$ yield $[\text{N}({}^4\text{He})/\text{Q}]$ (red circles) and ${}^6\text{Li}(\text{p},\alpha){}^3\text{He}$ yield $[\text{N}({}^3\text{He})/\text{Q}]$ (gray squares) evolution with accumulated charge for the Li metal target. The error bars come from the statistical error on $\text{N}({}^{3,4}\text{He})$ counts. . . . .	95
4.31	${}^7\text{Li}(\text{p},\alpha){}^4\text{He}$ yield $[\text{N}({}^4\text{He})/\text{Q}]$ (red circles) and ${}^6\text{Li}(\text{p},\alpha){}^3\text{He}$ yield $[\text{N}({}^3\text{He})/\text{Q}]$ (gray squares) evolution with accumulated charge for the $\text{Pd}_{94.1\%}\text{Li}_{5.9\%}$ target. The error bars come from the statistical error on $\text{N}({}^{3,4}\text{He})$ counts. . . . .	96
5.1	Left panel: Stopping cross section of Li for protons, $\epsilon_{\text{Li}}$ , as a function of $E_{\text{lab}}$ in the energy range 10 – 100 keV. The $\epsilon_{\text{Li}}$ values, given by SRIM [79], were $\chi^2$ fitted with a polynomial function (red line). Right panel: Stopping cross section of Li for protons, $\epsilon_{\text{Li}}$ , as a function of $E_{\text{lab}}$ in the energy range 90 – 1400 keV. The $\epsilon_{\text{Li}}$ values, given by SRIM [79], were $\chi^2$ fitted with a polynomial function (red line). . . . .	100
5.2	Schematic scattering event as seen in the laboratory and center-of-mass coordinate systems illustrating the angles and energies for nonrelativistic inelastic collisions. . . . .	102
5.3	Angular distributions of the ${}^4\text{He}$ particles for the ${}^7\text{Li}(\text{p},\alpha){}^4\text{He}$ reaction at the energies indicated. The solid lines represent the result of the Legendre polynomial fits given by Eqs. 5.24 (blue line) and 5.25 (red line). . . . .	104
5.4	Angular distributions of the ${}^4\text{He}$ particles for the ${}^7\text{Li}(\text{p},\alpha){}^4\text{He}$ reaction at the energies indicated. The solid lines represent the result of the Legendre polynomial fits given by Eqs. 5.24 (blue line) and 5.25 (red line). . . . .	105
5.5	Angular distributions of the ${}^4\text{He}$ particles for the ${}^7\text{Li}(\text{p},\alpha){}^4\text{He}$ reaction at the energies indicated. The solid lines represent the result of the Legendre polynomial fits given by Eqs. 5.24 (blue line) and 5.25 (red line). . . . .	106

- 5.6 Left panel: Deduced  $A_2(E)$  coefficient as a function of the energy. The solid curve represents a fourth order polynomial fit to the data. Right panel: Deduced  $A_4(E)$  coefficient as a function of the energy. The solid curve represents a linear fit to the data. . . . . 106
- 5.7 Deduced  $A_2(E)$  coefficient as a function of the energy. Comparison with previous works. 107
- 5.8 Energy dependence of the dominant coefficient,  $A_1$ , in the angular distribution for the  ${}^6\text{Li}(p,\alpha){}^3\text{He}$  reaction. Data taken from [50]. The solid curve represents a second order polynomial fit to data. . . . . 108
- 5.9 Left panel: The  $S$ -factor for the  ${}^7\text{Li}(p,\alpha){}^4\text{He}$  as a function of  ${}^7\text{Li} + p$  c.m. energy, measured for the  ${}^7\text{Li}$  implanted in Al target at  $124^\circ$  (black squares) and  $145^\circ$  (red circles). Right panel: Averaged  $S(E)$  values obtained from the two Si detectors (see text for details). . . . . 116
- 5.10 Left panel: The  $S$ -factor for the  ${}^7\text{Li}(p,\alpha){}^4\text{He}$  as a function of  ${}^7\text{Li} + p$  c.m. energy, measured for the LiF-Ag target at  $124^\circ$  (black squares) and  $145^\circ$  (red circles). Right panel: Averaged  $S(E)$  values obtained from the two Si detectors (see text for details). . 116
- 5.11 Left panel: The  $S$ -factor for the  ${}^7\text{Li}(p,\alpha){}^4\text{He}$  as a function of  ${}^7\text{Li} + p$  c.m. energy, measured for the LiF-Cu target at  $124^\circ$  (black squares) and  $145^\circ$  (red circles). Right panel: Averaged  $S(E)$  values obtained from the two Si detectors (see text for details). . 117
- 5.12 Left panel: Astrophysical  $S(E)$  factor of  ${}^7\text{Li}(p,\alpha){}^4\text{He}$  obtained using all targets. Right panel: Same plot zoomed over the energy interval below 900 keV. . . . . 117
- 5.13 Same plot of fig. 5.12, without distinction of target and with a few data points merged (see text for details). . . . . 118
- 5.14 The  $S$ -factor for the  ${}^7\text{Li}(p,\alpha){}^4\text{He}$  as a function of  ${}^7\text{Li} + p$  c.m. energy. The experimental points are from the present work (black squares), from Rolfs and Kavanagh [60] (red circles), Spinka *et al.* [59] (blue triangles), Harmon *et al.* [84] (green triangles) and Engstler *et al.* [50] (pink triangles). . . . . 119
- 5.15 Left panel: The  $S$ -factor for the  ${}^6\text{Li}(p,\alpha){}^3\text{He}$  as a function of  ${}^6\text{Li} + p$  c.m. energy, measured for the LiF-Cu target at  $124^\circ$  (black squares) and  $145^\circ$  (red circles). Right panel: Averaged  $S(E)$  values obtained from the two Si detectors (see text for details). The value of  $S(E = 291.4 \text{ keV}, \theta_{\text{lab}} = 145^\circ)$  was not considered in the average process. 121

- 5.16 The  $S$ -factor for the  ${}^6\text{Li}(p,\alpha){}^3\text{He}$  as a function of  ${}^6\text{Li} + p$  c.m. energy. The experimental points are from the present work (black squares) and from Elwyn *et al.* [68] (red circles) and Engstler *et al.* [50] (blue triangles). . . . . 122
- 5.17 The  $S(E)$ -factor data for the  ${}^7\text{Li}(p,\alpha){}^4\text{He}$  reaction. The solid curve is a fit with a 3rd-order polynomial function (eq. 5.53). The red portion of the curve defines the fitted energy region ( $E$  between 89.7 and 1740.3 keV – full energy range), and the green portions correspond to the extrapolated curve. P1, P2, P3 and P4 correspond respectively to parameters  $a, b, c$  and  $d$  of eq. 5.53. . . . . 124
- 5.18 The  $S(E)$ -factor data for the  ${}^7\text{Li}(p,\alpha){}^4\text{He}$  reaction. The solid curve is a fit with a 3rd-order polynomial function (eq. 5.53). The red portion of the curve defines the fitted energy region ( $E$  between 89.7 and 902.2 keV), and the green portions correspond to the extrapolated curve. P1, P2, P3 and P4 correspond respectively to parameters  $a, b, c$  and  $d$  of eq. 5.53. . . . . 125
- 5.19 The  $S(E)$ -factor data for the  ${}^7\text{Li}(p,\alpha){}^4\text{He}$  reaction. The solid curve is a fit with a 3rd-order polynomial function (eq. 5.53). The red portion of the curve defines the fitted energy region ( $E$  between 89.7 and 714.4 keV), and the green portions correspond to the extrapolated curve. P1, P2, P3 and P4 correspond respectively to parameters  $a, b, c$  and  $d$  of eq. 5.53. . . . . 126
- 5.20 The  $S(E)$ -factor data for the  ${}^6\text{Li}(p,\alpha){}^3\text{He}$  reaction. The solid curve is a fit with a 3rd-order polynomial function (eq. 5.53) to data from present work (black squares). P1, P2, P3 and P4 correspond respectively to parameters  $a, b, c$  and  $d$  of eq. 5.53. . . . . 128
- 5.21 The  $S(E)$ -factor data for the  ${}^6\text{Li}(p,\alpha){}^3\text{He}$  reaction. The solid curve is a fit with a 3rd-order polynomial function (eq. 5.53) to data from present work (black squares) plus Elwyn *et al.* (1979) [68] data (open circles). P1, P2, P3 and P4 correspond respectively to parameters  $a, b, c$  and  $d$  of eq. 5.53. . . . . 129
- 5.22 The  $S(E)$ -factor data of  ${}^7\text{Li}(p,\alpha){}^4\text{He}$  for different environments:  $\text{Li}_2\text{WO}_4$  insulator, Li metal, and  $\text{Pd}_{94.1\%}\text{Li}_{5.9\%}$  alloy. The solid curves through the data points include the bare  $S(E)$  factor (dotted curve) and the electron screening with the  $U_e$  values given in the text. . . . . 132

- 5.23 The  $S(E)$ -factor data of  ${}^6\text{Li}(p,\alpha){}^3\text{He}$  for different environments:  $\text{Li}_2\text{WO}_4$  insulator, Li metal, and  $\text{Pd}_{94.1\%}\text{Li}_{5.9\%}$  alloy. The solid curves through the data points include the bare  $S(E)$  factor (dotted curve) and the electron screening with the  $U_e$  values given in the text. . . . . 133
- 5.24 The  $S(E)$ -factor data of  ${}^7\text{Li}(p,\alpha){}^4\text{He}$  for the two  $\text{PdLi}_x$  alloys studied. The solid curves through the data points include the bare  $S(E)$  factor (dotted curve) and the electron screening with the  $U_e$  values given in the text. . . . . 140
- 6.1 The 1021.8 keV  $\text{H}^+$  backscattering spectrum of the LiF-Ag target measured at  $\theta_{\text{lab}} = 162^\circ$ . The red curve shows a  $\chi^2$  fit to the Ag peak with a gaussian plus a gaussian with a low energy lorentzian tail, and a two exponential fit to the continuum produced by the plural scattering events of protons on silver atoms. . . . . 145
- 6.2 Zoom of the 1021.8 keV  $\text{H}^+$  backscattering spectrum of the LiF-Ag target measured at  $\theta_{\text{lab}} = 162^\circ$ . The red curve shows a  $\chi^2$  simultaneous fit to the  ${}^6\text{Li}$  and  ${}^7\text{Li}$  peaks. The  ${}^6\text{Li}$  peak was fitted with a gaussian shape and the  ${}^7\text{Li}$  peak was fitted with a gaussian plus a gaussian with a low energy lorentzian tail. The lithium fits were done on top of the continuum and the carbon peak (green curve), fitted with two exponentials and a gaussian with a low energy lorentzian tail, respectively. See text for details. . . . . 146
- 6.3 Cross section of the reaction  ${}^7\text{Li}(p,p){}^7\text{Li}$  normalised to Rutherford cross section. The scattering angle measured in the laboratory frame is  $162^\circ$ . . . . . 148

# List of Tables

1.1	SBBN results at WMAP $\Omega_B h^2$ from different authors. . . . .	11
1.2	${}^7\text{Li}$ observational abundance results from different authors. . . . .	15
1.3	Influential reactions and their sensitivity to nuclear uncertainties for the production of ${}^4\text{He}$ , D, ${}^3\text{He}$ and ${}^7\text{Li}$ in SBBN. Table taken from [5]. . . . .	29
1.4	Test of yield sensitivity to reactions rate variations: factor of 10,100,1000 (see text). Table taken from [5]. . . . .	30
2.1	Energy window (in keV) of the Gamow peak for the ${}^{6,7}\text{Li} + \text{p}$ reactions during the BBN ( $T_6$ between 80 and 800), in the center of the Sun, and in the surface of halo stars. . . . .	36
2.2	Electron screening potential energy (in eV) for proton and deuterium induced reactions, in the adiabatic and sudden approximation. Experimental values obtained in laboratory experiments are also listed with respective references. . . . .	41
3.1	Legendre polynomials. . . . .	49
3.2	${}^7\text{Li}(\text{p},\alpha){}^4\text{He}$ : summary table for $S_b(0)$ and $U_e$ . . . . .	56
3.3	${}^6\text{Li}(\text{p},\alpha){}^3\text{He}$ : summary table for $S_b(0)$ and $U_e$ . . . . .	59
4.1	Analysing magnet calibration reactions. . . . .	68
4.2	SRIM simulation results and eq. 4.10 predictions for different metal backings at $E_{\text{lab}} = 5$ and 10 keV. $D_N$ max. gives the fluence necessary to obtain a saturated profile and $D_I$ is the retained fluence (see text for details). . . . .	81
4.3	478 keV $\gamma$ -ray yields produced in the implanted Al, Pb, Sn and Sb with $5 \times 10^{17} {}^7\text{Li}^+/\text{cm}^2$ . . . . .	83
4.4	Layer thicknesses and atomic fractions defined in XRUMP to fit the RBS spectrum of the ${}^7\text{Li}$ implanted in Al target. . . . .	86
4.5	$I_i$ and $I^{Av}$ values used to determine the first $\approx 10$ nm thick target stoichiometry. . . . .	91

5.1	${}^7\text{Li}(p,\alpha){}^4\text{He}$ reaction: $\epsilon_{\text{eff}}(E)$ 5% variation effects on $E$ and $S(E)$ for the ${}^7\text{Li}$ implanted target, and $\theta_{\text{lab}} = 124^\circ$ (see details in text). . . . .	112
5.2	${}^6\text{Li}(p,\alpha){}^3\text{He}$ reaction: $\epsilon_{\text{eff}}(E)$ 5% variation effects on $E$ and $S(E)$ for the LiF-Cu target, and $\theta_{\text{lab}} = 124^\circ$ (see details in text). . . . .	113
5.3	$S$ -factor data for the ${}^7\text{Li}(p,\alpha){}^4\text{He}$ reaction. The quoted uncertainties correspond to one standard deviation. . . . .	120
5.4	$S$ -factor data for the ${}^6\text{Li}(p,\alpha){}^3\text{He}$ reaction. The quoted uncertainties correspond to one standard deviation. . . . .	121
5.5	Polynomial expansion $S(E) = a + bE + cE^2 + dE^3$ fitted to the ${}^7\text{Li}(p,\alpha){}^4\text{He}$ reaction $S$ -factor for three different energy regions. The quoted uncertainties correspond to one standard deviation. . . . .	123
5.6	Polynomial expansion $S(E) = a + bE + cE^2 + dE^3$ fitted to the ${}^6\text{Li}(p,\alpha){}^3\text{He}$ reaction $S$ -factor considering only present work data and considering also Elwyn <i>et al.</i> (1979) [68] data. The quoted uncertainties correspond to one standard deviation. . . . .	127
5.7	$S$ -factor data for the ${}^7\text{Li}(p,\alpha){}^4\text{He}$ reaction measured for $E$ below 90 keV with the targets: $\text{Li}_2\text{WO}_4$ insulator, Li metal and $\text{Pd}_{94.1\%}\text{Li}_{5.9\%}$ . The quoted uncertainties correspond to one standard deviation. . . . .	131
5.8	$S$ -factor data for the ${}^6\text{Li}(p,\alpha){}^3\text{He}$ reaction measured for $E$ below 90 keV with the targets: $\text{Li}_2\text{WO}_4$ insulator, Li metal and $\text{Pd}_{94.1\%}\text{Li}_{5.9\%}$ . The quoted uncertainties correspond to one standard deviation. . . . .	131
5.9	${}^7\text{Li}(p,\alpha){}^4\text{He}$ and ${}^6\text{Li}(p,\alpha){}^3\text{He}$ $U_e$ values obtained from the $\chi^2$ fits to the $S$ -factor data for $E$ below 90 keV with the targets: $\text{Li}_2\text{WO}_4$ insulator, Li metal and $\text{Pd}_{94.1\%}\text{Li}_{5.9\%}$ . The quoted uncertainties correspond to one standard deviation. . . . .	134
5.10	$S$ -factor data for the ${}^7\text{Li}(p,\alpha){}^4\text{He}$ reaction measured for $E$ below 90 keV with the $\text{PdLi}_{0.016\%}$ target. The quoted uncertainties correspond to one standard deviation. . . . .	141
6.1	Differential cross section of elastic scattering of protons by ${}^7\text{Li}$ normalized to rutherford cross section values. The scattering angle is $\theta_{\text{lab}} = 162^\circ$ . The quoted uncertainties correspond to one standard deviation. . . . .	150

B.1	Angular distributions, $W(E, \theta)$ , of the ${}^4\text{He}$ particles for the ${}^7\text{Li}(p,\alpha){}^4\text{He}$ reaction at $E = 1740, 1609$ and $1477$ keV. The quoted uncertainties are only statistical. . . . .	166
B.2	Angular distributions, $W(E, \theta)$ , of the ${}^4\text{He}$ particles for the ${}^7\text{Li}(p,\alpha){}^4\text{He}$ reaction at $E = 1345, 1214$ and $1081$ keV. The quoted uncertainties are only statistical. . . . .	167
B.3	Angular distributions, $W(E, \theta)$ , of the ${}^4\text{He}$ particles for the ${}^7\text{Li}(p,\alpha){}^4\text{He}$ reaction at $E = 949, 817$ and $685$ keV. The quoted uncertainties are only statistical. . . . .	168
B.4	Angular distributions, $W(E, \theta)$ , of the ${}^4\text{He}$ particles for the ${}^7\text{Li}(p,\alpha){}^4\text{He}$ reaction at $E = 551, 418$ and $274$ keV. The quoted uncertainties are only statistical. . . . .	168
B.5	Angular distributions of the ${}^4\text{He}$ particles for the ${}^7\text{Li}(p,\alpha){}^4\text{He}$ reaction at $E = 150$ and $80$ keV. The quoted uncertainties are only statistical. . . . .	169
B.6	$A_2(E)$ and $A_4(E)$ coefficients values obtained from $\chi^2$ fits to the angular distributions of the ${}^4\text{He}$ particles for the ${}^7\text{Li}(p,\alpha){}^4\text{He}$ reaction. The quoted uncertainties correspond to one standard deviation. . . . .	170
D.1	${}^7\text{Li}(p,\alpha){}^4\text{He}$ $S$ -factor measured with the ${}^7\text{Li}$ implanted in Al target. The quoted uncertainties correspond to one standard deviation. . . . .	184
D.2	${}^7\text{Li}(p,\alpha){}^4\text{He}$ $S$ -factor measured with the LiF-Ag target. The quoted uncertainties correspond to one standard deviation. . . . .	185
D.3	${}^7\text{Li}(p,\alpha){}^4\text{He}$ $S$ -factor measured with the LiF-Cu target. The quoted uncertainties correspond to one standard deviation. . . . .	186
D.4	${}^6\text{Li}(p,\alpha){}^3\text{He}$ $S$ -factor measured with the LiF-Cu target. The quoted uncertainties correspond to one standard deviation. . . . .	187



# Introduction

Lithium is one of the most interesting and puzzling elements in the field of nucleosynthesis. Its most abundant isotope,  ${}^7\text{Li}$ , has the rather unique status of requiring three entirely different nucleosynthetic processes: Big Bang Nucleosynthesis (BBN), galactic cosmic ray spallation of interstellar matter, and a poorly identified stellar process.

The amount of  ${}^7\text{Li}$  present in stars, among other factors, depends on the rate of the  ${}^7\text{Li}(p,\alpha){}^4\text{He}$  reaction. However, very recently, it has been determined that the primordial lithium abundance expected on the basis of  ${}^7\text{Li}(p,\alpha){}^4\text{He}$  cross section measurements does not match that observed in several astrophysical sites such as very old Pop. II stars from the Milky Way halo. For the lighter isotope,  ${}^6\text{Li}$ , there is also no agreement between expected and observed primordial abundances.

These discrepancies have triggered a large amount of research in the fields of stellar evolution, cosmology, pre-galactic evolution and nuclear reactions. The accuracy of the predictions given by stellar and primordial nucleosynthesis models depends greatly on the accuracy of the cross sections of reactions that take place in those scenarios, and whose values can be measured in laboratories with particle accelerators. This is the field of experimental nuclear astrophysics, to which this work brings a contribution.

In astrophysical scenarios, charged particles nuclear reactions take place predominantly over the Gamow peak, an energy window situated at very low energies. For these reactions the Coulomb barrier makes these reactions very unlikely at such low energies, often requiring long data collection times with painstaking attention to background.

Another struggle in laboratory measurements comes from the presence of electrons around the nuclei. They screen the nuclear charges, therefore increasing the fusion probability by reducing the Coulomb repulsion. However, this electronic screening is not the same in astrophysical scenarios and in a laboratory experiment. For instance, inside stars, nuclear reactions occur in a

fully ionized plasma, where electrons move much faster than the nuclei. In a laboratory, an ion beam strikes a neutral atomic (or molecular) target, where electrons are much more confined around the target nucleus. So, due to their different electronic arrangement, electron screening is not the same in a star plasma and in a neutral target. This means that fusion cross sections measured in the laboratory have to be corrected by the electron screening when used as inputs of a stellar or primordial nucleosynthesis model.

Experimental studies of fusion reactions involving light nuclides have shown the expected exponential enhancement of the cross section at low energies. However, the observed enhancements were in several cases much larger than could be accounted for from available atomic-physics models. Suggested solutions of the large enhancement including aspects such as stopping power or thermal motion were not successful. Recently, an explanation came from a more radical approach, after studying the electron screening in  $D(d,p)T$  for deuterated metals, insulators, and semiconductors: the large screening, only observed in metals, is due to a star-plasma-like behaviour of the conduction electrons of a metal. This model predicted a temperature dependence which was verified with the  $D(d,p)T$  study, but also predicted a dependence with the target atomic number and an isotopic independence, which required experimental verification.

This experimental work was the motivation of this thesis. The low energy,  $E_{\text{lab}} \leq 100$  keV,  ${}^7\text{Li}(p,\alpha){}^4\text{He}$  and  ${}^6\text{Li}(p,\alpha){}^3\text{He}$  reactions cross sections (expressed in terms of the astrophysical  $S$ -factor) were measured concurrently in different environments (insulator and metallic targets), and the corresponding electron screenings were determined. A precise quantification of this screening effect requires an equally accurate knowledge of the cross section at higher energies where the electron screening effect is negligible. As the available data was not very accurate and presented discrepancies, a new study of both nuclear reactions at high energy,  $E_{\text{lab}} > 116$  keV, was done which included the cross section determination and the measurement of the  ${}^7\text{Li}$  reaction angular distributions.

The  ${}^7\text{Li}(p,p){}^7\text{Li}$  differential cross section was also measured in this work. Elastic scattering of protons by  ${}^7\text{Li}$  does not directly present an astrophysical interest but is important to describe the entrance channel of the  ${}^7\text{Li}(p,\alpha){}^4\text{He}$  reaction, and in this view is important for theoretical models.

The work is organized in the following way. The Chapter 1 presents a short review about the latest developments concerning the quantification of primordial lithium, and Chapter 2 ad-

addresses the determination of nuclear reaction rates, including the effects of the Coulomb barrier and electron screening. Chapter 3 presents the status, prior to this work, on the most relevant experimental data for both lithium reactions. The description of the experimental details is given in Chapter 4. It embraces the experimental setups, and details about target preparation and analysis. Chapter 5 describes the analysis used to obtain the astrophysical  $S$ -factor with estimation of associated uncertainties, the results obtained from this analysis and its interpretations. Chapter 6 describes the measurement of the  ${}^7\text{Li}(p,p){}^7\text{Li}$  reaction, and the results obtained. The conclusions are presented in Chapter 7.



# Chapter 1

## Primordial lithium in the universe

The Big Bang model is a broadly accepted theory for the origin and evolution of the universe. From this model, we know that during the first three minutes of the universe, hydrogen, deuterium, helium-3, helium-4 and trace amounts of lithium were formed. The amount of  ${}^7\text{Li}$  now present in the universe was almost entirely produced here.

This primordial abundance of light elements depends on the density of nucleons (baryons) and on the reaction rate of the weak and the nuclear reactions involved in the production of these elements. From the available measured data, the deduced primordial abundances may be compared with spectroscopic observations.

After the discovery, in 1982, that Pop. II old stars from the Milky Way galactic halo had a near constant lithium abundance, there was a near-universal association of this lithium abundance plateau (called Spite plateau) with primordial nucleosynthesis. However, recent and precise measurements of the baryon-to-photon ratio ( $\eta$ ) and the detection of the lighter isotope  ${}^6\text{Li}$  in some of the plateau stars, have cast serious doubts over that association. The standard model of the Big Bang with the most recent estimate of  $\eta$  predicts a lithium ( ${}^7\text{Li}$ ) abundance greater by a factor 3 than the value generally attributed to the Spite plateau, and a  ${}^6\text{Li}$  abundance several orders of magnitude below the values observed.

In this chapter we start with a brief description of the universe evolution, namely the primordial reactions involved in the production and destruction of lithium in the universe. A comparison between predicted and observed values is presented for the primordial elements with a special focus on lithium. To finish, the different mechanisms that try to explain the lithium discrepancies between prediction and observation are explored in some detail.

## 1.1 Big Bang Nucleosynthesis

The Big Bang model suggests that 13.7 billion years ago [1], a tremendous explosion, called the Big Bang, initiated the expansion of the universe. Before this explosion, all the matter in the universe was contained in a single point, no more than a few millimeters across. The universe has since expanded from this hot, dense state into the spacious and much cooler environment, which we now inhabit.

When the universe was roughly 1 s old, the temperature had fallen from an initial value greater than 86 MeV ( $= 10^{12}$  K<sup>1</sup>) to around 1 MeV, and consisted mostly of photons ( $\gamma$ ), electron-positron pairs ( $e^- - e^+$ ) and particle-antiparticle pairs of all known “flavours” of neutrinos ( $\nu_e, \nu_\mu, \nu_\tau$ ). There were also trace amounts of protons (p) and neutrons (n) with a ratio  $n/p \approx 1/6$ . These baryons reacted with each other forming deuterium through the reaction  $p + n \rightarrow d + \gamma$ , but the low binding energy of 2.22 MeV for deuterium combined with the high density of high-energy photons (around  $10^9$  photons per baryon) lead to immediate photodisintegration of deuterium. Thus, the synthesis of heavier and more stable nuclei such as  $^4\text{He}$  was blocked by the fragility of deuterium. Approximately 1 minute after the Big Bang, when the temperature of the universe reached  $\approx 0.1$  MeV ( $\approx 10^9$  K), deuterium became stable against photodissociation allowing protons and neutrons to undergo a series of nuclear reactions resulting predominantly in the production of  $^4\text{He}$  nuclei (99.99 % efficiency) with no free neutrons surviving<sup>2</sup>. Deuterium,  $^3\text{He}$  and  $^7\text{Li}$  were also synthesized to a much lower extent, though. Since there is no stable element of mass 5, nor of mass 8, additional nucleosynthesis via  $^4\text{He} + p$  or  $^4\text{He} + ^4\text{He}$  was not possible. This process of light element production in the early universe is known as Standard Big Bang Nucleosynthesis (SBBN) and was first suggested by Alpher and Gamow in 1948 in the so-called  $\alpha\beta\gamma$  paper [2]. Based on standard cosmology and particle physics, uniform baryon density, small degree of matter-antimatter asymmetry, and describing gravitation with general relativity, the theory has been strengthened over the last 30+ years, on the whole, computing abundances for these light elements comparable to those now observed (or, observable!) in a variety of astrophysical sites (e.g., stars; cool, neutral gas; hot, ionized gas).

---

<sup>1</sup>It is common in astrophysics to use the following temperature-energy relation:  $E = k_B T = 8.6171 \times 10^{-5} T$  (eV)  $= 8.6171 \times 10^4 T_9$  (eV)  $= 8.6171 \times 10^{-2} T_9$  (MeV).

<sup>2</sup> By this time,  $n/p$  had dropped to  $\approx 1/7$ , due to free neutron decay.

The main reactions involved in this process are listed in fig. 1.1.

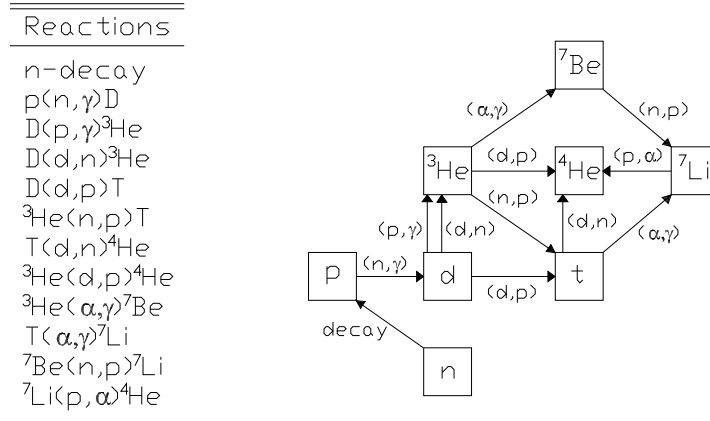


Figure 1.1: The 12 most important reactions affecting the predictions of the light element abundances ( $^4\text{He}$ ,  $D$ ,  $^3\text{He}$ ,  $^7\text{Li}$ ).

At the time of  $^4\text{He}$  production the universe was an ionized gas (plasma) composed mostly of protons, helium nuclei and electrons in thermal equilibrium with the photon sea. As the universe kept expanding, the temperature and density of matter and radiation continued to decrease steadily, dropping in a few minutes well below the levels needed to sustain further nuclear reactions. When the temperature dropped below 4500 K (379 000 years after the Big Bang [1]), the ions and electrons of the plasma combined, resulting in a neutral gas. With this charge neutralization, the previously opaque universe became transparent<sup>3</sup>, allowing radiation to travel unscattered through space, preserving an image of the plasma from which the photons were last scattered. Originally emitted as visible and infrared radiation, this background radiation has been redshifted by a factor of 1500 and is now reaching us primarily in the form of microwaves.

These photons, discovered in 1965 by Penzias and Wilson [3], are detected under the form of an almost perfect blackbody spectrum at a temperature of 2.725 K [1] and form the Cosmic Microwave Background, or CMB. It bathes the universe almost evenly (see fig. 1.2), showing patterns of tiny temperature differences<sup>4</sup>, which are considered the seeds that generated the cosmic structure we see today.

It is worth mentioning, before finishing this section, that even though the Big Bang theory is very successful in explaining the origin of the light elements (SBBN) and the cosmic microwave

<sup>3</sup>The main source of opacity was due to free electrons which interacted with photons through Thomson scattering.

<sup>4</sup>The temperature is uniform to better than one part in a thousand.

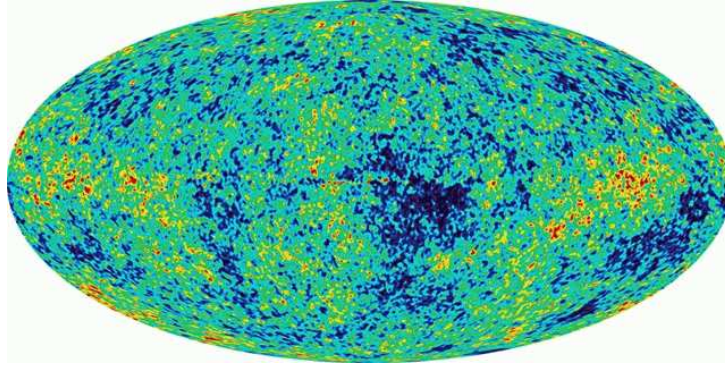


Figure 1.2: CMB full-sky map taken by NASA probe WMAP [1]. Colors indicate 'warmer' (red) and 'cooler' (blue) spots.

background radiation (CMB), it leaves open a number of important questions. For example, it does not explain why the universe is so non-uniform on smaller scales, i.e., how stars and galaxies came to be. So, a more complete understanding of our universe requires going beyond the Big Bang model. Many cosmologists suspect that Inflation theory, an extension of the Big Bang theory, may provide the framework for explaining some of the puzzles of the Big Bang model [1].

### 1.1.1 SBBN primordial abundances compared to observations

The primordial yields of light elements are determined by the competition between the expansion rate of the universe (the Hubble constant,  $H$ ) and the rates of the weak and nuclear reactions. It is the weak interaction, interconverting neutrons and protons, that largely determines the amount of  ${}^4\text{He}$  which may be synthesized, while the abundances of the other light nuclides depend mainly on the nuclear reaction rates which scale with the nucleon (baryon) density. Since the baryon density is always changing as the universe expands, it is convenient to express it in terms of a dimensionless parameter which is either conserved or, changes in a known and calculable fashion. From the very early universe till now the number of baryons in a comoving volume has been preserved and the same is roughly true for photons since the end of BBN <sup>5</sup>. Therefore, the ratio of number densities of baryons ( $n_{\text{B}}$ ) and photons ( $n_{\gamma}$ ), known as

---

<sup>5</sup>When the temperature dropped below the electron mass, the photons no longer had enough energy to create

the baryon-to-photon ratio, provides just such a measure of the universal baryon abundance:

$$\eta \equiv (n_{\text{B}}/n_{\gamma})_0 ; \eta_{10} \equiv 10^{10}\eta , \quad (1.1)$$

where the subscript ‘0’ refers to the present epoch (redshift  $z=0$ <sup>6</sup>).

An equivalent measure of the baryon density is provided by the baryon density parameter,  $\Omega_{\text{B}}$ , the ratio (at present) of the baryon mass density to the critical density ( $=9.9 \times 10^{-30} \text{ g/cm}^3 \Rightarrow 5.9 \text{ protons/m}^3$ ). In terms of the present value of the Hubble parameter,  $H_0 \equiv 100 \times h \text{ km s}^{-1} \text{ Mpc}^{-1}$  ( $= 71 \text{ km s}^{-1} \text{ Mpc}^{-1}$ ), these two measures are related by

$$\eta_{10} = 274\Omega_{\text{B}}h^2. \quad (1.2)$$

Fig. 1.3 shows the SBBN predicted abundances of primordial  ${}^4\text{He}$  (mass fraction) and D,  ${}^3\text{He}$  and  ${}^7\text{Li}$  (by number relative to H) as a function of baryon-to-photon ratio,  $\eta_{10}$ . With the mapping of the cosmic microwave background and analysis of its temperature anisotropies,  $\eta_{10}$  has been recently measured with great precision and quite independently of primordial abundances by the WMAP NASA probe team, obtaining the value  $\eta_{10} = 6.14 \pm 0.25$  [4] corresponding to  $\Omega_{\text{B}}h^2 = 0.0224 \pm 0.0009$ . Combining SBBN results with the  $\eta_{10}$  value from WMAP (quoted SBBN+WMAP in the following) we get primordial abundances for D,  ${}^3\text{He}$ ,  ${}^4\text{He}$  and  ${}^7\text{Li}$  with a very small uncertainty, as shown in fig. 1.3, where the WMAP  $\eta_{10}$  range intersecting the SBBN yield curves [5] is also represented. Table 1.1 shows the predicted values for the primordial light element abundances at WMAP  $\eta_{10}$ , obtained by different authors. The different predictions come from different methodologies to fit the experimental data (e.g., normalizations, fitting functions, experimental data used).

The comparison of these predicted abundances with the ones inferred from observational data obtained from a variety of astrophysical sites will allow to confirm the standard model of cosmology or, on the contrary, may open a window for new physics.

---

electron-positron pairs. This disrupted the equilibrium between photons and  $e^- - e^+$  pairs, since, while positrons and electrons continued to combine to produce photons, they could no longer be replaced by the reverse reaction. All positrons were eventually consumed leaving a small excess of electrons ( $n_e/n_{\gamma} \approx 10^{-9}$ ) and a constant number of photons.

<sup>6</sup>Redshift,  $z$ , is defined as the change in the wavelength,  $\lambda$ , of the light divided by the rest wavelength of the light:  $z = (\lambda_{\text{observed}} - \lambda_{\text{rest}})/\lambda_{\text{rest}}$ . In this case, we are talking about a cosmological redshift caused by the expansion of the universe.

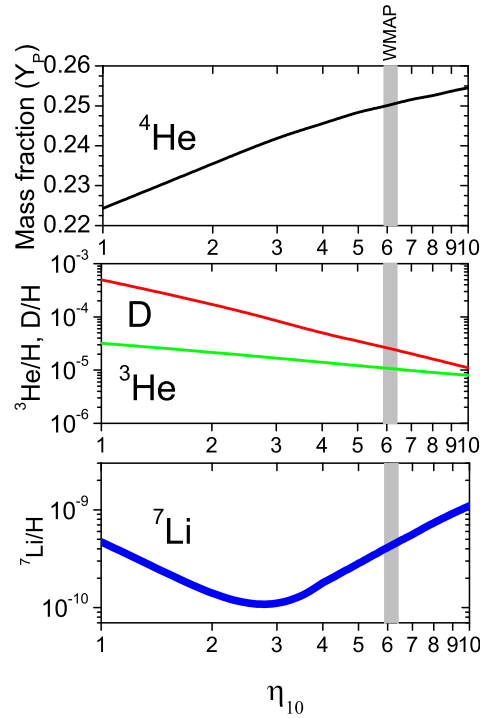


Figure 1.3: Abundance predictions for standard BBN [5]; the width of the curves give the  $1\sigma$  uncertainty range. The WMAP  $\eta_{10}$  range ( $\eta_{10} = 6.14 \pm 0.25$ ) is shown in the vertical (grey) band.

Starting this comparison with  ${}^4\text{He}$ , we know that its primordial abundance,  $Y_{\text{P}}$ , is relatively insensitive to the nuclear reaction rates and, therefore, to the baryon density, because of its large binding energy and the gap at mass 5.  ${}^4\text{He}$  observational abundance is probed via emission from its optical recombination lines in metal-poor, extragalactic ionized hydrogen ( $\text{H II}$ ) regions. Recent observations gave a relatively narrow ranges of abundances:  $Y_{\text{P}} = 0.2452 \pm 0.0015$  (Izotov *et al.* 1999 [8]),  $Y_{\text{P}} = 0.2391 \pm 0.0020$  (Luridiana *et al.* 2003 [9]) and,  $Y_{\text{P}} = 0.2421 \pm 0.0021$  (Izotov and Thuan 2003 [10]). Clearly, these results show statistical inconsistencies and are lower than the predicted values of table 1.1. However, this difference of 2–3% between observation and prediction is relatively modest and it may simply call for further exploration of the systematic effects in the abundance analysis.

Deuterium is considered the ideal baryometer. Deuterium burning, to tritium,  ${}^3\text{He}$  and  ${}^4\text{He}$ , is very fast and the higher the baryon density, the faster the burning and the less deuterium survives. This behaviour makes the SBBN-predicted  $\text{D}/\text{H}$  ratio a monotonic, rapidly decreasing function of the baryon density (fig. 1.3), so  $\text{D}/\text{H}$  is very sensitive to the  $\eta$  value. Furthermore,

	Coc et al. 2004 [5]	Cybert 2004 [6]	Serpico et al. 2004 [7]
D/H	$(2.60^{+0.19}_{-0.17}) \times 10^{-5}$	$(2.55^{+0.21}_{-0.20}) \times 10^{-5}$	$(2.58^{+0.19}_{-0.16}) \times 10^{-5}$
$Y_p$	$0.2479 \pm 0.0004$	$0.2485 \pm 0.0005$	$0.2479 \pm 0.0004$
${}^3\text{He}/\text{H}$	$(1.04 \pm 0.04) \times 10^{-5}$	$(1.01 \pm 0.07) \times 10^{-5}$	$(1.03 \pm 0.03) \times 10^{-5}$
${}^7\text{Li}/\text{H}$	$(4.15^{+0.49}_{-0.45}) \times 10^{-10}$	$(4.26^{+0.91}_{-0.86}) \times 10^{-10}$	$(4.6^{+0.4}_{-0.4}) \times 10^{-10}$

Table 1.1: SBBN results at WMAP  $\Omega_B h^2$  from different authors.

since deuterium is burned away whenever it is cycled through stars, and no mechanisms are known which may lead to deuterium production, any observed D abundance provides a lower bound to its primordial abundance. For systems at high redshift with very low metallicity, which have experienced a very limited stellar evolution, the observed D abundance should be close to the primordial value. Thus, although there are observations of deuterium in the solar system and the interstellar medium of the Galaxy, which provide lower bounds to the primordial abundance, it is the observations of relic D in a few, high redshift, low metallicity, cosmological clouds along the line of sight of quasars (Lyman- $\alpha$  radiation from the quasars are absorbed and re-emitted by the deuterium of those clouds) which are most valuable in enabling estimates of its primordial abundance.

The SBBN+WMAP predictions for D/H (listed in table 1.1) are all compatible within errors and are in good agreement with the average value  $(2.40 \pm 0.3) \times 10^{-5}$  of recent D/H observations as measured from 6 quasar absorption systems [11] (see fig. 1.4). This agreement strengthens the confidence on the estimated baryonic density of the universe and on the SBBN model itself. However, as shown in fig. 1.4, there is statistically significant scatter of the individual D/H measurements about the average. As deuterium destruction in these clouds is expected to be very low and since the primordial D/H is thought to be isotropic and homogeneous, the scatter is hard to explain. One explanation is that the systematic errors in measuring D/H have been underestimated by the authors. Nevertheless, with only a few quasar absorption systems studied so far, other explanations, such as some early mechanism for deuterium destruction or a non standard BBN, cannot be ruled out. More D/H measurements are needed to understand this scattering problem.

As may be seen from fig. 1.3, the predicted primordial abundance of  ${}^3\text{He}$  behaves similarly

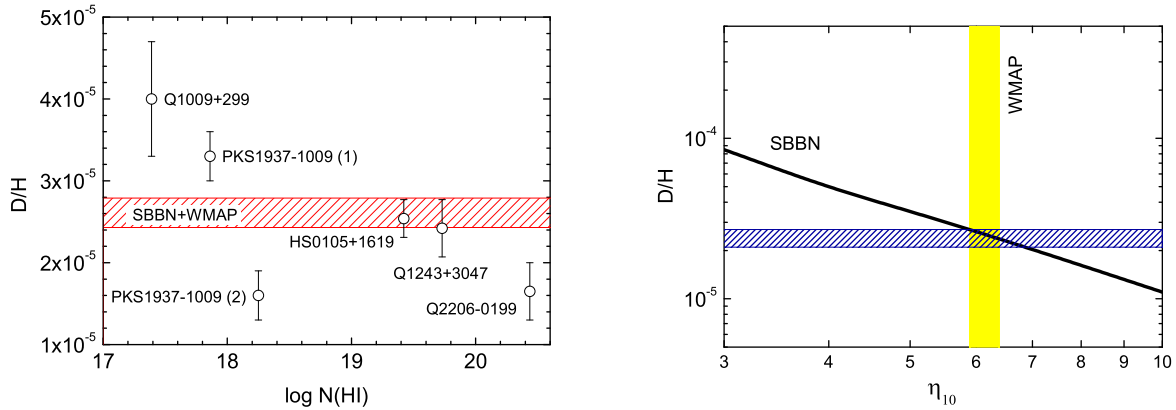


Figure 1.4: Left panel:  $D/H$  measurements as a function of  $\log N(\text{HI})$  [ $N(\text{HI})$  is the column density in units of  $\text{cm}^{-2}$ ] in the absorber where the measurement was made. The hashed region is the WMAP+SBBN prediction for  $D/H$  from Coc *et al.* 2004 [5]. Right panel: Ratio  $D/H$  as a function of  $\eta_{10}$ . The horizontal stripe represent the average primordial D abundance deduced from observational data,  $(2.40 \pm 0.3) \times 10^{-5}$  – see text. The vertical stripe represent the ( $1\sigma$  uncertainty range)  $\eta_{10}$  limits of WMAP.

to that of D, decreasing monotonically with  $\eta$ . Although the SBBN+WMAP predicted values show small uncertainties (see table 1.1), the complex and uncertain evolution of  ${}^3\text{He}$  with stellar destruction competing with primordial and stellar production makes difficult the use of current observational data to infer the primordial abundance of  ${}^3\text{He}$ , inhibiting the comparison between predicted and observational values [6].

The trend of the BBN-predicted primordial abundance of lithium (almost entirely  ${}^7\text{Li}$ ) with  $\eta$  is more ‘interesting’ than that of the other light nuclides (see fig. 1.3). The “lithium valley”, centered near  $\eta_{10} \approx 2 - 3$ , is the result of the competition between production and destruction in the two paths to mass-7 synthesis. At relatively low baryon abundance ( $\eta_{10} \lesssim 2$ ) mass-7 is mainly synthesized as  ${}^7\text{Li}$  via  $\text{T}(\alpha, \gamma){}^7\text{Li}$ . As the baryon abundance increases,  ${}^7\text{Li}$  is destroyed rapidly by the reaction  ${}^7\text{Li}(p, \alpha){}^4\text{He}$ . Hence the decrease in  ${}^7\text{Li}/\text{H}$  with increasing  $\eta$  seen (at low  $\eta$ ) in fig. 1.3. Were this the only route to primordial synthesis of mass-7, this monotonic trend would continue, similar to those for D and  ${}^3\text{He}$ . However, mass-7 may also be synthesized via  ${}^3\text{He}(\alpha, \gamma){}^7\text{Be}$ . The  ${}^7\text{Be}$  will decay to  ${}^7\text{Li}$  by electron capture ( ${}^7\text{Be}$  destruction by  ${}^7\text{Be}(n, p){}^7\text{Li}$  is inefficient because of the lower neutron abundance at high density). This channel is very im-

portant because it is much *easier* to destroy  ${}^7\text{Li}$  than  ${}^7\text{Be}$ . As a result, for relatively high baryon abundance ( $\eta_{10} \gtrsim 3$ ) this latter channel dominates mass-7 production and  ${}^7\text{Li}/\text{H}$  increases with increasing  $\eta$ . The WMAP results point towards the high  $\eta$  region.

From observations of 11 main-sequence stars belonging to the Milky Way Galactic halo <sup>7</sup> Spite & Spite 1982 [12] concluded that the lithium abundance was essentially independent of metallicity for halo stars hotter than 5600 K (the so-called Spite plateau), with the numerical value

$$\frac{{}^7\text{Li}}{\text{H}} = (1.12 \pm 0.38) \times 10^{-10}, \quad (1.3)$$

or, equivalently, on the usual astronomical scale <sup>8</sup>

$$A({}^7\text{Li}) = 2.05 \pm 0.15 \text{ dex}. \quad (1.4)$$

Halo stars, as the ones studied by Spite & Spite, are of Population II, which are the first long-lived stars to have formed after the Big Bang <sup>9</sup>. They are thought to be good lithium 'sources' because, contrary to Population I stars, they are not contaminated with elements produced in earlier generation of stars (*i.e.*, have low metal abundance). However, the elderness of these stars can also pose some problems, as some poorly known stellar mechanism(s) may have altered their lithium abundances by an uncertain amount which is not noticeable in our time scale. We will be back to this subject later in this chapter.

Now, more than two decades of measurements has followed since Spite & Spite first results, increasing the number of stars observed and the range of metallicity that they span, confirming a plateau in the warmer ( $T \gtrsim 5600$  K) and more metal-poor ( $[\text{Fe}/\text{H}] \lesssim -1.3$ ) <sup>10</sup> halo stars. Maurice, Spite, and Spite 1984 [13] showed that the dominant isotope in the plateau was  ${}^7\text{Li}$ : a limit  ${}^6\text{Li}/{}^7\text{Li} < 0.1$  was set for a couple of stars. Ryan, Norris, and Beers 1999 [14] showed that the Spite plateau is very "thin", with an intrinsic star-to-star scatter in derived lithium

---

<sup>7</sup>The galactic halo is a spheroidal region of space surrounding spiral galaxies, like the Milky Way.

<sup>8</sup> $A(X) \equiv \log(n_X/n_H) + 12$ , where  $n_X$  and  $n_H$  stand for the number density of atoms of element  $X$  and atoms of hydrogen, respectively; the term "dex" stands for decimal exponent.

<sup>9</sup>In fact, there are speculations about a new kind of stars, very massive and short lived, called Population III stars which are believed to have been formed in the early universe, before Population II stars. They have not been observed directly, but are thought to be the components of faint blue galaxies. The low-metallicity Population II stars are thought to contain the metals produced by population III stars.

<sup>10</sup> $[A/B] = \log(n_A/n_B) - \log(n_A/n_B)_\odot$ , where  $n_A$  and  $n_B$  stands for the number density of atoms of element A and B, respectively, and  $\odot$  refers to the Sun.

abundance  $\sigma < 0.02$  dex. These authors also claimed the existence of a statistically significant positive slope of  $A(^7\text{Li})$  with  $[\text{Fe}/\text{H}]$  in the plateau:

$$dA(^7\text{Li})/d[\text{Fe}/\text{H}] = 0.118 \pm 0.023 \text{ (dex per dex)} . \quad (1.5)$$

First detected by Thorburn 1994 [15] (+ 0.13), this slope is apparently due to the influence of early Galactic chemical evolution, namely from Galactic Cosmic Rays  $^7\text{Li}$  production (see section 1.2.2).

From the small star-to-star scatter in  $^7\text{Li}$  abundance at the plateau <sup>11</sup> it is usually inferred that these very old stars surface abundance cannot have changed greatly from its initial value, so the primordial lithium abundance is identified with the extrapolation of the observed lithium abundances to  $-\infty$  metallicity, *i.e.*,

$$A(^7\text{Li})_{\text{primordial}} \equiv A(^7\text{Li})_{[\text{Fe}/\text{H}] \rightarrow -\infty} . \quad (1.6)$$

In the year 2000, Ryan *et al.* [16], using a large number of observations (see fig. 1.5) predicted a primordial abundance ( $2\sigma$  uncertainty):

$$\frac{^7\text{Li}}{\text{H}} = (1.23_{-0.32}^{+0.68}) \times 10^{-10} \Leftrightarrow A(^7\text{Li}) = 2.09_{-0.11}^{+0.24} \text{ dex} , \quad (1.7)$$

a value compatible with the original value given by Spite & Spite. These authors have extensively studied and quantified the various sources of uncertainty such as stellar depletion and stellar atmosphere parameters. This  $^7\text{Li}/\text{H}$  value, was considered, before the WMAP  $\Omega_{\text{B}}h^2$  value, as the most reliable constraint on SBBN and hence on  $\Omega_{\text{B}}h^2$ .

More recent publications confirm Ryan *et al.* 2000 results apart some small variations. Table 1.2 summarizes the more relevant data from some of these publications (including Ryan *et al.* 2000).

Excluding the  $^7\text{Li}$  abundance value calculated by Melendez and Ramirez 2004 <sup>12</sup>, the observational average value taken from table 1.2 is:

---

<sup>11</sup>In fact, there are a few stars which should inhabit the Spite plateau but show very large depletions of lithium, and are set aside in estimations of the intrinsic dispersion. Others, very very few, show a lithium abundance clearly in excess of the plateau's value, and are also not considered in the plateau's analysis. The nature of these stars is currently under debate, but a plausible scenario is that they may have suffered a mass transfer process from/to nearby stars.

<sup>12</sup>This higher  $^7\text{Li}$  abundance value is essentially due to a controversial temperature scale adopted by Melendez and Ramirez which, for the lowest metallicity stars, gives temperatures  $\approx 400$  K above the other temperature scales (see, for example the comments of Asplund *et al.* 2005 [20] on this subject).

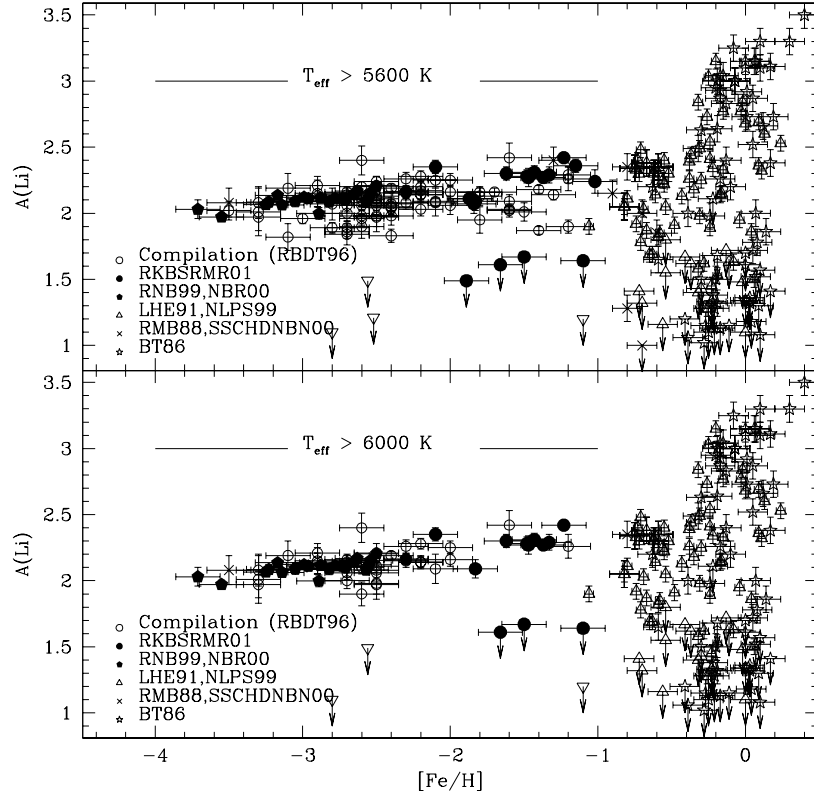


Figure 1.5: Top panel:  $A(\text{Li})$  on  $[\text{Fe}/\text{H}]$  for halo stars with  $T_{\text{eff}} > 5600$  K. Bottom panel: As for the top panel, but restricting the halo sample to  $T_{\text{eff}} > 6000$  K to avoid the  $T_{\text{eff}}$  dependence. Plot taken from [16].

Author(s)	Nb of stars	$[\text{Fe}/\text{H}]$ range	$A(^7\text{Li})$ (dex)
Ryan <i>et al.</i> 2000 [16]	(a)	$-3.3 \rightarrow -2.3$	$2.09^{+0.24}_{-0.11}$
Bonifacio <i>et al.</i> 2003 [17]	18	$-3.6 \rightarrow -2.5$	$2.20 \pm 0.1$
Melendez and Ramirez 2004 [18]	62	$-3.4 \rightarrow -1.0$	$2.37 \pm 0.06$
Charbonnel and Primas 2005 [19]	(b)	$-3.5 \rightarrow -1.5$	$2.21 \pm 0.09$
Asplund <i>et al.</i> 2005 [20]	24	$-3.0 \rightarrow -1.0$	$\approx 2.15$

Analysis of observational data: (a) compilation from 1986 to 2000; (b) compilation from the early nineties onwards.

Table 1.2:  $^7\text{Li}$  observational abundance results from different authors.

$$\frac{{}^7\text{Li}}{\text{H}} = (1.45 \pm 0.17) \times 10^{-10} \Leftrightarrow A({}^7\text{Li}) = 2.16 \pm 0.05 \text{ dex} , \quad (1.8)$$

which is about 0.5 dex (or a factor three) lower than the SBBN+WMAP average value (obtained averaging the three values in table 1.1):

$$\left(\frac{{}^7\text{Li}}{\text{H}}\right)_{\text{SBBN+WMAP}} = (4.34^{+0.29}_{-0.28}) \times 10^{-10} \Leftrightarrow A({}^7\text{Li})_{\text{SBBN+WMAP}} = 2.64 \pm 0.03 \text{ dex} . \quad (1.9)$$

This discrepancy is perfectly visible in fig. 1.6 where the WMAP  $\eta_{10}$  range and the average inferred observational abundance (eq. 1.8) range intersecting the SBBN yield curve for  ${}^7\text{Li}$  are represented. It is surprising that the major discrepancy between WMAP and observational abundances affects  ${}^7\text{Li}$  since it could a priori lead to a more reliable primordial value than deuterium, because of much higher observational statistics, and an expected easier extrapolation to primordial values.

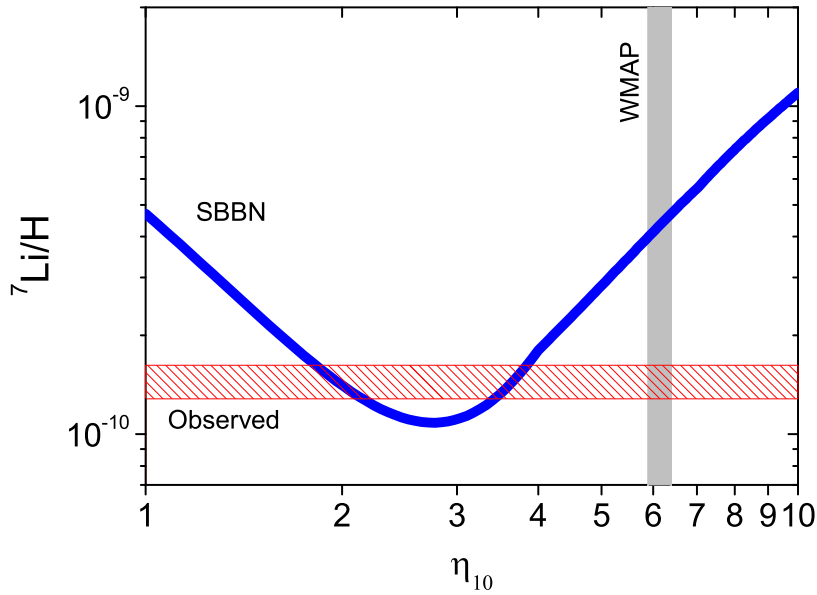


Figure 1.6: Abundance of  ${}^7\text{Li}$  as a function of the baryon over photon ratio. The horizontal stripe represents the primordial  ${}^7\text{Li}$  abundance deduced from observational data, and the vertical stripe represents the ( $1\sigma$  uncertainty)  $\eta_{10}$  limits provided by WMAP.

Another intriguing discrepancy comes from the lighter lithium isotope:  ${}^6\text{Li}$  is more readily destroyed by proton bombardment, so, its presence in the atmosphere of population II stars is

usually considered as a very severe limit on the amount of  ${}^7\text{Li}$  depletion. This argument is very often used in favor of the Li plateau abundance being the primordial value, a conclusion that is now challenged by the WMAP constraint.

The first probable detection of  ${}^6\text{Li}$  in a very metal-poor star was reported by Smith *et al.* 1993 [21] with  ${}^6\text{Li}/{}^7\text{Li} = 0.06 \pm 0.03$ . Confirmation was provided by Hobbs & Thorburn 1994, 1997 [22, 23], Smith *et al.* 1998 [24] and subsequently by Cayrel *et al.* 1999 [25] who obtained  ${}^6\text{Li}/{}^7\text{Li} = 0.052 \pm 0.019$ . Smith *et al.* 1998 observed seven single stars and reported  ${}^6\text{Li}$  in one additional very metal-poor star. Cayrel *et al.* 1999 provided a possible detection of  ${}^6\text{Li}$  in another star as did Nissen *et al.* 2000 [26] for even another star. Very recently, Asplund *et al.* 2005 [20] detected  ${}^6\text{Li}$  in 9 out of 24 metal-poor halo stars at the  $2\sigma$  significance level, suggesting a  ${}^6\text{Li}$  plateau at the level of (see fig. 1.7):

$$A({}^6\text{Li}) \approx 0.8 \text{ dex} \Leftrightarrow \frac{{}^6\text{Li}}{{}^7\text{Li}} \approx 0.04 \Leftrightarrow \frac{{}^6\text{Li}}{\text{H}} \approx 5.8 \times 10^{-11}, \quad (1.10)$$

which extends in metallicity range from  $[\text{Fe}/\text{H}]=-2.7$  to  $[\text{Fe}/\text{H}]=-0.6$  (the two highest metallicity stars (at  $[\text{Fe}/\text{H}]=-0.6$ ) are not shown in fig. 1.7 and correspond to the observations of Cayrel *et al.* 1999 [25] and Nissen *et al.* 2000 [26]).

To this estimate it should be added the expected  ${}^6\text{Li}$  depletion, which is greater than 0.3 dex during the pre-main sequence, during which  ${}^7\text{Li}$  remains largely intact (if, in addition, some  ${}^7\text{Li}$  has been destroyed as well this would increase the  ${}^6\text{Li}$  depletion further).

The predicted SBBN+WMAP abundance of  ${}^6\text{Li}$  is exceedingly low,  ${}^6\text{Li}/{}^7\text{Li} \approx 10^{-5}$ , several orders of magnitude lower than the detected one.

So, in summary, several questions now face the scientists that study the abundances of  ${}^6\text{Li}$  and  ${}^7\text{Li}$  in very metal-poor stars. Assuming that the WMAP  $\eta_{10}$  value is correct, which tightly constrains the predictions of the nucleosynthesis by the Big Bang, what can explain the difference between the predicted and observed  ${}^7\text{Li}$  and  ${}^6\text{Li}$  abundances? Do they imply that the standard picture of primordial nucleosynthesis needs modification? Or is it that the true primordial abundances of  ${}^7\text{Li}$  and  ${}^6\text{Li}$  differ from the abundances identified by observers as the primordial ones? For  ${}^7\text{Li}$ , this last option means that stars on the Spite plateau have had their surface lithium abundance reduced over their lifetime of more than 10 billion years. Here, the challenging issue is to identify the mechanism(s) by which a reduction of 0.5 dex can occur so uniformly in all the plateau stars. For  ${}^6\text{Li}$ , the high abundance observed in some halo stars may

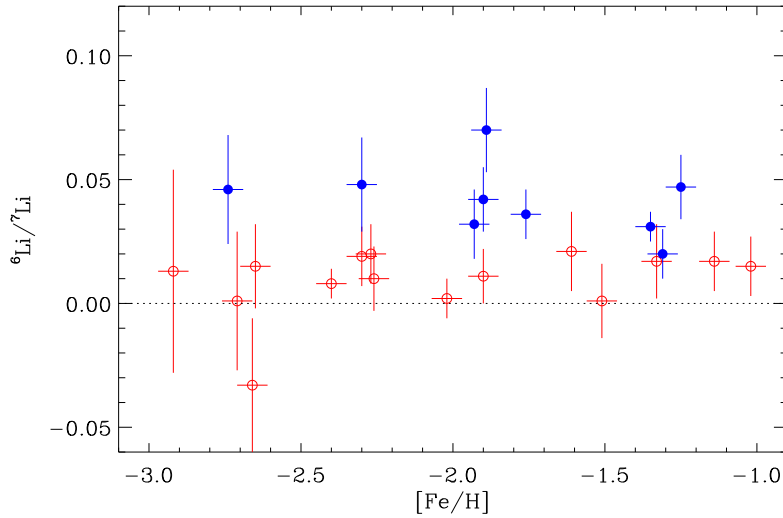


Figure 1.7: Derived  ${}^6\text{Li}/{}^7\text{Li}$  as a function of  $[\text{Fe}/\text{H}]$ . The stars considered to have a significant detection ( $\geq 2\sigma$ ) of  ${}^6\text{Li}$  are shown as solid circles while non-detections are plotted as open circles. Plot taken from [20].

suggest that the major fraction of this isotope may have been synthesized prior to the onset of star formation in the galaxy.

In the next section, we take up the questions just outlined: how can one reconcile the predicted  ${}^7\text{Li}$  abundance using the WMAP-based  $\eta_{10}$  with the measurement of the abundance for the Spite plateau? How does one account for those  ${}^6\text{Li}$  abundances that greatly exceed the Big Bang prediction?

## 1.2 Search for solutions to the lithium discrepancies

In order to solve the lithium discrepancies, research has focused essentially on the following propositions:

1. stellar: systematic error affects the determinations of the  ${}^6\text{Li}$  and  ${}^7\text{Li}$  abundances of metal-poor stars, and/or these abundances are not those of the primordial gas;
2. pre-galactic evolution: while primordial lithium implies its production in the early universe, either during the period of Big Bang nucleosynthesis or shortly after, i.e. through the decay of an unstable (super-)particle, pre-galactic lithium implies its production prior

to star or galaxy formation;

3. cosmology: the standard physics incorporated into the Big Bang nucleosynthesis predictions is incomplete;
4. nuclear: the nuclear reaction rates adopted for primordial nucleosynthesis is incomplete and/or errors in the adopted reaction rates result in a systematic overestimate of the predicted  ${}^7\text{Li}$  abundance, and/or gross underestimate of the  ${}^6\text{Li}$  abundance.

In the following sections, we comment on these four propositions.

### 1.2.1 Stellar

Among the primordial light elements, lithium is one of the easiest to observe, despite being several orders of magnitude less abundant than the others. Lithium appears in a stellar absorption spectrum with few transitions, namely the resonant line at 670.8 nm, and a much weaker line at 610.4 nm (as shown in the Grotrian diagram of fig. 1.8).

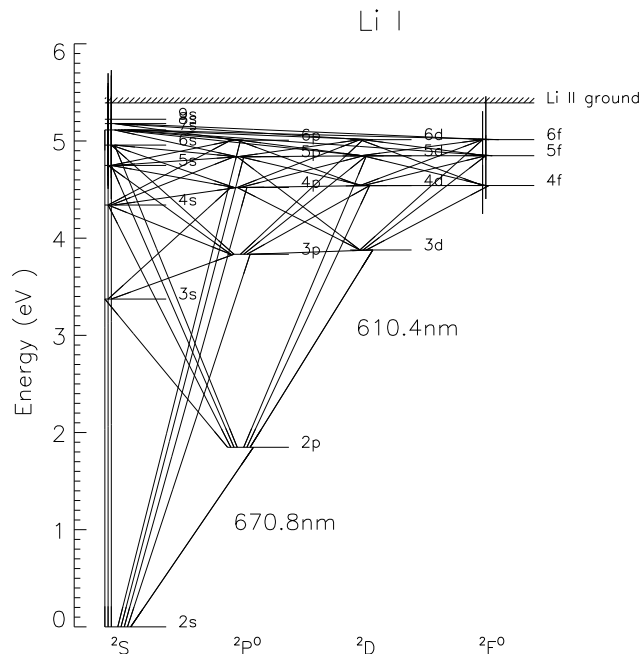


Figure 1.8: Grotrian diagram for the 21-level Li atom model. All levels are connected with the Li II ground state by photo-ionization transitions. The astrophysically relevant 670.8 and 610.4 nm lines correspond to the  $2s - 2p$  and  $2p - 3d$  transitions, respectively. Diagram taken from [27].

The 670.8 nm and 610.4 nm lines fall in a clean spectral region (see fig. 1.9), especially in metal-poor stars. This is important since  ${}^7\text{Li}$  and  ${}^6\text{Li}$  abundances are derived from the width ( $W_\lambda$ ) of these spectral lines [19], allowing precise measurements of this parameter for both lithium isotopes (the presence of the low abundance isotope,  ${}^6\text{Li}$ , manifests itself as an asymmetry in the Li I 670.8 nm and 610.4 nm lines). These observed line widths are inputs into the standard atmosphere model<sup>13</sup> that simulate lithium evolution in a star characterized by a given set of input parameters such as, star's effective temperature ( $T_{\text{eff}}$ ), surface gravity ( $g$ ), composition (metallicity), and microturbulence ( $\xi$ )<sup>14</sup>. These models have been widely used since they predict a negligible  ${}^7\text{Li}$  depletion for halo stars in different evolutionary stages, thus leading to the Spite plateau and, explain quite well the decline in the lithium abundances for metal-poor stars with  $T \lesssim 5600$  K due to the first dredge-up<sup>15</sup>. This plateau is, however, a factor 3 (0.5 dex) lower than the SBBN+WMAP prediction. These models also predict that  ${}^6\text{Li}$  should be thoroughly destroyed by protons ( $> 0.3$  dex) on the stars attaining the main sequence, contrary to what has been observed in several halo stars.

Even if we consider the uncertainties on the stellar input parameters mentioned before, the discrepancies between predicted and observed abundances don't disappear. With the exception of  $T_{\text{eff}}$ , all other parameters have a small effect on the derived  ${}^7\text{Li}$  and  ${}^6\text{Li}$  abundances [20]. Common uncertainties on  $\log(g)$ ,  $[\text{Fe}/\text{H}]$  and  $\xi$  ( $\pm 0.25$  dex,  $\pm 0.15$  dex, and 0.3 km/s, respectively) affect the final  ${}^7\text{Li}$  abundances by at most 0.005 dex, 0.015 dex, and 0.003 dex. When summed over quadrature, the resulting uncertainty is around 0.0017 dex only [19]. For  $T_{\text{eff}}$ , an uncertainty of  $\pm 70$  K (commonly quoted as a reasonable uncertainty on this parameter) translates into a  $\pm 0.05$  dex on the lithium abundance<sup>16</sup>. In order the inferred primordial  ${}^7\text{Li}$

---

<sup>13</sup>The standard atmosphere model is based on the assumptions of plane-parallel homogeneous layers, hydrostatic equilibrium, local thermodynamic equilibrium (LTE), and constant flux with the energy carried by a combination of radiation and convection.

<sup>14</sup>Microturbulence: small-scale motions (up to 5 km/s) in a stellar atmosphere that broaden the star's spectral lines and may contribute to their effective width.

<sup>15</sup>According to the standard stellar evolution theory, the only opportunity for low mass stars to modify their surface abundances happens on their way to the red giant branch (RGB) when they undergo the so-called first dredge-up. During this event their convective envelope deepens in mass, leading to the dilution of the surface primordial material within regions that have undergone partial nuclear processing on the main sequence. This leads to the decrease of the surface abundances of several elements like lithium.

<sup>16</sup>The large uncertainty associated to  $T_{\text{eff}}$  comes from the fact that since these metal-poor stars are too distant

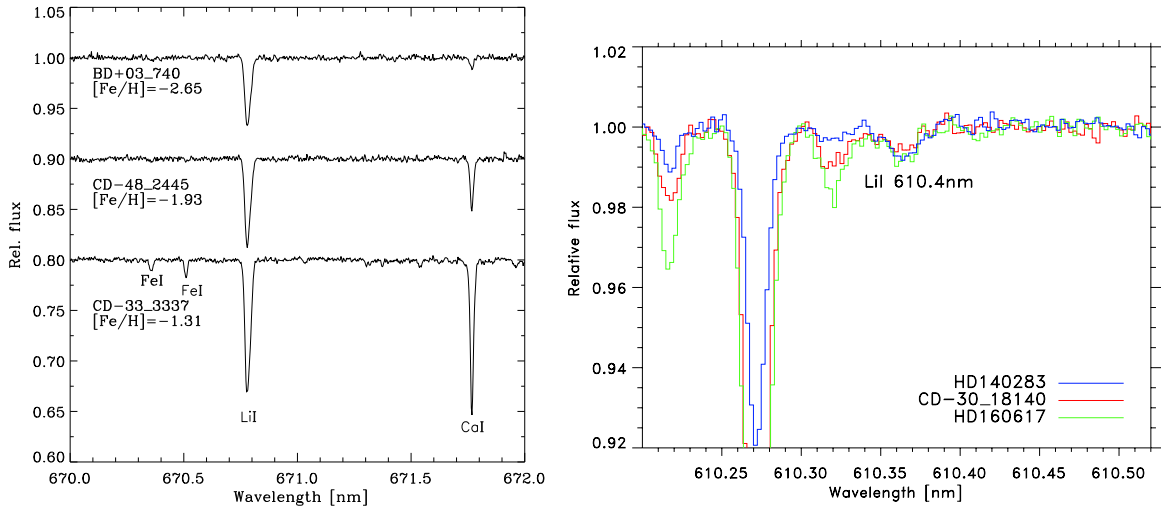


Figure 1.9: Left panel: Sample spectra around the Li I 670.8 nm line for three metal-poor halo stars. Plot taken from [20]. Right panel: The region around the Li I 610.4 nm for three metal-poor stars. The Fe I 610.22 nm, Ca I 610.27 nm, and Fe I 610.32 nm lines are also present in this region. These lines have a different strength in each star. In contrast, the Li I line has a very similar strength in the three stars – an illustration of the Spite plateau. Plot taken from [28].

abundance to raise by 0.5 dex to the SBBN+WMAP prediction, the temperatures must be raised by about 900 K, an impossible systematic error [28].

So, evidently, depletion of  ${}^7\text{Li}$  according to standard models is not the answer to the lithium problem.

The search for a solution to the lithium problem then turns to investigation of non-standard models of stellar evolution. Physical processes neglected by standard models but incorporated into non-standard models in connection with halo stars in recent years include rotationally-induced mixing (e.g. Pinsonneault et al. 1999 [29], 2002 [30]), diffusion<sup>17</sup> (e.g. Richard et al. 2002 [31]; 2005 [32]) and internal gravity waves (e.g. Charbonnel & Talon 2005 [34]), sometimes working in tandem with other mechanisms such as mass loss (e.g. Vauclair & Charbonnel 1995 [35]) and turbulent mixing. In most cases, the predictive power of these processes is restricted by their need to introduce one or more free parameters [20].

We comment briefly on two (more studied) non-standard models drawn from the suite of  


---

to measure their angular diameters, indirect methods have to be used to estimate their temperatures – e.g., spectroscopy, or photometry.

<sup>17</sup>The term diffusion normally includes the effects of gravitational settling, thermal diffusion and radiative acceleration.

proposals: rotationally-induced mixing and diffusion. An obvious requirement of successful non-standard models is that they provide a depletion of surface lithium by about 0.5 dex over the 10-13 Gyr life of the observed stars (we take it as given that the stars began life with the WMAP-inferred predicted lithium abundance). Surely, a more demanding requirement (and a certain clue to the dominant process) is that this depletion be achieved uniformly over the observed sample of stars spanning a range in mass, metallicity, age, and rotational angular momentum: the depletion of about 0.5 dex can not present a star-to-star scatter of more than about 0.03 dex. In identifying non-standard models that may solve the lithium problem we will obtain also an estimate of the correction to be applied to a  ${}^6\text{Li}$  abundance to obtain the star's original  ${}^6\text{Li}$  abundance.

A description of lithium destruction from rotationally-induced mixing depends on quantities that are as yet poorly known: the distribution of initial angular momentum in the star, how the loss of angular momentum proceeds, the internal transport of angular momentum and the accompanying mixing, and the effects of rotation on the overall stellar structure. Pinsonneault et al. 1999 [29] found that depletion of  ${}^7\text{Li}$  ( $D_7$  in dex) was related to the dispersion ( $\sigma$  in dex) where  $\sigma/D_7 \simeq 0.4$  and, hence, the required depletion by 0.5 implies  $\sigma = 0.2$ , a value far in excess of the observed value, 0.03 dex. The depletions of  ${}^7\text{Li}$  and  ${}^6\text{Li}$  were predicted to be correlated:  $D_7/D_6 \simeq 0.4$  yielding  $D_6 \simeq 1.2$  dex. Given that the observed  $A({}^6\text{Li}) \simeq 0.8$  for the stars with detected  ${}^6\text{Li}$ , the initial abundance would have been  $A({}^6\text{Li}) \simeq 2.0$ , the value that has historically been identified with the Spite plateau for  ${}^7\text{Li}$ , and, more importantly, a value that implies most or all of the  ${}^7\text{Li}$  came from synthesis by cosmic rays and not from the Big Bang! (Cosmic rays spallation predicts a production ratio  ${}^6\text{Li}/{}^7\text{Li} \approx 1$  to 2 – see section 1.2.2.) In summary, rotationally-induced mixing, by itself, appears not to be the solution to the  ${}^7\text{Li}$  problem.

Stars on the Spite plateau have a thin convective envelope of uniform composition. Atomic diffusion occurs in the radiative zone below the convective envelope. The base of the latter mixes with and attains the composition of the top of the radiative zone. Diffusion is a slow process but is predicted to be effective in the halo stars because of their great age and their thin convective envelopes. Lithium is predicted to diffuse inwards in the radiative zone and the surface abundance to decrease. Inward diffusion of lithium can result in its destruction by protons via  ${}^7\text{Li}(p, \alpha){}^4\text{He}$  and  ${}^6\text{Li}(p, \alpha){}^3\text{He}$  reactions.

Model calculations including diffusion suggest that the lithium abundance for stars on the Spite plateau is essentially flat in the temperature range 5800 – 6200 K, with an uniform decrease of  $\approx 0.3$  dex [28] in lithium abundance. This result would quite shorten the gap between observed and SBBN+WMAP predictions. However, diffusion also predicts a significant drop in lithium abundance for stars hotter than about 6200 K, a drop not seen by observers. In order to solve this new discrepancy, turbulent diffusion is introduced in the radiative zone, changing the predictions in two ways. First, the lithium depletion among the hottest stars is reduced so that the plateau can be extended across a wider temperature range than is possible with atomic diffusion acting alone. Second, mixing in the radiative zone destroys lithium and leads to a lower surface lithium abundances across the plateau. This would make observational and SBBN+WMAP values compatible. However, it is not yet clear that the lack of scatter on the observed plateau is reproduced by these models. Turbulent diffusion of the strength necessary to bridge the gap between WMAP-based prediction and observed lithium abundances leads to a larger destruction of  ${}^6\text{Li}$  than  ${}^7\text{Li}$  and, hence, a reduction of the surface  ${}^6\text{Li}/{}^7\text{Li}$  ratio below the initial value. This result is strongly incompatible with standard primordial nucleosynthesis.

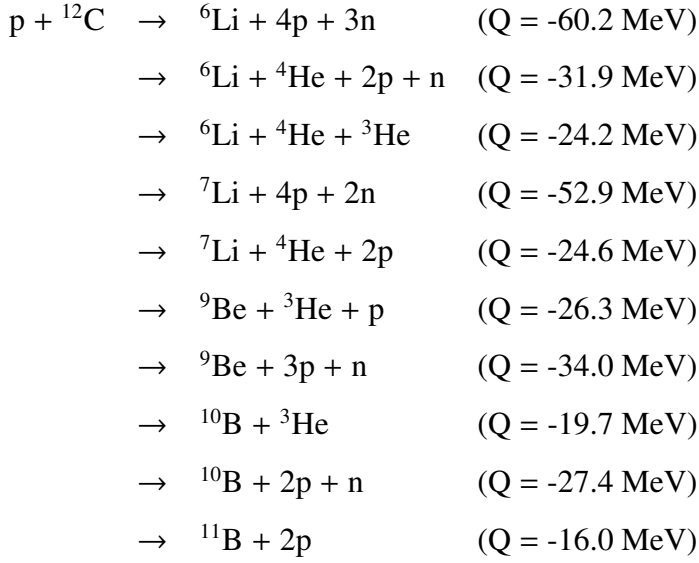
In summary, rotationally-induced mixing and diffusion shows that these plausible (rotationally-induced mixing) and seemingly inevitable (diffusion) processes may solve the  ${}^7\text{Li}$  problem, but the observers' challenge to fit the Spite plateau's shallow slope with respect to  $[\text{Fe}/\text{H}]$  and its smoothness are as yet unmet. These potential solutions to the  ${}^7\text{Li}$  problem indicate that the observed  ${}^6\text{Li}$  abundance is almost certainly a lower bound to the initial  ${}^6\text{Li}$  abundance.

### 1.2.2 Pre-galactic evolution

In 1970, Reeves *et al.* [36] showed that the light elements Li, Be and B are produced by the interaction of the energetic nuclei of galactic cosmic rays (GCR) with the nuclei of the interstellar medium (ISM). The two leading processes are the  $\alpha+\alpha$  fusion reactions and spallation reactions<sup>18</sup> involving protons (also  $\alpha$ s) and  ${}^{16}\text{O}$ ,  ${}^{14}\text{N}$  and  ${}^{12}\text{C}$  such as [37]:

---

<sup>18</sup>Nuclear reactions, in which several particles are emitted in the exit channel, are called spallation reactions.



In these reactions the production ratio  ${}^6\text{Li}/{}^7\text{Li} \approx 1$  to 2 (Mercer *et al.* 2001 [38]). Even though primordial and pre-galactic evolution of the light element abundances was not considered in Reeves *et al.* model, it was, nevertheless, able to reproduce the abundances of  ${}^6\text{Li}$ ,  ${}^9\text{Be}$ ,  ${}^{10}\text{B}$  and  ${}^{11}\text{B}$  observed in meteorites and in cosmic rays, *i.e.*, after  $\approx 10^{10}$  years of galactic evolution.

According to this model,  ${}^6\text{Li}$  abundance is expected to rise continuously during galactic evolution (*i.e.*, rise with the metallicity), similar to the one displayed by  ${}^9\text{Be}$ , which is only synthesized by cosmic rays. Taking into account the observed abundance of  ${}^9\text{Be}$  in stars of metallicity  $[\text{Fe}/\text{H}] \approx -3$  and the respective production cross-sections, it is expected that the  ${}^6\text{Li}/\text{H}$  ratio at such low metallicities would be considerably less than  $10^{-12}$ .

However, the reported  ${}^6\text{Li}$  by Asplund *et al.* 2005 [20] in halo stars of the Milky Way, shows a  ${}^6\text{Li}/\text{H}$  value at  $[\text{Fe}/\text{H}] = -2.7$  of  $\approx 5.8 \times 10^{-11}$  (eq. 1.10), which is much larger than expected if “standard” galactic cosmic rays are the only source of  ${}^6\text{Li}$ <sup>19</sup>. Even more, this  ${}^6\text{Li}$  plateau seems to be independent of metallicity (in the range  $-2.7 \lesssim [\text{Fe}/\text{H}] \lesssim -0.6$ ), which also contradicts the predictions of Reeves *et al.* [36]. So, on the assumption that the standard Big Bang sequence is the correct representation of the primordial fireball, the observation of a  ${}^6\text{Li}$  plateau suggests a pre-galactic origin for this isotope.

Pre-galactic cosmic rays were devoid of CNO nuclei, so in this era  ${}^6\text{Li}$  was mainly produced through  $\alpha+\alpha$  fusion reactions.

---

<sup>19</sup>It is worth mentioning that this problem was already noticed by Ramaty *et al.* 2000 [40] after preliminary reports of  ${}^6\text{Li}$  detection in very low metallicity halo stars.

Recently, Prantzos 2006 [39] calculated the energy requirements for pre-galactic  ${}^6\text{Li}$  production through this process. He concluded that it takes at least  $10^7$  J/g to reach the observed  ${}^6\text{Li}$  plateau ( $10^7$  J in accelerated particles for each gram of the ISM). This author has also “investigated” a few accelerating sources: normal core collapse supernovae (SN), atypical SN (energetic with a low Fe yield), shocks from cosmic structure formation, and the supermassive black hole lying in the galactic center. In summary, Prantzos concluded that the energy requirements for large early  ${}^6\text{Li}$  production are very constraining and hard to fulfill by these sources. Nevertheless, assuming that  ${}^6\text{Li}$  was already present in the earliest moments of the formation of the stars and galaxies, at an abundance level as high as suggested by the observations of Asplund *et al.* 2005 [20],  ${}^6\text{Li}$  observed in halo stars must also consider subsequent  ${}^6\text{Li}$  production by fusion of energetic alpha particles and spallation of CNO nuclei. This tracking is done using models which simulate the Milky’s Way’s chemical evolution (see Prantzos 2006 [39] and references therein).

Fig. 1.10 shows the evolution of  ${}^7\text{Li}$ ,  ${}^6\text{Li}$  and  ${}^9\text{Be}$  as predicted by Prantzos 2006 [39]. This author adopted a pre-galactic  ${}^7\text{Li}$  value that is either “low”, *i.e.*, at the level of the observed Spite plateau (eq. 1.8), or “high”, *i.e.*, at the level of SBBN+WMAP (eq. 1.9). Similarly, and for consistency, a “low” and a “high” value are adopted for pre-galactic  ${}^6\text{Li}$ , respectively  ${}^6\text{Li}/\text{H} \approx 5.8 \times 10^{-11}$  and 0.5 dex higher (assuming its depletion has been equal to the one of  ${}^7\text{Li}$ , and which is the minimal possible amount of  ${}^6\text{Li}$  depletion since, as already mentioned, this isotope is more fragile than  ${}^7\text{Li}$  and should be more depleted). It can be seen that:

- production of  ${}^7\text{Li}$  via cosmic rays may account for the slope of the Spite plateau with metallicity (see eq. 1.5);
- the evolution of  ${}^9\text{Be}$  is satisfactorily reproduced and the cosmic ray component of  ${}^6\text{Li}$  is sufficient to produce the solar value of that isotope;
- Assuming that the  ${}^6\text{Li}$  plateau is real and extends to metallicities as high as  $[\text{Fe}/\text{H}]=-0.6$ , one sees that the GCR component of  ${}^6\text{Li}$  alone (dotted curve in fig. 1.10) crosses that plateau value slightly earlier (around  $[\text{Fe}/\text{H}]=-1.8$ ). A depletion mechanism *depending on metallicity* should be introduced to justify a plateau in the range  $-1.8 < [\text{Fe}/\text{H}] < -0.6$ . When the assumed pre-galactic  ${}^6\text{Li}$  component is also taken into account (either “low” or “high”), the  ${}^6\text{Li}$  abundance curve leaves the plateau value even earlier, around  $[\text{Fe}/\text{H}]=-2.4$ .

In order to cancel the effect of the cosmic ray contribution and to keep  ${}^6\text{Li}$  at the level of the

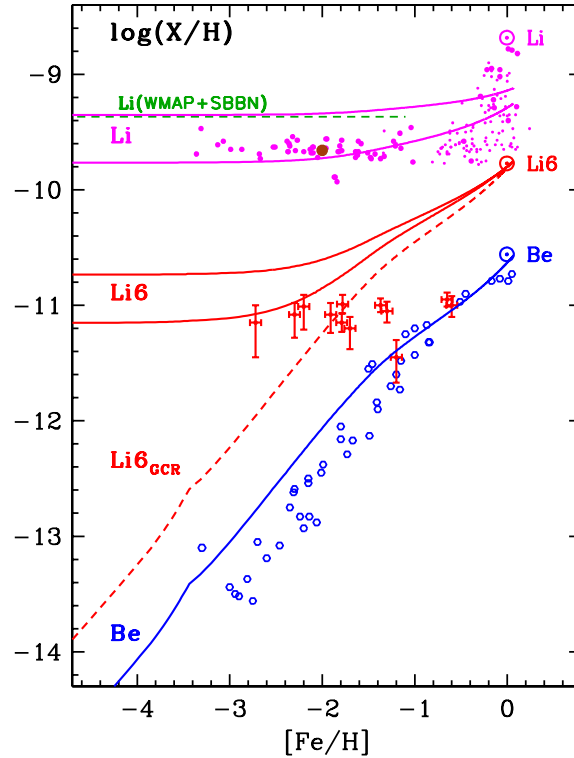


Figure 1.10: Evolution of  ${}^7\text{Li}$ ,  ${}^6\text{Li}$ , and Be in the Milky Way. The  ${}^7\text{Li}$  abundance corresponding to the baryonic density of the universe derived by WMAP is indicated as *dashed horizontal line*. The other curves correspond to a simple chemical evolution model where the metallicity dependent stellar yields component comes from production of  ${}^7\text{Li}$  and  ${}^6\text{Li}$  by GCR. The GCR composition is assumed primary in order to reproduce the Be observations. The contribution of the GCR component of  ${}^6\text{Li}$  is indicated by a *dashed curve*. Plot taken from [39].

observed plateau, stellar depletion has to be progressively greater with increasing metallicity in the case of  ${}^6\text{Li}$ . In the case of  ${}^7\text{Li}$ , a metallicity independent (or slowly increasing with metallicity) is requested. Whether a realistic stellar environment can indeed produce such a differential (and fine-tuned to preserve the plateau values) depletion, remains to be discovered.

### 1.2.3 Cosmology

A potential site for  ${}^6\text{Li}$  synthesis is the Big Bang. In a standard Big Bang much too little  ${}^6\text{Li}$  is produced to explain observations. An extension of the standard model for particle physics such as supersymmetry predicts the existence of various exotic particles, including the

gravitino, axion and the neutralino; the first two of these particles are predicted to be unstable but the neutralino is likely stable. The decay and the annihilation during or shortly after the era of Big Bang nucleosynthesis can alter the resulting light element abundances, provided the masses and life-times of these putative particles are right [20]. The annihilation of the neutralino can release sufficient energy to produce  ${}^6\text{Li}$  by non-thermal reactions like  ${}^3\text{H}(\alpha, n){}^6\text{Li}$  and  ${}^3\text{He}(\alpha, p){}^6\text{Li}$ . The amount of  ${}^6\text{Li}$  produced depends on the mass of the neutralino and the exact annihilation channels but can reach the levels observed in some very metal-poor stars; this scenario does not, however, resolve the  ${}^7\text{Li}$  dilemma described above. Another option to produce  ${}^6\text{Li}$  is through the decay of particles like the gravitino and axion. While the electromagnetic decay routes of such particles result in  ${}^3\text{He}/\text{D}$  ratios inconsistent with observations [20], the injection of energetic nucleons through the hadronic decay about  $10^3$  s after Big Bang can lead to substantial  ${}^6\text{Li}$  production without spoiling the agreement with D and the He isotopes. Indeed, for the right combination of particle properties, a simultaneous production of  ${}^6\text{Li}$  and destruction of  ${}^7\text{Li}$  appears achievable and may explain both the observed  ${}^6\text{Li}$  plateau and the low  ${}^7\text{Li}$  abundances in comparison with standard Big Bang nucleosynthesis. Thus, both of the Li problems can conceivably be solved at the same time. While these ideas are very attractive, they rest on as yet unproven and speculative physics.

## 1.2.4 Nuclear

As previously mentioned, within the standard model of BBN, the primordial abundances of D,  ${}^4\text{He}$ ,  ${}^3\text{He}$  and  ${}^7\text{Li}$  depend only on the baryon density and on the reaction rates of the 12 most important reactions listed in fig. 1.1 . The baryonic density provided by WMAP,  $\eta_{10} = 6.14 \pm 0.25$  [4], has dramatically increased the precision of this cosmological parameter with respect to earlier experiments.

Also, over the past decade, a major research effort has been done in SBBN in order to increase the rigor of the analysis. On the experimental side, 10 out of the 12 key reaction rates have been measured or remeasured close to or at the energies relevant to the Big Bang nucleosynthesis, between 0.01 and 0.1 MeV (n-decay and  $p(n, \gamma)\text{D}$  are taken from theory). On the theory side, the key innovation was the calculation of the uncertainties in the primordial element predictions in a systematic and statistically careful way. This was done using Monte Carlo

analyses (Smith *et al.* 1993 [41], Nollett and Burles 2000 [42], Coc *et al.* 2004 [5], and Cyburt 2004 [6], among others) which account for nuclear reaction uncertainties and their propagation into uncertainties in the primordial element abundance predictions. These Monte-Carlo programs fit the astrophysical  $S$ -factors<sup>20</sup> obtained experimentally either with spline functions (Nollett and Burles 2000 [42]), or with Breit-Wigner formula (the shape of nuclear resonances) plus low order polynomial functions for non-resonant contributions (Cyburt 2004 [6]), or through a R-matrix analysis (Coc *et al.* 2004 [5]), which provides a more rigorous energy dependence. Using this last approach Coc *et al.* 2004 [5] have calculated the maximum uncertainties on D,  $^4\text{He}$ ,  $^3\text{He}$  and  $^7\text{Li}$  abundances arising from the rates of the 10 main nuclear reactions involved in SBBN. Their results are plotted in table 1.3.  $X_H$  (respectively  $X_L$ ) represents the mass fraction of a given isotope when one of the reaction rate is set to its  $+1\sigma$  limit (respectively  $-1\sigma$  limit) and the *maxima* of the quantities  $X_H - X_L$  for  $^4\text{He}$  and  $\log(X_H/X_L)$  [i.e. dex] for the other isotopes. By *maximum*, it is meant the value having the maximum absolute value when  $\eta_{10}$  spans the range between 1 and 10. Variations lower than 0.01 dex ( $10^{-3}$  for  $Y_p$ ) are not shown. From this table, we see that the reactions whose uncertainties affect most  $^7\text{Li}$  abundance are  $\text{D}(p,\gamma)^3\text{He}$ ,  $\text{T}(\alpha,\gamma)^7\text{Li}$ ,  $^7\text{Li}(p,\alpha)^4\text{He}$  for the low  $\eta$  region and  $^3\text{He}(\alpha,\gamma)^7\text{Be}$ ,  $^7\text{Li}(p,\alpha)^4\text{He}$  for the high  $\eta$  region. Here, we conclude that the variation of the cross sections between the  $+1\sigma$  and  $-1\sigma$  limits corresponds to a variation of around 9% in the  $^7\text{Li}$  abundance ( $10^{-0.039} = 0.914$ , for the  $^7\text{Li}(p,\alpha)^4\text{He}$  reaction). This means that the  $^7\text{Li}$  discrepancy could only be removed if one or more of these reactions cross sections were wrong by many  $\sigma$ 's, which is quite unlikely. However, as will be seen in the two following chapters, the  $^7\text{Li}(p,\alpha)^4\text{He}$  reaction still shows discrepancies which can be significant amongst the authors who have measured its cross section, and the electron screening effects on laboratory cross section measurements are still poorly understood. These factors justify a careful remeasurement of the  $^7\text{Li}(p,\alpha)^4\text{He}$  reaction cross section, even though it can not, by itself, solve the  $^7\text{Li}$  problem.

Coc *et al.* 2004 [5] also checked if whether other, less important, nuclear reactions are sufficiently known and do not induce any further uncertainties on the primordial abundances. To do so, the rates of 43 reactions between  $\text{D}(n,\gamma)\text{T}$  and  $^{11}\text{C}(p,\gamma)^{12}\text{N}$  (whose rate uncertainties

---

<sup>20</sup>To compensate the fast energy dependence of charged particles cross section, nuclear astrophysicists usually use the  $S$ -factor defined as:  $S(E) = \sigma(E) E \exp(2\pi\eta)$ , where  $E$  is the C.M. energy,  $\sigma(E)$  is the cross section and  $\eta$  is the Sommerfeld parameter (see section 2.2).

Reactions	${}^4\text{He}$	D	${}^3\text{He}$	${}^7\text{Li}$
	$(X_H - X_L)_{max}$	$(\log(X_H/X_L))_{max}$		
D(p, $\gamma$ ) ${}^3\text{He}$	.-	-0.030	0.022	0.034
D(d,n) ${}^3\text{He}$	.-	-0.009	0.007	0.011
D(d,p)T	.-	-0.008	-0.008	0.003
T(d,n) ${}^4\text{He}$	.-	.-	-0.003	-0.004
T( $\alpha$ , $\gamma$ ) ${}^7\text{Li}$	.-	.-	.-	0.038
${}^3\text{He}$ (d,p) ${}^4\text{He}$	0.0022	.-	-0.018	-0.017
${}^3\text{He}$ (n,p)T	.-	.-	-0.006	-0.004
${}^3\text{He}$ ( $\alpha$ , $\gamma$ ) ${}^7\text{Be}$	.-	.-	.-	0.049
${}^7\text{Li}$ (p, $\alpha$ ) ${}^4\text{He}$	.-	.-	.-	-0.039
${}^7\text{Be}$ (n,p) ${}^7\text{Li}$	.-	.-	.-	-0.003

Table 1.3: Influential reactions and their sensitivity to nuclear uncertainties for the production of  ${}^4\text{He}$ , D,  ${}^3\text{He}$  and  ${}^7\text{Li}$  in SBBN. Table taken from [5].

are not documented) were allowed to vary by factors of 10, 100 and 1000 above their nominal rate and calculated the corresponding variation on the  ${}^4\text{He}$ , D,  ${}^3\text{He}$  and  ${}^7\text{Li}$  yields. Table 1.2.4 lists the few reactions, for which a variation of their rates by up to an arbitrary factor of 1000 induces a variation of the yields by more than 0.01 dex for the primordial elements. It shows that there are only four reactions that can lead to a factor of at least 3 (0.5 dex) on  ${}^7\text{Li}$  yield when their rates are artificially increased by up to a factor of 1000 : T(p, $\gamma$ ) ${}^4\text{He}$ ,  ${}^4\text{He}$ ( $\alpha$ ,n) ${}^7\text{Be}$ ,  ${}^7\text{Li}$ (d,n) $2{}^4\text{He}$  and  ${}^7\text{Be}$ (d,p) $2{}^4\text{He}$ . From the existing experimental data, these authors concluded that, with the exception of the last reaction, these changes are ruled out. For  ${}^7\text{Be}$ (d,p) $2{}^4\text{He}$ , there was no data in the SBBN energy range.  ${}^7\text{Be}$ +d could be an alternative to  ${}^7\text{Be}$ (n,p) ${}^7\text{Li}$  for the destruction of  ${}^7\text{Be}$  (which is the source of  ${}^7\text{Li}$  at high  $\eta$ ), by compensating the scarcity of neutrons at high  $\eta$ . A factor of  $\gtrsim 100$  could alleviate the  ${}^7\text{Li}$  discrepancy. Due to this seducing possibility, the reaction  ${}^7\text{Be}$ (d,p) $2{}^4\text{He}$  was measured very recently by Angulo *et al.* 2005 [43] in the energy range of interest. They found that the cross section was a factor 10 smaller than derived from earlier measurements, so this reaction can not reconcile SBBN,  ${}^7\text{Li}$  and CMB observations.

Reaction	${}^4\text{He}$	D	${}^3\text{He}$	${}^7\text{Li}$
	$(X_H - X_L)_{max}$	$(\log(X_H/X_L))_{max}$		
D(n, $\gamma$ )T	0.003	-.-	-.-	-.-
	0.025	-0.010	-.-	-0.011
	0.110	-0.073	-0.048	-0.078
T(p, $\gamma$ ) ${}^4\text{He}$	-.-	-.-	0.012	0.074
	0.003	-0.017	0.055	0.26
	0.018	-0.058	0.14	-0.56
${}^3\text{He}(t,np){}^4\text{He}$	-.-	-.-	-.-	-.-
	-.-	-.-	-.-	-0.012
	-.-	0.053	-0.026	-0.092
${}^4\text{He}(\alpha,n){}^7\text{Be}$	-.-	-.-	-.-	-0.056
	-.-	-.-	-.-	-0.36
	-.-	-.-	-.-	-1.1
${}^7\text{Li}(d,n)2{}^4\text{He}$	-.-	-.-	-.-	-0.10
	-.-	-.-	-.-	-0.44
	-.-	-.-	-.-	-1.1
${}^7\text{Li}(t,2n)2{}^4\text{He}$	-.-	-.-	-.-	-.-
	-.-	-.-	-.-	-.-
	-.-	-.-	-.-	-0.055
${}^7\text{Be}(d,p)2{}^4\text{He}$	-.-	-.-	-.-	-0.047
	-.-	-.-	-.-	-0.34
	-.-	-.-	-.-	-1.0

Table 1.4: Test of yield sensitivity to reactions rate variations: factor of 10,100,1000 (see text). Table taken from [5].

# Chapter 2

## Determination of nuclear reaction rates

The previous chapter was dedicated to describe the mechanisms responsible for the production and destruction of lithium in the universe, showing that they largely depend on our knowledge of nuclear reaction rates. In this chapter we present the equations necessary to compute the reaction rates, and how the Coulomb barrier and electron screening affect this determination.

### 2.1 Nuclear reaction rate

Consider the interaction between nuclides  $A + B \rightarrow C + D$ . From energy conservation, the  $Q$ -value is given by

$$Q = (m_A + m_B - m_C - m_D) c^2, \quad (2.1)$$

where  $m_i$  is the mass of the  $i$ -th particle and  $c$  is the speed of light. Both  ${}^7\text{Li}(p,\alpha){}^4\text{He}$  and  ${}^6\text{Li}(p,\alpha){}^3\text{He}$  are exothermic reactions as they have positive  $Q$ -values, 17.35 MeV and 4.02 MeV, respectively. Consider also that the two particles  $A$  and  $B$  have positions  $\vec{r}_A$  and  $\vec{r}_B$ . We assume that the forces exerted on these particles are derived from a potential energy  $V(\vec{r}_A - \vec{r}_B)$  which depends only on the relative position,  $\vec{r}_A - \vec{r}_B$ . This is true if there are no forces originating outside the system (that is, the system is isolated), and if the interactions between the two particles are derived from a potential. This potential must depend only on  $\vec{r}_A - \vec{r}_B$ , since only the relative positions of the two particles are involved. It can be shown that the study of such an interacting system can be reduced to that of a single particle placed in the potential  $V(\vec{r})$  with the following properties [44]: its mass is the reduced mass  $\mu$  of the two real particles  $\mu =$

$m_A m_B / (m_A + m_B)$ ; its position is characterized by the relative coordinates  $\vec{r} = \vec{r}_A - \vec{r}_B$  (therefore we can consider particles of either type  $A$  or type  $B$  as the projectiles); and its momentum is the relative momentum  $\vec{p}$ :  $\vec{p}/\mu = \vec{p}_A/m_A - \vec{p}_B/m_B$ .

Since the cross section  $\sigma$  for a nuclear reaction between nuclei depends only on the relative velocity, we can use the relative particle formalism to express it. The cross section is proportional to the interacting area of the involved nuclei, given quantum-mechanically by

$$\sigma(v) \propto \pi \lambda^2 = \pi \left( \frac{\hbar}{\mu v} \right)^2 = \pi \frac{\hbar^2}{2\mu E}, \quad (2.2)$$

where  $\lambda$  is the reduced de Broglie wavelength,  $\hbar$  is the reduced Planck constant, and  $E$  the center of mass energy,  $E = 1/2 \mu v^2$ .

Now consider that particles  $A$  and  $B$  make up a gas with  $n_A$  particles per cubic centimeter of type  $A$  and  $n_B$  particles per cubic centimeter of type  $B$ , moving with relative velocities  $v$ . If nuclei  $A$  are arbitrarily chosen as the projectiles moving with the velocity  $v$ , then the nuclei  $B$  must be considered at rest. Consequently, the projectile sees an effective area (per cubic centimeter) for collision  $F$  equal to the cross section for a single target nucleus  $\sigma(v)$ , multiplied by the number of target nuclei  $n_B$  per cubic centimeter:  $F = \sigma(v) n_B$ . Since each projectile sees this area  $F$ , the total number of nuclear reactions occurring depends on the flux  $J$  of incident particles,  $J = n_A v$ . The rate of nuclear reactions  $r$  is therefore given by the product of both quantities

$$r = n_A n_B v \sigma(v), \quad (2.3)$$

where  $r$  is in units of reactions per cubic centimeter per second.

In a gas the velocity of the particles changes over a wide range of values, given by the probability function  $\phi(v)$ , where

$$\int_0^{\infty} \phi(v) dv = 1. \quad (2.4)$$

Due to this velocity distribution, the product  $v \sigma(v)$  in equation 2.3 has to be replaced by the integral

$$\langle \sigma v \rangle = \int_0^{\infty} \phi(v) v \sigma(v) dv. \quad (2.5)$$

The bracketed quantity  $\langle \sigma v \rangle$  is the reaction rate per particle pair. The total reaction rate  $r$  is then

$$r = n_A n_B \langle \sigma v \rangle (1 + \delta_{AB})^{-1}, \quad (2.6)$$

where the term with the Kronecker symbol  $\delta_{AB}$  was introduced to avoid that, in case of identical nuclei  $A$  and  $B$  the number of intervening particles be counted twice.

During the Big Bang nucleosynthesis (BBN) and in normal stellar matter, the gas of particles is nondegenerate and the nuclei move nonrelativistically [37]. The gas is in thermodynamic equilibrium, and the velocities of the nuclei can be described by a Maxwell-Boltzmann velocity distribution,

$$\phi(v) = 4\pi v^2 \left( \frac{\mu}{2\pi k_B T} \right)^{3/2} \exp\left(-\frac{\mu v^2}{2k_B T}\right), \quad (2.7)$$

which is normalized to unity (eq. 2.4). Here  $T$  refers to the absolute temperature of the gas, and  $k_B$  is the Boltzmann constant.

Inserting eq. 2.7 in eq. 2.5 we get

$$\langle \sigma v \rangle = 4\pi \left( \frac{\mu}{2\pi k_B T} \right)^{3/2} \int_0^\infty v^3 \sigma(v) \exp\left(-\frac{\mu v^2}{2k_B T}\right) dv. \quad (2.8)$$

Using the center of mass energy  $E$ , this equation can be written in the form

$$\langle \sigma v \rangle = \left( \frac{8}{\pi \mu} \right)^{1/2} \frac{1}{(k_B T)^{3/2}} \int_0^\infty \sigma(E) E \exp\left(-\frac{E}{k_B T}\right) dE. \quad (2.9)$$

This equation characterizes the reaction rate at a given temperature  $T$ . During the BBN and during stellar evolution, temperature changes, and hence the reaction rate  $\langle \sigma v \rangle$  must be evaluated for each temperature of interest. In order to do that, the cross section  $\sigma(E)$  has to be calculated in the relevant energy range, the so called Gamow peak, defined in the following section.

## 2.2 Coulomb barrier and Gamow peak

In the universe, charged-particle induced nuclear reactions usually occur at very low energies, far below the Coulomb barrier ( $E_c$ ). Let's take, for instance, the reactions  ${}^7\text{Li}(p,\alpha){}^4\text{He}$  and  ${}^6\text{Li}(p,\alpha){}^3\text{He}$ : the potential energy for the Coulomb repulsive force between the lithium nucleus and the proton is given by the well known equation

$$V_c(r) = \frac{1}{4\pi\epsilon_0} \frac{Z_{\text{Li}}Z_p e^2}{r} \quad (\text{J}), \quad (2.10)$$

where  $Z_{\text{Li}}$  and  $Z_p$  represent the atomic number of the interacting nuclei,  $r$  is the relative distance, and  $\epsilon_0$  is the permittivity of free space. This potential, when combined with the potential for

the short-range attractive nuclear force (a square potential, in the simplest case), which comes into play at distances equal to the nuclear radius  $R_n = R_{\text{Li}} + R_p$ <sup>1</sup> ( $\approx 3.79 \times 10^{-15}$  m = 3.79 fm and 3.66 fm for the reactions  ${}^7\text{Li} + p$  and  ${}^6\text{Li} + p$ , respectively), leads to an effective potential shown in fig. 2.1.

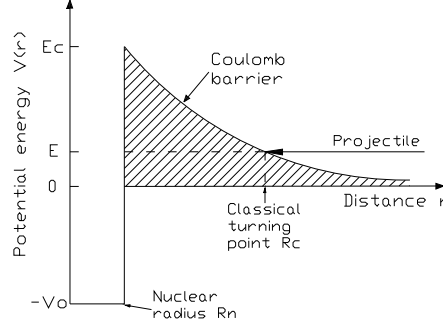


Figure 2.1: Schematic representation of the combined square nuclear and Coulomb potentials. A projectile incident with energy  $E < E_c$  has to penetrate the Coulomb barrier in order to reach the nuclear domain.

In this figure the shaded area represents the Coulomb barrier, which inhibits nuclear reactions. For the  ${}^7\text{Li} + p$  reaction, the effective height  $E_c$  of this Coulomb barrier is, by eq. 2.10, equal to 1141 keV and for the  ${}^6\text{Li} + p$  reaction is 1181 keV. Classically, these reactions can occur only when the energy of the protons exceeds  $E_c$ , which corresponds to a temperature ( $E_c = k_B T$ ) of  $T \approx 13.5 \times 10^9$  K, far higher than the temperatures observed during the BBN and in stellar environments. Therefore, these reactions only take place in the universe by quantum tunneling through the Coulomb barrier, with a probability  $P$  given by (considering  $s$ -waves)

$$P = \exp(-2\pi\eta) , \quad (2.11)$$

with the Sommerfeld parameter given by

$$\eta = \frac{1}{4\pi\epsilon_0} \frac{e^2}{\hbar} \left( \frac{\mu}{2E} \right)^{1/2} Z_{\text{Li}} Z_p . \quad (2.12)$$

In numerical units the exponent is

$$2\pi\eta = \left( \frac{E_G}{E} \right)^{1/2} = 31.29 Z_{\text{Li}} Z_p \left( \frac{\mu}{E} \right)^{1/2} , \quad (2.13)$$

where  $E_G = (31.29 Z_{\text{Li}} Z_p \mu^{1/2})^2$  is the Gamow energy. Both  $E_G$  and  $E$  are given in units of keV, and  $\mu$  is in unified atomic mass units ( $u$ ).

<sup>1</sup>The nuclear radius is  $R = R_0 A^{1/3}$ , where  $R_0 = 1.3 \times 10^{-15}$  m, and  $A$  is the nucleus mass number.

This exponential behavior of the tunneling probability leads to cross sections for charged-particle induced nuclear reactions that drop rapidly for energies below the Coulomb barrier:

$$\sigma(E) \propto \exp(-2\pi\eta) . \quad (2.14)$$

Another non-nuclear energy dependent term involves the de Broglie wavelength (eq. 2.2):

$$\sigma(E) \propto \pi\lambda^2 \propto \frac{1}{E} . \quad (2.15)$$

Using both relations, we can express the cross section as

$$\sigma(E) = \frac{1}{E} \exp(-2\pi\eta) S(E) , \quad (2.16)$$

where the function  $S(E)$ , defined by this equation is called the nuclear or astrophysical  $S$ -factor. For nonresonant reactions this factor is a smoothly varying function of energy which varies much less rapidly with beam energy than the cross section. Because of these characteristics,  $S(E)$  is much more useful in extrapolating measured cross sections to astrophysical energies.

Inserting eq. 2.16 in eq. 2.9, we obtain for the reaction rate per particle pair

$$\langle \sigma v \rangle = \left( \frac{8}{\pi\mu} \right)^{1/2} \frac{1}{(k_B T)^{3/2}} \int_0^\infty S(E) \exp\left(-\frac{E}{k_B T} - \frac{E_G^{1/2}}{E^{1/2}}\right) dE , \quad (2.17)$$

In those cases in which  $S(E)$  can be considered constant in the energy range in which the exponential term in the integrand of eq. 2.17 is significantly larger than zero, the last expression shows a peak (known as Gamow peak, see fig. 2.2) with a maximum at:

$$E_0 = \left( E_G^{1/2} k_B \frac{T}{2} \right)^{2/3} = 1.22 \left( Z_{\text{Li}}^2 Z_{\text{p}}^2 \mu T_6^2 \right)^{1/3} \text{ (keV)} . \quad (2.18)$$

This peak can be fairly well approximated by a gaussian function:

$$\exp\left(-\frac{E}{k_B T} - \frac{E_G^{1/2}}{E^{1/2}}\right) = \exp(-\tau) \exp\left[-\left(\frac{E - E_0}{\Delta E_0/2}\right)^2\right] , \quad (2.19)$$

where  $\tau = 3E_0/(k_B T)$ , and  $\Delta E_0$  is the effective width

$$\Delta E_0 = \frac{4}{3^{1/2}} (E_0 k_B T)^{1/2} = 0.749 \left( Z_{\text{Li}}^2 Z_{\text{p}}^2 \mu T_6^5 \right)^{1/6} \text{ (keV)} . \quad (2.20)$$

Nuclear-burning reactions take place predominantly over the energy window  $E = E_0 \pm \Delta E_0/2$ . It is over this range where information regarding the nuclear processes must be obtained. For the  ${}^7\text{Li}(p,\alpha){}^4\text{He}$  and  ${}^6\text{Li}(p,\alpha){}^3\text{He}$  reactions at BBN energies ( $T_6$  between 80 and 800), in the center of the Sun ( $T_6 = 15$ ), and in the surface of halo stars ( $T_6 \approx 6 \times 10^{-3}$ ), the energy windows are given in table 2.1 .

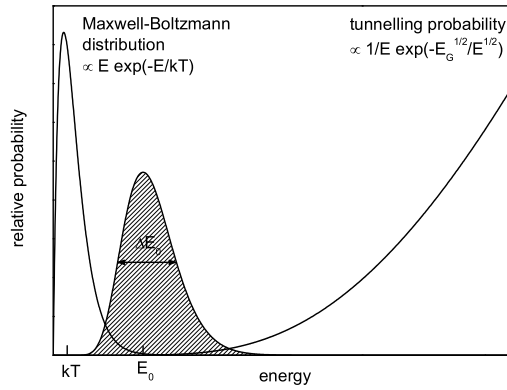


Figure 2.2: Dominant energy dependencies for fusion reactions. While both the Maxwell-Boltzmann function and the tunneling probability function, are small in the overlapping region, the convolution of both functions leads to a peak, the Gamow peak (shaded area), at energy  $E_0$  and width  $\Delta E_0$ .

	$T_6 = 800$	$T_6 = 80$	$T_6 = 15$	$T_6 = 6 \times 10^{-3}$
${}^7\text{Li}(p, \alpha){}^4\text{He}$	$209 \pm 139$	$45.0 \pm 20.4$	$14.7 \pm 5.0$	$0.081 \pm 0.007$
${}^6\text{Li}(p, \alpha){}^3\text{He}$	$207 \pm 139$	$44.7 \pm 20.3$	$14.7 \pm 5.0$	$0.080 \pm 0.007$

Table 2.1: Energy window (in keV) of the Gamow peak for the  ${}^{6,7}\text{Li} + p$  reactions during the BBN ( $T_6$  between 80 and 800), in the center of the Sun, and in the surface of halo stars.

## 2.3 Electron screening

In the above treatments, it was assumed that the Coulomb potential of the target nucleus as seen by the projectile is that resulting from a bare nucleus and thus would extend to infinity (fig. 2.1). However, due to the presence of electrons around the nuclei, this assumption does not hold neither in the primordial and stellar plasmas nor in laboratory measurements. In the former case we are dealing with a fully ionized plasma where the electrons occupy mainly continuum states. In the latter case, ionic beams are directed against a neutral atomic (or molecular) target, where electrons, confined around the target nucleus, provide a partial shielding of the nucleus charge. This screening effect is represented in fig. 2.3; an incoming projectile sees no repulsive Coulomb force until it penetrates beyond the atomic radius  $R_a$ , then it effectively sees a reduced Coulomb barrier.

The electrostatic potential of the electron cloud at distances less than the atomic radius  $R_a$  is constant, with the approximate value  $1/(4\pi\epsilon_0) Z_{\text{Li}} e/R_a$ . Consequently, the reduced height of

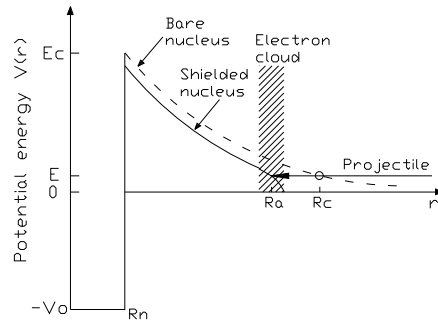


Figure 2.3: Effect of the atomic electron cloud on the Coulomb potential of a bare nucleus (shown in an exaggerated and idealized way). This potential is reduced at all distances and goes essentially to zero beyond the atomic radius  $R_a$ .

the Coulomb barrier seen by the incoming projectile is

$$E'_c = \frac{1}{4\pi\epsilon_0} \frac{Z_{Li}Z_p e^2}{R_n} - \frac{1}{4\pi\epsilon_0} \frac{Z_{Li}Z_p e^2}{R_a}. \quad (2.21)$$

From this equation we estimate the effect of the electron shielding on the height of the Coulomb barrier to be equal to  $(E_c - E'_c)/E_c = R_n/R_a \approx 10^{-5}$ . In general, this shielding correction is negligible. However, when the classical turning point  $R_c$  of an incoming projectile for the bare nucleus is near or outside the atomic radius  $R_a$ , the magnitude of the shielding effect becomes significant. Since the classical turning point is related to the projectile energy  $E$  by the equation  $E = 1/(4\pi\epsilon_0) Z_{Li}Z_p e^2/R_c$ , the condition  $R_c \geq R_a$  can be written as

$$E \leq U_e = \frac{1}{4\pi\epsilon_0} \frac{Z_{Li}Z_p e^2}{R_a}, \quad (2.22)$$

where  $U_e$  is referred to as the electron screening potential energy, and corresponds to the energy transfer from the electronic cloud to the incoming projectile, *i.e.*, the tunneling through a shielded Coulomb barrier at projectile energy  $E$  is equivalent to that of bare nuclei at energy  $E_{eff} = E + U_e$ . Setting  $R_a$  equal to the radius of the innermost electrons of the target (or projectile) atoms,  $R_a \approx R_H/Z_{Li}$ , where  $R_H$  is the Bohr radius<sup>2</sup>,  $U_e = 244.9$  eV for the two lithium reactions. This shielding effect reduces the Coulomb barrier and increases the penetration of the Coulomb barrier. Thus, it increases the cross sections of nuclear fusion reactions. It is common to express this increase by a *screening factor* which is the ratio between the cross section of

<sup>2</sup> $R_H = 5.2918 \times 10^{-11}$  m.

screened nucleus  $\sigma_s$  and bare nucleus  $\sigma_b$ :

$$f(E) = \frac{\sigma_s(E)}{\sigma_b(E)} = \frac{\sigma_b(E + U_e)}{\sigma_b(E)}. \quad (2.23)$$

Expressing this ratio in terms of the astrophysical  $S$ -factor (eq. 2.16) we get

$$f(E) = \frac{S_b(E + U_e)}{S_b(E)} \frac{E \exp[-2\pi\eta(E + U_e)]}{(E + U_e) \exp[-2\pi\eta(E)]} \approx \exp\left(\pi\eta(E) \frac{U_e}{E}\right), \quad (2.24)$$

where the approximation results from considering that  $U_e \ll E$  and  $S_b(E + U_e) = S_b(E)$  [45]. According to eq. 2.24, it is expected an exponential enhancement of the cross section (or, equivalently of the  $S$ -factor) at low energies and this enhancement should be described by a single parameter  $U_e$ . It is an experimental evidence that for energies  $E/U_e > 1000$  the screening effects are negligible [ $f(E = 240\text{keV}) \approx 1.003$  for the  ${}^6,7\text{Li} + \text{p}$  reactions] and laboratory experiments can be regarded as measuring essentially the bare cross section. However, at energies  $E/U_e < 100$  the shielding effect cannot be disregarded [ $f(E = 24\text{keV}) \approx 1.09$  for the  ${}^6,7\text{Li} + \text{p}$  reactions], and it must be considered in order to have a correct extrapolation to lower energies of the bare cross section. This issue of a precise determination of the electron screening is of paramount importance for the astrophysicist since the bare cross section obtained from laboratory measurements will be used in the determination of primordial and stellar reaction rates.

For the high temperatures occurring in astrophysical scenarios, the atoms are generally completely stripped of their atomic electrons. These electrons form a sea of particles which tend to cluster around the nucleus, resulting in an effect similar to the one observed with atomic orbital electrons. For the condition that  $k_B T$  is much larger than the Coulomb energy between the particles, the electrons tend to cluster into spherical shells around a nucleus at the Debye-Hückel radius,  $R_D$  [37]:

$$R_D = \left( \frac{k_B T \epsilon_0}{e^2 \rho N_A \zeta} \right)^{1/2}, \quad (2.25)$$

where the  $N_A$  is the Avogadro's number and  $\rho$  is the density (in  $\text{g/cm}^3$ ). The quantity  $\zeta$  is defined as [37]:

$$\zeta = \sum (Z_i^2 + Z_i) \frac{X_i}{A_i}, \quad (2.26)$$

where the sum is performed over all positive ions and  $X_i$  is the mass fraction of nuclei of type  $i$ , with mass number  $A_i$ .

So, in plasmas we also observe a cross section enhancement due to electron shielding:

$$\sigma_p(E) = f_p(E)\sigma_b(E) , \quad (2.27)$$

where  $\sigma_p(E)$  is the fusion cross section for shielded nuclei in the plasma, and  $f_p(E)$  is the screening factor in plasmas. For energies of the Gamow peak  $E_0$  much greater than the energy  $U_e$ , we have

$$f_p = \exp\left(\frac{U_e}{k_B T}\right) . \quad (2.28)$$

For relatively low densities, the number of screening electrons at the Debye-Hückel radius  $R_D$  is nearly equal to the number of protons in the nucleus ( $Z_{Li}$ ). In this case, the quantity  $U_e$  is given by:

$$U_e = \frac{1}{4\pi\epsilon_0} \frac{Z_{Li}Z_p e^2}{R_D} . \quad (2.29)$$

In view of the above discussions improved theoretical considerations appeared desirable in part to substantiate the above conclusions and in part to stimulate experimental work at low energies, where the electron screening effects should become more clearly visible.

### 2.3.1 Theoretical models

#### Static models

The model used to introduce the subject of electron screening in laboratory measurements – eqs. 2.21 and 2.22 – is a very simple one and is classified as a static model since it is assumed an a priori electron distribution, which does not change during the collision process. A slightly more elaborated static model was proposed by Bencze 1989 [46], where the electron cloud, instead of being all concentrated on the atomic radius  $R_a = R_H/Z_{Li}$ , is spread with uniform density in a spherical shell that goes from the nuclear radius to the screening radius  $R_a$  defined by

$$R_a = 0.8853R_H(Z_{Li}^{2/3} + Z_p^{2/3})^{-1/2} , \quad (2.30)$$

in agreement with atomic scattering studies. The  $U_e$  value deduced is

$$U_e = \frac{3}{2} \frac{1}{4\pi\epsilon_0} \frac{Z_{Li}Z_p e^2}{R_a} . \quad (2.31)$$

For the  ${}^6,7\text{Li} + p$  reactions,  $U_e = 244$  eV, the same value which was obtained with the simplest static model,  $U_e = 244.9$  eV.

## Dynamic models

In a typical low energy experiment the electron and nucleus velocities are comparable when the center-of-mass energy  $E$  is around a few keV. So the assumption of a static electron distribution can easily fail because there will be “time” for the projectile to alter the electron cloud configuration, and by this change the screening effect. Therefore, a dynamic approach that considers changes in the electron cloud when it transfers energy to the incoming nucleus is required. Obtaining the screening expression for arbitrary projectile velocity in this approach requires complex calculus, so usually only the two limiting cases of very low or very high relative nuclear velocity, as compared with typical electron velocities, are computed. The first case – the adiabatic limit – corresponds to the maximum energy which can be transferred from the electronic to the nuclear motion. From this limit we can derive an upper bound for the energy transfer, even in the case of a finite velocity. The other extreme – the sudden limit – corresponds to an electron distribution at fusion time almost the same as it was in the initial state, *i.e.*, essentially the static model approach. It gives the lower bound for the energy transfer. For the case of any finite velocity, the energy transfer will be in between that of the adiabatic and that of the sudden case.

Bracci *et al.* 1990 [47] did the calculations for both limits and applied their method for the estimates of electron screening effects in a series of nuclear reactions. They assumed the target to be a neutral atomic system, neglecting any molecular structure effect. Since the energies in play are relatively low, the projectile will not be in a definite ionization state at the moment of fusion, since it can gain and loose electrons when interacting with the surrounding atoms. Thus, Bracci *et al.* also considered the screening effect for the different possible ionization states of the projectile. Table 2.2 lists the values for the adiabatic and sudden screening limits, respectively  $U_e^{ad}$  and  $U_e^{sud}$ , obtained for several reactions by these authors, and also lists experimental values obtained in laboratory experiments.

From this table we observe that the theoretical predictions for the  $U_e$  are usually below the experimental values. Focusing now on the  ${}^7\text{Li}$  reaction values, we get that: the difference between H and p is rather weak, a few eV to be compared with  $U_e$  values of hundreds of eV; and there is an appreciable difference between the energy transfer as calculated in the adiabatic limit and in the sudden limit. This difference is about 40%.

Target	Projectile	$U_e^{ad}$	$U_e^{sud}$	$U_e^{exp}$	Ref.
D	d	20.4	13.6	$25 \pm 5$	[48]
D	D	36.6	27.2		
$^3\text{He}$	d	119	54	$120 \pm 10$	[49]
$^3\text{He}$	D	110	76		
$^7\text{Li}$	p	186	134	$300 \pm 280$	[50]
$^7\text{Li}$	H	182	144		
$^{11}\text{B}$	p	347	281	$430 \pm 80$	[51]
$^{11}\text{B}$	H	345	292		

Table 2.2: Electron screening potential energy (in eV) for proton and deuterium induced reactions, in the adiabatic and sudden approximation. Experimental values obtained in laboratory experiments are also listed with respective references.

### 2.3.2 Electron screening in D(d,p)T

The understanding of the electron screening mechanism in laboratory experiments has known major advances in the last couple of years that started with the study of the D(d,p)T reaction. Electron screening for this reaction was first measured in 1995 by Greife *et al.* [48] using a gas target, where  $U_e = 25 \pm 5$  eV was obtained, in good agreement with theoretical models. In subsequent years this same reaction was remeasured in deuterated solid targets, which provided confusing results: in some samples  $U_e$  values were consistent with the gas target value (*e.g.*, Ti:  $U_e = 36 \pm 11$  eV [52]), while in other samples  $U_e$  values were reported to be about one order of magnitude higher than expected (*e.g.*, Ta:  $U_e = 322 \pm 15$  eV [53]). Since there was no explanation for these results, the LUNA<sup>3</sup> collaboration decided to tackle this issue, developing an experimental setup and experimental procedures to study the D(d,p)T reaction at  $E_{\text{lab}} \leq 100$  keV in 58 different deuterated solid targets (backings). The details of this work, are in the thesis of my friend and colleague physicist Francesco Raiola [54].

Briefly, at room temperature ( $\approx 20^\circ\text{C}$ ) all deuterated metal backings showed a large screening effect ( $U_e > 150$  eV) while insulator and semiconductor deuterated backings exhibited a small effect ( $U_e < 70$  eV) consistent with the case of the gas target. The exceptions were the metals of groups 3 and 4 and the lanthanides, showing all a small screening effect ( $U_e < 70$

<sup>3</sup>Laboratory for Underground Nuclear Astrophysics.

eV). However, these metals were characterized by a high deuterium solubility, of the order of 1:1 ratio, and thus these deuterated metals were no longer metals, but insulators. In metals with large effects, the solubility was low (typically around 10%).

It is known that the deuterium solubility in metals decreases with increasing temperature. Thus it is reasonable to admit that for sufficiently high temperatures the solubility of the metals of groups 3 and 4 and of the lanthanides will drop to values (a few percent) which will allow to obtain high  $U_e$  values. This was what indeed happened. At  $T = 200^\circ\text{C}$  all these metals presented a small solubility and a large screening effect ( $U_e > 150$  eV). Fig. 2.4 (left panel) shows the  $S$ -factor measured at room temperature and at  $200^\circ\text{C}$  for Hf, a group 4 metal. It is perfectly clear the effect of the electron screening on the enhancement of the cross section. As a consistency check, an insulator, carbon, was also studied at  $200^\circ\text{C}$ : the deuterium solubility decreased, but no enhanced screening was observed ( $U_e < 50$  eV). It was also observed that for metals with low solubility at room temperature, a temperature increase results in a decrease of the  $U_e$  value. Fig. 2.4 (right panel) shows this decrease for Pt.

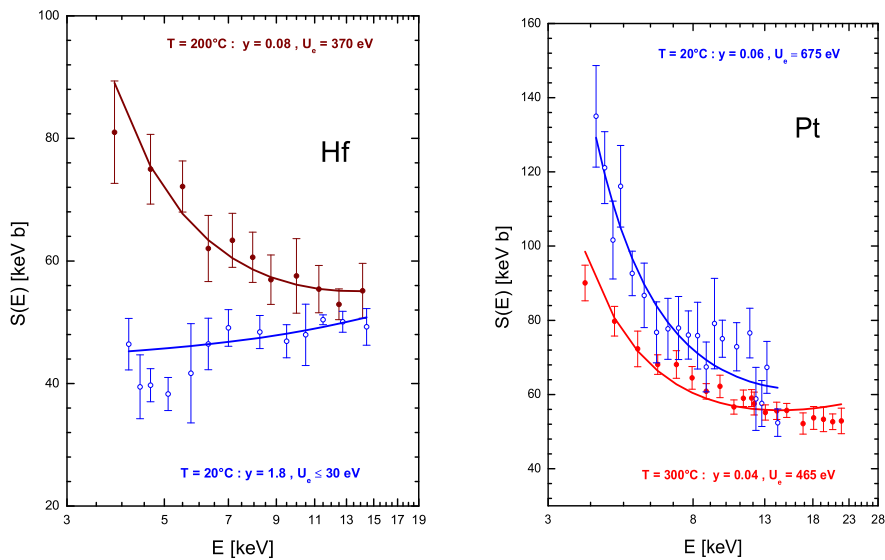


Figure 2.4: Left panel:  $S(E)$  factor of  $D(d,p)T$  for Hf at  $T = 200^\circ\text{C}$  and  $T = 20^\circ\text{C}$ , with the deduced solubilities  $y$  and  $U_e$  given at each temperature. The curve for  $T = 20^\circ\text{C}$  represents well the bare  $S(E)$  factor, while the curve for  $T = 200^\circ\text{C}$  includes the electron screening with the given  $U_e$  value. Right panel:  $S(E)$  factor of  $D(d,p)T$  for Pt at  $T = 20^\circ\text{C}$  and  $300^\circ\text{C}$ , with the deduced solubilities  $y$  and  $U_e$  given at each temperature. In both figures, the curves through the data points are the  $S(E)$  fits to these points. Both plots were taken from [55].

Fig. 2.5 shows the periodic table, where the elements studied are coloured: yellow for those with low  $U_e$  values ( $U_e < 70$  eV), and green for those with high  $U_e$  values ( $U_e > 150$  eV).

1																		18		
1	H																	2	He	
3	Li	4	Be																	
11	Na	12	Mg	3	4	5	6	7	8	9	10	11	12	13	14	15	16	17	18	
19	K	20	Ca	21	22	23	24	25	26	27	28	29	30	31	32	33	34	35	36	
37	Rb	38	Sr	39	40	41	42	43	44	45	46	47	48	49	50	51	52	53	54	
55	Cs	56	Ba	Lu	Hf	Ta	W	Re	Os	Ir	Pt	Au	Hg	81	82	83	84	85	86	
				Lanthanides																
				57	58	59	60	61	62	63	64	65	66	67	68	69	70			
				La	Ce	Pr	Nd	Pm	Sm	Eu	Gd	Tb	Dy	Ho	Er	Tm	Yb			

Figure 2.5: Periodic table showing the elements studied, where those with low  $U_e$  values ( $U_e < 70$  eV) are colored yellow and those with high  $U_e$  values ( $U_e > 150$  eV) are colored green.

From this description of the results it is clear that the D(d,p)T cross section enhancement is linked to properties of the metallic environment. Several mechanisms of the metals were suggested to explain the data [54]: stopping power, thermal motion, channeling, diffusion, conductivity, crystalline structure, electron configuration, and “Fermi shuttle” mechanism. However, none of these scenarios provided a solution for the observations.

An explanation came from a more radical approach: the quasi-free conduction electrons in the metallic mesh can be described by the Debye plasma model (see eq. 2.25) since both these conduction electrons and the electrons in a plasma occupy mainly continuum states. This approach consists in a combination of the Drude model of metals (with a kinetic energy  $3kT/2$  for the quasi-free conduction electrons) with the Debye model of plasmas: the Drude-Debye model, or in short, the Debye model. The electron Debye radius around the deuterons in the

lattice is given by [54]

$$R_D = \left( \frac{k_B T \epsilon_0}{e^2 n_{\text{eff}} \rho_a} \right)^{1/2} = 69 \left( \frac{T}{n_{\text{eff}} \rho_a} \right)^{1/2} \text{ (m)}, \quad (2.32)$$

with the temperature  $T$  of the quasi-free electrons in units of K,  $n_{\text{eff}}$  the number of these electrons per metallic atom, and  $\rho_a$  the atomic density in units of  $\text{m}^{-3}$ . For  $T = 293 \text{ K}$ ,  $\rho_a = 6 \times 10^{28} \text{ m}^{-3}$ , and  $n_{\text{eff}} = 1$ , the radius  $R_D$  is about a factor 10 smaller than the Bohr radius of a hydrogen atom.

With the Coulomb energy between two deuterons at  $R_D$  set equal to  $U_e \equiv U_D$ , we get

$$U_D = \frac{1}{4\pi\epsilon_0} \frac{Z_d Z_d e^2}{R_D} = 2.09 \times 10^{-11} \left( \frac{n_{\text{eff}} \rho_a}{T} \right)^{1/2} \text{ (eV)}. \quad (2.33)$$

For the example above, we get  $U_D = 300 \text{ eV}$ , which is of the order of magnitude of the observed  $U_e$  values.

Using eq. 2.33, the  $n_{\text{eff}}$  value for each metallic backing can be calculated using the obtained  $U_D$ . These  $n_{\text{eff}}$  values can, in turn, be compared with those derived from the Hall coefficient  $R_{\text{Hall}}$ :

$$R_{\text{Hall}} = \frac{1}{e n_{\text{eff}}(\text{Hall}) \rho_a} \text{ (m}^3\text{C}^{-1}\text{)}, \quad (2.34)$$

whose values can easily be found in literature (*e.g.*, [56]).

The comparison between these two independent methods showed that within two standard deviations the two quantities agree well for all metals with a known Hall coefficient, except for Ir and Pd.

Eq. 2.33 also predicts a temperature dependence,  $U_D \propto T^{-1/2}$ , which was verified experimentally for several metals, as exemplified in fig. 2.4.

Finally, eq. 2.33 predicts a nuclear charge dependence for the interacting nuclei,  $U_D \propto Z_1 Z_2$ , and also predicts that electron screening should not have any isotopic dependence. In the case of the  $d(d,p)t$  reaction these predictions are not, by itself, verifiable. So, the study of nuclear reactions with interacting nuclei of atomic number higher than 1 is necessary to verify the Debye model. The study of electron screening effects for the  ${}^7\text{Li}(p, \alpha){}^4\text{He}$  and  ${}^6\text{Li}(p, \alpha){}^3\text{He}$  reactions in insulating and metallic backings are perfect choices to verify both the  $Z$  dependence and isotopic independence predicted by the Debye model.

# Chapter 3

## Available data on the ${}^7\text{Li}(p,\alpha){}^4\text{He}$ and ${}^6\text{Li}(p,\alpha){}^3\text{He}$ reactions

This chapter presents the status, prior to this work, on the most relevant experimental  $S$ -factor data for the  ${}^7\text{Li}(p,\alpha){}^4\text{He}$  and  ${}^6\text{Li}(p,\alpha){}^3\text{He}$  reactions, and the fits performed on those data. Angular distributions data on both reactions are also addressed as it gives important information on the entrance channel partial waves and energy levels properties of the compound nucleus involved in the nuclear reactions.

### 3.1 Methods for fitting data

#### 3.1.1 $S$ -factor

The Gamow peak,  $E_0 \pm \Delta E_0/2$ , is usually situated at so low energies that it is very difficult to have a direct measurement of the cross section. The standard solution to this problem is to measure  $S(E)$  over a wide range of energies and to the lowest energies possible and to extrapolate the data downward to  $E_0$  with the help of theoretical and other arguments. Thus an extrapolation formula or procedure becomes a crucial necessity.

A simple way to do this extrapolation is to use a polynomial approximation. This is usually used to investigate electron screening effects, where the cross section between bare nuclei is derived from a polynomial extrapolation of high-energy data. This polynomial approximation,

although very simple, is not based on a rigorous treatment of the energy dependence of the cross section, and may introduce significant inaccuracies [58]. A more rigorous approach is based on the  $R$ -matrix technique, which goal is to parameterize some experimentally known quantities, such as cross sections or angular distributions, with a small number of parameters which are then used to extrapolate the cross section down to astrophysical energies. The  $R$ -matrix framework assumes that the space is divided into two regions: the internal region (with radius  $a$ ), where nuclear forces are important, and the external region, where the interaction between the nuclei is governed by the Coulomb force alone <sup>1</sup>. The physics of the internal region is parameterized by a number  $N$  of poles (resonances), which are characterized by energy  $E_\lambda$  and reduced width  $\tilde{\gamma}_\lambda$ . In a multichannel problem, the  $R$ -matrix at energy  $E$  is defined as

$$R_{ik}(E) = \sum_{\lambda=1}^N \frac{\tilde{\gamma}_{\lambda i} \tilde{\gamma}_{\lambda k}}{E_\lambda - E}, \quad (3.1)$$

which must be given for each partial wave. Indices  $i$  and  $k$  refer to the channels.

Definition (3.1) can be applied to resonant as well as to non-resonant partial waves. In the latter case, the non-resonant behavior is simulated by a high-energy pole, referred to as the background contribution, which makes the  $R$ -matrix almost energy independent <sup>2</sup>.

The  ${}^7\text{Li}(\text{p},\alpha){}^4\text{He}$  and  ${}^6\text{Li}(\text{p},\alpha){}^3\text{He}$  are transfer reactions. For two colliding nuclei with masses ( $A_1, A_2$ ), charges ( $Z_1e, Z_2e$ ) and spins ( $j_1, j_2$ ) the transfer cross section  $\sigma_t(E)$  from the initial state to a final state is defined as

$$\sigma_t(E) = \frac{\pi}{k^2} (1 + \delta_{12}) \sum_{J^\pi} \frac{2J + 1}{(2j_1 + 1)(2j_2 + 1)} \sum_{\ell' j'} |U_{\ell' j'}^{J^\pi}(E)|^2, \quad (3.2)$$

where  $\delta_{12}$  is 1 or 0, for symmetric and non-symmetric systems, respectively, and  $k$  is the wavenumber of the incident wave. The collision matrix  $U^{J^\pi}(E)$  contains the information about the transfer process (quantum numbers  $(\ell j)$  and  $(\ell' j')$  refer to the entrance and exit channels, respectively, and  $J^\pi$  is the spin and parity of the resonant state in the compound nucleus). This matrix is obtained from the  $R$ -matrix and from the Coulomb functions [58].

<sup>1</sup>Although the  $R$ -matrix parameters do depend on the channel radius  $a$ , the sensitivity of the cross section with respect to its choice is quite weak.

<sup>2</sup>The pole properties ( $E_\lambda, \tilde{\gamma}_{\lambda i}$ ) are known to be associated with the physical energy and width of resonances, but not strictly equal. This is known as the difference between “formal” parameters ( $E_\lambda, \tilde{\gamma}_{\lambda i}$ ) and “observed” parameters ( $E'_\lambda, \gamma_{\lambda i}$ ), deduced from experiment. In a general case, involving more than one pole, the link between those two sets is not straightforward [58].

### 3.1.2 Angular distributions

Angular momentum and parity are conserved in reactions governed by the strong or electromagnetic interaction. Conservation of angular momentum enables us to relate the spin assignments of the reacting particles and the orbital angular momentum carried by the outgoing particle (which can be deduced by measuring its angular distribution): angular momentum conservation requires the sum of the spins of the particles in the entrance/exit channel,  $\vec{j}_1$  and  $\vec{j}_2$ , plus their relative orbital angular momentum  $\vec{\ell}$ , to add up to the spin of the resonant state  $\vec{J}$ :

$$\vec{j}_1 + \vec{j}_2 + \vec{\ell} = \vec{J}. \quad (3.3)$$

Conservation of parity means that the net parity before the reaction must equal the net parity after the reaction, which is equal to the parity of the resonant state,  $\pi(J)$ :

$$(-1)^\ell \pi(j_1) \pi(j_2) = \pi(J), \quad (3.4)$$

where  $\pi(j_1)$  and  $\pi(j_2)$  are the parities of the particles in the entrance/exit channel, and  $\ell$  is the orbital angular momentum in the respective channel.

So, by determining the orbital angular momentum carried by the outgoing particle, the angular distribution measurements allows us to deduce spins and parities of excited nuclear states, and which partial waves must be taken into account for the description of the reaction entrance channel.

For the  ${}^7\text{Li}(p,\alpha){}^4\text{He}$  reaction, the spins and parities of  ${}^7\text{Li}$ ,  $p$  and  ${}^4\text{He}$  are:  $j^\pi({}^7\text{Li}) = 3/2^-$ ;  $j^\pi(p) = 1/2^+$  and  $j^\pi({}^4\text{He}) = 0^+$ . They must combine with the orbital angular momenta in the initial and final states so that angular momentum and parity are conserved according to equations 3.3 and 3.4. The final state is two identical spinless particles in relative motion and its wavefunction must be symmetric, *i.e.*, must not change sign under the interchange of the two  ${}^4\text{He}$  particles. In this case, the wavefunction of the two-particle system is only spatial, since  ${}^4\text{He}$  has no spin, and can be written, in spherical coordinates, as the product of a radial and an angular function,  $R(r)$  and  $Y_{\ell m}(\theta, \phi)$ , respectively:

$$\psi(r) = R(r) Y_{\ell m}(\theta, \phi). \quad (3.5)$$

An interchange of the coordinates of the two particles is equivalent to the change:  $r \rightarrow r$ ,  $\theta \rightarrow \pi - \theta$  and  $\phi \rightarrow \phi + \pi$ . Thus, the radial function remains unchanged. However, under this

transformation

$$Y_{\ell m}(\theta, \phi) \rightarrow Y_{\ell m}(\pi - \theta, \phi + \pi) = (-1)^\ell Y_{\ell m}(\theta, \phi). \quad (3.6)$$

Thus, in order to keep the wavefunction symmetric the two  ${}^4\text{He}$  system must have even orbital angular momentum, *i.e.*,  $\ell_f = 0, 2, 4, \dots$  and since parity is defined by the rule  $(-1)^\ell$ , the parity of the final state must be positive, *i.e.*,  $0^+, 2^+, 4^+, \dots$

To reach these spin-parity values in the initial system, an odd orbital angular momentum is necessary and we could have  $1^-, 3^-, 5^-, \dots$ . At low bombarding energies, particles with high orbital angular momentum do not approach the nucleus close enough to produce the reaction, so we assume the two lowest possible orbital momenta. Adding angular momenta can be done using different schemes. One common method is to couple the projectile spin  $\vec{j}_1$  and the target spin  $\vec{j}_2$  to form a channel spin  $\vec{s}$ , as indicated by the equation

$$\vec{j}_1 + \vec{j}_2 = \vec{s}, \quad (3.7)$$

where the vector notation is short-hand for  $|j_2 - j_1| < s < j_1 + j_2$ . The spin is then coupled to the orbital angular momentum  $\vec{\ell}$  to obtain the total angular momentum  $\vec{J}$ :

$$\vec{s} + \vec{\ell} = \vec{J}. \quad (3.8)$$

This procedure is referred to as the channel coupling scheme.

So, from eqs 3.7 and 3.8 and remembering that parity is multiplicative we get for  $\ell = 1$ :

$$\frac{3^-}{2} + \frac{1^+}{2} + 1^- \rightarrow 0^+, 1^+, 2^+, 3^+ \quad (3.9)$$

and for  $\ell = 3$ :

$$\frac{3^-}{2} + \frac{1^+}{2} + 3^- \rightarrow 1^+, 2^+, 3^+, 4^+, 5^+ \quad (3.10)$$

of which only  $0^+, 2^+$  and  $4^+$  satisfy the requirements of the final system.

For the  ${}^6\text{Li}(\text{p},\alpha){}^3\text{He}$  reaction, the spins and parities of  ${}^6\text{Li}$  and  ${}^3\text{He}$  are:  $j^\pi({}^6\text{Li}) = 1^+$ ;  $j^\pi({}^3\text{He}) = 1/2^+$ . Here, the only restriction is that  $\ell_i$  and  $\ell_f$  are either both even or both odd.

Cross sections for reactions which involve partial waves with  $\ell > 0$  exhibit a dependence on the angle of the outgoing particle. The angular component of the  $\ell$ th outgoing partial wave is given in terms of the Legendre polynomial  $P_\ell(\cos \theta)$  (see table 3.1). The angular distribution that results is expressed as a linear combination of  $P_\ell(\cos \theta)$ :

$$W(E, \theta) = \sum_{\ell=0} A_\ell(E) P_\ell(\cos \theta), \quad (3.11)$$

where  $\theta$  is the center-of-mass angle of the reaction products.

$$\begin{aligned}
 P_0(\cos \theta) &= 1 \\
 P_1(\cos \theta) &= \cos \theta \\
 P_2(\cos \theta) &= (3 \cos^2 \theta - 1)/2 \\
 P_3(\cos \theta) &= (5 \cos^3 \theta - 3 \cos \theta)/2 \\
 P_4(\cos \theta) &= (35 \cos^4 \theta - 30 \cos^2 \theta + 3)/8
 \end{aligned}$$

Table 3.1: Legendre polynomials.

Eq. 3.11 is valid for the case of a point detector. However, since the detector subtends a finite solid angle  $d\Omega$ , reaction products emitted at a range of angles ( $\theta'$ ,  $\phi'$ ) will be detected with the detector axis at  $\theta$ . The measured distribution  $\overline{W}(E, \theta)$  is

$$\overline{W}(E, \theta) = \frac{\int W(E, \theta') d\Omega}{\int d\Omega}. \quad (3.12)$$

This integral can be solved by transforming any  $P_\ell(\cos \theta')$  into variables ( $\beta$ ,  $\gamma$ ) which describe the orientation of the reaction product relative to the detector axis, and ( $\theta$ ,  $\phi$ ) which describe the orientation of the detector axis relative to the beam axis. This is accomplished using the spherical-harmonic addition theorem

$$\begin{aligned}
 P_\ell(\cos \theta') &= \frac{4\pi}{2\ell+1} \sum Y_{\ell m'}(\theta, \phi) Y_{\ell m'}(\beta, \gamma) \\
 &= P_\ell(\cos \theta) P_\ell(\cos \beta) \\
 &\quad + \text{terms in } m' > 0.
 \end{aligned} \quad (3.13)$$

Because of the general azimuthal symmetry in both  $\theta$  and  $\gamma$ , only the  $m = 0$  terms contribute.

The  $W(E, \theta)$  is a sum, so the expression for  $\overline{W}(E, \theta)$  involves terms:

$$\begin{aligned}
 \int P_\ell(\cos \theta') d\Omega &= \int P_\ell(\cos \theta) P_\ell(\cos \beta) d\Omega = \\
 &= P_\ell(\cos \theta) \int P_\ell(\cos \beta) \sin \beta d\beta = P_\ell(\cos \theta) J_\ell(\beta),
 \end{aligned} \quad (3.14)$$

where  $J_\ell(\beta)$  is a Bessel function. We can then define solid angle correction factors to the various terms in the angular distribution as

$$Q_\ell = \frac{J_\ell(\beta)}{J_0(\beta)}, \quad (3.15)$$

which depend on the detector geometry only and are always less than one. The observed angular distribution is then

$$\overline{W}(E, \theta) = \sum_{\ell=0} Q_{\ell} A_{\ell}(E) P_{\ell}(\cos \theta) . \quad (3.16)$$

## 3.2 Fits to ${}^7\text{Li}(p,\alpha){}^4\text{He}$ data

### 3.2.1 $S$ -factor

Engstler *et al.* (1992) [50] measured the  ${}^7\text{Li}(p,\alpha){}^4\text{He}$  cross section for center of mass (c.m.) energies  $E = 12.70 - 1004.1$  keV, using both normal kinematics with atomic  ${}^7\text{Li}$  solid targets and inverse kinematics with molecular hydrogen gas targets (fig. 3.1). They used a 2 step procedure to fit their data. In the first step only data in the energy range above 100 keV were fitted in order to keep electron screening effects negligible ( $f(E) \leq 0.8\%$ ). In this energy interval they also used earlier  $S$ -factor measurements by Spinka *et al.* [59] ( $E = 114 - 491$  keV) and by Rolfs and Kavanagh [60] ( $E = 24.6 - 873$  keV), and the overall fit was done assuming a polynomial energy dependence for the  $S$ -factor:

$$S(E) = S_b(E) = a + b E + c E^2 + d E^3 , \quad (3.17)$$

with  $a$ ,  $b$ ,  $c$  and  $d$  as free parameters. The fit gave the following results:

$$a = S_b(0) = 59.3 \text{ keV b}, \quad b = 0.193 \text{ b}, \quad c = -0.356 \times 10^{-3} \text{ keV}^{-1} \text{ b}, \\ d = 0.236 \times 10^{-6} \text{ keV}^{-2} \text{ b} .$$

In the second step, with their own data normalized to these higher-energy data, Engstler *et al.* fitted their low energy data ( $E < 100$  keV) using eq. 2.24 ,

$$S(E) = S_b(E) \exp \left[ \pi \eta(E) \frac{U_e}{E} \right] , \quad (3.18)$$

with  $U_e$  as free parameter, and where  $S_b(E)$  was determined in the first step. The best fit values obtained were  $U_e = 300 \pm 280$  eV (solid target) and  $U_e = 300 \pm 160$  eV (gas target). These are to be compared with  $U_e \approx 134-186$  eV estimated from atomic-physics models (see section 2.3.1).

Lattuada *et al.* (2001) [61] used the Trojan-Horse Method (THM) to extract relative values of the bare  $S$ -factor for  ${}^7\text{Li}(p,\alpha){}^4\text{He}$  for  $E$  from 10 to 380 keV. These were normalized to the

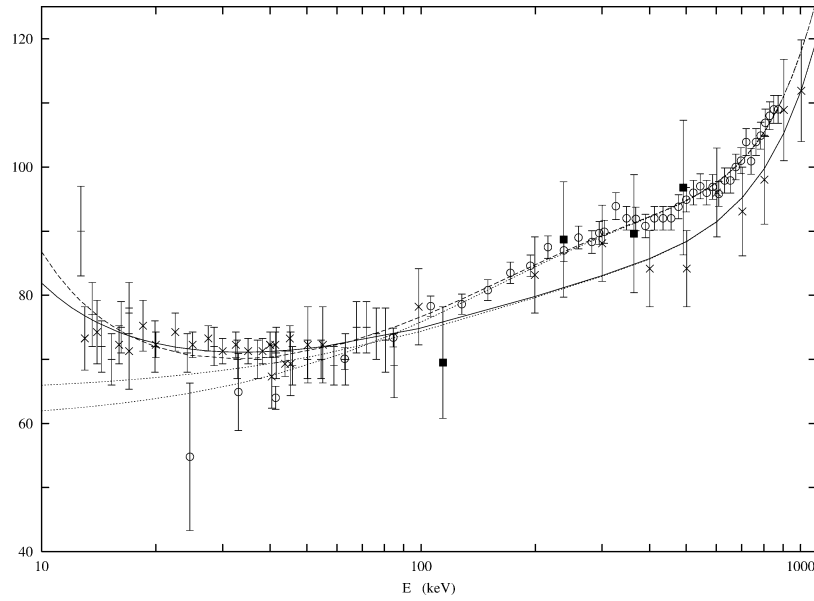


Figure 3.1:  $S$ -factor for the  ${}^7\text{Li}(p,\alpha){}^4\text{He}$  as a function of  ${}^7\text{Li} + p$  c.m. energy. The experimental points are from Engstler *et al.* [50] (atomic target: pluses; molecular target: crosses), Spinka *et al.* [59] (solid squares), and Rolfs and Kavanagh [60] (circles). The solid curve is an  $R$ -matrix best fit to the data from Engstler *et al.*, together with angular-distribution data also from Engstler *et al.*, and  $\alpha + \alpha$   $d$ -wave phase shifts values. The dashed curve is the best fit when the  $S$ -factor data for  $E \geq 100$  keV are from Refs.[59, 60] rather than from Ref.[50]. The dotted curves give the corresponding bare  $S$ -factor. Plot taken from [62].

direct data [50, 60] in the energy range  $E = 200 - 400$  keV. A two step procedure was also used by these authors. Firstly, they fitted their normalized values assuming a quadratic energy dependence for  $S_b(E)$ , obtaining

$$\begin{aligned} a = S_b(0) &= 55 \pm 3 \text{ keV b}, & b &= 0.210 \text{ b}, \\ c &= -0.310 \times 10^{-3} \text{ keV}^{-1} \text{ b}, & d &= 0. \end{aligned}$$

In the second step, the low energy data of Engstler *et al.* [50] was fitted with eq. 3.18 giving  $U_e = 330 \pm 40$  eV.

Barker (2002) [62] re-fitted the data of Engstler *et al.* [50], Spinka *et al.* [59] and Rolfs and Kavanagh [60] in four different approaches, as follows:

1.  $R$ -matrix fit: the determination of  $S_b(E)$  involved seven  ${}^8\text{Be}$  levels (the  $R$ -matrix poles) – two  $0^+$ , four  $2^+$  and one  $4^+$  (see  ${}^8\text{Be}$  level scheme of fig. 3.2). The lower  $0^+$  level is at about 20 MeV; the lowest  $2^+$  level represents the known  $2^+$  levels at 16.6 and 16.9 MeV,

which lie below the  ${}^7\text{Li} + \text{p}$  threshold, and the other two are at about 20 and 22 MeV; the  $4^+$  level is near 20 MeV; and two broad background  $0^+$  and  $2^+$  levels located at 30 MeV.  $p$  and  $f$  waves ( $\ell_i = 1, 3$ ) were considered in the entrance channel. As source data, Barker fitted  $S$ -factor data from Engstler *et al.* [50] for  $E < 100$  keV, and data from Spinka *et al.* [59] and Rolfs and Kavanagh [60] for  $E \geq 100$  keV. In this procedure the  ${}^7\text{Li}(\text{p},\alpha){}^4\text{He}$  angular distribution as measured by Engstler *et al.* [50] between 26 and 1000 keV was also fitted. Including  $U_e$  as a free parameter, the results of the fit (shown by the dashed curve in fig. 3.1) can be summarized by the following quantities:

$$S_b(0) = 60 \text{ keV b}, \quad U_e = 242 \text{ eV}.$$

2. polynomial fit:  $S_b(E)$  and  $U_e$  were fitted simultaneously by the function

$$S(E) = (a + bE + cE^2 + dE^3) \exp\left[\pi\eta(E)\frac{U_e}{E}\right], \quad (3.19)$$

to the  $S$ -factor data from Engstler *et al.* [50] for  $E < 100$  keV, and data from Spinka *et al.* [59] and Rolfs and Kavanagh [60] for  $E \geq 100$  keV. This fit gave:

$$a = S_b(0) = 62.1 \text{ keV b}, \quad b = 0.159 \text{ b}, \quad c = -0.280 \times 10^{-3} \text{ keV}^{-1} \text{ b},$$

$$d = 0.186 \times 10^{-6} \text{ keV}^{-2} \text{ b}; \quad U_e = 204 \text{ eV}.$$

This fit differs from that of Engstler *et al.* only in that all the parameters were here varied simultaneously, leading to a reduction in  $U_e$  from 300 eV [50] to 204 eV, and an increase of  $S_b(0)$  from 59.3 keV b to 62.1 keV b.

3.  $R$ -matrix fit: only to the data of Engstler *et al.* [50] over their whole energy range. The fit 2) did not consider the data of Engstler *et al.* for  $E > 100$  keV and of Rolfs and Kavanagh [60] for  $E < 100$  keV, which are considerably distant from the fitted curve (dashed curve in fig. 3.1). If we only consider Engstler *et al.* data, the  $R$ -matrix approach leads to a fit (shown by the solid curve in fig. 3.1):

$$S_b(0) \approx 65 \text{ keV b}, \quad U_e = 155 \text{ eV}.$$

4. polynomial fit: identical to fit 2) but the  $S$ -factor data is from Engstler *et al.* only. The fitted values obtained were:

$$a = S_b(0) = 66.2 \text{ keV b}, \quad b = 0.090 \text{ b}, \quad c = -0.136 \times 10^{-3} \text{ keV}^{-1} \text{ b},$$

$$d = 0.094 \times 10^{-3} \text{ keV}^{-2} \text{ b}; \quad U_e = 134 \text{ eV}.$$

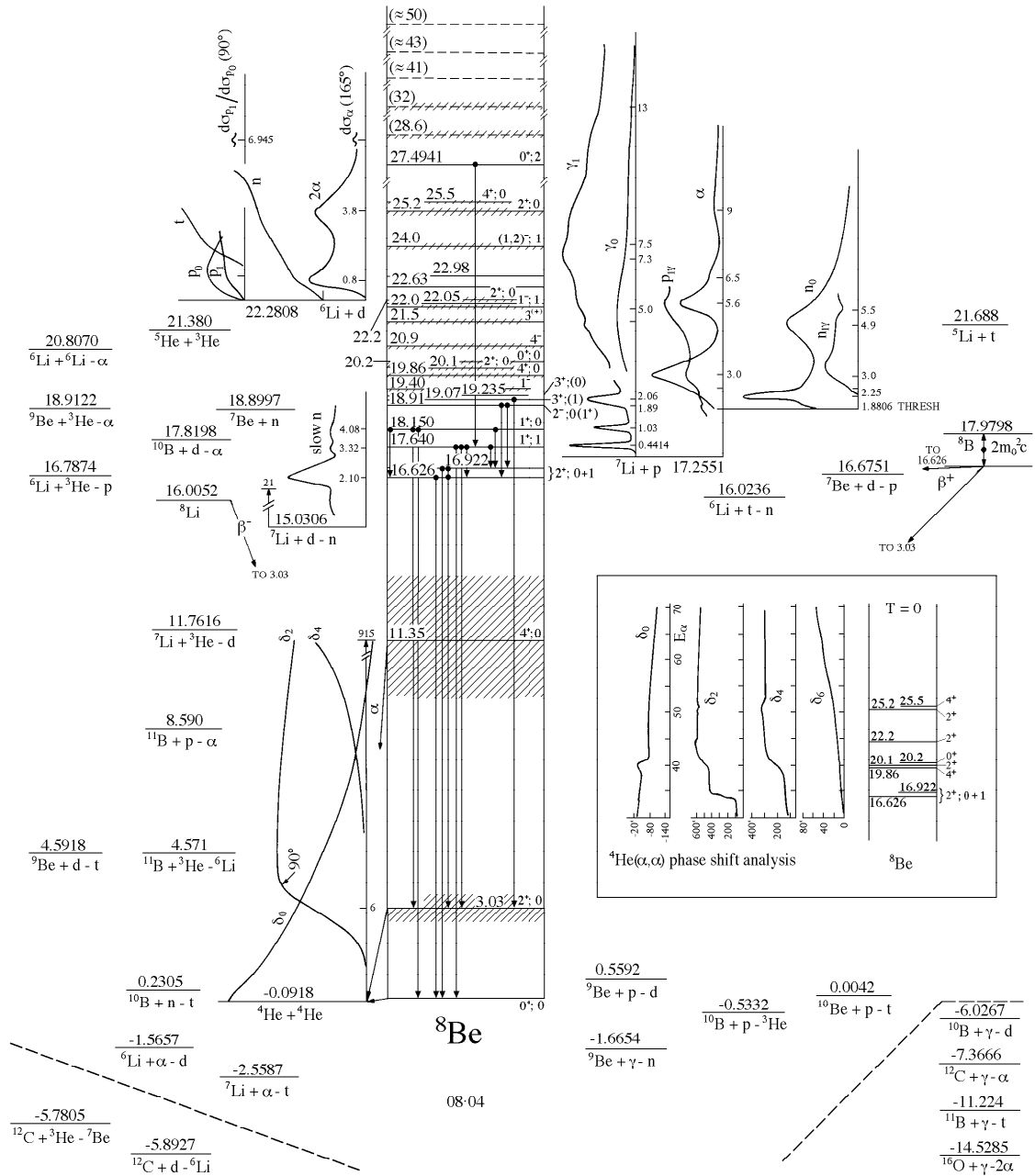


Figure 3.2:  ${}^8\text{Be}$  level scheme.

These last two  $U_e$  values are consistent with the adiabatic limit of 186 eV, and are smaller than those obtained in fits 1) and 2) because the high-energy  $S$ -factor data of Engstler *et al.* [50] have a smaller slope than those of Spinka *et al.* [59] and Rolfs and Kavanagh [60].

The above fits give  $S_b(0) = 60.0 - 66.2$  keV b, which are considerably higher than the value  $55 \pm 3$  keV obtained by Lattuada *et al.* [61] using the THM.

More recently Descouvemont *et al.* (2004) [58], used a  $R$ -matrix fit which involved three  ${}^8\text{Be}$  levels: one broad background level  $0^+$  at  $E \approx 30$  MeV, and two  $2^+$  levels. The lowest energy  $2^+$  level at  $E = 16.774$  MeV represents the subthreshold  $2^+$  levels at 16.6 and 16.9 MeV, and the second  $2^+$  is located at  $E = 20$  MeV. As source data, Descouvemont *et al.* used  $S$ -factor data obtained from Cassagnou *et al.* (1962) [63], Fiedler *et al.* (1967) [64], Spinka *et al.* (1971) [59], Rolfs and Kavanagh (1986) [60], Engstler *et al.* (1992) [50], and Lattuada *et al.* (2001) [61], as shown in fig. 3.3.

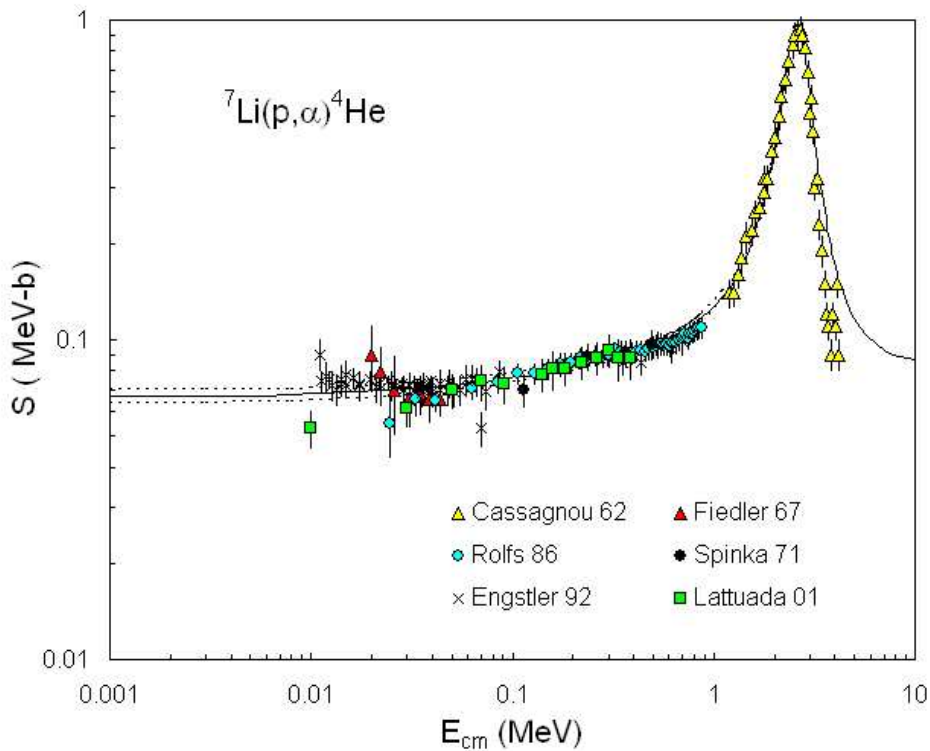


Figure 3.3:  ${}^7\text{Li}(p,\alpha){}^4\text{He}$   $S$ -factor as a function of  ${}^7\text{Li} + p$  c.m. energy. The data are taken from Ref. [63] (Cassagnou 62), Ref. [64] (Fiedler 67), Ref. [59] (Spinka 71), Ref. [60] (Rolfs 86), Ref. [50] (Engstler 92), and Ref. [61] (Lattuada 01). The solid curve represents the  $R$ -matrix fit done by Descouvemont *et al.* [58], and the dotted curves represent the lower and upper  $1\sigma$  limits. Plot taken from [58].

The  $R$ -matrix fit has been applied at energies unaffected by screening effects, which according to these authors is  $E > 40$  keV, and a screening potential has been deduced from eq. 3.18. The results of the fit (shown by the solid curve in fig. 3.3) can be summarized by the following quantities:

$$S_b(0) = 67 \pm 4 \text{ keV b}, \quad U_e = 100 \pm 25 \text{ eV}.$$

The  $U_e$  value obtained by this authors is much lower than the value deduced by Engstler *et al.* [50] ( $U_e = 300$  eV), and also lower than the values obtained by Barker [62] ( $U_e = 134 - 242$  eV). Descouvemont *et al.* question the reliability of the polynomial fit to the bare  $S$ -factor, since the low-energy  $S$ -factor depends on a subthreshold state whose effect is negligible beyond 100 keV. This translates into a higher bare  $S$ -factor and therefore a lower  $U_e$ . However, this subthreshold state does not help in explaining the results of the fits made by Barker, where the  $U_e$  values obtained from a  $R$ -matrix fit are higher than the ones obtained by a polynomial fit, and the  $S_b(0)$  values behave in the opposite way.

This very low  $U_e$  value obtained by Descouvemont *et al.* can also be due to the fact that screening effects were considered negligible down to 40 keV, which is questionable since, according to eq. 2.24, the expected screening factor at this energy is:  $f(E = 40 \text{ keV}) = 1.035$  (for  $U_e = 200$  eV). This energy limit also had the effect of pushing the  $S_b(0)$  to higher values, significantly higher than the value obtained by Lattuada *et al.* [61] and Engstler *et al.* [50], and also higher (but compatible) to the values obtained by Barker [62].

Kasagi *et al.* (2002/04) [65] measured the  ${}^7\text{Li}(\text{p},\alpha){}^4\text{He}$  cross section using a  $\text{PdLi}_x$  ( $x = 5-7\%$ ) alloy target, finding an extremely high value of  $U_e = 1500 \pm 310$  eV, but no explanation of this observation was given.

Table 3.2 below summarizes this section in terms of the  $S_b(0)$  and  $U_e$  values obtained by the different authors for the  ${}^7\text{Li}(\text{p},\alpha){}^4\text{He}$  reaction.

In brief, as seen from the fits of Engstler *et al.*, Barker, and Descouvemont *et al.*, the  $S_b(0)$  and  $U_e$  values are very sensitive to which particular data sets are used on the fits, whether a polynomial fit is done in one or two steps, and at which energy can screening effects be considered negligible. Also, Kasagi *et al.* value for  $U_e$  is disturbing as it is almost an order of magnitude higher than expected from theoretical models. For these reasons a new measurement of this reaction cross section for energies above 100 keV is necessary in order to define more accurately the bare contribution,  $S_b(E)$ , which then enters the calculation of  $U_e$ .

Fitting procedure	Data fitted	$S_b(0)$ (keV b)	$U_e$ (eV)	$\chi^2/\text{ndf}$	Ref.	Obs.
cubic	[50, 59, 60]	59.3	300±280	0.1	[50]	solid target
cubic	[50, 59, 60]	59.3	300±160	0.6	[50]	gas target
quadratic	[61, 50, 60]	55±3	330±40	–	[61]	–
cubic	[50]	66.2	134	0.43	[62]	–
cubic	[50, 59, 60]	62.1	204	0.67	[62]	–
R-matrix	[50]	64.8	155	0.46	[62]	–
R-matrix	[50, 59, 60]	60.0	242	0.60	[62]	–
–	[65]	–	1500±310	–	[65]	solid target

Table 3.2:  ${}^7\text{Li}(p,\alpha){}^4\text{He}$ : summary table for  $S_b(0)$  and  $U_e$ .

### 3.2.2 Angular distributions

Rolfs *et al.* (1986) [60] and Engstler *et al.* (1992) [50] measured  ${}^7\text{Li}(p,\alpha){}^4\text{He}$  angular distributions, respectively in the angular range  $\theta_{lab} = 30^\circ - 90^\circ$  for energies between 44 keV and 790 keV, and in the angular range  $\theta_{lab} = 60^\circ - 160^\circ$  for energies between 26 keV and 1000 keV. Engstler *et al.* fits to their data with eq. 3.16 have shown that angular distributions are well described with an  $A_2$  coefficient ( $A_4 \approx 0$ ). Sample angular distributions for this reaction are illustrated in fig. 3.4 - left panel, and the energy dependence of the deduced  $A_2$  coefficient is shown in fig. 3.4- right panel. The latter figure contains also data from Rolfs *et al.*; good agreement is noted in the overlapping energy region, even though Rolfs *et al.* data show a tendency to be lower than Engstler *et al.* data, between 100 and 500 keV.

## 3.3 Fits to ${}^6\text{Li}(p,\alpha){}^3\text{He}$ data

### 3.3.1 S-factor

Engstler *et al.* (1992) [50] measured the  ${}^6\text{Li}(p,\alpha){}^3\text{He}$  cross section for c.m. energies  $E = 10.74 - 500.8$  keV, using both normal kinematics with atomic  ${}^6\text{Li}$  solid targets and inverse

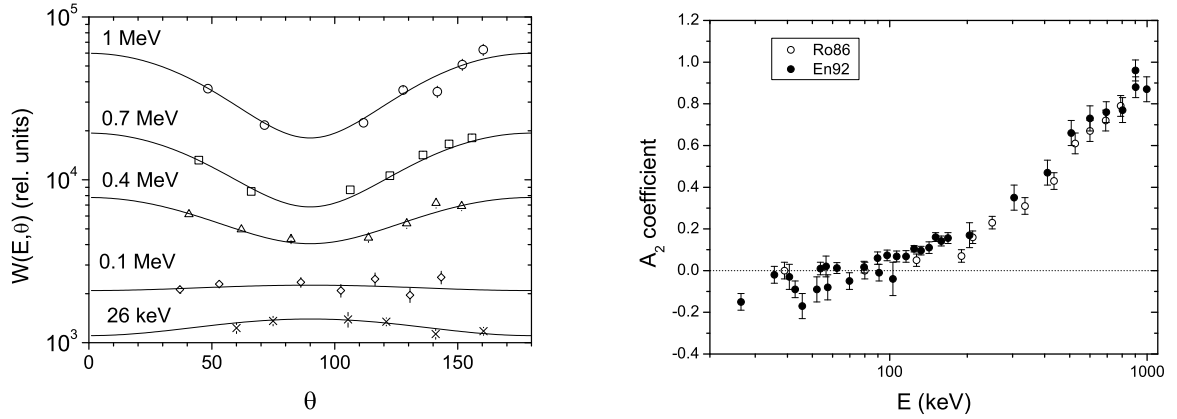


Figure 3.4: Left panel: Angular distribution  $W(E, \theta)$  at representative c.m. energies for the  ${}^7\text{Li}(p, \alpha){}^4\text{He}$  reaction. Data taken from [50]. Right panel: Energy dependence of the dominant coefficient,  $A_2$ , in the angular distribution for the  ${}^7\text{Li}(p, \alpha){}^4\text{He}$  reaction. Data taken from [50] and [60].

kinematics with molecular hydrogen gas targets (fig. 3.5). The fitting procedure to their  $S$ -factor data was identical to the one used for the  ${}^7\text{Li}$ : a two step procedure. The best fit values obtained, using also previous data from other authors (Marion *et al.* (1956) [66], Gemeinhardt *et al.* (1966) [67], Fiedler *et al.* (1967) [64], Spinka *et al.* (1971) [59], Elwyn *et al.* (1979) [68], Shinozuka *et al.* (1979) [69], Szabo *et al.* (1983) [70], and Kwon *et al.* (1989) [71]), were:

$$\begin{aligned} \text{First step: } a &= S_b(0) = 3.09 \text{ MeV b}, & b &= -0.923 \text{ b}, \\ c &= -0.444 \text{ MeV}^{-1} \text{ b}, & d &= 0. \end{aligned}$$

Second step:  $U_e = 470 \pm 150 \text{ eV}$  (solid target);  $U_e = 440 \pm 150 \text{ eV}$  (gas target).

Barker (2002) [62] made polynomial fits to the  $S$ -factor data of  ${}^6\text{Li}(p, \alpha){}^3\text{He}$ . According to this author, a  $R$ -matrix fit to this reaction is not feasible because some of the required  ${}^7\text{Be}$  levels are too uncertain to be used in the calculations. Four different polynomial fits were performed:

1. polynomial fit: to the data of Engstler *et al.* [50].  $S_b(E)$  and  $U_e$  were fitted simultaneously by the function

$$S(E) = (a + bE + cE^2) \exp\left[\pi\eta(E)\frac{U_e}{E}\right]. \quad (3.20)$$

A reasonable fit was obtained, with  $U_e = 265 \text{ eV}$ , but  $S(E)$  rises as the energy increases above the fitted region (i.e., for  $E > 500.8 \text{ keV}$ ), contrary to other measurements (Marion *et al.* [66], Shinozuka *et al.* [69], and Elwyn *et al.* [68]).

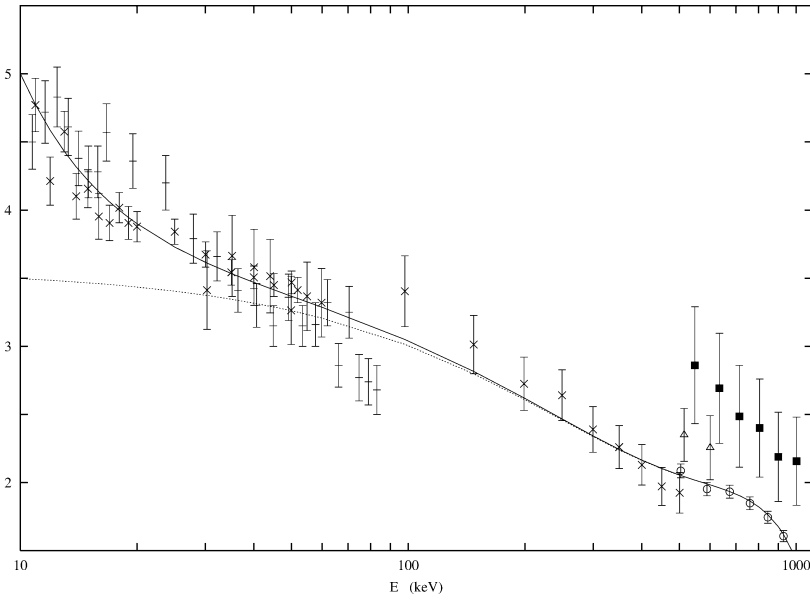


Figure 3.5:  $S$ -factor for the  ${}^6\text{Li}(p,\alpha){}^3\text{He}$  as a function of  ${}^6\text{Li} + p$  c.m. energy. The experimental points are from Engstler *et al.* [50] (atomic target: pluses; molecular target: crosses); Marion *et al.* [66] (solid squares); Shinozuka *et al.* [69] (triangles); Elwyn *et al.* [68] (circles). The solid curve is a best fit, based on a cubic form for the bare  $S$ -factor, which is shown by the dotted curve. Plot taken from [62].

2. polynomial fit: to the data of Engstler *et al.* [50].  $S_b(E)$  and  $U_e$  were fitted simultaneously by the function

$$S(E) = (a + bE + cE^2 + dE^3) \exp\left[\pi\eta(E)\frac{U_e}{E}\right]. \quad (3.21)$$

Again, a reasonable fit was obtained, with  $U_e = 209$  eV, but the fit becomes negative for  $E \geq 650$  keV.

3. polynomial fit: to the data of Engstler *et al.* [50], Marion *et al.* [66], Shinozuka *et al.* [69], and Elwyn *et al.* [68].  $S_b(E)$  and  $U_e$  were fitted simultaneously by eq. 3.20. The best fit value for  $U_e$  was 300 eV. This fit differs from that of Engstler *et al.* ( $U_e = 440$ – $470$  eV) essentially only in that the polynomial parameters and  $U_e$  are varied simultaneously.
4. polynomial fit: to the data of Engstler *et al.* [50], Marion *et al.* [66], Shinozuka *et al.* [69], and Elwyn *et al.* [68].  $S_b(E)$  and  $U_e$  were fitted simultaneously by eq. 3.21. The best fit values obtained were

$$a = S_b(0) = 3.56 \text{ MeV b}, \quad b = -6.44 \text{ b}, \quad c = 9.39 \text{ MeV}^{-1} \text{ b},$$

$$d = -5.07 \text{ MeV}^{-2} \text{ b}; \quad U_e = 260 \text{ eV}.$$

Tumino *et al.* (2003) [72] studied the  ${}^6\text{Li}(p,\alpha){}^3\text{He}$  reaction from  $E = 2.4$  MeV down to astrophysical energies by means of the Trojan-Horse Method applied to the  $\text{D}({}^6\text{Li},\alpha){}^3\text{He}n$  three-body reaction. The relative values of  $S_b(E)$  were normalized to the data of Elwin *et al.* (1979) [68] at the top of the  $E=1.6$  MeV resonance. The authors fitted their normalized values with a second order polynomial, obtaining

$$a = S_b(0) = 3.00 \pm 0.19 \text{ MeV b},$$

$$b = -3.02 \text{ b}, \quad c = 1.93 \text{ MeV}^{-1} \text{ b},$$

pointing out, however, that their very low energy part of the  $S(E)$  spectrum had to be “substantiated”.

Table 3.3 below summarizes this section in terms of the  $S_b(0)$  and  $U_e$  values obtained by the different authors for the  ${}^6\text{Li}(p,\alpha){}^3\text{He}$  reaction.

Fitting procedure	Data fitted	$S_b(0)$ (MeV b)	$U_e$ (eV)	$\chi^2/\text{ndf}$	Ref.	Obs.
quadratic	[50, 59] and [64] to [71]	3.09	$470 \pm 150$	0.6	[50]	solid target
quadratic	[50, 59] and [64] to [71]	3.09	$440 \pm 150$	1.8	[50]	gas target
quadratic	[50, 66, 68, 69]	3.41	300	1.77	[62]	–
cubic	[50, 66, 68, 69]	3.56	260	1.51	[62]	–
quadratic	[72]	3.00	–	–	[72]	–

Table 3.3:  ${}^6\text{Li}(p,\alpha){}^3\text{He}$ : summary table for  $S_b(0)$  and  $U_e$ .

From the  $S(E)$  plot (fig 3.5) and from the values of the fits performed by Engstler *et al.* , by Barker, and by Tumino *et al.* , we also conclude that the  $S_b(0)$  and  $U_e$  values obtained for the  ${}^6\text{Li}(p,\alpha){}^3\text{He}$  are very sensitive to which particular data sets are used on the fits, and whether a polynomial fit is done in one or two steps. So, also in this case, and for the same reasons presented for the  ${}^7\text{Li}(p,\alpha){}^4\text{He}$  reaction, a new measurement of the  ${}^6\text{Li}(p,\alpha){}^3\text{He}$  cross section is necessary.

### 3.3.2 Angular distributions

Elwyn *et al.* (1979) [68] measured the angular distributions for the  ${}^6\text{Li}(p,\alpha){}^3\text{He}$  reaction at laboratory angles between  $35^\circ$  and  $155^\circ$  at energies up to 1 MeV, and from  $20^\circ$  (or  $25^\circ$  in some cases) to  $90^\circ$  at energies up to 3 MeV. Engstler *et al.* (1992) [50] made a similar study for the angular range  $\theta_{lab} = 60^\circ - 160^\circ$  for energies between 25 keV and 550 keV. They showed that their data are dominated by an  $A_1$  coefficient whose energy dependence is plotted in fig. 3.6, with a small  $A_2$  coefficient of the analytic form  $A_2(E) = -0.029 - 2.6 \times 10^{-4}E$ , with  $E$  in keV. These results are in excellent agreement with the results of Elwyn *et al.* in the overlapping energy region (not shown in fig. 3.6).

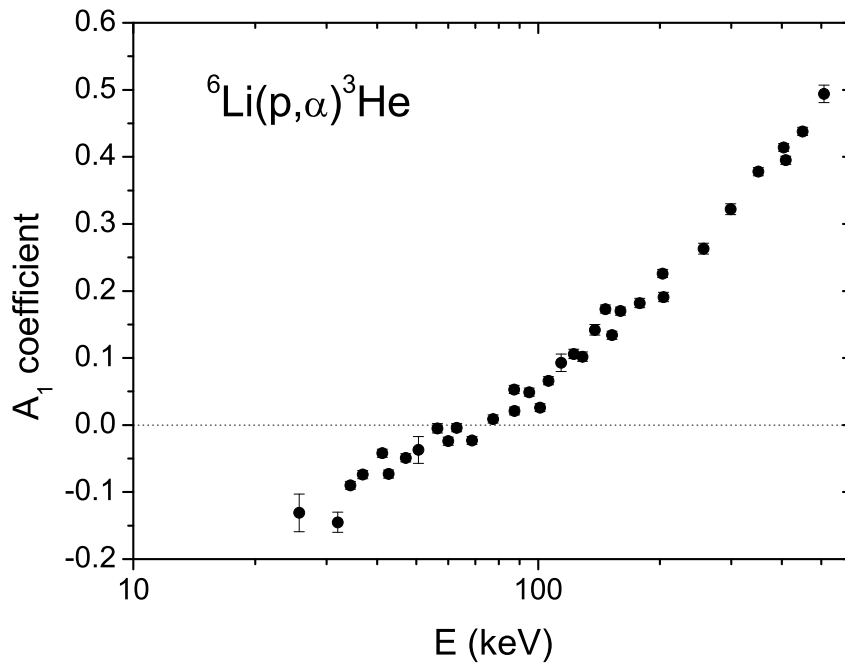


Figure 3.6: Energy dependence of the dominant coefficient,  $A_1$ , in the angular distribution for the  ${}^6\text{Li}(p,\alpha){}^3\text{He}$  reaction. Data taken from [50].

# Chapter 4

## Experimental details

The previous chapters have shown the importance of remeasuring the  ${}^7\text{Li}(p,\alpha){}^4\text{He}$  and  ${}^6\text{Li}(p,\alpha){}^3\text{He}$  reactions cross sections. This chapter describes the experimental details for these measurements, which took place in two laboratory facilities: Ion Beam Laboratory at ITN (Instituto Tecnológico e Nuclear) located close to Sacavém, Portugal; and DTL (Dynamitron-Tandem-Laboratorium) at the Ruhr-Universität Bochum, Germany. This chapter is divided in two major sections. The first section, concerning the experimental setup, describes the accelerator machines, target chambers, electronics and acquisition systems used to measure the lithium cross sections (expressed in terms of the  $S$ -factor) and angular distributions. The second section, concerning the target preparation and analysis, describes the production and analysis of the different lithium targets used in this work.

### 4.1 Experimental setup

The  ${}^7\text{Li}(p,\alpha){}^4\text{He}$  and  ${}^6\text{Li}(p,\alpha){}^3\text{He}$  reactions cross section measurement at high energy ( $E_{\text{lab}} > 116$  keV), as well as the angular distributions measurements for the  ${}^7\text{Li}(p,\alpha){}^4\text{He}$  reaction were done at the Van de Graaff 2.5 MeV accelerator at ITN, while the low energy part ( $E_{\text{lab}} < 100$  keV) cross section measurements for these two reactions was done at the DTL 100 keV accelerator.

### 4.1.1 ITN setup

The 2.5 MV Van de Graaff accelerator of the Ion Beam Laboratory provided  $H^+$ ,  $H_2^+$  and  $H_3^+$  beams <sup>1</sup> in the energy range  $E_{lab} = 116$  to 2000 keV, with a beam current on target of up to 200 nA. The absolute beam energy was known with a precision of  $1.1 \times 10^{-3}$  (as observed at the narrow  $E_p = 992$  keV resonance in  $^{27}Al(p,\gamma)^{28}Si$  – see fig. 4.1), which leads to a negligible uncertainty in the  $^7Li(p,\alpha)^4He$  and  $^6Li(p,\alpha)^3He$  cross sections, *i.e.*, 0.65% error at the lowest energy.

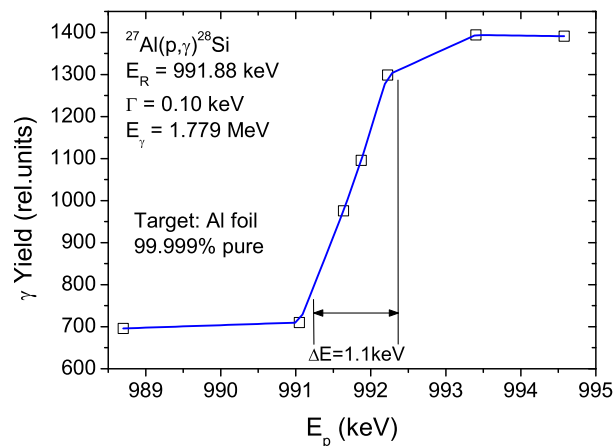


Figure 4.1: The excitation function of the  $^{27}Al(p,\gamma)^{28}Si$  reaction at  $E_{r,lab} = 992$  keV using an Al target 99.999% pure ( $E_\gamma = 1.779$  MeV). The curve through the data points is to guide the eye only.  $E_{r,lab}$  corresponds to the mid-point on the excitation function curve halfway between the 12% and 88% height of the net yield. The energy difference between these points is the energy spread of the beam, 1.1 keV in our case.

The beam produced from the accelerator rf ion source is focused by an einzel lens just outside this source and then goes through x- and y- electrostatic deflectors located after the accelerator tank. From here the beam enters one of the three beam lines after passing a  $25^\circ$  analysing magnet and through a pair of slits (1 mm opening). Our beam line is schematized in fig. 4.2, with the target chamber located 2.2 meters downstream of the slits.

The beam line and target chamber system were pumped by two turbomolecular pumps, as shown in the diagram of fig. 4.2. In addition, the beam entering the chamber passed through an inline liquid-nitrogen cooled copper tube (length = 219.5 mm,  $\varnothing_{internal} = 20$  mm). With this

<sup>1</sup> $H_2^+$  and  $H_3^+$  molecular ions were used to give proton energies at the target of 1/2 and 1/3 of the terminal voltage, respectively.



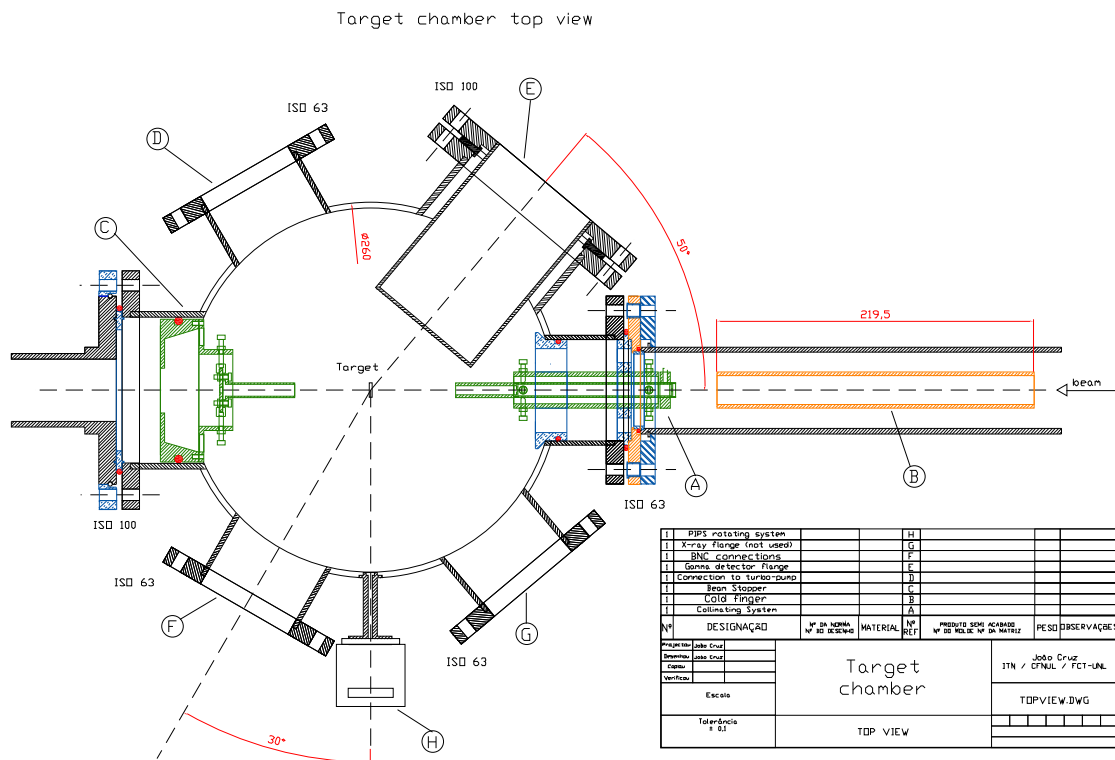


Figure 4.3: Top view drawing of target chamber used at ITN. Colour legend: green – steel AISI 304; orange – other metals; blue – insulator; red – o-rings.

when targets are thin enough to allow a fraction of the beam going through them and hitting the beam stopper;

3. insulating rotating flanges: mounted in the flanges connected to the beam line and to the turbo-pump connecting flange (see below);
4. insulating rings (not shown in figure 4.3): mounted in the screws that support the target chamber;
5. 6.3  $\mu\text{m}$  mylar foil: covered the GEM-45190-P HPGe detector sleeve (see below).

The detailed blueprints of these pieces are in Appendix A.

With this setup the electric impedance of the target chamber was around 150 M $\Omega$ .

The solid targets were mounted on a target holder and positioned in the center of the target chamber, oriented with its normal at an angle of either 0° or 45° with respect to the beam

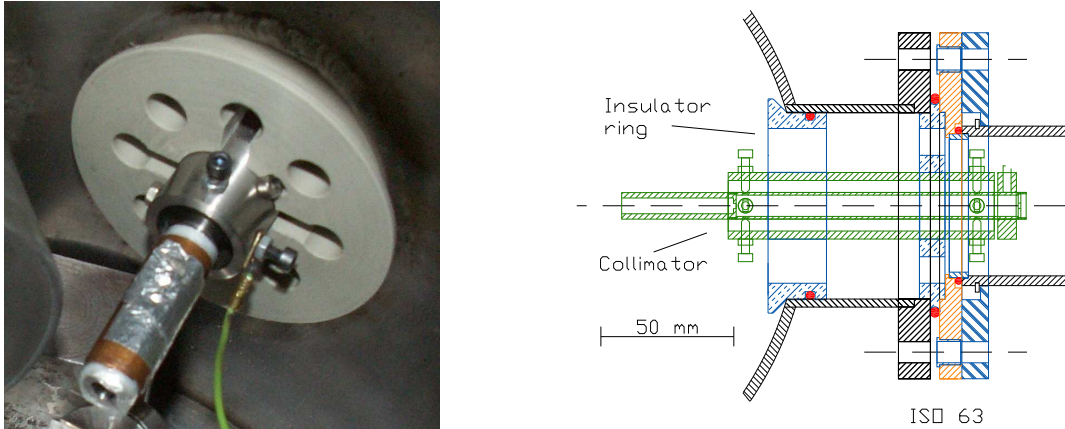


Figure 4.4: Left panel: Photo of collimating system - view from inside the target chamber. Right panel: drawing of the collimating system and insulating supports.

direction.

This chamber is equipped with three radiation detectors:

1. charged particles detection with 2 Canberra PIPS (Passivated Implanted Planar Silicon) detectors (PD-50-12-100 RM: active area = 50 mm<sup>2</sup>, effective thickness = 100 μm, resolution = 12 keV for 5486 keV alphas from <sup>241</sup>Am decay to <sup>237</sup>Np), called MOVE and MOVD in the following. Each detector was closed inside a teflon and metal box with a Ø = 6 mm aperture and mounted on a movable arm within the chamber, 21° apart (fixed angular distance), in IBM geometry<sup>2</sup>. Their angular position can be changed and controlled from outside the target chamber in the angular range  $\theta_{\text{lab}}=84^{\circ}-165^{\circ}$ , with a precision around 1°. With the Si detectors positioned at 124° (MOVE) and 145° (MOVD), the distance between the target and the detector at 145° was measured to be 88±1 mm. This geometry corresponds to a solid angle of  $\Omega = \pi r^2/d^2 \Rightarrow \Omega = \pi 3^2/88^2 = 3.651 \pm 0.083$  msrad. With an isotopic <sup>241</sup>Am α source placed in the target holder it was verified that the number of detected α-particles by both detectors was a function of their angular position and of the detector itself, as shown in fig. 4.6, meaning that the detectors were not exactly centered with the target holder. The subsequent change in the solid angle was corrected assuming a linear dependence of the solid angle with the angle  $\theta_{\text{lab}}$ , which is a

<sup>2</sup>IBM geometry: the incident beam, the scattered beam (directed at the detector), and the sample normal are all in the same plane.

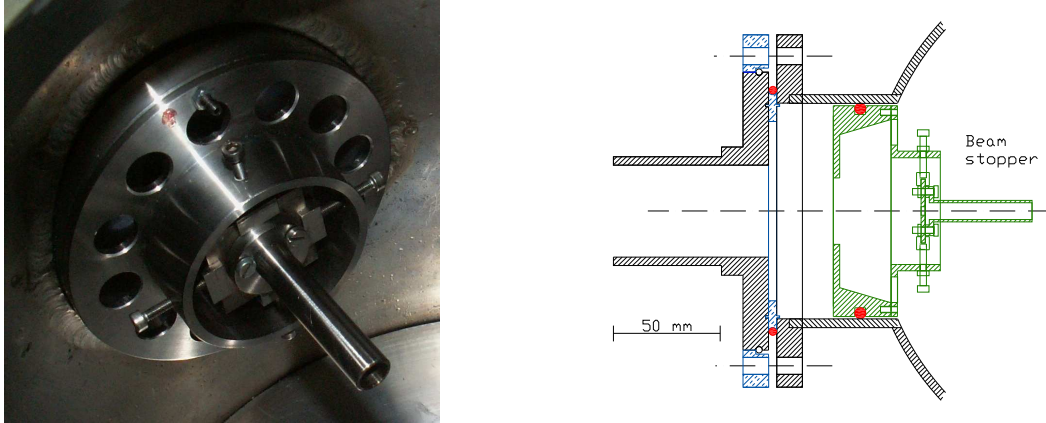


Figure 4.5: Left panel: Photo of beam stopper - view from inside the target chamber. Right panel: beam stopper drawing.

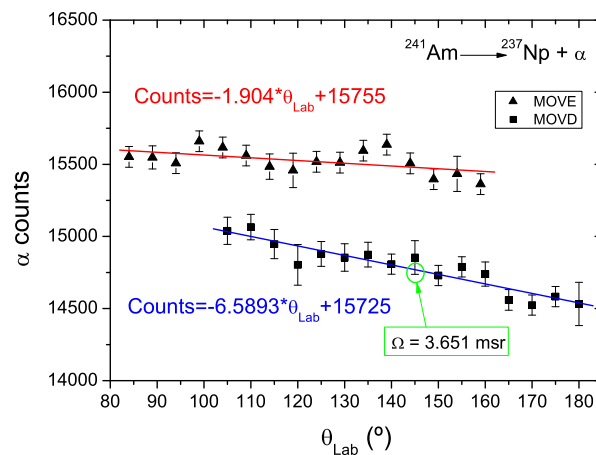


Figure 4.6: Number of  $\alpha$ 's detected by each Si detector as a function of its angular position. The full lines represents the results of the linear fits to the data, as reported in the text.

good assumption as shown by the linear fits shown as solid lines in fig. 4.6.

For proton energies lower than  $\approx 300$  keV, the detectors were shielded with a  $6.3 \mu\text{m}$  thick mylar foil to stop the intense flux of elastically scattered particles.

2.  $\gamma$ -rays detection with 1 EG&G Ortec GEM-45190-P HPGe detector (crystal diameter = 64.0 mm, crystal length = 62.6 mm, resolution=1.76 keV, and relative efficiency=45% at 1.332 MeV,  $^{60}\text{Co}$ ). It is positioned at a distance of 55.5 mm from the target and makes an angle of  $130^{\circ}$  with the beam line as shown in fig. 4.3.

The radiation entering the detectors is “converted” to an electrical pulse. These pulses from the detectors (and associated preamplifiers) are amplified and digitized with 1024 (or 4096)-channel analog-to-digital converters (ADCs), inserted in ISA bus slots of a PC computer, and interfaced via GENIE-2000 GUI<sup>3</sup>. The data are stored as pulse-height spectra. A typical spectrum of the charged particles from reactions of protons with a LiF-Ag target (see section 4.2) is shown in fig. 4.7 – left panel. Besides the pulses corresponding to the  ${}^4\text{He}$  particles produced in the  ${}^7\text{Li}(p,\alpha){}^4\text{He}$  reaction, the spectrum also show pulses from elastically scattered protons, and  $\alpha$  particles from the  ${}^{19}\text{F}(p,\alpha){}^{16}\text{O}$  reaction ( $Q = 8.1$  MeV). A spectrum of  $\gamma$ -rays acquired during a run with a  ${}^7\text{Li}$  implanted in Al target (see section 4.2) is shown in fig. 4.7 – right panel. Here, besides the target produced 478 keV  $\gamma$ -ray from the  ${}^7\text{Li}(p,p'\gamma){}^7\text{Li}$  reaction there are also present background  $\gamma$ -rays, identified in the spectrum.

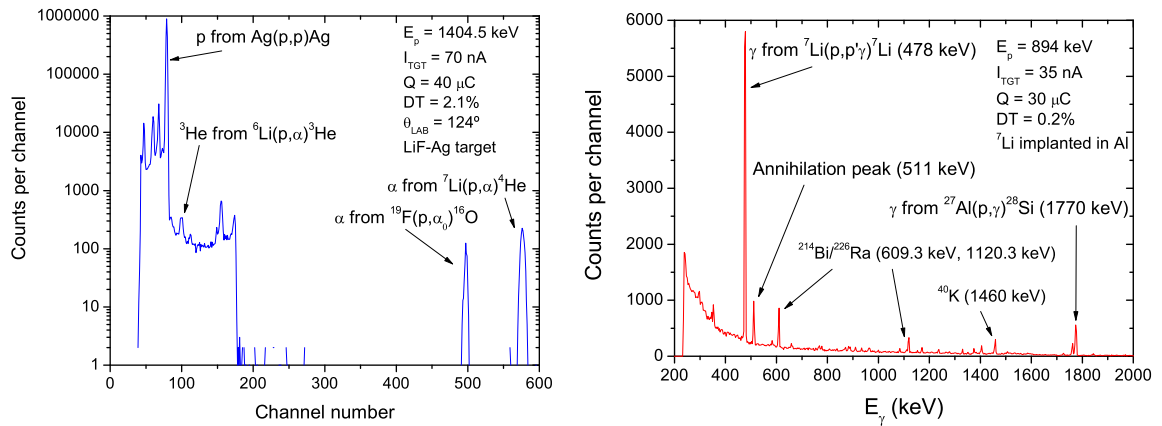


Figure 4.7: Left panel: Particle spectrum obtained with the Si detector at an angle of  $124^\circ$  by bombarding the LiF-Ag target with protons of incident energy  $E_p = 1404.5$  keV. Right panel:  $\gamma$ -ray spectrum obtained with the HPGe detector at an angle of  $130^\circ$  by bombarding the  ${}^7\text{Li}$  implanted in Al target with protons of incident energy  $E_p = 894$  keV.

### Analysing magnet calibration

The  $25^\circ$  analysing magnet was calibrated by the measurement of the resonance reactions listed in table 4.1 (also listed are the corresponding  $\gamma$ -rays, its widths and resonance energies).

Three targets were used to measure the excitation functions (or  $\gamma$ -ray yields) at resonances: LiF (thickness =  $1.85 \times 10^{18}$  at/cm<sup>2</sup> =  $40.0$   $\mu\text{g}/\text{cm}^2$ ), NaF (thickness =  $1.11 \times 10^{18}$  at/cm<sup>2</sup> =  $38.6$

<sup>3</sup>GUI stands for Graphics User Interface.

Proton Energy (keV)	Detected $\gamma$ radiation [Energy (MeV)]	Width $\Gamma$ (keV)	Reaction	Ion beam calibration
163.0	11.68, 4.43	5.2	$^{11}\text{B}(p,\gamma)^{12}\text{C}$	$\text{H}_3^+$
$340.46 \pm 0.04$	7.12, 6.92, 6.13	$2.34 \pm 0.04$	$^{19}\text{F}(p,\alpha\gamma)^{16}\text{O}$	$\text{H}_2^+, \text{H}_3^+$
483.6	7.12, 6.92, 6.13	0.9	$^{19}\text{F}(p,\alpha\gamma)^{16}\text{O}$	$\text{H}_2^+$
$872.11 \pm 0.20$	7.12, 6.92, 6.13	$4.7 \pm 0.2$	$^{19}\text{F}(p,\alpha\gamma)^{16}\text{O}$	$\text{H}^+, \text{H}_2^+$
1373.2	7.12, 6.92, 6.13	11.0	$^{19}\text{F}(p,\alpha\gamma)^{16}\text{O}$	$\text{H}^+, \text{H}_2^+$
1645.1	0.440	8.0	$^{23}\text{Na}(p,p'\gamma)^{23}\text{Na}$	$\text{H}^+$
1930.7	0.440	6.9	$^{23}\text{Na}(p,p'\gamma)^{23}\text{Na}$	$\text{H}^+$

Table 4.1: Analysing magnet calibration reactions.

$\mu\text{g}/\text{cm}^2$ ), and boron (thickness =  $\infty$ ) targets. For this last target, a thick target, the energy of the resonance corresponds to the midpoint on the yield curve halfway between the 12% and 88% height of the net yield (fig. 4.8 – left panel). For the LiF and NaF thin targets the maximum on the yield curve corresponds to the resonance energy plus half the target energy loss ( $\Delta E$ ):  $E_{\text{max}} = E_{\text{R}} + \Delta E/2$  (fig. 4.8 – right panel). This  $\Delta E$  is related with the experimental (observed) width,  $\Gamma'$ , and the resonance natural width,  $\Gamma$ , by the equation:

$$\Gamma' = \sqrt{\Delta E^2 + \Gamma^2}. \quad (4.1)$$

The experimental width corresponds to the  $\gamma$  yield profile FWHM. However, since this profile is obtained as a function of  $B^2$ , where  $B$  is the magnetic induction, the FWHM in Gauss<sup>2</sup> must be converted to a FWHM in keV. This requires an apriori energy calibration and subsequent iterative process for the determination of  $\Gamma'$ , where in the first step an approximate calibration is assumed, which is, after each iteration, corrected for new values. This iterative process stops when the energy calibration parameters stop changing.

The absolute energy calibrations thus obtained are (where  $B$  is in units of Gauss):

$$\text{H}^+ \text{ beam : } E \text{ (keV)} = 3.4799 \frac{B^2}{10^4} + 6.5435 \quad (4.2)$$

$$\text{H}_2^+ \text{ beam : } E \text{ (keV)} = 0.8743 \frac{B^2}{10^4} - 2.0094 \quad (4.3)$$

$$\text{H}_3^+ \text{ beam : } E \text{ (keV)} = 0.3847 \frac{B^2}{10^4} - 1.3657 \quad (4.4)$$

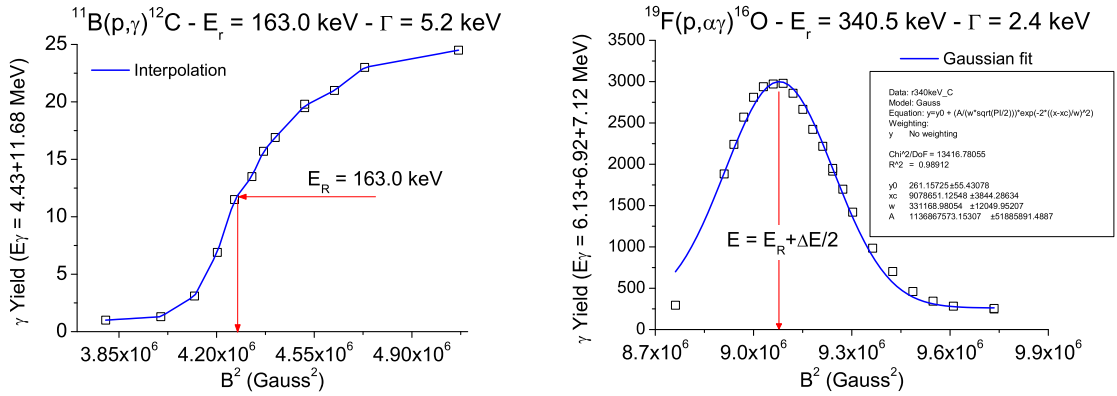


Figure 4.8: Left panel: The excitation function of the  $^{11}\text{B}(p,\gamma)^{12}\text{C}$  reaction at  $E_{r,\text{lab}} = 163.0$  keV using a thick boron foil. The blue line connecting the data points are an interpolation curve and is to guide the eye only. Right panel: The excitation function of the  $^{19}\text{F}(p,\alpha\gamma)^{16}\text{O}$  reaction at  $E_{r,\text{lab}} = 340.5$  keV using a thin LiF film. The blue line corresponds to a gaussian function fitted to the data points (see text for details).

## 4.1.2 DTL setup

The DTL 100 keV accelerator, schematized in fig. 4.9, provided a proton beam in the energy range  $E_{\text{lab}} = 25$  to 100 keV, with a beam current on target of up to  $100 \mu\text{A}$ . The absolute beam energy was known with a precision of  $5 \times 10^{-5}$  (as obtained by a resistor chain calibrated at the Physikalisch-Technische Bundesanstalt in Braunschweig), which leads to a negligible uncertainty in the  $^7\text{Li}(p,\alpha)^4\text{He}$  and  $^6\text{Li}(p,\alpha)^3\text{He}$  cross sections, *i.e.*, 0.04% error at the lowest energy.

The accelerator ion source was of the duo-plasmatron type, which provides beams with high current and small energy spread [54], necessary for measurements of nuclear reactions induced by very low energy charged particles. After leaving the ion source, the ion beam is focused by an einzel lens through the entrance aperture of a short (20 cm long) grounded accelerating tube, and then deflected by a  $90^\circ$  double focusing magnet through a pair of slits into a retractable Faraday cup. From here the beam goes through an electrostatic quadrupole triplet and a pair of magnetic steerers to the experimental site. The beam direction is defined by the 25 mm width analyzing magnet slits and a  $\varnothing = 8$  mm aperture located 2.5 m downstream of the slits. This aperture was placed 46 cm before the target. The beam was focused on the target into a spot

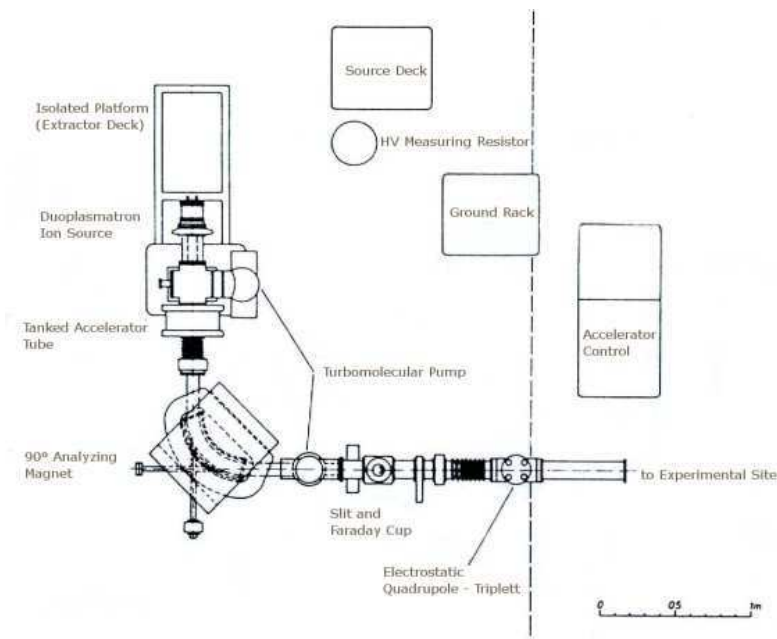


Figure 4.9: Schematic diagram of the main components of the 100 kV accelerator at DTL, Bochum. Figure taken from [54].

of  $\varnothing \approx 15$  mm, using x- and y- scanners located just before the  $\varnothing = 8$  mm aperture. The solid targets ( $\varnothing 40$  mm and  $\approx 0.5$  mm thick) were oriented perpendicular to the beam direction, and were water cooled (either directly or indirectly). A liquid-nitrogen dewar was used to cool a Cu pipe (length = 41 cm,  $\varnothing_{\text{internal}} = 4.7$  cm) which extended from the aperture to within 5 cm of the target. With this Cu pipe plus two turbo pumps (450 l/s pumping speed, each) and one cryogenic pump, all located near the entrance of the target chamber (cylinder of length = 20 cm and  $\varnothing = 17$  cm) carbon buildup on the target surface was minimized (pressure inside the target chamber  $< 2 \times 10^{-8}$  mbar). Inside the target chamber, 4 Canberra PIPS detectors (Pd600-22-100: active area = 600 mm<sup>2</sup>, effective thickness = 100  $\mu\text{m}$ , resolution = 22 keV) were installed at a laboratory angle,  $\theta_{\text{lab}}$ , of 130°, around the beam axis, and at a distance of 5 cm from the target (see fig. 4.10). The detectors were shielded with a 0.75  $\mu\text{m}$  thick Ni foil to stop the intense flux of elastically scattered particles. As we have seen in section 3.2.2, the angular distributions obtained for  $E_{\text{lab}}$  below 100 keV are almost flat, so for the chosen detection angle the effects of angular distributions are negligible. From this geometry, it is expected a solid angle covered by the 4 Si detectors of  $\Omega \approx 0.076$  sr, in good agreement with the measured value  $\Omega =$

$0.0689 \pm 0.0009$  srad using a calibrated  $\alpha$ -source placed at the center of the target holder <sup>4</sup>.

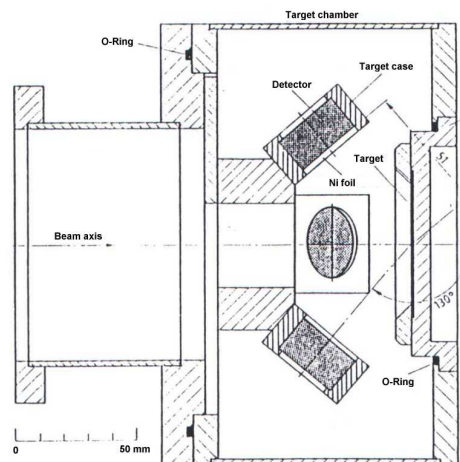


Figure 4.10: Schematic view of the target chamber at DTL, Bochum. Figure taken from [54].

The target, together with the chamber and the detector holders (including the Ni foils) formed a Faraday cup for beam integration, provided that they were electrically insulated from the aperture, the Cu pipe and the beam line. A voltage of  $-200$  V was applied to the Cu pipe for the suppression of secondary electrons from the target. The current on target was measured with an estimated precision of about 2% including the error of the beam current integrator.

At low energies, we can not rule out that the ion beam, on its way from the analyzing magnet to the target, can capture electrons from the rest gas in the beam line ( $P \approx 2 \times 10^{-7}$  mbar), which would lead to an incorrect determination of the number of incident protons based on charge measurement. It was observed, though, by Raiola [54] that the neutral current was negligible:  $I_{\text{neutral}} / I_{\text{charged}} < 0.2\%$ .

The pulses from the Si detectors (and associated preamplifiers) are amplified and digitized with 1024-channel ADCs inserted in ISA bus slots of a PC computer, and interfaced via a Canberra GUI. Typical spectra of the charged particles from reactions of protons with a  $\text{Li}_2\text{WO}_4$  target (see section 4.2) are shown in fig. 4.11 for two different energies. Besides the pulses corresponding to the  ${}^4\text{He}$  and  ${}^3\text{He}$  particles produced by the  ${}^7\text{Li}(p,\alpha){}^4\text{He}$  and  ${}^6\text{Li}(p,\alpha){}^3\text{He}$  reactions, the spectra also show other pulses which have different origins: the lowest energy channels show electronic noise, while the intermediate energy region has some cosmic rays events. No

<sup>4</sup>It was also verified that the summed number of counts in the 4 detectors was independent from the actual position and dimension of the beam spot on the target [54].

accelerator induced background was found. Neither of them gave noticeable background to the  $^4\text{He}$  and  $^3\text{He}$  peaks coming from the  $^7\text{Li}$  and  $^6\text{Li}$  reactions, respectively. The  $^4\text{He}$  peak from the  $^6\text{Li}+p$  reaction was partially overlapped by the electronic noise at the lowest energies, so it was not included in the analysis.

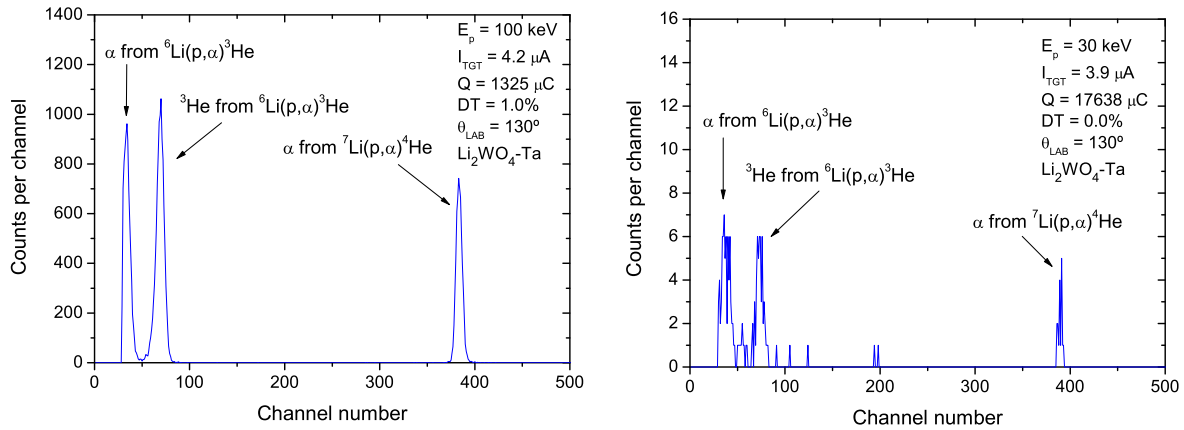


Figure 4.11: Particle spectra obtained with a Si detector at an angle of  $130^\circ$  by bombarding the  $\text{Li}_2\text{WO}_4$  target with protons of incident energy  $E_p = 100$  keV (left panel) and 30 keV (right panel).

## 4.2 Target preparation and analysis

A precise knowledge of the target composition, stoichiometry and thickness is an essential ingredient for an absolute cross section measurement. Moreover, these properties have to be stable under beam bombardment during the experiment. Repeated measurements at different energies allowed for monitoring of the target quality and stability.

For the present work, a total of seven different targets were produced: LiF vacuum-evaporated onto Ag and Cu backings,  $^7\text{Li}$  implanted into Al,  $\text{Li}_2\text{WO}_4$  vacuum-evaporated onto a steel backing, Li metal, and  $\text{PdLi}_x$  alloys produced by plasma discharge techniques. This section describes, for each target, the production, analysis, and yield stability with time during bombardment with a proton beam.

### 4.2.1 LiF targets

The LiF targets were produced by vacuum-evaporating 99% pure LiF powder of natural

Li isotopic composition (92.58%  ${}^7\text{Li}$ , 7.42%  ${}^6\text{Li}$ ) over a thin Ag film (previously vacuum-evaporated) and over a thick 99.99% pure Cu foil (backings). These evaporations were made under a vacuum better than  $9 \times 10^{-7}$  mbar, to minimize contamination by other elements, namely carbon and oxygen.

The lithium fluoride film vacuum-evaporated over Ag target (LiF-Ag target hereafter) was characterized in terms of stoichiometry, areal density and impurities distributions by Rutherford Backscattering Spectroscopy (RBS) [73], using a 1.574 MeV  ${}^4\text{He}^+$  beam. The target was tilted  $45^\circ$  in relation to the beam line, and the two Si detectors were positioned at  $\theta_{lab}=94^\circ$  and  $115^\circ$ . Fig. 4.12 shows the two RBS spectra acquired, where the labeled peaks are the Rutherford backscattered  ${}^4\text{He}^+$  beam particles from those elements, *i.e.*,  ${}^7\text{Li}(\alpha, \alpha){}^7\text{Li}$ ,  $\text{C}(\alpha, \alpha)\text{C}$ ,  $\text{O}(\alpha, \alpha)\text{O}$ ,  $\text{F}(\alpha, \alpha)\text{F}$  and  $\text{Ag}(\alpha, \alpha)\text{Ag}$ .

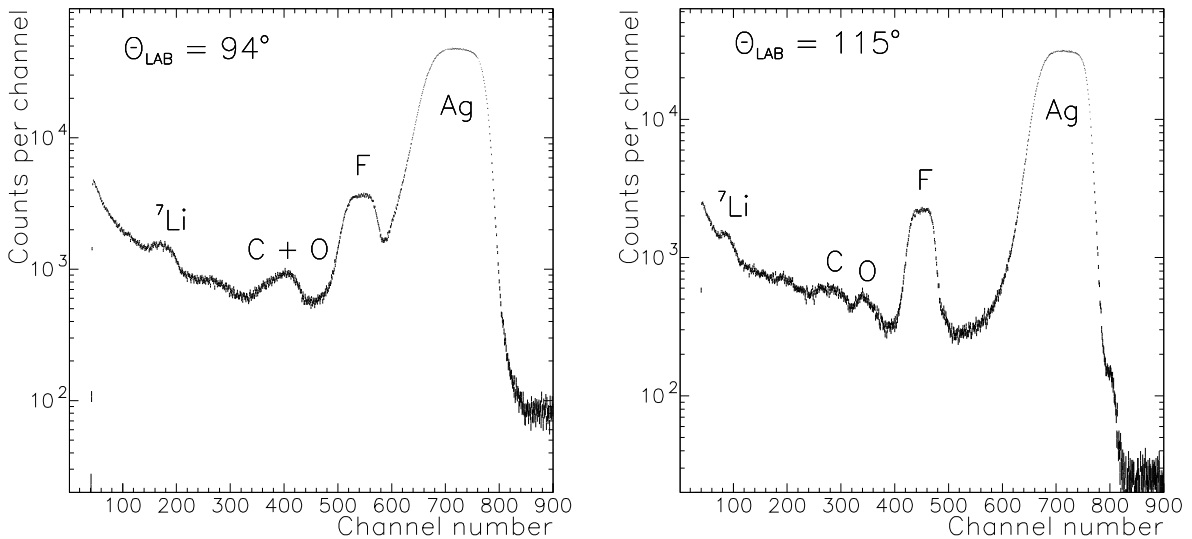


Figure 4.12: The 1.574 MeV  ${}^4\text{He}^+$  backscattering spectra of the LiF-Ag target, measured simultaneously at two different angles,  $\theta_{lab}=94^\circ$  and  $115^\circ$ .

The observed continuum that runs under the fluoride, carbon, oxygen and lithium peaks corresponds to plural scattering events of helium ions by silver atoms. This mechanism is hard to simulate, so it was classified as background which had to be subtracted from the spectra in order to get clean  ${}^7\text{Li}$ , C, O and F peaks. This operation was done performing a series of fits as exemplified in the sequence of plots of figs. 4.13 and 4.14 for the RBS spectrum acquired at  $\theta_{lab}=115^\circ$ .

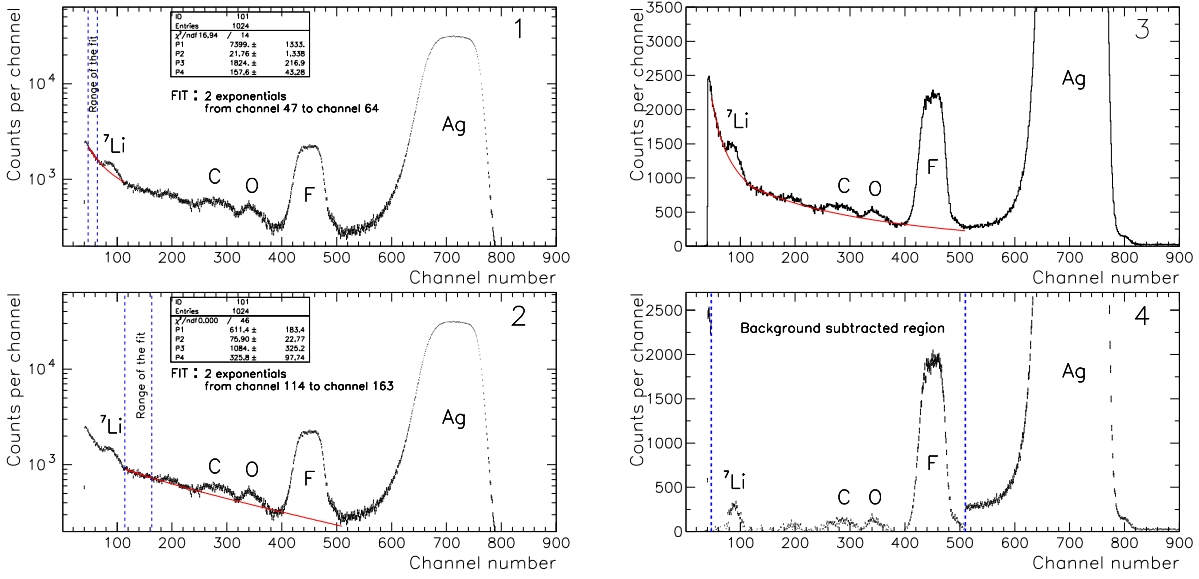


Figure 4.13: The 1.574 MeV  ${}^4\text{He}^+$  backscattering spectra of the LiF-Ag target, measured at  $\theta_{lab} = 115^\circ$ . Ag plural scattering events (background) subtraction under the  ${}^7\text{Li}$ , C, O and F peaks. The background events are fitted with exponentials and then subtracted from the spectrum.

The fitting routines, built in FORTRAN language are based on the Minuit package [78], a tool designed to find the minimum value of a multiparameter function, giving the best-fit parameter values and uncertainties. In the case of  $\chi^2$  minimization, the final fitted parameter values correspond to the minimum of the  $\chi^2$  function as defined below:

$$\frac{\chi^2}{ndf} = \frac{1}{ndf} \sum_{i=1}^n \left( \frac{y(x_i) - F(x_i, P_1, P_2, \dots, P_k)}{\delta y(x_i)} \right)^2, \quad (4.5)$$

where  $n$  is the number of fitted data points  $y(x)$ ,  $ndf$  is the number of degrees of freedom defined as the difference between  $n$  and  $k$  (the number of fitted parameters),  $F$  is the parametric function to be fitted to the data points, and  $\delta y(x)$  is the data points uncertainties. A fit is considered successful when  $\chi^2/ndf \approx 1$ . The fits with  $\chi^2/ndf < 1$  are statistically equivalent.

In fig. 4.13, the plural scattering events were fitted with two exponentials under the  ${}^7\text{Li}$  peak and also under the C, O and F peaks:

$$F(x_i, P_1, \dots, P_4) = P_1 \exp\left(-\frac{x}{P_2}\right) + P_3 \exp\left(-\frac{x}{P_4}\right). \quad (4.6)$$

In fig. 4.14, the plural scattering events under the  ${}^7\text{Li}$  peak were fitted with the function

$$F(x_i, P_1, P_2) = P_1 E^{-P_2}, \quad (4.7)$$

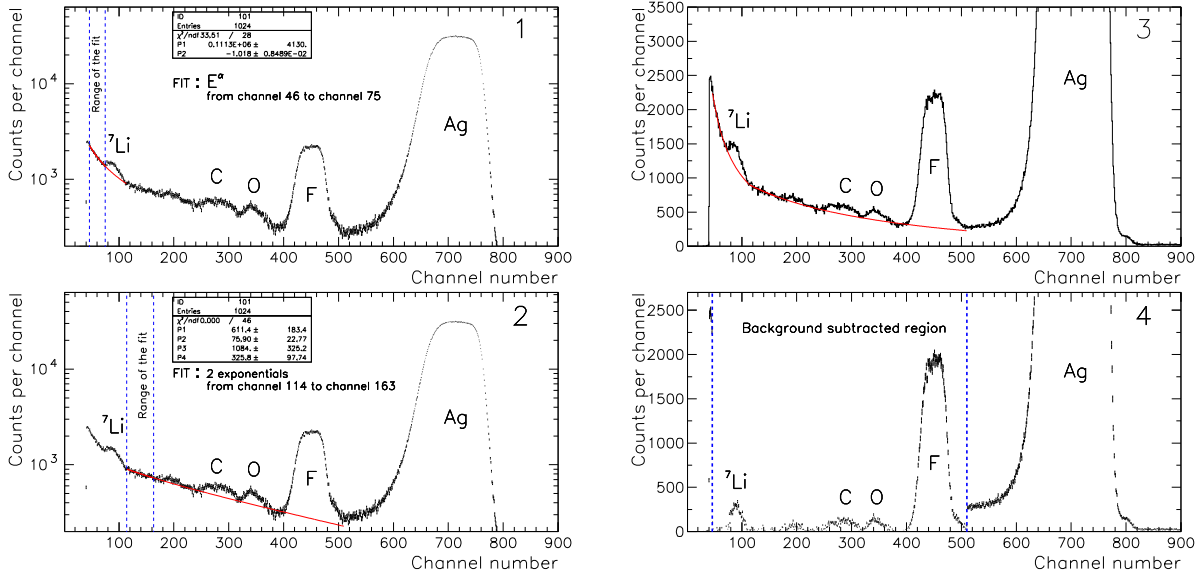


Figure 4.14: The 1.574 MeV  ${}^4\text{He}^+$  backscattering spectra of the LiF-Ag target, measured at  $\theta_{\text{lab}} = 115^\circ$ . Ag plural scattering events (background) subtraction under the  ${}^7\text{Li}$ , C, F and O peaks. The background events are fitted with an  $E^{-\alpha}$  dependence under the  ${}^7\text{Li}$  peak and by two exponentials under the C, O and F peaks. The fitted functions are then subtracted from the spectrum.

and with two exponentials under the C, O and F peaks (a  $P_1 E^{-P_2}$  fit did not converge for this region).

The net areas obtained in the two fits for the  ${}^7\text{Li}$  peak, presented a 5.6% difference, showing that the parametrization function used to describe the Ag plural scattering events has a small effect on the final results.

The analysis of both RBS spectra ( $\theta_{\text{lab}} = 94^\circ$  and  $115^\circ$ ) after background subtraction, was done by two methods:

1. peak integration method: since the backscattering peaks are well separated, the integrated peak counts of the  $i$ th element in the film,  $A_i$ , can be accurately determined from the spectra. The areal density,  $N_i$ , in atoms per unit area for each element is then given by

$$N_i = \frac{A_i}{N_p \Omega_{\text{lab}} \frac{d\sigma_i(E_{\text{lab}}, \theta_{\text{lab}})}{d\Omega_{\text{lab}}}} \quad (4.8)$$

where  $N_p$  is the number of incident projectiles. For the beam energy used, the scattering is Rutherford (pure Coulomb scattering), then the differential cross section  $\frac{d\sigma_i(E_{\text{lab}}, \theta_{\text{lab}})}{d\Omega_{\text{lab}}}$  may

be calculated from

$$\frac{d\sigma_{\text{Ruth}}(E_{\text{lab}}, \theta_{\text{lab}})}{d\Omega_{\text{lab}}} = \left( \frac{Z_1 Z_2 e^2}{4 E_{\text{lab}}} \right)^2 \frac{4 \left[ \sqrt{m_2^2 - m_1^2 \sin^2 \theta_{\text{lab}}} + m_2 \cos \theta_{\text{lab}} \right]^2}{m_2 \sin^4 \theta_{\text{lab}} \sqrt{m_2^2 - m_1^2 \sin^2 \theta_{\text{lab}}}}, \quad (4.9)$$

where  $m_1$  and  $Z_1$ , and  $m_2$  and  $Z_2$  are the masses and atomic numbers of the incident and target ions, respectively. The quantity  $N_p \Omega_{\text{lab}}$  is confirmed from the Ag substrate yield.

2. XRUMP [74], a simulator software for RBS calculations: this program also uses eq. 4.8 for areal densities determination. It has, however, the advantage of allowing an easier and faster approach to do these calculations considering also the presence of impurities whose peaks are observable in the spectra (in this case carbon and oxygen). Fig 4.15 shows, for the spectrum taken at  $\theta_{\text{lab}} = 115^\circ$ , the obtained XRUMP simulated spectrum – red curve.

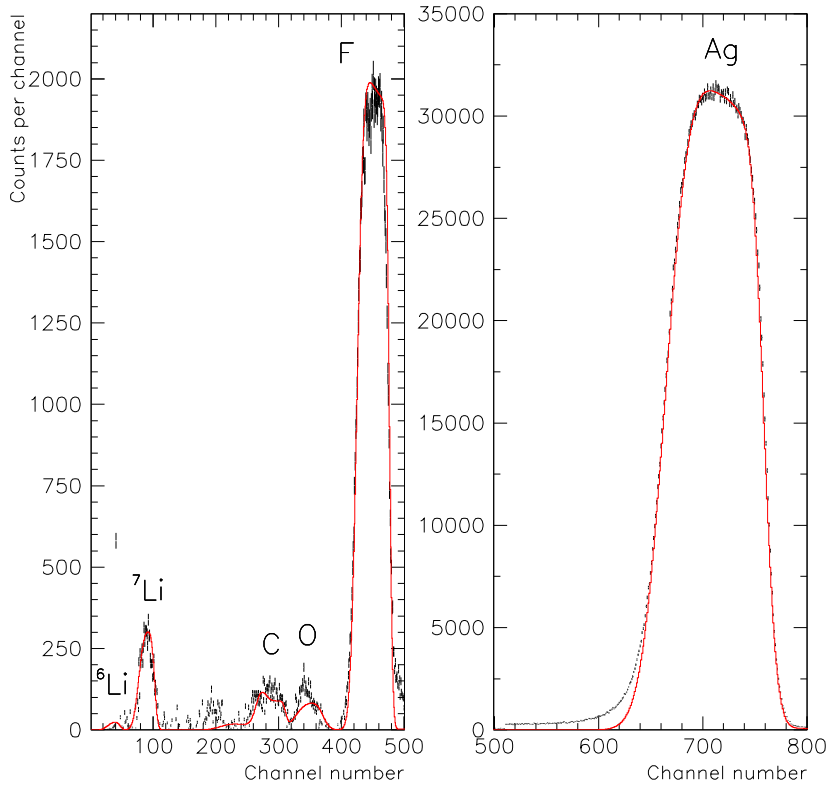


Figure 4.15: The 1.574 MeV  ${}^4\text{He}^+$  backscattering spectrum of the LiF-Ag target measured at  $\theta_{\text{lab}} = 115^\circ$  (after background subtraction), and the XRUMP simulated spectrum (red curve).

From these two methods we got for the LiF-Ag target:

1. lithium fluoride film stoichiometry:  $\text{Li}_{0.48}\text{F}_{0.48}\text{C}_{0.04}$  (oxygen contamination not detected);
2. lithium fluoride film areal density:  $1.38 \times 10^{18}$  at/cm<sup>2</sup> ( $\Delta E = 5.8$  keV for 1 MeV protons)  $\Rightarrow$   ${}^7\text{Li}$  areal density,  $N_{7\text{Li}} = (6.14 \pm 0.25) \times 10^{17}$  at/cm<sup>2</sup> (the included 4.1% uncertainty results from the dispersion of  $N_{7\text{Li}}$  values obtained using the two methods described above in the two RBS spectra, and also considering both parametrization functions used to get a “clean”  ${}^7\text{Li}$  peak);
3. silver layer thickness and composition:  $6.35 \times 10^{17}$  at/cm<sup>2</sup> of which 93.2% are Ag ( $N_{\text{Ag}} = 5.92 \times 10^{17}$  at/cm<sup>2</sup>) and 6.8% are C and O.

The LiF-Ag target was used to measure the  ${}^7\text{Li}(p,\alpha){}^4\text{He}$  reaction cross section in the energy range 270.6 – 1225.0 keV (48 energy points) accumulating a total charge of 2620  $\mu\text{C}$  ( $\text{H}^+$  beam) plus 1405  $\mu\text{C}$  ( $\text{H}_2^+$  beam) plus 2950  $\mu\text{C}$  ( $\text{H}_3^+$  beam).

The composition and thickness of the lithium fluoride film vacuum-evaporated over Cu target (LiF-Cu target, hereafter) were obtained in several steps, since a direct RBS analysis of this target is useless as the Cu barrier masks the Li and F peaks. The lithium fluoride vacuum-evaporation was done on the Cu foil and on a Ag thin film, simultaneously. This last target was analysed by RBS, as described previously for the LiF-Ag target, giving a film with composition  $\text{Li}_{0.48}\text{F}_{0.48}\text{C}_{0.04}$  and thickness  $1.54 \times 10^{18}$  at/cm<sup>2</sup>. A PIGE (Proton Induced Gamma-ray Emission) [75] analysis of both targets was done by measuring the  $\gamma$ -ray yields from the  ${}^7\text{Li}(p,p'\gamma){}^7\text{Li}$  and  ${}^{19}\text{F}(p,\alpha\gamma){}^{16}\text{O}$  reactions,  $E_\gamma = 478$  keV and  $E_\gamma = 3070 - 7120$  keV, respectively (fig. 4.16). These measurements were done at  $E_{\text{lab}} = 1134$  keV, where the  ${}^7\text{Li}(p,p'\gamma){}^7\text{Li}$  reaction has a broad resonance ( $\sigma = 35$  mb). Comparing these yields for both targets, we concluded that the ratio of atomic fractions Li/F was the same for both targets and that the LiF film evaporated onto Cu was thicker by a factor  $1.31 \pm 0.03$  (this 2.6 % uncertainty results from the oscillations in the  $\gamma$ -ray peak areas for the two targets. This last result was confirmed for the LiF-Cu target by measuring the excitation function of the  ${}^{19}\text{F}(p,\alpha\gamma){}^{16}\text{O}$  reaction at  $E_{r,\text{lab}} = 483.6$  keV (fig. 4.17).

So, for the LiF-Cu target the lithium fluoride film areal density is  $2.03 \times 10^{18}$  at/cm<sup>2</sup>  $\Rightarrow$   ${}^7\text{Li}$  areal density,  $N_{7\text{Li}} = (9.02 \pm 0.44) \times 10^{17}$  at/cm<sup>2</sup> (the quoted uncertainty of 4.9% is the quadratic sum of the 4.1% uncertainty associated to the RBS analysis and the 2.6% uncertainty mentioned above).

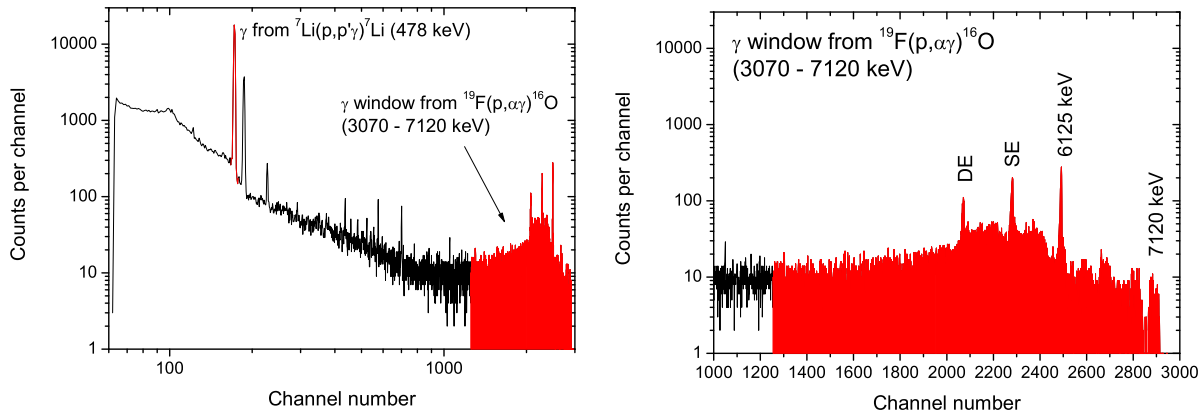


Figure 4.16: Left panel:  $\gamma$ -ray spectrum taken from the LiF-Cu target at  $E_{\text{lab}} = 1134$  keV. Right panel: Same spectrum zoomed over the  $\gamma$  window from the  $^{19}\text{F}(p,\alpha\gamma)^{16}\text{O}$  reaction. The SE and DE peaks correspond, respectively, to the single escape and double escape peaks of the 6125 keV photo peak.

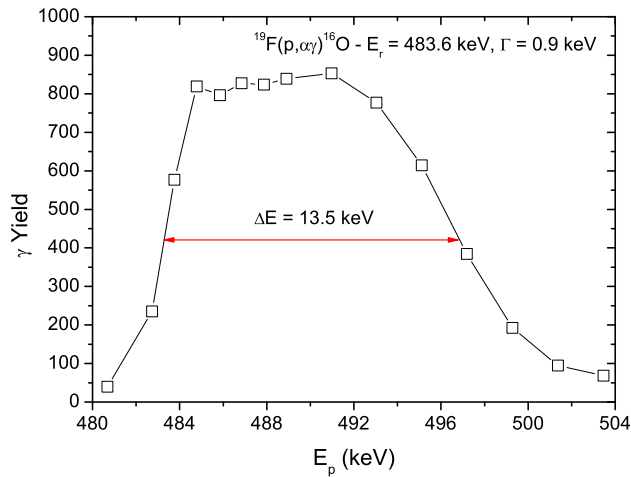


Figure 4.17: The excitation function of the  $^{19}\text{F}(p,\alpha\gamma)^{16}\text{O}$  reaction at  $E_{r,\text{lab}} = 483.6$  keV using the LiF-Cu target. The curve through the data points is to guide the eye only.

This target was used to measure concurrently both  $^7\text{Li}(p,\alpha)^4\text{He}$  and  $^6\text{Li}(p,\alpha)^3\text{He}$  reactions cross section in the energy range 92.4 – 1471.7 keV (28 energy points) and 90.5 – 579.9 keV (20 energy points) for the  $^7\text{Li}$  and  $^6\text{Li}$  reactions respectively, accumulating a total charge of 490  $\mu\text{C}$  ( $\text{H}^+$  beam) plus 15613  $\mu\text{C}$  ( $\text{H}_2^+$  beam).

## 4.2.2 $^7\text{Li}$ implanted into Al target

High fluence low energy ion implantation is a technique frequently used to improve mechanical/chemical surface properties. Implantation causes changes in surface composition and chemical bond structure, leading to the formation of metastable compounds and alloy layers, which strengthen the implanted materials. However, ion bombardment may also form lattice imperfections due to radiation damage and cause undesirable structural changes within the near surface region of the solid. Here, the purpose of  $^7\text{Li}$  implantation was the formation of a high stability alloy that withstands high fluence radiations for a relatively long time period. The implantations were done at the 210 kV Danfysik 1090 High Current Implanter machine, with a Chordis 920 type ion source, of the Ion Beam Laboratory at ITN.

The process of choosing the backing material, energy and implantation fluence was done according to the following steps:

1<sup>st</sup> step: the selection of metallic backing candidates for  $^7\text{Li}$  implantation was done consulting the handbook of binary alloy phase diagrams [76] (see example of fig. 4.18 for the Li-Sn alloy) and the handbook of crystallographic data for intermetallic phases [77]; it was concluded that the most promising metals for  $^7\text{Li}$  implantation were:

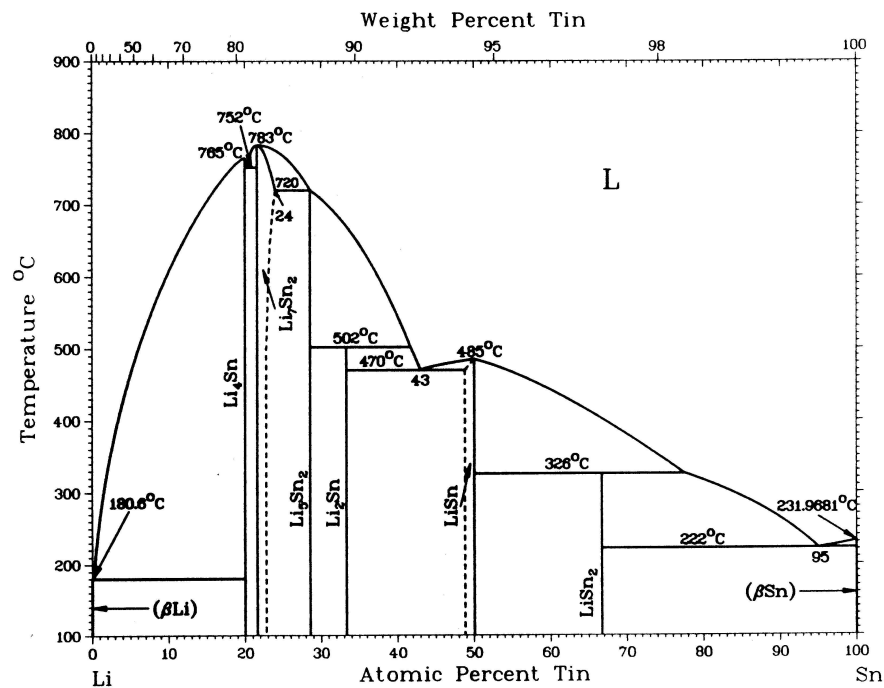


Figure 4.18: The Sn-Li alloy phase diagram. Plot taken from [76].

1. Aluminium (Al): at room temperature forms the stable compounds  $\text{AlLi}$ ,  $\text{Al}_2\text{Li}_3$  and  $\text{Al}_4\text{Li}_9$ ;
2. Zinc (Zn): at room temperature forms the stable compound  $\text{LiZn}_2$ ;
3. Palladium (Pd): at room temperature forms the stable compounds  $\text{Li}_5\text{Pd}$ ,  $\text{Li}_{15}\text{Pd}_4$ ,  $\text{Li}_2\text{Pd}$ ,  $\text{LiPd}$ ,  $\text{LiPd}_2$  and  $\text{LiPd}_7$ ;
4. Lead (Pb): at room temperature forms the stable compounds  $\text{Li}_{10}\text{Pb}_3$ ,  $\text{Li}_3\text{Pb}$  and  $\text{LiPb}$ ;
5. Antimony (Sb): at room temperature forms the stable compounds  $\text{Li}_3\text{Sb}$  and  $\text{Li}_2\text{Sb}$ ;
6. Tin (Sn): at room temperature forms the stable compounds  $\text{Li}_4\text{Sn}$ ,  $\text{Li}_5\text{Sn}_2$ ,  $\text{Li}_2\text{Sn}$ ,  $\text{LiSn}$  and  $\text{LiSn}_2$ .

2<sup>nd</sup> step: Monte-Carlo simulations (with Ziegler and Biersack's program SRIM2003 [79]) of range, straggling, sputtering yield and back-scattered  $^7\text{Li}$  ions implanted in different metallic backings. Several incident energies were simulated. The theoretical  $^7\text{Li}$  implanted profile,  $n(x)$  in  $\text{at}/\text{cm}^3$ , is given, for each energy, by the equation [80]

$$n(x) = \frac{n_a(1 - BS)}{2S} \left[ \text{erf} \left( \frac{x - R_p + D_N(S/n_a)}{\sqrt{2} \Delta R_p} \right) - \text{erf} \left( \frac{x - R_p}{\sqrt{2} \Delta R_p} \right) \right], \quad (4.10)$$

where  $x$  stands for depth and  $R_p$  for the projected range of the ions in the substrate, being  $\Delta R_p$  its straggling;  $n_a$  stands for the substrate atomic density,  $BS$  for the fraction of backscattered ions, and  $S$  is the sputtering coefficient or sputtering yield, being defined as the number of atoms ejected per incoming ion;  $D_N$  is the nominal fluence. From this equation, the number of ions remaining in the substrate  $D_I$  (retained fluence) is given simply as:

$$D_I = \int_0^{\infty} n(x) dx . \quad (4.11)$$

Eq. 4.10 is based on the assumptions that the sputtering yield is constant, and equal for both substrate and implanted ions, there is no knock-on effect and the volume change due to radiation damage can be neglected. It also does not take into account any saturation or diffusion towards the surface effect, so it may start failing to predict correctly high fluence implantation profiles. It is, nevertheless, a good starting point.

Table 4.2 shows the simulation results and eq. 4.10 predictions for several metallic backings at 5 and 10 keV implantation energy. From this table we immediately conclude that Zn and Pd are not good materials for  ${}^7\text{Li}$  implantation; Zn because the sputtering yield is very high, and Pd because  $R_p$  is low. In both cases the retained fluence would be very small.

$E_{\text{lab}}$ (keV)	Target	$R_p$ (Ang)	$\Delta R_p$ (Ang)	Sputt. Yield (atoms/ion)	Backscattered ${}^7\text{Li}$	$D_N$ max. (at/cm $^2$ )	$D_I$ (at/cm $^2$ )
5	Al	337	161	0.414	5.91 %	1.00e18	4.49e17
	Zn	228	125	1.507	22.08 %	–	–
	Sn	292	160	0.356	27.70 %	5.00e17	2.07e17
	Sb	311	170	0.359	26.72 %	5.00e17	2.01e17
	Pb	281	155	0.459	36.15 %	3.50e17	1.23e17
10	Al	637	273	0.276	3.58 %	2.50e18	1.32e18
	Zn	421	223	1.150	17.44 %	–	–
	Pd	272	143	0.517	20.35 %	–	–
	Sn	500	265	0.306	22.73 %	1.20e18	4.57e17
	Sb	537	284	0.323	22.29 %	1.00e18	4.13e17
	Pb	466	254	0.434	31.63 %	6.50e17	2.35e17

Table 4.2: SRIM simulation results and eq. 4.10 predictions for different metal backings at  $E_{\text{lab}} = 5$  and 10 keV.  $D_N$  max. gives the fluence necessary to obtain a saturated profile and  $D_I$  is the retained fluence (see text for details).

Fig. 4.19 shows the implanted profile evolution with increasing fluence as predicted by eq. 4.10, for  ${}^7\text{Li}$  implantation into aluminium at 10 keV. Here, we can see that for low fluences, the implanted profile is gaussian, and as the fluence increases the center of the original gaussian profile “moves” towards the surface due to sputtering effects, and finally a flat-like topped profile is obtained, which is called a saturated profile. For cross section measurements, saturated profiles are the best option since they present the highest density of  ${}^7\text{Li}$  atoms with its maximum at the surface.

3<sup>rd</sup> step: From the simulations results it was concluded that the most suitable implantation energy was  $E_{\text{lab}} = 10$  keV, a compromise between retained fluence and nominal fluence required to get a saturated profile. Also from this table, we concluded that the best metallic

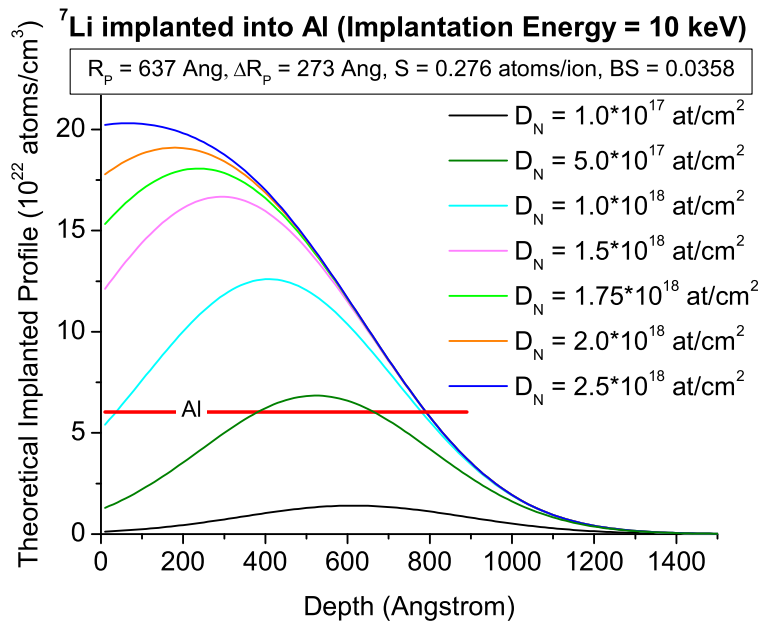


Figure 4.19: Implanted profile evolution with increasing fluence as predicted by eq. 4.10, for  ${}^7\text{Li}$  implantation into aluminium at 10 keV. The red horizontal line indicates the atomic density of pure Al.

candidate for  ${}^7\text{Li}$  implantation is Al since it shows a saturated profile with the highest retained fluence. However, these predictions needed experimental confirmation, and for that, the Al, Sn, Sb and Pb metallic backings were implanted with a nominal fluence of  $5 \times 10^{17} \text{ }^7\text{Li}^+/\text{cm}^2$  [ $E_{\text{lab}} = 10 \text{ keV}$ ,  $I = 200 \text{ } \mu\text{A}$ ;  $P = 0.083 \text{ W/cm}^2$ ]. The relative amount of retained  ${}^7\text{Li}$  was determined by PIGE, measuring the 478 keV  $\gamma$ -ray yield associated to the  ${}^7\text{Li}(p,p'\gamma){}^7\text{Li}$  reaction. These measurements were taken at  $E_{\text{lab}} = 1800 \text{ keV}$ , where the  ${}^7\text{Li}(p,p'\gamma){}^7\text{Li}$  cross section is a slowly varying function with energy. Table 4.3 shows the 478 keV  $\gamma$ -ray yields produced by the four implanted targets. These values show that Al was the metal capable of retaining more lithium, and as such was selected as the backing for producing  ${}^7\text{Li}$  implanted targets. As a side note, aluminium is also the most suitable backing material since it has, amongst the 4 metals studied, the highest thermal conductivity [ $k = 202 \text{ W/(m}^\circ\text{C)}$ ] and melting temperature ( $T_{\text{melting}} = 660.32^\circ\text{C}$ ), relevant properties to take into account when choosing a material that must withstand high intensity beams.

4<sup>th</sup> step: According to table 4.2, for an implantation at 10 keV, the nominal fluence necessary to get a saturated profile is  $D_N = 2.5 \times 10^{18} \text{ }^7\text{Li}^+/\text{cm}^2$ , with a corresponding retained dose of

Material	$\gamma$ -ray yield (rel.units)
Al	15878
Pb	10890
Sn	6011
Sb	5281

Table 4.3: 478 keV  $\gamma$ -ray yields produced in the implanted Al, Pb, Sn and Sb with  $5 \times 10^{17}$   ${}^7\text{Li}^+/\text{cm}^2$ .

$1.32 \times 10^{18}$   ${}^7\text{Li}^+/\text{cm}^2$ . In order to test these values, two aluminium foils were implanted with  ${}^7\text{Li}$  at 10 keV. One foil was implanted with  $D_N = 1.0 \times 10^{18}$   ${}^7\text{Li}^+/\text{cm}^2$  and the other with  $D_N = 2.5 \times 10^{18}$   ${}^7\text{Li}^+/\text{cm}^2$  [ $I = 200\text{--}300$   $\mu\text{A}$ ;  $P = 0.22\text{--}0.33$   $\text{W}/\text{cm}^2$ ].

The amount of retained  ${}^7\text{Li}$  in the implanted targets was determined by measuring the excitation function of the  ${}^7\text{Li}(p,\gamma){}^8\text{Be}$  reaction at  $E_{r,\text{lab}} = 441.4$  keV (fig. 4.20) using the two implanted targets and a reference thin target of LiF, vacuum evaporated over a thin Ag film. By RBS analysis, the lithium fluoride target showed a stoichiometry  $\text{Li}_{1.39}\text{F}$ , with  $N_{7\text{Li}} = (2.96 \pm 0.12) \times 10^{17}$   ${}^7\text{Li}^+/\text{cm}^2$  (the quoted 4% uncertainty is associated to the RBS analysis).

Comparing the areas in fig. 4.20, we conclude that the amount of retained  ${}^7\text{Li}$  was  $\approx 7\%$  lower in the lowest dose implanted target, indicating that for this target a saturated profile was not reached, as expected (this result was confirmed by RBS analysis). From the obtained areas, we get that the highest dose implantation retained an amount of  ${}^7\text{Li}$  of

$$N_{7\text{Li}} = \frac{1613 \pm 40}{722 \pm 27} (2.96 \pm 0.12) \times 10^{17} \text{ }^7\text{Li}^+/\text{cm}^2 = (6.61 \pm 0.40) \times 10^{17} \text{ }^7\text{Li}^+/\text{cm}^2, \quad (4.12)$$

a factor of two lower than the predicted value of  $1.32 \times 10^{18}$   ${}^7\text{Li}^+/\text{cm}^2$ , of table 4.2 which is not at all unexpected due to the simplifying assumptions behind eq. 4.10. We must also not forget that the nominal fluence of  $2.5 \times 10^{18}$   ${}^7\text{Li}^+/\text{cm}^2$  as associated an experimental uncertainty. The quoted uncertainty of 6.1% is the quadratic sum of the 4% uncertainty associated to the RBS analysis of the LiF target and the 4.6% uncertainty associated to the areas uncertainties (taken from fig. 4.20).

Considering only the  $D_N = 2.5 \times 10^{18}$   ${}^7\text{Li}^+/\text{cm}^2$  implanted target, different analytical techniques were used to complement its characterization. A RBS spectrum was taken, and fitted

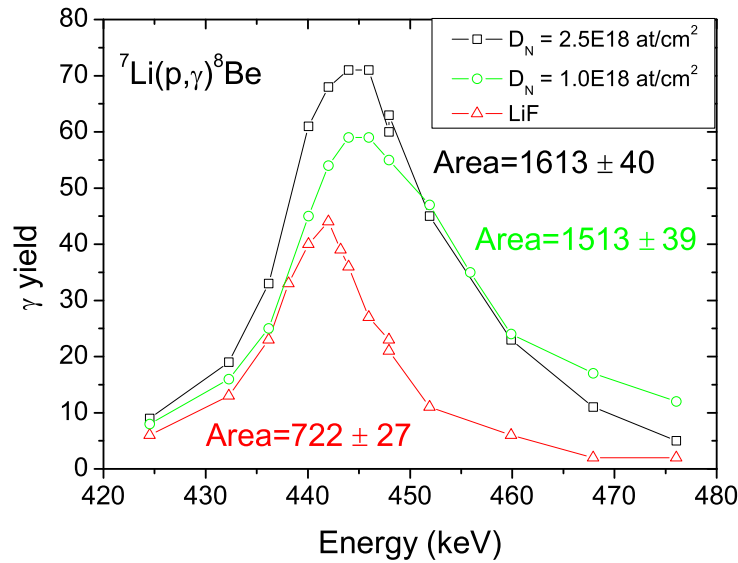


Figure 4.20: The excitation function of the  ${}^7\text{Li}(p,\gamma){}^8\text{Be}$  reaction at  $E_{r,\text{lab}} = 441.4$  keV using the two implanted targets and a vacuum evaporated LiF thin target. The quoted uncertainties are only of statistical nature and the lines through the data points are to guide the eye only.

with XRUMP using the deficiency method to analyse the near surface several-element materials, as the lithium peak is not visible in this spectrum. In this method, the spectrum for the heavier pure element (Al) is compared with that for the implanted material. The deficiency in the Al signal caused by the presence of the  ${}^7\text{Li}$ , carbon and oxygen (the last two, visible in the spectra) is noted and used to obtain the material stoichiometry at the sample surface, considering also the amount of retained  ${}^7\text{Li}$  given by eq. 4.12. In order to fit correctly the O and C peaks, the Al barrier is partially fitted with 2 exponentials as shown in fig. 4.21 (left panel) and then removed from under the carbon and oxygen peaks [fig. 4.21 (right panel)]. The spectrum thus obtained, with the C and O peaks well defined, can be fitted with XRUMP.

Fig. 4.22 (left panel) shows the 2.0 MeV  ${}^4\text{He}^+$  backscattering spectrum of the implanted target (with the Al barrier partially subtracted), which has superimposed the curve obtained from the XRUMP fit. The right panel shows the original RBS spectrum, superimposed on the XRUMP fit red curve. This fit was achieved by dividing the target in thin layers with varying thicknesses and stoichiometry. In fig. 4.23 the atomic fraction depth profile of  ${}^7\text{Li}$ , Al, O and C obtained from the XRUMP fit are plotted.

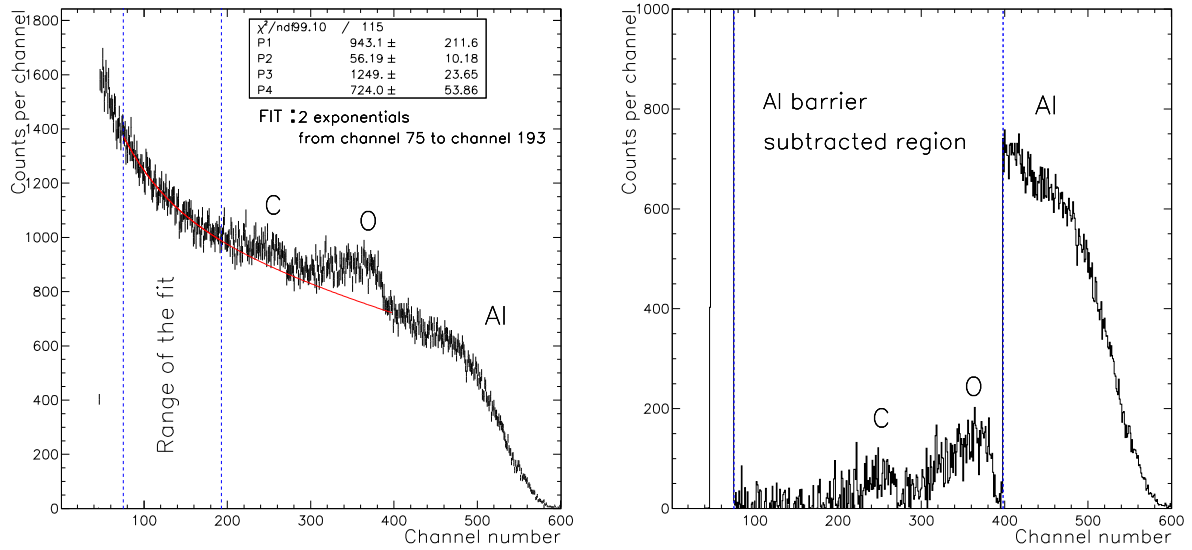


Figure 4.21: The 2.0 MeV  $^4\text{He}^+$  backscattering spectra of the  $^7\text{Li}$  implanted target, measured at  $\theta_{lab}=140^\circ$ . The left panel shows the  $\chi^2$  fit to the Al barrier with two exponentials (red curve). The right panel shows the RBS spectrum after subtracting the Al barrier with the fitted exponentials.

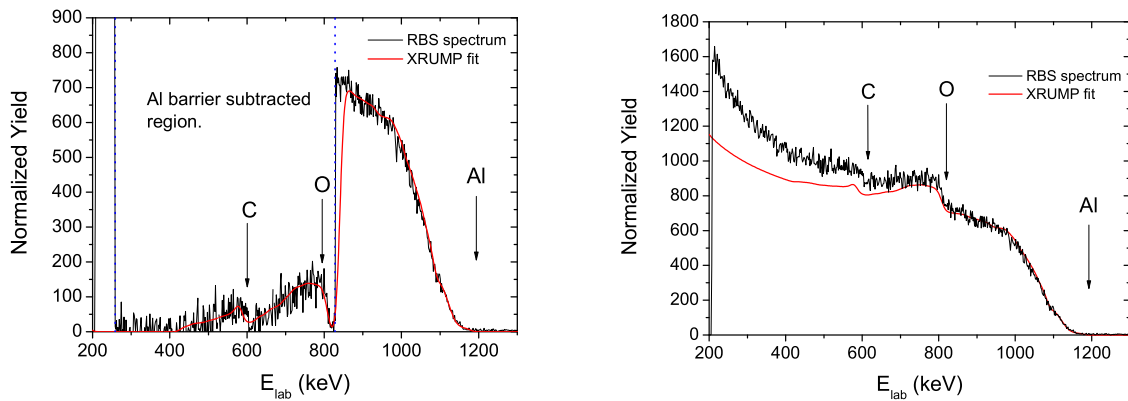


Figure 4.22: Left panel: The 2.0 MeV  $^4\text{He}^+$  backscattering spectrum of the  $^7\text{Li}$  implanted in Al target measured at  $\theta_{lab}=140^\circ$  (with the Al barrier partially subtracted), and the XRUMP simulated spectrum (red curve). Right panel: Original RBS spectrum, superimposed on the XRUMP fit (red curve).

Table 4.4 lists the atomic fractions and thicknesses of the simulated layers (only the layers containing  $^7\text{Li}$  are listed).

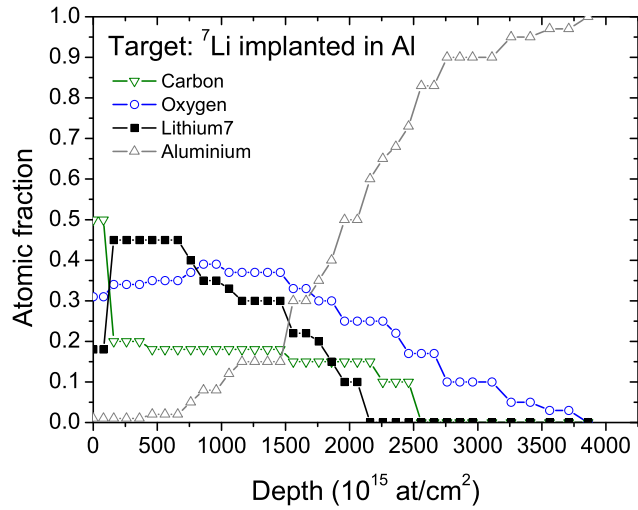


Figure 4.23: Depth profile of  ${}^7\text{Li}$ , Al, O and C predicted by the XRUMP fit to the RBS spectrum of the  ${}^7\text{Li}$  implanted in Al target. The lines through the data points are to guide the eye only.

layer number	Thickness ( $10^{15}$ at/cm $^2$ )	Elemental composition			
		Al	${}^7\text{Li}$	O	C
1	160	0.01	0.18	0.31	0.5
2	300	0.01	0.45	0.34	0.2
3	200	0.02	0.45	0.35	0.18
4	100	0.02	0.45	0.35	0.18
5	100	0.05	0.40	0.37	0.18
6	200	0.08	0.35	0.39	0.18
7	100	0.12	0.33	0.37	0.18
8	400	0.15	0.30	0.37	0.18
9	200	0.30	0.22	0.33	0.15
10	100	0.35	0.20	0.30	0.15
11	100	0.40	0.15	0.30	0.15
12	200	0.50	0.10	0.25	0.15

Table 4.4: Layer thicknesses and atomic fractions defined in XRUMP to fit the RBS spectrum of the  ${}^7\text{Li}$  implanted in Al target.

The RBS simulation results were confirmed by three independent techniques:  $^{27}\text{Al}(p,\gamma)^{28}\text{Si}$  excitation function measurement, Secondary Ion Mass Spectrometry (SIMS) [81], and X-ray Photoelectron Spectroscopy (XPS) [81]. In the first technique, an accurate Al depth distribution is obtained by measuring the excitation function of the  $^{27}\text{Al}(p,\gamma)^{28}\text{Si}$  reaction at  $E_{r,\text{lab}} = 992$  keV ( $\Gamma = 0.10$  keV,  $E_\gamma = 1.779$  MeV). Fig. 4.24 (left panel) shows the excitation function before and after  $^7\text{Li}$  implantation. The depth profile thus obtained can be compared to the depth profile predicted by the RBS spectrum (gray points in fig. 4.23). For that, we must convert thickness in  $\text{at}/\text{cm}^2$  to energy loss in keV. This is done using the definition of stopping power cross section,  $\epsilon(E)$ :

$$\Delta E = \epsilon(E) \Delta x , \quad (4.13)$$

where  $\Delta E$  gives the energy loss in a target layer of thickness  $\Delta x$ .  $\epsilon(E)$  is calculated assuming a simple linear additivity rule of energy loss in compounds (Bragg's rule): for a target layer of stoichiometry  $\text{Al}_W^7\text{Li}_X\text{O}_Y\text{C}_Z$ , where  $W$ ,  $X$ ,  $Y$  and  $Z$  are the atomic fractions of elements Al,  $^7\text{Li}$ , O and C, respectively, we have for  $\epsilon(E)$

$$\epsilon(E) = \frac{W \epsilon_{\text{Al}}(E) + X \epsilon_{\text{Li}}(E) + Y \epsilon_{\text{O}}(E) + Z \epsilon_{\text{C}}(E)}{W + X + Y + Z} . \quad (4.14)$$

The values of  $W$ ,  $X$ ,  $Y$  and  $Z$  for each target layer, and its respective thickness  $\Delta x$  are taken from table 4.4. The stopping cross sections for each element are tabulated or can be calculated by the SRIM2003 [79] program. The Al depth profile obtained using this transformation is plotted in Fig. 4.24 (right panel) superimposed on the  $^{27}\text{Al}(p,\gamma)^{28}\text{Si}$  excitation function. The match between both curves is excellent, confirming the XRUMP RBS spectrum analysis for aluminium.

SIMS is a very powerful surface analysis technique, with low detection limits and the capacity of detecting all elements (including hydrogen), its isotopes and molecular aggregates [81]. Using a focused beam of primary ions which can be deflected in a controlled way, it is possible to define accurately the target area to be analysed. The primary beam induced sputtering can be used to make successive depth analysis which allows to get the target depth composition distribution. However, the SIMS technique has two drawbacks, the sputtering rate and the ionizing probability of the secondary (sputtered) particles depends on the surface composition (matrix effects) [81]. It is also a destructive method, at the microscopic level, though.

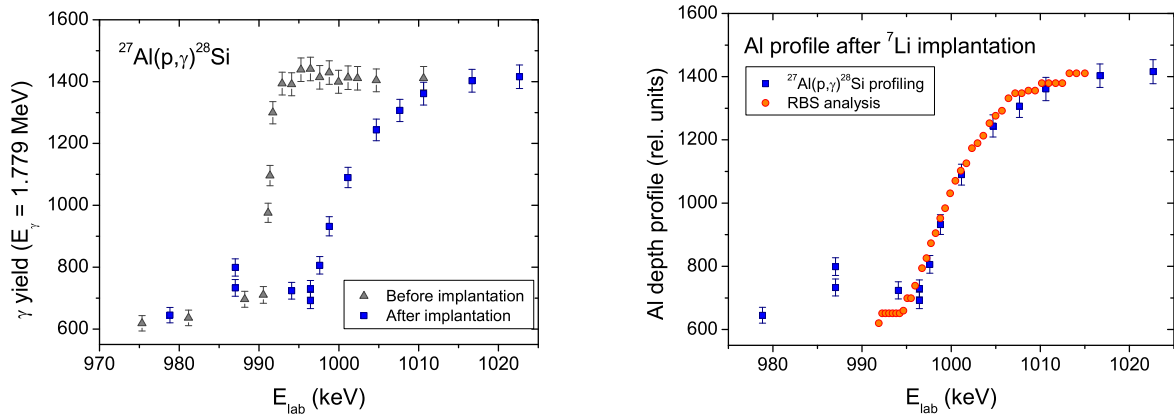


Figure 4.24: Left panel: The excitation function of the  $^{27}\text{Al}(p,\gamma)^{28}\text{Si}$  reaction at  $E_{r,\text{lab}} = 992$  keV using the Al target before (gray triangles) and after  $^7\text{Li}$  implantation (blue squares). Right panel: Comparison of Al depth profiles obtained by the  $^{27}\text{Al}(p,\gamma)^{28}\text{Si}$  excitation function measurement (blue squares) and RBS measurements (orange circles) – see text for details.

The matrix effects can be controlled if there is a standard target for comparison. As we did not have such standard for the  $^7\text{Li}$  implanted target, we will limit our discussion to a qualitative level. SIMS measurements were performed at the Multitechnique Surface Analysis System [81] in the GIDS/CeFITec-Physics department of the Faculty of Sciences and Technology - UNL, Lisbon. Fig. 4.25 shows the normalized sputtered  $^7\text{Li}_2^+$  and  $\text{Al}_2^+$  yield as a function of sputtering time (in arbitrary units) for the  $^7\text{Li}$  implanted target obtained with a 4 keV  $\text{Ar}^+$  primary beam in an  $\text{O}_2$  atmosphere ( $P = 1.0 \times 10^{-6}$  mbar). These distributions are comparable with the RBS depth profiles for these two elements as for both cases we have: the amount of  $^7\text{Li}$  and Al is, respectively, small and negligible at the target surface;  $^7\text{Li}$  concentration shows a step increase while Al concentration is still negligible; Al concentration starts to increase when  $^7\text{Li}$  concentration is already dropping.

By doing SIMS of positive and negative ions with a lower sputtering rate (fig. 4.26) we verified that the target surface has indeed  $^7\text{Li}$ , aluminium, carbon and oxygen at the surface, but their concentrations are inconclusive. In terms of molecules,  $\text{CO}$  ( $m=28$ ),  $^7\text{LiAl}$  ( $m=34$ ) and  $^7\text{LiAl}_2$  ( $m=61$ ) are not seen.  $^7\text{Li}_2\text{Al}$  ( $m=41$ ) concentration is very small, similar to the one observed for  $\text{H}^+$ .

X-ray Photoelectron Spectroscopy (XPS) allows a quantitative analysis of the first  $\approx 10$  nm

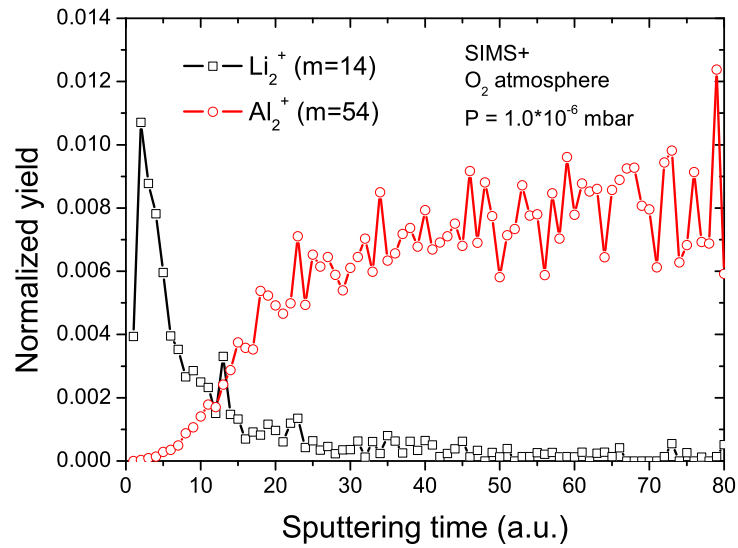


Figure 4.25: The normalized sputtered  ${}^7\text{Li}_2^+$  and  $\text{Al}_2^+$  yield as a function of sputtering time (in arbitrary units) for the  ${}^7\text{Li}$  implanted target obtained with a 4 keV  $\text{Ar}^+$  primary beam in an  $\text{O}_2$  atmosphere ( $P = 1.0 \times 10^{-6}$  mbar). The lines through the data points are to guide the eye only.

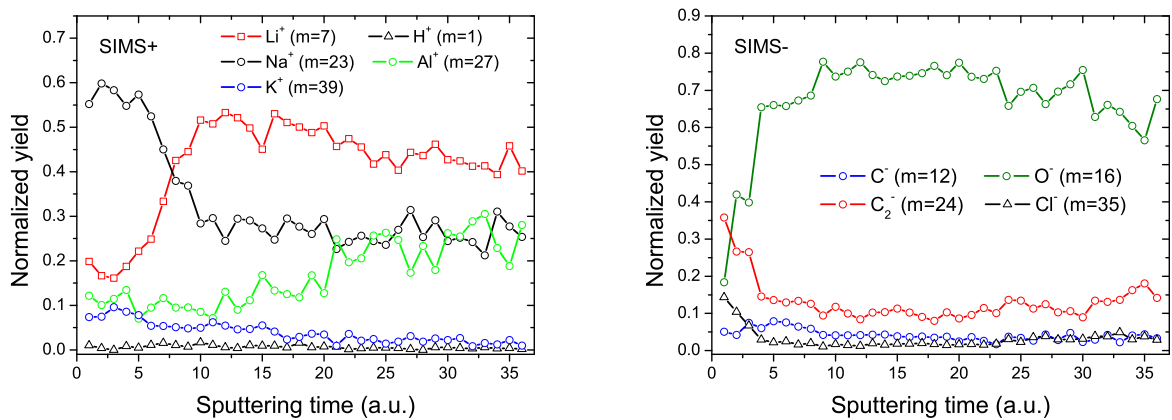


Figure 4.26: Left panel: The normalized sputtered  $\text{H}^+$ ,  ${}^7\text{Li}^+$ ,  $\text{Na}^+$ ,  $\text{Al}^+$  and  $\text{K}^+$  yield as a function of sputtering time (in arbitrary units) for the  ${}^7\text{Li}$  implanted target obtained with a 4 keV  $\text{Ar}^+$  primary beam. Right panel: The normalized sputtered  $\text{C}^-$ ,  $\text{O}^-$ ,  $\text{C}_2^-$  and  $\text{Cl}^-$  yield as a function of sputtering time (in arbitrary units) for the  ${}^7\text{Li}$  implanted target obtained with a 4 keV  $\text{Ar}^+$  primary beam. The lines through the data points are to guide the eye only.

of the implanted target: the atomic fraction of element  $A$ ,  $X_A$ , is given by

$$X_A = \frac{I_A/I_A^{Av}}{\sum_i I_i/I_i^{Av}}, \quad (4.15)$$

where the  $I_i$  are the measured peak area intensities for the element  $i$  in the sample, and  $I^{Av}$  are the Average Matrix Sensitive Factors (AMRSFs) for XPS. These factors are given in tables for Mg  $K_\alpha$  X-rays and are ratioed to C as unity. XPS measurements were also made at Multitechnique Surface Analysis System. Fig. 4.27 shows a Mg  $K_\alpha$  X-rays XPS spectrum for the  $^7\text{Li}$  implanted into Al target surface. The most important peaks were identified and were fitted with gaussians in order to extract the  $I_i$  values.

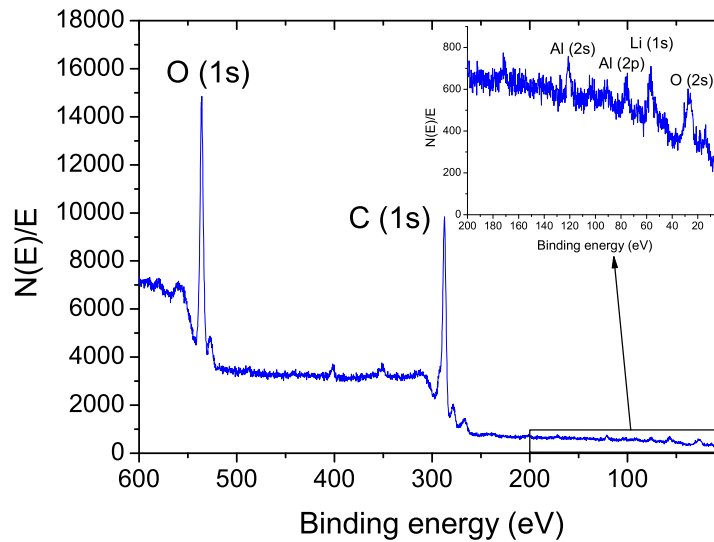


Figure 4.27: Mg  $K_\alpha$  X-rays XPS spectrum that shows the detected photo-emitted electrons as a function of the binding energy for the  $^7\text{Li}$  implanted in Al target surface.

Table 4.5 shows the  $I_i$  values obtained from the spectrum of fig. 4.27, and the corresponding  $I^{Av}$  values. Applying eq. 4.15 for  $^7\text{Li}$ , Al, C and O, we obtained the following target stoichiometry of the first  $\approx 10$  nm layer:  $^7\text{Li}_{0.18}\text{C}_{0.50}\text{O}_{0.31}\text{Al}_{0.01}$ . This result was feedbacked to the XRUMP simulation of RBS spectrum in order to define more accurately the first target layers, particularly in what concerns the  $^7\text{Li}$  distribution.

The  $^7\text{Li}$  implanted in Al target was used to measure the  $^7\text{Li}(p,\alpha)^4\text{He}$  reaction cross section in the energy range 89.7 – 1740.3 keV (45 energy points) accumulating a total charge of 1490  $\mu\text{C}$  ( $\text{H}_2^+$  beam) plus 9590  $\mu\text{C}$  ( $\text{H}_3^+$  beam).

	Li(1s)	C(1s)	O(1s)	Al(2s)	Al(2p <sub>3/2</sub> )
$I_i$	741	30387	41922	504	464
$I^{Av}$	0.0697	1	2.29	0.768	0.441

Table 4.5:  $I_i$  and  $I^{Av}$  values used to determine the first  $\approx 10$  nm thick target stoichiometry.

### 4.2.3 PdLi<sub>x</sub> targets

Two PdLi<sub>x</sub> alloys, Pd<sub>94.1%</sub>Li<sub>5.9%</sub> and PdLi<sub>0.016%</sub>, of natural Li isotopic content, were produced by plasma discharge techniques and rolled into a 0.2 mm thick foil at the company Lattice Energy, LLC (Chicago, USA). These foils were polished with sand paper to remove any surface LiO<sub>2</sub> and annealed in vacuum at 850°C for one hour to form crystals with a stress-free structure (the PdLi<sub>x</sub> alloys crystalline structure gets very distorted during the rolling process).

The measurement of the excitation function of the  ${}^7\text{Li}(\alpha, \gamma){}^{11}\text{B}$  reaction at  $E_{r,\text{lab}} = 953$  keV (see fig. 4.28) demonstrated that the Li content in the PdLi<sub>x</sub> alloys started at the surface with a homogeneous depth distribution. The atomic fraction of lithium in palladium was measured by PIGE using the 478 keV  $\gamma$ -ray yield from the  ${}^7\text{Li}(p, p'\gamma){}^7\text{Li}$  reaction. These measurements were taken at  $E_{\text{lab}} = 2200$  keV, where the  ${}^7\text{Li}(p, p'\gamma){}^7\text{Li}$  cross section is a slowly varying function with energy.

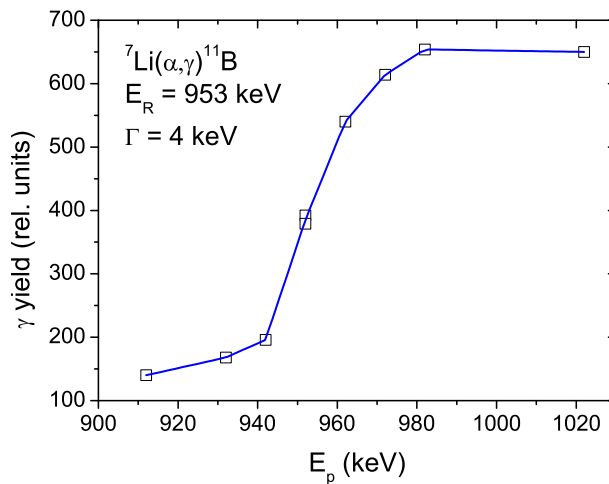


Figure 4.28: The excitation function of the  ${}^7\text{Li}(\alpha, \gamma){}^{11}\text{B}$  reaction at  $E_{r,\text{lab}} = 953$  keV using a Pd<sub>94.1%</sub>Li<sub>5.9%</sub> target. The line through the data points is to guide the eye only.

The PdLi<sub>x</sub> targets were used to measure concurrently both  ${}^7\text{Li}(p,\alpha){}^4\text{He}$  and  ${}^6\text{Li}(p,\alpha){}^3\text{He}$  reactions cross section in the energy range 32.0 – 83.3 keV and 31.3 – 81.6 keV for the  ${}^7\text{Li}$  and  ${}^6\text{Li}$  reactions, respectively (7 energy points), accumulating a total charge of 724.635 mC for the Pd<sub>94.1%</sub>Li<sub>5.9%</sub> target and 49047.507 mC for the PdLi<sub>0.016%</sub> target ( $\text{H}^+$  beam).

#### 4.2.4 Li metal target

The Li metal target was prepared from a thick lithium metal sheet of natural isotopic content. Lithium, as an element of group I in the periodical table, is very reactive in air and so is stored in oil to avoid oxidation. This means that preparing a Li metal target with a clean surface requires some effort. The first effort was done with sand paper (mesh 80 and 180) polishing in normal atmosphere. The black oxide layer is removed, but the fresh shining Li metal surface starts oxidizing immediately and, after 15–20 seconds, all the surface is completely black again. Polishing was also tried with the Li metal inside a glove box under  $\text{N}_2$  inert atmosphere. This process was difficult due to the gloves itself, but we were able to get a shining clean surface. However, there was the problem of carrying the clean lithium sample from the glove box to the target chamber without oxidizing.

Sputter cleaning with an  $\text{Ar}^+$  beam also showed to be fruitless: a Li metal sheet was polished and placed in vacuum ( $\approx 1$  minute was the shortest time possible between finishing polishing and start pumping down the implanter target chamber). These tests were carried out at the 210 kV Danfysik 1090 High Current Implanter machine of the Ion Beam Laboratory at ITN. With a pressure in the  $10^{-7}$  mbar range,  $\text{Ar}^+$  implantation at an energy of 35 keV was done with increasing beam intensity (from 60  $\mu\text{A}$  to 600  $\mu\text{A}$  in a  $7\times 5$  cm<sup>2</sup> area). After an accumulated charge of 3.85 C ( $7.2\times 10^{17}$   $\text{Ar}^+/\text{cm}^2$ ), a visual inspection of the lithium surface showed no oxide removal. An  $\text{Ar}^+$  beam of 5 keV ( $I = 200$   $\mu\text{A}$ , area =  $3\times 3$  cm<sup>2</sup>) also showed no cleaning effect after an accumulated charge of 4.61 C ( $3.2\times 10^{18}$   $\text{Ar}^+/\text{cm}^2$ ). So, it was concluded that *in situ* sputter cleaning was not feasible.

Chemical cleaning was also tried with ethanol and methanol. The first alcohol showed no effect in the black lithium-oxidized surface, while the second reacted too fast consuming the Li.

From these trials, it was decided to prepare the Li metal target in several steps. Firstly,

Li metal sheet was cut (2 mm thick,  $\varnothing = 40$  mm), polished and mounted on the target holder inside a  $N_2$  atmosphere glove box. The clean lithium surface was then covered with toluene – an inert solvent which does not react with lithium and has a boiling temperature of  $140^\circ\text{C}$  (at normal atmospheric pressure) – preventing lithium oxidation during transit from the glove box to the target chamber. When mounted inside the target chamber, the toluene fell down to the chamber, but it did not evaporate immediately and a thin protective layer was expected to remain until the pressure inside the target chamber dropped enough to prevent surface contamination. This solution failed as the toluene inside the target chamber prevented the system of getting a good vacuum. So, the toluene “step” had to be removed from the procedure, and that was accomplished by mechanically cleaning (with a knife, faster and cleaner than sand paper) the surface of the Li metal sheet to a silvery color in Ar gas atmosphere and transferred also in Ar gas to the target chamber. The result was successful as we were able to get a Li target with a clean surface inside the target chamber.

Inspection of the sample, at the end of data taking, showed a dark color at the beam spot area indicating hydrogen incorporation: a hydrogen solubility of 8.6% was observed by measuring the excitation function of the  $^1\text{H}(^{15}\text{N},\alpha\gamma)^{12}\text{C}$  reaction at  $E_{r,\text{lab}} = 8.40$  MeV, which was taken into consideration in the analysis.

The Li metal target was used to measure concurrently both  $^7\text{Li}(p,\alpha)^4\text{He}$  and  $^6\text{Li}(p,\alpha)^3\text{He}$  reactions cross section in the energy range 24.7 – 83.4 keV and 24.2 – 81.7 keV for the  $^7\text{Li}$  and  $^6\text{Li}$  reactions, respectively (9 energy points) accumulating a total charge of 1232.875 mC ( $H^+$  beam).

#### 4.2.5 $\text{Li}_2\text{WO}_4$ target

The  $\text{Li}_2\text{WO}_4$  targets ( $360 \mu\text{g}/\text{cm}^2$  thickness,  $\varnothing = 40$  mm) of natural Li isotopic composition were fabricated by vacuum-evaporation on a steel backing, at Münster University.

The  $\text{Li}_2\text{WO}_4$  targets were used to measure concurrently both  $^7\text{Li}(p,\alpha)^4\text{He}$  and  $^6\text{Li}(p,\alpha)^3\text{He}$  reactions cross section in the energy range 29.0 – 74.7 keV and 28.3 – 73.2 keV for the  $^7\text{Li}$  and  $^6\text{Li}$  reactions, respectively (7 energy points) accumulating a total charge of 340.4 mC ( $H^+$  beam).

## 4.2.6 Targets stability

The target stability tests were performed by observing the evolution of the  ${}^6,7\text{Li}(p,\alpha)$  reaction yields, *i.e.*, the ratios  $N({}^3\text{He})/Q$ , with the accumulated charge, at different proton energies. Figs. 4.29, 4.30 and 4.31 show these evolutions for the LiF-Cu target, the Li metal target and the  $\text{Pd}_{94.1\%}\text{Li}_{5.9\%}$  target, respectively. From these figures, and from similar data for the other targets, it was verified that all targets remained stable in yield to better than 10% at all energies. The exception was the Li metal, where the first run yield between  $60\text{ keV} \leq E_{\text{lab}} \leq 100\text{ keV}$  was  $\approx 30\%$  higher than the subsequent runs. We believe, this happened because the metallic Li surface changed from pure Li to  $\text{LiH}_{8.6\%}$  (see description above). For that reason, these data points were not considered in our analysis.

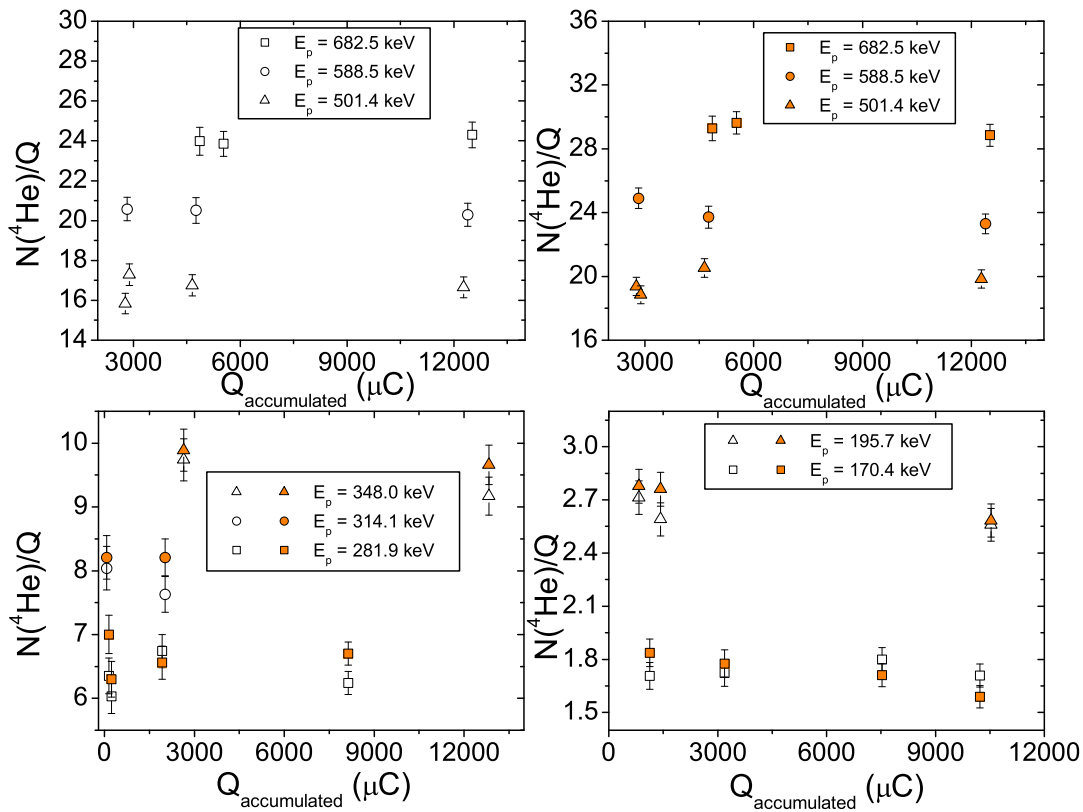


Figure 4.29:  ${}^7\text{Li}(p,\alpha){}^4\text{He}$  yield  $[N({}^4\text{He})/Q]$  evolution with accumulated charge for the LiF-Cu target, at different energies. The white and orange data points correspond to the Si detectors at  $124^\circ$  and  $145^\circ$ , respectively. The error bars come from the statistical error on  $N({}^4\text{He})$  counts.

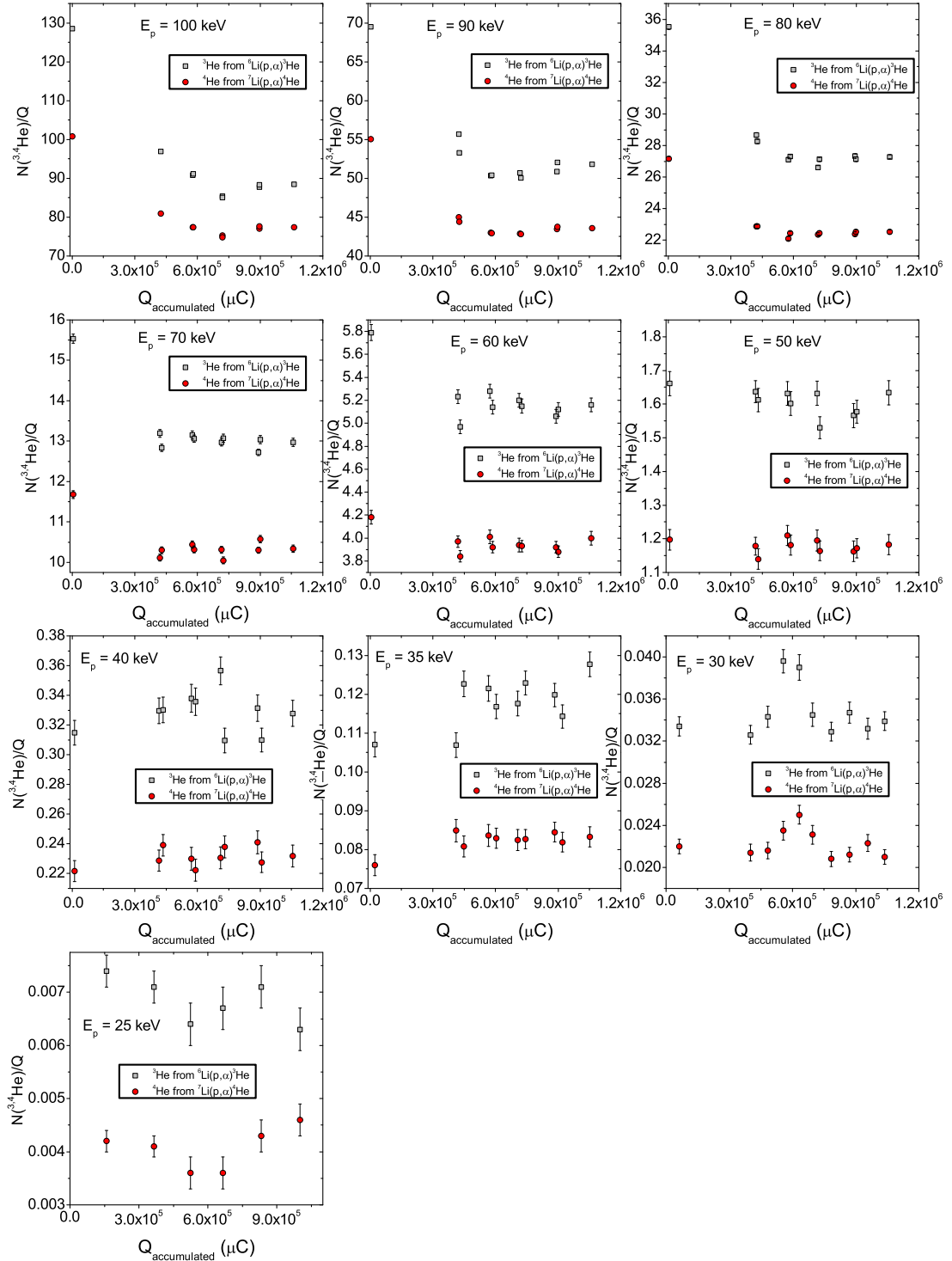


Figure 4.30:  $^7\text{Li}(p,\alpha)^4\text{He}$  yield [ $N(^4\text{He})/Q$ ] (red circles) and  $^6\text{Li}(p,\alpha)^3\text{He}$  yield [ $N(^3\text{He})/Q$ ] (gray squares) evolution with accumulated charge for the Li metal target. The error bars come from the statistical error on  $N(^{3,4}\text{He})$  counts.

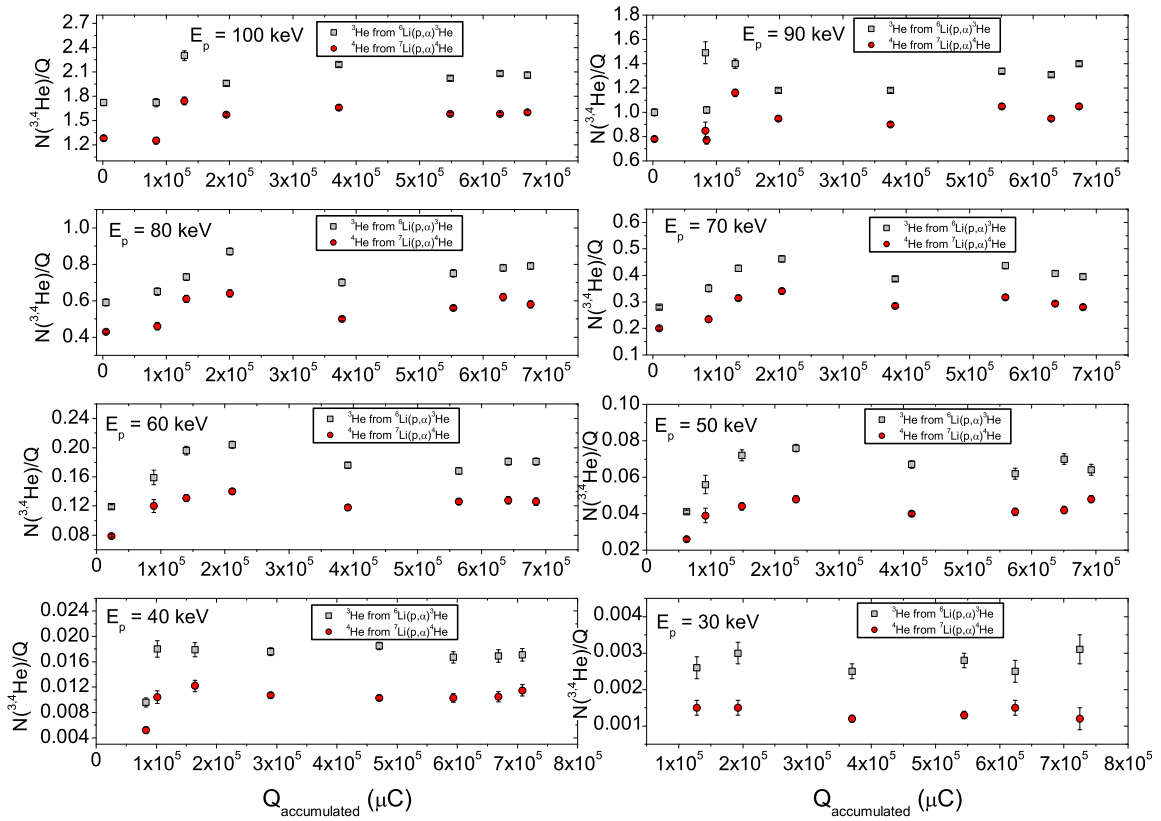


Figure 4.31:  $^7\text{Li}(p,\alpha)^4\text{He}$  yield [ $N(^4\text{He})/Q$ ] (red circles) and  $^6\text{Li}(p,\alpha)^3\text{He}$  yield [ $N(^3\text{He})/Q$ ] (gray squares) evolution with accumulated charge for the  $\text{Pd}_{94.1\%}\text{Li}_{5.9\%}$  target. The error bars come from the statistical error on  $N(^3,4\text{He})$  counts.

# Chapter 5

## Analysis and results

This chapter, analysis and results, is divided in three major sections. The first one describes the procedure used to extract the  $S(E)$  values and corresponding uncertainties. The second section describes the fits to  $S(E)$  values, done to determine the bare component of  $S(E)$  and the electron screening potential energy,  $U_e$ . The last section applies the Debye screening model to our data.

### 5.1 $S$ -factor determination

#### 5.1.1 Integral method

This section describes the method used to extract the values of  $S(E)$  for a thin target setup (ITN setup). For an incident energy  $E_0$ , a target thickness  $\Delta$ , and an effective stopping cross section  $\epsilon_{\text{eff}}(E)$  (all in c.m. system), the number of counts in a detector placed at  $\theta_{\text{lab}}$ ,  $N(E_0, \theta_{\text{lab}})$ , is related to the cross section  $\sigma(E)$  via the equation [37]

$$N(E_0, \theta_{\text{lab}}) = 1.01 (1 + \delta) N_p \frac{\Omega_{\text{lab}}}{4\pi} \eta \int_{E_{\text{min}}}^{E_{\text{max}}} K_{\Omega}(E, \theta_{\text{lab}}) W(E, \theta) \frac{\sigma(E)}{\epsilon_{\text{eff}}(E)} dE, \quad (5.1)$$

where 1.01 is a charge correction factor defined in section 5.1.6, and  $\delta = 1$  or 0 in the case of identical or non-identical ejectiles. The quantity  $N_p$  is the number of incident protons (measured by a charge integrator), and  $\Omega_{\text{lab}}$  and  $\eta$  are the solid angle in the laboratory frame and efficiency of the detector, respectively (here,  $\eta = 1$  for the Si detectors used). The solid angle transformation between the laboratory and center-of-mass systems is described by  $K_{\Omega}(E, \theta_{\text{lab}})$

and the angular distributions are described by  $W(E, \theta)$ , where  $E$  and  $\theta$  are c.m. coordinates. The integration limits are  $E_{\min} = E_0 - \Delta$  and  $E_{\max} = E_0$ . The ratio  $N(E_0, \theta_{\text{lab}})/N_p$  was obtained by calculating the arithmetic mean (average) of up to 4 runs.

Expressing  $\sigma(E)$  in terms of the  $S$ -factor, eq. 2.16, we get

$$N(E_0, \theta_{\text{lab}}) = 1.01 (1 + \delta) N_p \frac{\Omega_{\text{lab}}}{4\pi} \int_{E_{\min}}^{E_{\max}} K_{\Omega}(E, \theta_{\text{lab}}) W(E, \theta) \frac{S(E)}{E \epsilon_{\text{eff}}(E)} \exp(-2\pi\eta) dE . \quad (5.2)$$

Assuming that  $S(E)$ ,  $K_{\Omega}(E, \theta_{\text{lab}})$  and  $W(E, \theta)$  are approximately constant over the target thickness  $\Delta$ , eq. 5.2 simplifies to

$$N(E_0, \theta_{\text{lab}}) = 1.01 (1 + \delta) N_p \frac{\Omega_{\text{lab}}}{4\pi} K_{\Omega}(E, \theta_{\text{lab}}) W(E, \theta) Y(E_0) , \quad (5.3)$$

where the reaction yield per incident projectile,  $Y(E_0)$ , is given by

$$\begin{aligned} Y(E_0) &= S(E) \int_{E_{\min}}^{E_{\max}} \frac{\exp(-2\pi\eta)}{E \epsilon_{\text{eff}}(E)} dE \\ &= 2 S(E) \int_E^{E_{\max}} \frac{\exp(-2\pi\eta)}{E^* \epsilon_{\text{eff}}(E^*)} dE^* , \end{aligned} \quad (5.4)$$

where the effective energy  $E$ , defined by this equation, corresponds to that energy within the target, at which one-half of the reaction yield is obtained. This effective energy is then associated with the deduced value of the  $S(E)$  factor, or equivalently of  $\sigma(E)$ . For the determination of  $S(E)$  by the integral method, a set of Fortran programs were implemented which included routines from the CERNLIB package [82] to calculate numerically the integral of eq. 5.4. Some of these programs are listed in Appendix C.

For an infinitely thick target one has  $E_{\min} = 0$  and the extraction of  $S(E)$ , or  $\sigma(E)$ , from the observed count rates requires a different approach since  $S(E)$  can not be assumed constant over  $\Delta$  and eq. 5.4 is no longer valid.

### 5.1.2 Differential method

This section describes the method used to extract the value of  $S(E)$  for a infinitely thick target setup (Bochum setup). From eq. 5.1 we can define the reaction yield of an infinitely thick target as:

$$Y^{\infty}(E_0, \theta_{\text{lab}}) = N(E_0, \theta_{\text{lab}})/N_p , \quad (5.5)$$

where  $N(E_0, \theta_{\text{lab}})/N_p$  was obtained by the average of up to 13 runs from  $E_{\text{lab}} = 30$  to 100 keV.

In order to arrive at a thin-target yield curve  $Y(E_0, \theta_{\text{lab}})$ , the thick target yield curve was differentiated, *i.e.*, the yield difference between two adjacent points,  $Y^\infty(E_0, \theta_{\text{lab}})$  and  $Y^\infty(E_0 - \Delta E_0, \theta_{\text{lab}})$ , was calculated and divided by  $\Delta E_0$  (with  $\Delta E_0 \approx 4.4$  to 8.7 keV) to correct for variations in the energy step:

$$Y(E_0, \theta_{\text{lab}}) = \frac{Y^\infty(E_0, \theta_{\text{lab}}) - Y^\infty(E_0 - \Delta E_0, \theta_{\text{lab}})}{\Delta E_0}. \quad (5.6)$$

For small energy steps, the quantities  $K_\Omega(E, \theta_{\text{lab}})$ ,  $W(E, \theta)$  and  $\epsilon_{\text{eff}}(E)$  are approximately constant over  $\Delta E_0 = \Delta$ , and eq. 5.1 simplifies to

$$Y(E_0, \theta_{\text{lab}}) = \frac{1 + \delta}{\Delta} \frac{\Omega_{\text{lab}}}{4\pi} \frac{K_\Omega(E_0, \theta_{\text{lab}}) W(E_0, \theta)}{\epsilon_{\text{eff}}(E_0)} \int_{E_0 - \Delta}^{E_0} \sigma(E) dE. \quad (5.7)$$

Since  $\sigma(E)$  is not constant over  $\Delta$ , we define again an effective energy,  $E$ , within the energy step  $\Delta$ , at which one-half of the reaction yield is obtained:

$$Y(E_0, \theta_{\text{lab}}) = (1 + \delta) \frac{\Omega_{\text{lab}}}{4\pi} \frac{K_\Omega(E_0, \theta_{\text{lab}}) W(E_0, \theta)}{\epsilon_{\text{eff}}(E_0)} \sigma(E). \quad (5.8)$$

Assuming a linear decrease in cross section from  $\sigma_1$  at  $E_0$  to  $\sigma_2$  at  $E_0 - \Delta$ , the effective energy is given by [37]:

$$E = E_0 - \Delta + \Delta \left( -\frac{\sigma_2}{\sigma_1 - \sigma_2} + \left[ \frac{\sigma_1^2 + \sigma_2^2}{2(\sigma_1 - \sigma_2)^2} \right]^{1/2} \right), \quad (5.9)$$

which is a good approximation (to better than 6% for ratios  $\sigma_1/\sigma_2 \leq 10$ ). In order to satisfy this condition, we chose the energy steps mentioned above.

For the present energy range and for  $\theta_{\text{lab}} = 130^\circ$ , we have  $W(E, \theta) = 1$ , so

$$Y(E_0, \theta_{\text{lab}}) = C \frac{\sigma(E)}{\epsilon_{\text{eff}}(E_0)}. \quad (5.10)$$

with the constant  $C$  defined as:

$$C = (1 + \delta) \frac{\Omega_{\text{lab}}}{4\pi} K_\Omega(E_0, \theta_{\text{lab}}). \quad (5.11)$$

Expressing  $\sigma(E)$  in terms of  $S(E)$  we get for eq. 5.10

$$Y(E_0, \theta_{\text{lab}}) = C \frac{\exp(-2\pi\eta) S(E)}{E \epsilon_{\text{eff}}(E_0)}. \quad (5.12)$$

### 5.1.3 Effective stopping cross section

For a target with  $N_a$  active atoms (nuclei under study) per square centimeter and  $N_i$  inactive atoms per square centimeter, the effective stopping cross section,  $\epsilon_{\text{eff}}(E)$ , is expressed as a function of active and inactive atoms stopping cross sections by the relation (Bragg's rule):

$$\epsilon_{\text{eff}}(E) = \epsilon_a(E) + \frac{1}{N_a} \sum_i N_i \epsilon_i(E) \quad [eV/(\text{atoms}/\text{cm}^2)]. \quad (5.13)$$

For example, in the  $\text{Li}_{0.48}\text{F}_{0.48}\text{C}_{0.04}$  target with  ${}^7\text{Li}$  as the active nuclei –  ${}^7\text{Li}(p,\alpha){}^4\text{He}$  reaction – we have, considering Li of natural isotopic content (92.58%  ${}^7\text{Li}$ , 7.42%  ${}^6\text{Li}$ ):

$$\begin{aligned} \epsilon_{\text{eff}}(E) &= \epsilon_{7\text{Li}}(E) + \frac{1}{N_{7\text{Li}}} \left( N_{6\text{Li}} \epsilon_{6\text{Li}}(E) + N_{\text{F}} \epsilon_{\text{F}}(E) + N_{\text{C}} \epsilon_{\text{C}}(E) \right) \Rightarrow \\ \Rightarrow \epsilon_{\text{eff}}(E) &= \epsilon_{7\text{Li}}(E) + \frac{1}{0.48 \times 0.9258} \times \\ &\times \left[ (0.48 \times 0.0742) \epsilon_{6\text{Li}}(E) + (0.48) \epsilon_{\text{F}}(E) + (0.04) \epsilon_{\text{C}}(E) \right]. \end{aligned} \quad (5.14)$$

The stopping cross sections of each target element, as Li or F, for protons, is calculated using the software SRIM [79] (version 2003.36). The  $\epsilon$  values are calculated for different energies and parametrized by polynomial functions as exemplified in fig. 5.1. These functions are then used in eq. 5.4 and eq. 5.12.

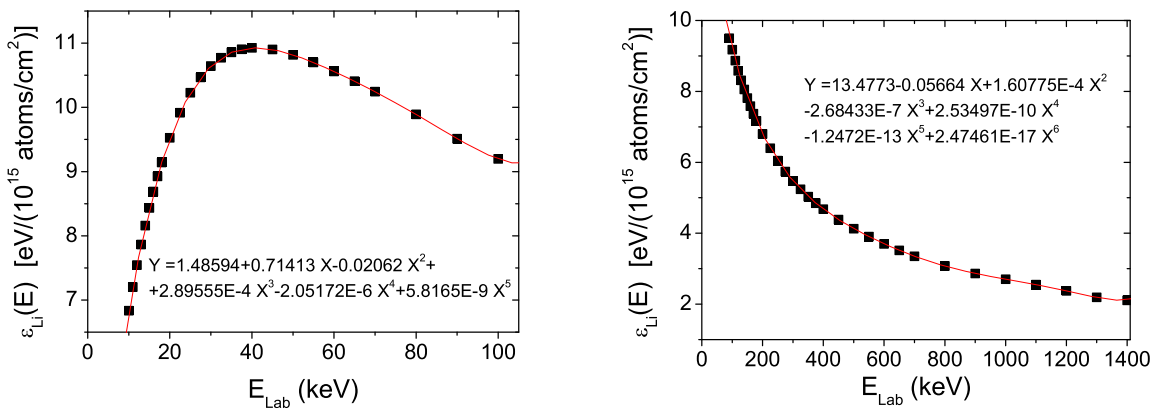


Figure 5.1: Left panel: Stopping cross section of Li for protons,  $\epsilon_{\text{Li}}$ , as a function of  $E_{\text{lab}}$  in the energy range 10 – 100 keV. The  $\epsilon_{\text{Li}}$  values, given by SRIM [79], were  $\chi^2$  fitted with a polynomial function (red line). Right panel: Stopping cross section of Li for protons,  $\epsilon_{\text{Li}}$ , as a function of  $E_{\text{lab}}$  in the energy range 90 – 1400 keV. The  $\epsilon_{\text{Li}}$  values, given by SRIM [79], were  $\chi^2$  fitted with a polynomial function (red line).

Bragg's rule assumes the interaction between the incident ion and the target atom to be independent of the environment. The chemical and physical state of the medium is, however, observed to have an effect on the energy loss [73]. The deviations from Bragg's rule predictions are most pronounced, of the order of 10–20%, around the stopping maximum for light organic gases and for solid compounds containing heavier constituents, such as oxides, nitrides, etc.

To allow for chemical state effects, Ziegler and Manoyan (1988) [83] developed the 'cores and bonds' (CAB)-model, where it is assumed that the energy loss of ions in a compound to be due to two contributions: the effect of the cores, *i.e.*, the closed electron shells of atoms and the effect of the chemical bonds, such as C–O or C=C bonds. In Ziegler and Manoyan's paper, the CAB-model stopping cross section of protons at  $E_{\text{lab}} = 125$  keV is defined as

$$\epsilon_{p,CAB}(125 \text{ keV}) = \sum \epsilon_{\text{cores}} + \sum \epsilon_{\text{bonds}} . \quad (5.15)$$

To calculate the CAB-correction to Bragg's rule, the bond-structure of the compound needs to be known, as well as their respective  $\epsilon_{\text{cores}}$  and  $\epsilon_{\text{bonds}}$  values. From the available literature [73], the chemical bonds of interest for the present work are restricted to the C-O bonds and C=O bonds. We assumed that these bonds are present in the CO surface layer of the  $^7\text{Li}$  implanted target (see section 4.2.2). In this case, we have for this surface layer a modified effective stopping cross section given by

$$\begin{aligned} \epsilon_{\text{eff}}(E_{\text{lab}}) &= \epsilon_{7\text{Li}}(E) + \frac{1}{N_{7\text{Li}}} \left[ N_{\text{Al}} \epsilon_{\text{Al}}(E_{\text{lab}}) + \left( N_{\text{C}} \epsilon_{\text{C}}(E_{\text{lab}}) + N_{\text{O}} \epsilon_{\text{O}}(E_{\text{lab}}) \right) f(E_{\text{lab}}) \frac{\epsilon_{p,CAB}(125 \text{ keV})}{\epsilon_{p,Bragg}(125 \text{ keV})} \right] \\ f(E_{\text{lab}}) &= \frac{1}{1 + \exp \left[ 1.48 \left( 6.325 \sqrt{E_{\text{lab}}/m_p} - 7 \right) \right]} , \end{aligned} \quad (5.16)$$

where  $m_p$  is the projectile mass,  $E_{\text{lab}}/m_p$  is in MeV/u and  $\epsilon_{p,Bragg}$  is the proton stopping cross section calculated using Bragg's rule. The largest differences between the CAB-calculations and Bragg's rule predictions are found around the stopping maximum. The differences reduces with increasing energy, eventually disappearing. The average accuracy of the calculation is better than 2% when compared to data from several hydrocarbon targets [73].

Giving numerical values to the variables, and assuming there is the same number of C-O

and C=O bonds, we get

$$\begin{aligned}
\sum \epsilon_{cores} &= 0.31 \times \epsilon_{cores}^C + 0.5 \times \epsilon_{cores}^O \Rightarrow \\
\Rightarrow \sum \epsilon_{cores} &= 0.31 \times 6.145 + 0.5 \times 5.446 \text{ eV}/(10^{15} \text{ at/cm}^2) \\
\sum \epsilon_{bonds} &= \frac{\epsilon_{bonds}^{C-O} + \epsilon_{bonds}^{C=O}}{2} \Rightarrow \sum \epsilon_{bonds} = \frac{6.168 + 13.926}{2} \text{ eV}/(10^{15} \text{ at/cm}^2) \\
\epsilon_{p,Bragg}(125 \text{ keV}) &= 0.31 \times \epsilon_{p,Bragg}^C(125 \text{ keV}) + 0.5 \times \epsilon_{p,Bragg}^O(125 \text{ keV}) \Rightarrow \\
\Rightarrow \epsilon_{p,Bragg}(125 \text{ keV}) &= 0.31 \times 14.03 + 0.5 \times 15.44 \text{ eV}/(10^{15} \text{ at/cm}^2) , \quad (5.17)
\end{aligned}$$

where 0.31 and 0.5 are the atomic fractions of C and O in the surface layer, respectively. The values of  $\epsilon_{cores}$  and  $\epsilon_{bonds}$  for carbon and oxygen were taken from [73]. With this correction, the CO layer  $\epsilon_{eff}$  value increases by 8.2 % at the lowest proton energy,  $E = 89.7$  keV. This increase becomes less pronounced as we climb in energy, disappearing for energies around 550 keV.

#### 5.1.4 Solid angle transformation between the laboratory and center of mass systems

Consider the scattering event schematized in fig. 5.2 for a nonrelativistic inelastic collision.

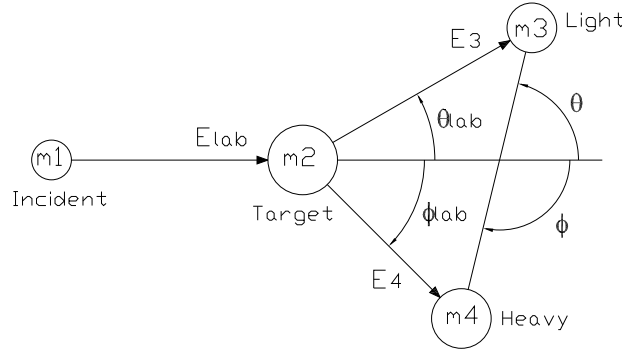


Figure 5.2: Schematic scattering event as seen in the laboratory and center-of-mass coordinate systems illustrating the angles and energies for nonrelativistic inelastic collisions.

The solid angle transformation between the laboratory and center of mass systems,  $K_{\Omega}(E, \theta_{lab})$ , for the light product is given by [73]:

$$K_{\Omega}(E, \theta_{lab}) = \frac{\sin \theta d\theta}{\sin \theta_{lab} d\theta_{lab}} = \frac{E_3/E_T}{(AC)^{1/2}(D/B - \sin^2 \theta_{lab})^{1/2}} , \quad (5.18)$$

where  $E_3$  is the light product laboratory energy,  $E_T = E_{\text{lab}} + Q$ ,  $Q$  is the reaction  $Q$ -value, and

$$A = \frac{m_1 m_4 (E_{\text{lab}}/E_T)}{(m_1 + m_2)(m_3 + m_4)} \quad (5.19)$$

$$B = \frac{m_1 m_3 (E_{\text{lab}}/E_T)}{(m_1 + m_2)(m_3 + m_4)} \quad (5.20)$$

$$C = \frac{m_2 m_3}{(m_1 + m_2)(m_3 + m_4)} \left(1 + \frac{m_1 Q}{m_2 E_T}\right) \quad (5.21)$$

$$D = \frac{m_2 m_4}{(m_1 + m_2)(m_3 + m_4)} \left(1 + \frac{m_1 Q}{m_2 E_T}\right), \quad (5.22)$$

which gives for  $E_3/E_T$ :

$$\frac{E_3}{E_T} = B \left[ \cos \theta_{\text{lab}} + \left( \frac{D}{B} - \sin^2 \theta_{\text{lab}} \right)^{1/2} \right]^2. \quad (5.23)$$

### 5.1.5 Angular distributions

#### ${}^7\text{Li}(\text{p},\alpha){}^4\text{He}$

The angular distributions  $W(E, \theta)$  for the  ${}^7\text{Li}(\text{p},\alpha){}^4\text{He}$  reaction were measured for 14 energies from  $E = 80$  to  $1740$  keV. For each energy, measurements were made at up to 13 angles between  $\theta_{\text{lab}} = 84^\circ$  and  $165^\circ$ . The results are plotted in figs. 5.3, 5.4 and 5.5 and listed in Appendix B. The error bars shown are related only to statistical uncertainties.

The angular distributions were fitted with eq. 3.16. Since the system of two  ${}^4\text{He}$  can only have orbital angular momentum  $\ell = 0, 2$  and  $4$  (see section 3.1.2), two different fits were performed:

$$W(E, \theta) = 1 + Q_2 A_2(E) P_2(\cos\theta), \quad (5.24)$$

which considers only  $\ell = 0$  and  $2$ , and

$$W(E, \theta) = 1 + Q_2 A_2(E) P_2(\cos\theta) + Q_4 A_4(E) P_4(\cos\theta), \quad (5.25)$$

which considers  $\ell = 0, 2$  and  $4$ . For the ITN setup, the Si detectors have an opening angle,  $\beta = 2^\circ$ , which corresponds to correction factors:  $Q_2 = Q_4 = 1$ .

The center-of-mass angle of the light product,  $\theta$ , is given by [73]:

$$\sin \theta = \left( \frac{E_3/E_T}{D} \right)^{1/2} \sin \theta_{\text{lab}}, \quad (5.26)$$

with  $D$  and  $E_3/E_T$  defined above in eqs. 5.22 and 5.23, respectively.

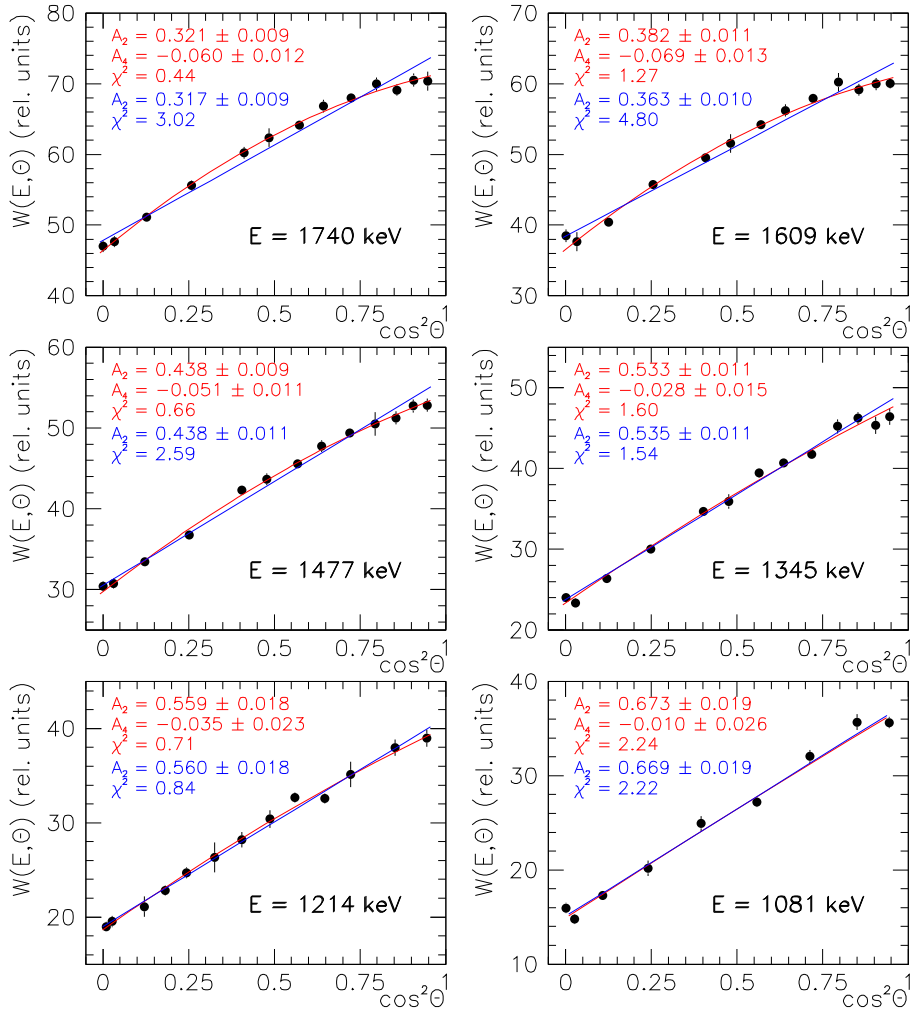


Figure 5.3: Angular distributions of the  $^4\text{He}$  particles for the  $^7\text{Li}(p,\alpha)^4\text{He}$  reaction at the energies indicated. The solid lines represent the result of the Legendre polynomial fits given by Eqs. 5.24 (blue line) and 5.25 (red line).

The results of the  $\chi^2$  fits are listed in Appendix B and plotted in figs. 5.3, 5.4 and 5.5 with solid lines: blue line for eq. 5.24 and red line for eq. 5.25. To our knowledge, these fits show for the first time that  $A_4$  is not negligible for  $E$  higher than  $\approx 1100$  keV. This means that, for this energy range, incoming protons with  $\ell = 3$  must also be considered (besides the  $\ell = 1$  contribution) in theoretical calculations. For energies below 1100 keV, the inclusion of the  $A_4 P_4(\cos\theta)$  term does not change the fit, so we consider  $A_4 = 0$  for  $E < 1100$  keV.

The deduced  $A_2(E)$  and  $A_4(E)$  coefficients are successfully parametrized with polynomial

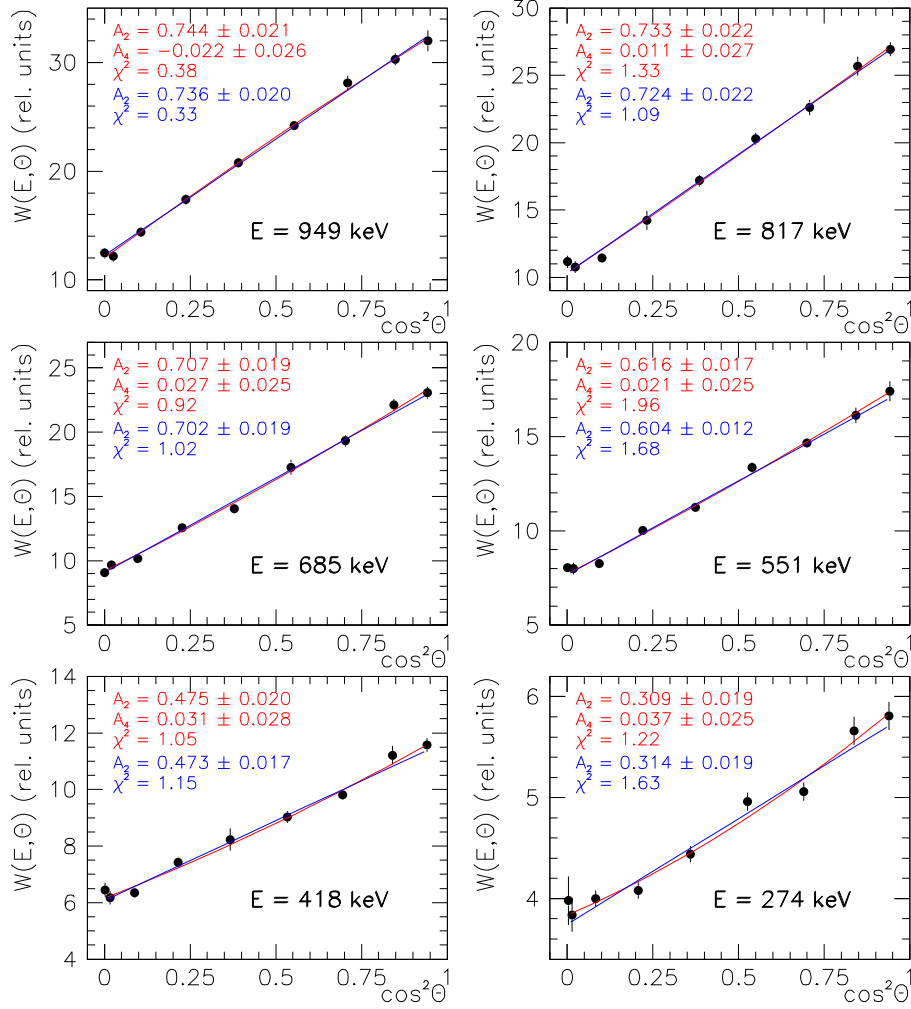


Figure 5.4: Angular distributions of the  ${}^4\text{He}$  particles for the  ${}^7\text{Li}(p,\alpha){}^4\text{He}$  reaction at the energies indicated. The solid lines represent the result of the Legendre polynomial fits given by Eqs. 5.24 (blue line) and 5.25 (red line).

functions:

$$A_2(E) = -1.02 \times 10^{-1} + 1.67 \times 10^{-3}E - 3.02 \times 10^{-7}E^2 - 9.33 \times 10^{-10}E^3 + 3.65 \times 10^{-13}E^4 \quad (5.27)$$

$$A_4(E) = 5.58 \times 10^{-2} - 7.06 \times 10^{-5}E, \quad (5.28)$$

as shown in the fits of fig. 5.6.

Comparing with previous works, we conclude that our data are in good agreement with the results of Engstler *et al.* (1992) [50] except in the high energy end where Engstler *et al.* data are higher than ours, as shown in fig. 5.7. Concerning the energy range, between 100 and 500 keV,

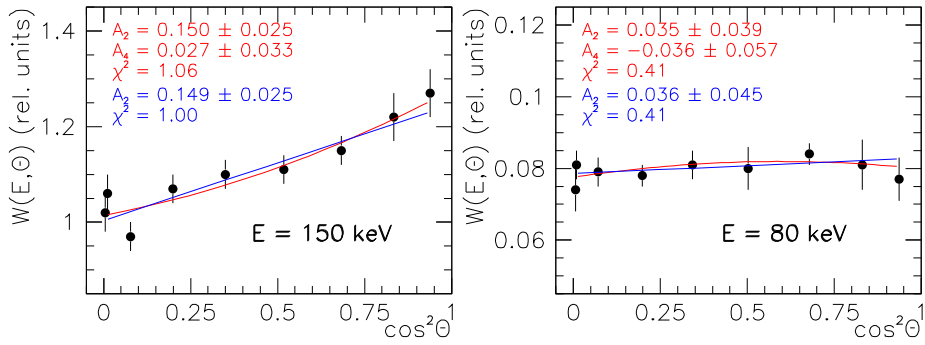


Figure 5.5: Angular distributions of the  $^4\text{He}$  particles for the  $^7\text{Li}(p,\alpha)^4\text{He}$  reaction at the energies indicated. The solid lines represent the result of the Legendre polynomial fits given by Eqs. 5.24 (blue line) and 5.25 (red line).

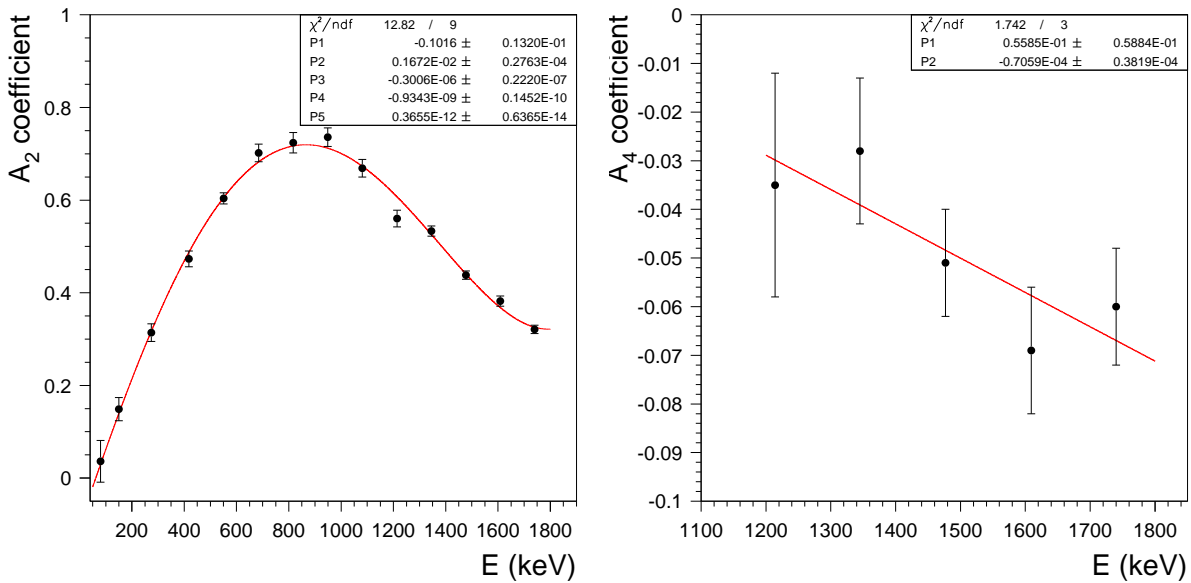


Figure 5.6: Left panel: Deduced  $A_2(E)$  coefficient as a function of the energy. The solid curve represents a fourth order polynomial fit to the data. Right panel: Deduced  $A_4(E)$  coefficient as a function of the energy. The solid curve represents a linear fit to the data.

that showed a slight discrepancy between Engstler *et al.* and Rolfs *et al.* (1986) [60] data, our values confirm Engstler *et al.* results.

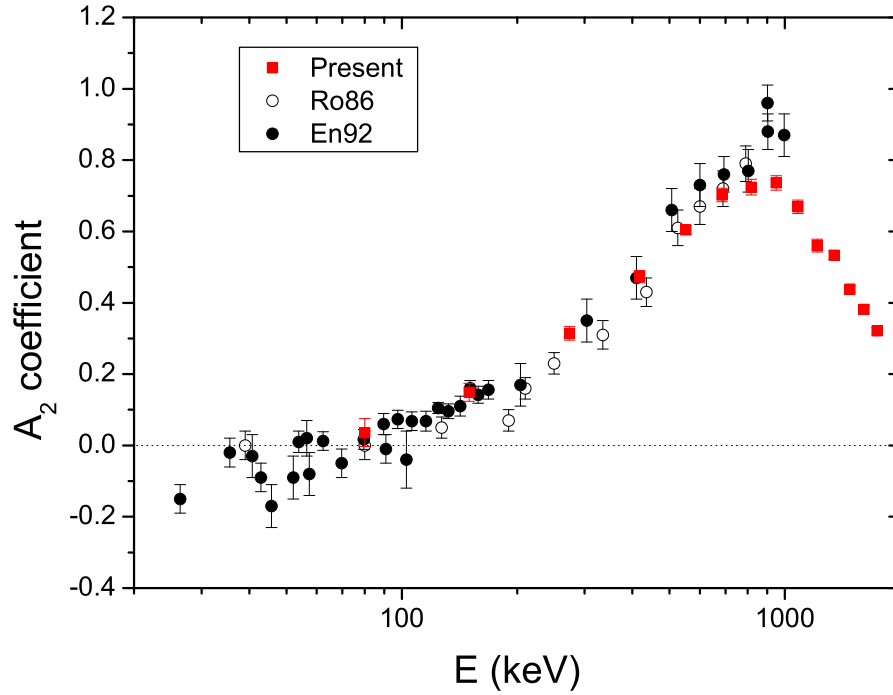


Figure 5.7: Deduced  $A_2(E)$  coefficient as a function of the energy. Comparison with previous works.

### ${}^6\text{Li}(p,\alpha){}^3\text{He}$

According to section 3.3.2, angular distributions  $W(E, \theta)$  for the  ${}^6\text{Li}(p,\alpha){}^3\text{He}$  are defined by the equation:

$$W(E, \theta) = 1 + A_1(E) P_1(\cos\theta) + A_2(E) P_2(\cos\theta) , \quad (5.29)$$

where,

$$A_1(E) = -1.49 \times 10^{-1} + 2.24 \times 10^{-3} E - 2.10 \times 10^{-6} E^2 \quad (5.30)$$

$$A_2(E) = -2.9 \times 10^{-2} - 2.6 \times 10^{-4} E . \quad (5.31)$$

The parametrization of  $A_1(E)$  was obtained by fitting Engstler *et al.* (1992) [50] data, as shown in fig. 5.8. The  $A_2(E)$  parametrization was taken directly from these authors.

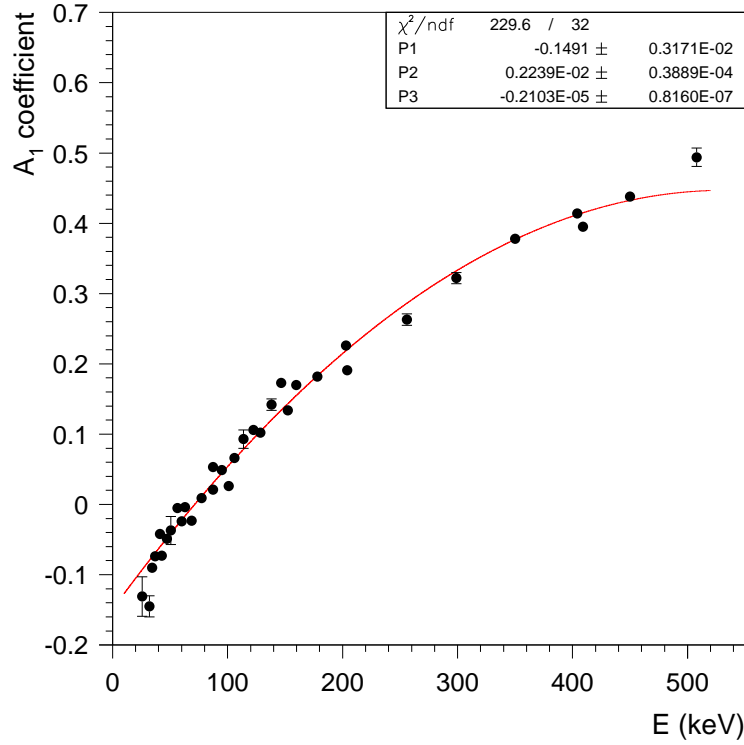


Figure 5.8: Energy dependence of the dominant coefficient,  $A_1$ , in the angular distribution for the  ${}^6\text{Li}(p,\alpha){}^3\text{He}$  reaction. Data taken from [50]. The solid curve represents a second order polynomial fit to data.

## 5.1.6 Error analysis

### Integral method

The quoted uncertainties for  $S(E)$  arises from four sources, which are added quadratically:

$$\begin{aligned} \left[\delta S(E)\right]^2 &= \left[\frac{\partial S(E)}{\partial(N_p\Omega_{\text{lab}})}\right]^2 \left[\delta(N_p\Omega_{\text{lab}})\right]^2 + \left[\frac{\partial S(E)}{\partial N(E_0, \theta_{\text{lab}})/N_p}\right]^2 \left[\delta N(E_0, \theta_{\text{lab}})/N_p\right]^2 + \\ &+ \left[\frac{\partial S(E)}{\partial \epsilon_{\text{eff}}(E)}\right]^2 \left[\delta \epsilon_{\text{eff}}(E)\right]^2 + \left[\frac{\partial S(E)}{\partial W(E, \theta)}\right]^2 \left[\delta W(E, \theta)\right]^2. \end{aligned} \quad (5.32)$$

These terms were calculated as follows.

1. the correct determination of  $N_p$ , the number of projectiles, requires an accurate and reliable setup for charge measurement. These wanted characteristics may be verified using a

different approach for cross section calculation. For  $E_{\text{lab}}$  around 900 keV and above, the LiF-Ag target thickness is small enough ( $\Delta_{\text{lab}} < 5.8$  keV) so that we can consider that the integrand function in eq. 5.1 is constant within the integration limits. So, for this energy interval, the  ${}^7\text{Li}(p,\alpha){}^4\text{He}$  reaction differential cross section in the laboratory system of reference is related to the observed number of  $\alpha$ -particles,  $N(E_{\text{lab}}, \theta_{\text{lab}})$ , by the relation

$$\begin{aligned} N(E_{\text{lab}}, \theta_{\text{lab}}) &= (1 + \delta) N_p \frac{d\sigma(E_{\text{lab}}, \theta_{\text{lab}})}{d\Omega_{\text{lab}}} \Omega_{\text{lab}} \frac{\Delta_{\text{lab}}}{\epsilon_{\text{eff}}(E_{\text{lab}})} = \\ &= 2 N_p \frac{d\sigma(E_{\text{lab}}, \theta_{\text{lab}})}{d\Omega_{\text{lab}}} \Omega_{\text{lab}} N_{7\text{Li}} \Leftrightarrow \\ &\Leftrightarrow \frac{d\sigma(E_{\text{lab}}, \theta_{\text{lab}})}{d\Omega_{\text{lab}}} = \frac{1}{2} \frac{N(E_{\text{lab}}, \theta_{\text{lab}})}{N_p \Omega_{\text{lab}}} \frac{1}{N_{7\text{Li}}} , \end{aligned} \quad (5.33)$$

where  $N_{7\text{Li}} = \Delta_{\text{lab}}/\epsilon_{\text{eff}}(E_{\text{lab}})$  gives the  ${}^7\text{Li}$  nuclei areal density for the LiF-Ag target, and  $\delta = 1$ . For the energy range mentioned above, the  ${}^7\text{Li}(p,\alpha){}^4\text{He}$  reaction products are observed in the Si detectors concurrently with the elastically scattered protons from the Ag layer (see fig. 4.7). From the ratio of observed counts in the two peaks, we get an expression for the differential cross section which is independent of both  $N_p$  and  $\Omega_{\text{lab}}$ :

$$\begin{aligned} \frac{N(E_{\text{lab}}, \theta_{\text{lab}})}{N_{\text{Ag}}(E_{\text{lab}}, \theta_{\text{lab}})} &= \frac{2 N_p N_{7\text{Li}} \frac{d\sigma(E_{\text{lab}}, \theta_{\text{lab}})}{d\Omega_{\text{lab}}} \Omega_{\text{lab}}}{N_p N_{\text{Ag}} \frac{d\sigma_{\text{Ruth}}^{\text{Ag}}(E_{\text{lab}} - \Delta_{\text{lab}}, \theta_{\text{lab}})}{d\Omega_{\text{lab}}} \Omega_{\text{lab}}} = \frac{2 N_{7\text{Li}} \frac{d\sigma(E_{\text{lab}}, \theta_{\text{lab}})}{d\Omega_{\text{lab}}}}{N_{\text{Ag}} \frac{d\sigma_{\text{Ruth}}^{\text{Ag}}(E_{\text{lab}} - \Delta_{\text{lab}}, \theta_{\text{lab}})}{d\Omega_{\text{lab}}}} \Rightarrow \\ &\Rightarrow \frac{d\sigma(E_{\text{lab}}, \theta_{\text{lab}})}{d\Omega_{\text{lab}}} = \frac{1}{2} \frac{N(E_{\text{lab}}, \theta_{\text{lab}})}{N_{\text{Ag}}(E_{\text{lab}}, \theta_{\text{lab}})} \frac{d\sigma_{\text{Ruth}}^{\text{Ag}}(E_{\text{lab}} - \Delta_{\text{lab}}, \theta_{\text{lab}})}{d\Omega_{\text{lab}}} \frac{1}{r} , \end{aligned} \quad (5.34)$$

where  $N_{\text{Ag}}$  is the Ag areal density,  $r$  is the ratio of areal densities  $r = N_{7\text{Li}}/N_{\text{Ag}}$ , and  $d\sigma_{\text{Ruth}}^{\text{Ag}}(E_{\text{lab}} - \Delta_{\text{lab}}, \theta_{\text{lab}})/d\Omega_{\text{lab}}$  is the differential Rutherford cross section of protons scattered from Ag nuclei (eq. 4.9), and is calculated for  $E_{\text{lab}} - \Delta_{\text{lab}}$  which corresponds to the proton beam energy that enters the Ag layer after crossing the LiF film.

The values of  $N_{7\text{Li}}$  and  $N_{\text{Ag}}$  were determined in section 4.2.1, and the ratio  $r$  is then

$$r = \frac{N_{7\text{Li}}}{N_{\text{Ag}}} \Rightarrow r = \frac{(6.14 \pm 0.25) \times 10^{17} \text{at/cm}^2}{5.92 \times 10^{17} \text{at/cm}^2} = 1.04 \pm 0.04 . \quad (5.35)$$

So, eqs. 5.33 and 5.34 give the same quantity, *i.e.*, the  ${}^7\text{Li}(p,\alpha){}^4\text{He}$  reaction differential cross section, which is computed in the energy interval  $E_{\text{lab}} = 943$  keV to 1405 keV ( $E = 824$  keV to 1228 keV in the center-of-mass frame), in a total of 10 data points. Comparing the results of both equations we get the following relation

$$\left. \frac{d\sigma(E_{\text{lab}}, \theta_{\text{lab}})}{d\Omega_{\text{lab}}} \right|_{\text{eq. 5.34}} = (1.01 \pm 0.04) \left. \frac{d\sigma(E_{\text{lab}}, \theta_{\text{lab}})}{d\Omega_{\text{lab}}} \right|_{\text{eq. 5.33}} , \quad (5.36)$$

indicating that the product  $N_p \Omega_{\text{lab}}$  was quite well measured, and with an uncertainty of 4%. Despite its negligible normalizing effect, this correction factor was included in the calculus of the astrophysical  $S$ -factor, and its uncertainty entered the calculation of the  $S$ -factor associated uncertainty:

$$\left[ \frac{\partial S(E)}{\partial(N_p \Omega_{\text{lab}})} \right]^2 = \left( \frac{S(E)}{1.01} \right)^2 \quad (5.37)$$

$$\left[ \delta(N_p \Omega_{\text{lab}}) \right]^2 = 0.04^2 \quad (5.38)$$

As this uncertainty is related to the procedure used to obtain the value of  $N_{7\text{Li}}$  for the LiF-Ag target, the corresponding uncertainties in  $N_{7\text{Li}}$  for the other targets must also be included when analysing their respective data. So, we have

$$\left[ \delta(N_p \Omega_{\text{lab}}) \right]^2 = 0.05^2 \quad \text{and} \quad \left[ \delta(N_p \Omega_{\text{lab}}) \right]^2 = 0.06^2, \quad (5.39)$$

respectively for the LiF-Cu and the  $^7\text{Li}$  implanted in Al targets.

2. for each run,  $j$ , the ratio  $[N(E_0, \theta_{\text{lab}})/N_p]_j$  has associated a statistical uncertainty:

$$\delta[N(E_0, \theta_{\text{lab}})/N_p]_j = [\sqrt{N(E_0, \theta_{\text{lab}})/N_p}]_j, \quad (5.40)$$

where  $N_p$  value is assumed precise, since its uncertainty was already taken into account (as described above). Since several runs were done, repeating the same energies, we get for each energy an average value  $N(E_0, \theta_{\text{lab}})/N_p$  given by:

$$N(E_0, \theta_{\text{lab}})/N_p = \frac{\sum_{j=1}^n [N(E_0, \theta_{\text{lab}})/N_p]_j}{n}, \quad (5.41)$$

where  $n$  is the number of runs. The associated uncertainty is defined as

$$\delta N(E_0, \theta_{\text{lab}})/N_p = \max(\delta N_i, \delta N_e), \quad (5.42)$$

where  $\delta N_i$  is the internal uncertainty and  $\delta N_e$  is the external uncertainty of the measured points, and are defined generically as:

$$\delta N_i = \left[ \sum_{j=1}^n \frac{1}{y_j^2} \right]^{-1/2} \quad (5.43)$$

$$\delta N_e = \left[ \frac{\sum_{j=1}^n (y - y_j)^2 (1/\delta y_j)^2}{(n-1) \sum_{j=1}^n (1/\delta y_j)^2} \right]^{1/2}. \quad (5.44)$$

where the variable  $y$  stands for  $N(E_0, \theta_{\text{lab}})/N_p$ .

So, we have,

$$\left[ \frac{\partial S(E)}{\partial N(E_0, \theta_{\text{lab}})/N_p} \right]^2 = \left( \frac{S(E)}{N(E_0, \theta_{\text{lab}})/N_p} \right)^2 \quad (5.45)$$

$$\left[ \delta N(E_0, \theta_{\text{lab}})/N_p \right]^2 = [\max(\delta N_i, \delta N_e)]^2 \quad (5.46)$$

- the uncertainty in SRIM2003 tables [79] of stopping cross sections for a given element is  $\approx 5\%$ , which propagates into an identical uncertainty for  $\epsilon_{\text{eff}}(E)$ . This uncertainty affects not only the  $S(E)$  factor but also the effective energy,  $E$  (from eq. 5.4). Assuming that Bragg's rule and the CAB-model are correct, the  $\epsilon_{\text{eff}}(E)$  5% uncertainty effect on  $E$  and  $S(E)$  is evaluated by calculating these two quantities for  $\epsilon'_{\text{eff}}(E) = 0.95\epsilon_{\text{eff}}(E)$  and  $\epsilon'_{\text{eff}}(E) = 1.05\epsilon_{\text{eff}}(E)$ ,  $E_d$  and  $S_d(E_d)$ , and  $E_u$  and  $S_u(E_u)$ , respectively. Tables 5.1 and 5.2 show the results of this exercise for the  ${}^7\text{Li}(p,\alpha){}^4\text{He}$  reaction (with the  ${}^7\text{Li}$  implanted target) and for  ${}^6\text{Li}(p,\alpha){}^3\text{He}$  reaction (with the LiF-Cu target), respectively. From here we conclude that the 5% variation produces very small energy variations, which decrease with increasing energy; the effect of this uncertainty is negligible for the determination of  $S(E)$  in the energy ranges studied. Variations in  $S(E)$  are also small, and also decrease with increasing energy. For each energy, the relative uncertainty in  $S(E)$  was considered in the final uncertainty estimation.
- The uncertainty associated to the measurement of the angular distributions,  $W(E, \theta)$ , comes from the polynomial fits to the  $A_2(E)$  coefficient for the  ${}^7\text{Li}(p,\alpha){}^4\text{He}$  reaction and to the  $A_1(E)$  coefficient for the  ${}^6\text{Li}(p,\alpha){}^3\text{He}$  reaction. With respect to the  ${}^7\text{Li}$  reaction we have,

$$\begin{aligned} \left[ \delta W(E, \theta) \right]^2 &= \left[ \frac{dW(E, \theta)}{dA_2(E)} \right]^2 \left[ \delta A_2(E) \right]^2 \\ \left[ \delta A_2(E) \right]^2 &= \sum_{i=1}^5 \left[ \frac{\partial A_2(E)}{\partial P_i} \right]^2 (\delta P_i)^2, \end{aligned} \quad (5.47)$$

where  $P_i$  are the polynomial coefficients whose uncertainties are plotted in fig. 5.6 and listed in Appendix B. The relative uncertainty in  $S(E)$  obtained from eq. 5.47 is extremely small, below 0.2%, and decrease with decreasing energy. A similar behaviour is observed for the  ${}^6\text{Li}(p,\alpha){}^3\text{He}$  reaction.

$E$ (keV)	$S(E)$ (keV b)	$E_d$ (keV)	$S_d(E_d)$ (keV b)	$E_u$ (keV)	$S_u(E_u)$ (keV b)	$\frac{E}{E_{d(u)}}$	$\frac{S(E)}{S_{d(u)}(E_{d(u)})}$
89.71	77.37	89.79	74.60	89.65	80.19	1.001	1.037
95.09	75.10	95.21	72.59	94.99	77.67	1.001	1.035
115.83	72.65	116.22	70.82	115.50	74.53	1.003	1.026
125.83	74.02	126.33	72.40	125.37	75.68	1.004	1.022
136.52	71.63	137.14	70.28	135.95	73.02	1.005	1.019
147.91	74.52	148.62	73.31	147.25	75.76	1.005	1.017
159.98	78.17	160.76	77.09	159.23	79.29	1.005	1.014
172.66	80.94	173.48	79.98	171.85	81.93	1.005	1.012
185.91	81.17	186.76	80.34	185.07	82.02	1.005	1.010
199.69	85.47	200.57	84.72	198.83	86.24	1.004	1.009
213.98	80.29	214.87	79.68	213.11	80.90	1.004	1.008
228.75	80.96	229.63	80.43	227.87	81.49	1.004	1.007
244.05	82.78	244.93	82.31	243.18	83.26	1.004	1.006
259.72	84.45	260.59	84.03	258.86	84.87	1.003	1.005
275.87	84.93	276.73	84.57	275.02	85.30	1.003	1.004
292.44	84.17	293.28	83.86	291.60	84.49	1.003	1.004
309.42	90.22	310.25	89.92	308.60	90.52	1.003	1.003
318.81	88.34	319.63	88.07	318.00	88.61	1.003	1.003
344.71	86.76	345.50	86.54	343.92	86.98	1.002	1.003
352.50	88.64	353.29	88.43	351.72	88.85	1.002	1.002
381.71	89.60	382.47	89.42	380.96	89.78	1.002	1.002
387.58	89.43	388.33	89.26	386.83	89.61	1.002	1.002
424.33	87.20	425.05	87.07	423.62	87.34	1.002	1.002
462.45	87.58	463.13	87.48	461.77	87.69	1.001	1.001
502.13	92.74	502.78	92.65	501.49	92.83	1.001	1.001
543.28	95.75	543.89	95.68	542.67	95.83	1.001	1.001
586.00	94.86	586.58	94.80	585.41	94.92	1.001	1.001
630.12	96.55	630.67	96.50	629.56	96.60	1.001	1.001
675.65	97.76	676.18	97.72	675.11	97.80	1.001	1.000
722.64	100.08	723.15	100.05	722.13	100.12	1.001	1.000
746.72	99.22	747.23	99.19	746.22	99.25	1.001	1.000
772.11	102.02	772.60	101.99	771.61	102.05	1.001	1.000

Table 5.1:  ${}^7\text{Li}(p,\alpha){}^4\text{He}$  reaction:  $\epsilon_{\text{eff}}(E)$  5% variation effects on  $E$  and  $S(E)$  for the  ${}^7\text{Li}$  implanted target, and  $\theta_{\text{lab}} = 124^\circ$  (see details in text).

$E$ (keV)	$S(E)$ (MeV b)	$E_d$ (keV)	$S_d(E_d)$ (MeV b)	$E_u$ (keV)	$S_u(E_u)$ (MeV b)	$\frac{E}{E_{d(u)}}$	$\frac{S(E)}{S_{d(u)}(E_{d(u)})}$
90.46	3.27	90.75	3.21	90.17	3.33	1.003	1.018
99.04	3.23	99.36	3.18	98.73	3.28	1.003	1.016
108.06	3.01	108.40	2.97	107.72	3.05	1.003	1.013
117.51	3.11	117.86	3.07	117.16	3.14	1.003	1.011
127.39	3.09	127.76	3.06	127.03	3.12	1.003	1.010
137.67	3.01	138.05	2.99	137.31	3.04	1.003	1.008
159.47	2.93	159.85	2.91	159.10	2.95	1.002	1.006
182.83	2.86	183.21	2.85	182.46	2.87	1.002	1.005
207.72	2.76	208.08	2.75	207.36	2.77	1.002	1.003
234.13	2.65	234.48	2.65	233.77	2.66	1.002	1.003
262.05	2.64	262.39	2.63	261.71	2.64	1.001	1.002
291.44	2.63	291.77	2.63	291.11	2.64	1.001	1.001
322.31	2.41	322.63	2.40	322.00	2.41	1.001	1.001
354.67	2.37	354.97	2.36	354.37	2.37	1.001	1.001
388.51	2.41	388.80	2.41	388.22	2.41	1.001	1.001
423.84	2.29	424.11	2.29	423.56	2.29	1.001	1.001
460.64	2.16	460.90	2.16	460.37	2.17	1.001	1.000
498.92	2.27	499.17	2.27	498.66	2.27	1.001	1.000
538.67	2.07	538.91	2.07	538.43	2.07	1.000	1.000
579.91	2.05	580.14	2.05	579.68	2.05	1.000	1.000

Table 5.2:  ${}^6\text{Li}(p,\alpha){}^3\text{He}$  reaction:  $\epsilon_{\text{eff}}(E)$  5% variation effects on  $E$  and  $S(E)$  for the LiF-Cu target, and  $\theta_{\text{lab}} = 124^\circ$  (see details in text).

A possible uncertainty associated to an error in the angular position,  $\theta$ , of the Si detectors was neglected since they were mechanically positioned with a precision around  $1^\circ$ .

## Differential method

The quoted uncertainty for  $S(E)$  arises only from one source:

$$\delta S(E) = \left[ \frac{\partial S(E)}{\partial N(E_0, \theta_{\text{lab}})/N_p} \right] \left[ \delta N(E_0, \theta_{\text{lab}})/N_p \right], \quad (5.48)$$

already defined by eqs. 5.43 to 5.46. The other sources of uncertainty are small when compared with this one. For instance, in the specific cases of Pd and Li, the stopping power cross sections for protons were measured for energies down to 20 keV and 40 keV, respectively, with very small uncertainties, 0.9% for Pd and 2.7% for Li [79].

## 5.2 Results for $S_b(E)$ and $U_e$

### 5.2.1 Integral method – $S_b(E)$

For energies above 90 keV there are still no electron screening effects and, as such, the  $S(E)$  values correspond to the bare component:  $S(E) = S_b(E)$ . The extracted values of  $S(E)$ , using the integral method, for the LiF-Ag, LiF-Cu and  $^7\text{Li}$  implanted in Al targets and corresponding uncertainties are plotted in figs. 5.9 to 5.11 [for the  $^7\text{Li}(p,\alpha)^4\text{He}$  reaction] and fig. 5.15 [for the  $^6\text{Li}(p,\alpha)^3\text{He}$  reaction]. Appendix D lists all values of  $S(E)$  plotted in these figures. The ITN setup used two Si detectors at two different angles, so for each target and for each energy measured there are two  $S(E)$  values, one for the Si detector at  $\theta_{\text{lab}} = 124^\circ$  and the other for the Si detector at  $\theta_{\text{lab}} = 145^\circ$ . The  $S(E)$  obtained for each target is then the average value:

$$S(E) = \frac{S(E, \theta_{\text{lab}} = 124^\circ) + S(E, \theta_{\text{lab}} = 145^\circ)}{2}, \quad (5.49)$$

and the corresponding uncertainty is

$$\delta S(E) = \max(\delta S_i, \delta S_e), \quad (5.50)$$

where  $\delta S_i$  is the internal uncertainty and  $\delta S_e$  is the external uncertainty, and have the same form as eqs. 5.43 and 5.44:

$$\delta S_i = \left[ \frac{1}{[\delta S(E, \theta_{\text{lab}} = 124^\circ)]^2} + \frac{1}{[\delta S(E, \theta_{\text{lab}} = 145^\circ)]^2} \right]^{-1/2} \quad (5.51)$$

$$\delta S_e = \left[ \frac{\left( \frac{S(E) - S(E, \theta_{\text{lab}} = 124^\circ)}{\delta S(E, \theta_{\text{lab}} = 124^\circ)} \right)^2 + \left( \frac{S(E) - S(E, \theta_{\text{lab}} = 145^\circ)}{\delta S(E, \theta_{\text{lab}} = 145^\circ)} \right)^2}{[\delta S(E, \theta_{\text{lab}} = 124^\circ)]^2 + [\delta S(E, \theta_{\text{lab}} = 145^\circ)]^2} \right]^{1/2} \quad (5.52)$$

The  ${}^7\text{Li}(p, \alpha){}^4\text{He}$  reaction  $S$ -factor was measured using the LiF-Ag, LiF-Cu and  ${}^7\text{Li}$  implanted in Al targets. The values of the three  $S(E)$  data sets are in excellent agreement in the overlapping energy regions, as shown in fig. 5.12. These data sets were merged, producing a final data set for the  ${}^7\text{Li}$  reaction with 94 energy points (when the energy difference between consecutive data points was below  $\approx 2$  keV, they were averaged applying the same procedure of eqs. 5.50, 5.51 and 5.52), which are plotted in fig. 5.13 and listed in table 5.3 (the quoted uncertainties correspond to one standard deviation). The comparison of our data with previous works shows that this work has smaller error bars derived essentially from a more careful error analysis. Our data is in excellent agreement with Rolfs and Kavanagh [60] data (red circles of fig. 5.14) for energies above  $\approx 400$  keV. Below this energy, our data is consistently below by  $\approx 5\%$ , even though both data sets are compatible within errors (data from other authors are not conclusive). This difference can not be justified by an experimental error, as charge collection or target deterioration, since for the  ${}^6\text{Li}(p, \alpha){}^3\text{He}$  reaction, which was measured concurrently with the  ${}^7\text{Li}(p, \alpha){}^4\text{He}$  reaction, there is very good agreement with available data from other authors, as shown in fig. 5.16.

The  ${}^6\text{Li}(p, \alpha){}^3\text{He}$  reaction  $S$ -factor was measured using the LiF-Cu target, in a total of 20 energy points which are plotted in fig. 5.16 and listed in table 5.4 (the quoted uncertainties correspond to one standard deviation). As already mentioned, our data is in very good agreement with previous data, defining more precisely the energy region between 90 keV and 580 keV.

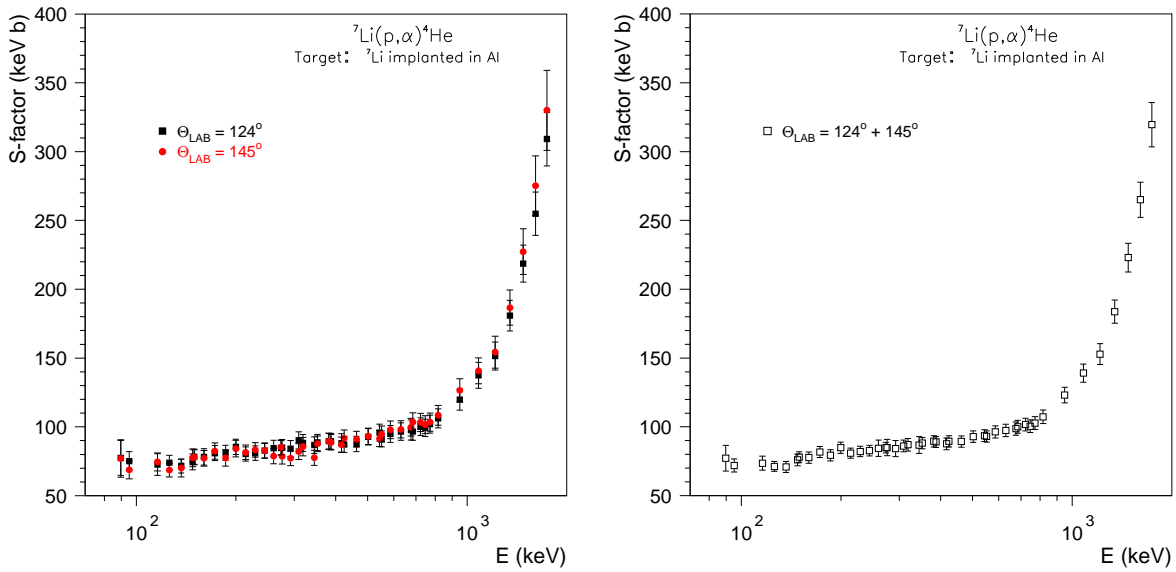


Figure 5.9: Left panel: The  $S$ -factor for the  ${}^7\text{Li}(p,\alpha){}^4\text{He}$  as a function of  ${}^7\text{Li} + p$  c.m. energy, measured for the  ${}^7\text{Li}$  implanted in Al target at  $124^\circ$  (black squares) and  $145^\circ$  (red circles). Right panel: Averaged  $S(E)$  values obtained from the two Si detectors (see text for details).

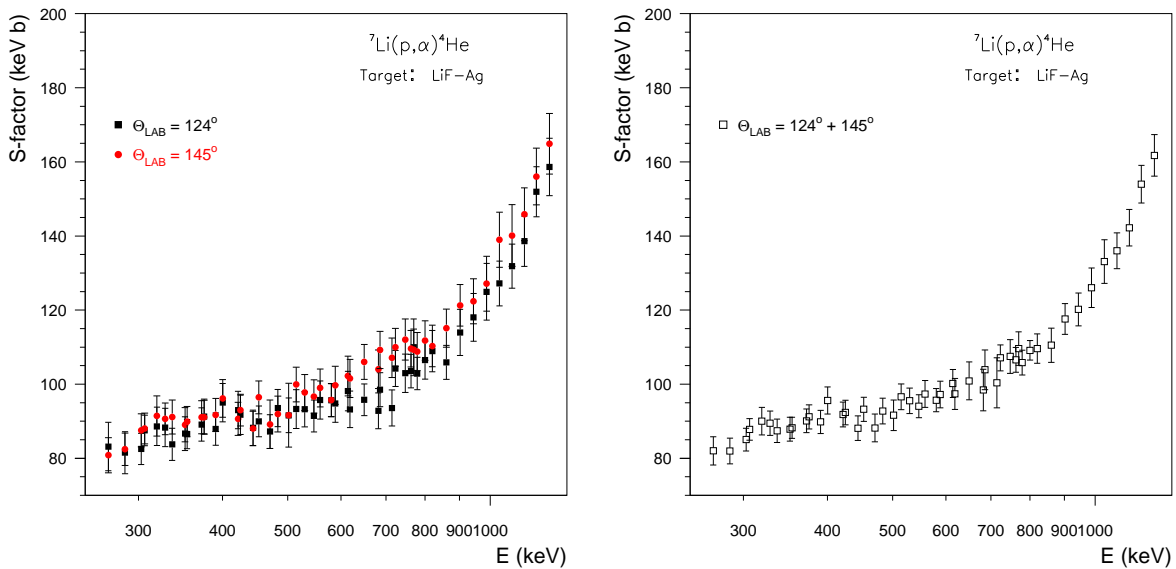


Figure 5.10: Left panel: The  $S$ -factor for the  ${}^7\text{Li}(p,\alpha){}^4\text{He}$  as a function of  ${}^7\text{Li} + p$  c.m. energy, measured for the LiF-Ag target at  $124^\circ$  (black squares) and  $145^\circ$  (red circles). Right panel: Averaged  $S(E)$  values obtained from the two Si detectors (see text for details).

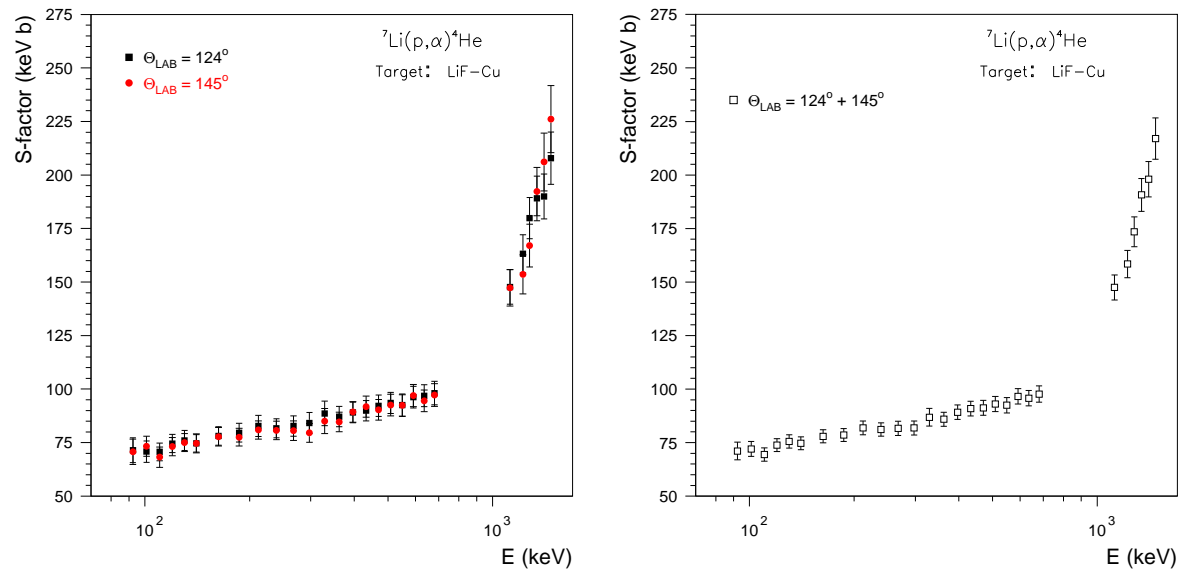


Figure 5.11: Left panel: The  $S$ -factor for the  ${}^7\text{Li}(p,\alpha){}^4\text{He}$  as a function of  ${}^7\text{Li} + p$  c.m. energy, measured for the LiF-Cu target at  $124^\circ$  (black squares) and  $145^\circ$  (red circles). Right panel: Averaged  $S(E)$  values obtained from the two Si detectors (see text for details).

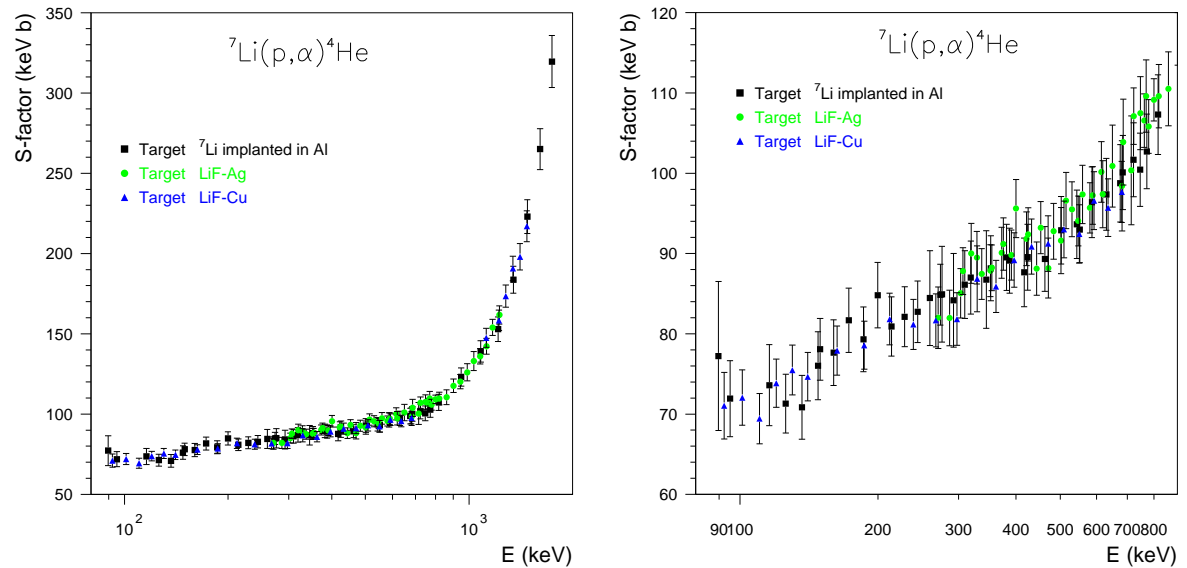


Figure 5.12: Left panel: Astrophysical  $S(E)$  factor of  ${}^7\text{Li}(p,\alpha){}^4\text{He}$  obtained using all targets. Right panel: Same plot zoomed over the energy interval below 900 keV.

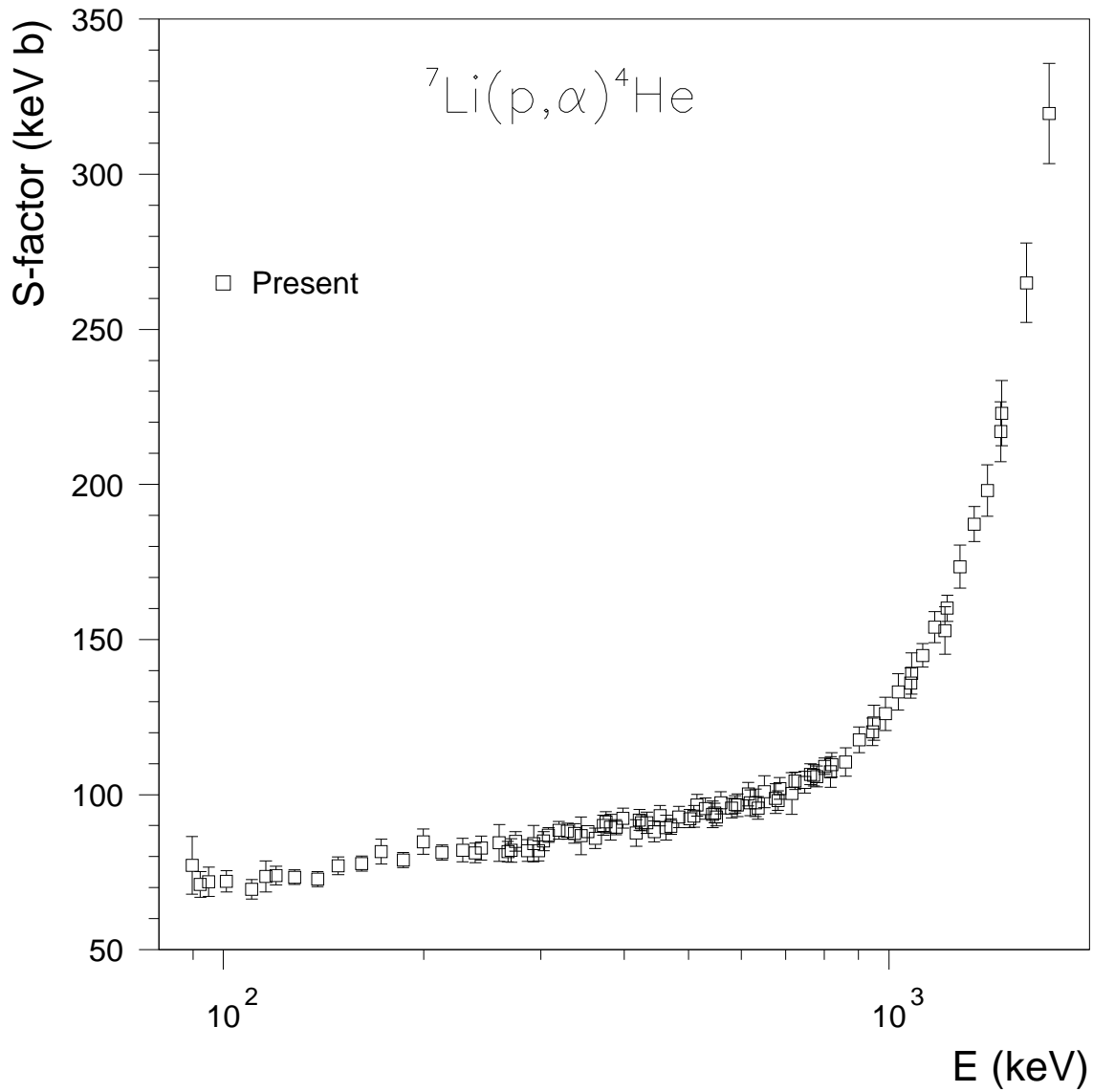


Figure 5.13: Same plot of fig. 5.12, without distinction of target and with a few data points merged (see text for details).

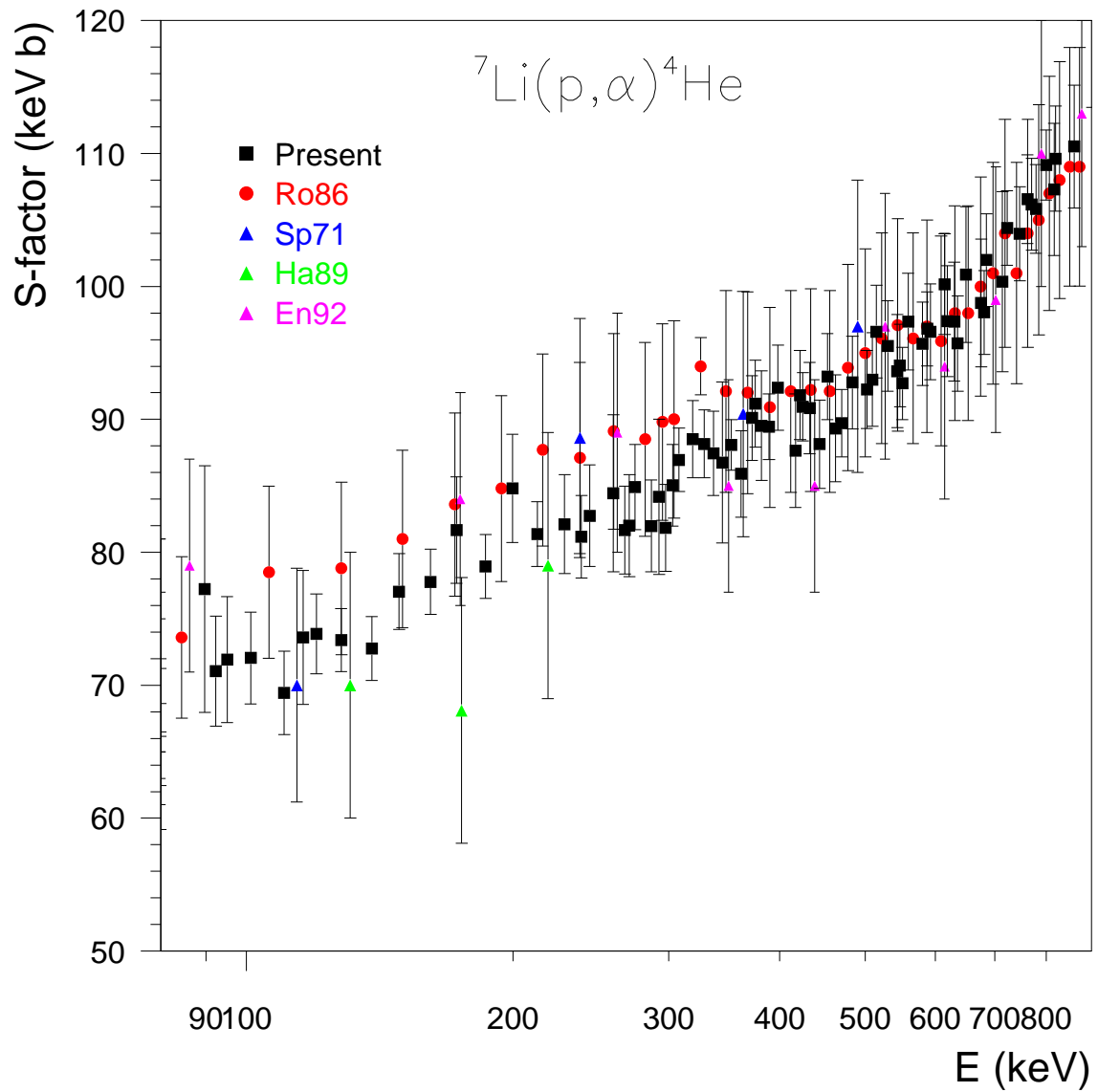


Figure 5.14: The  $S$ -factor for the  ${}^7\text{Li}(p, \alpha){}^4\text{He}$  as a function of  ${}^7\text{Li} + p$  c.m. energy. The experimental points are from the present work (black squares), from Rolfs and Kavanagh [60] (red circles), Spinka *et al.* [59] (blue triangles), Harmon *et al.* [84] (green triangles) and Engstler *et al.* [50] (pink triangles).

${}^7\text{Li}(p,\alpha){}^4\text{He}$					
$E$	$S(E)$	$\delta S(E)$	$E$	$S(E)$	$\delta S(E)$
(keV)	(keV b)	(keV b)	(keV)	(keV b)	(keV b)
89.7	77.23	9.28	502.0	92.26	2.94
92.4	71.05	4.14	509.3	93.00	3.53
95.1	71.92	4.73	514.8	96.60	3.49
101.1	72.05	3.45	530.0	95.51	3.41
110.3	69.43	3.13	543.3	93.63	4.26
115.8	73.60	5.04	547.1	94.06	3.11
120.0	73.85	3.00	550.6	92.71	2.72
127.9	73.39	2.37	558.9	97.35	3.63
138.5	72.76	2.41	580.5	95.69	3.14
148.7	77.04	2.85	587.2	96.81	2.79
161.4	77.78	2.45	592.0	96.58	3.60
172.7	81.68	4.00	614.6	100.17	3.78
186.3	78.94	2.40	618.9	97.38	4.17
199.7	84.81	4.08	630.1	97.37	4.47
213.0	81.37	2.43	635.6	95.71	3.59
228.8	82.12	3.73	649.9	100.90	5.11
239.0	81.17	3.11	675.6	98.75	4.81
244.0	82.75	3.83	681.3	98.05	3.15
259.7	84.45	5.91	685.2	101.98	3.49
267.5	81.67	3.31	714.4	100.36	6.77
270.6	82.00	3.84	722.8	104.40	2.80
274.7	84.90	3.20	747.3	103.97	3.53
286.5	81.98	3.46	762.4	106.56	3.33
292.4	84.17	5.84	770.9	106.17	3.45
297.4	81.84	3.27	779.3	105.83	3.34
302.8	85.05	3.07	800.2	109.14	2.64
307.9	86.96	2.40	817.1	107.30	4.96
319.2	88.51	2.89	820.2	109.61	3.95
328.9	88.16	2.56	860.8	110.52	4.61
336.7	87.45	3.16	902.2	117.62	4.16
344.7	86.76	6.07	944.5	120.20	4.43
352.9	88.08	1.89	949.4	123.15	5.67
362.1	85.90	3.25	988.0	126.03	5.31
372.4	90.10	3.18	1032.4	133.08	5.90
375.6	91.18	3.27	1077.7	135.99	4.83
381.7	89.53	4.12	1081.4	139.06	6.64
389.2	89.46	2.47	1123.0	144.86	3.77
398.4	92.39	3.21	1171.5	153.98	5.06
417.0	87.65	4.27	1214.3	152.86	7.64
421.9	91.83	3.35	1223.6	160.08	4.22
424.9	90.95	2.58	1278.4	173.47	6.95
432.7	90.86	3.44	1343.3	187.21	5.66
444.0	88.13	3.32	1405.7	198.02	8.26
453.0	93.22	3.24	1471.7	216.99	9.63
462.4	89.33	4.03	1477.1	222.98	10.46
470.4	89.71	2.54	1608.7	265.03	12.78
483.4	92.77	3.48	1740.3	319.57	16.15

Table 5.3:  $S$ -factor data for the  ${}^7\text{Li}(p,\alpha){}^4\text{He}$  reaction. The quoted uncertainties correspond to one standard deviation.

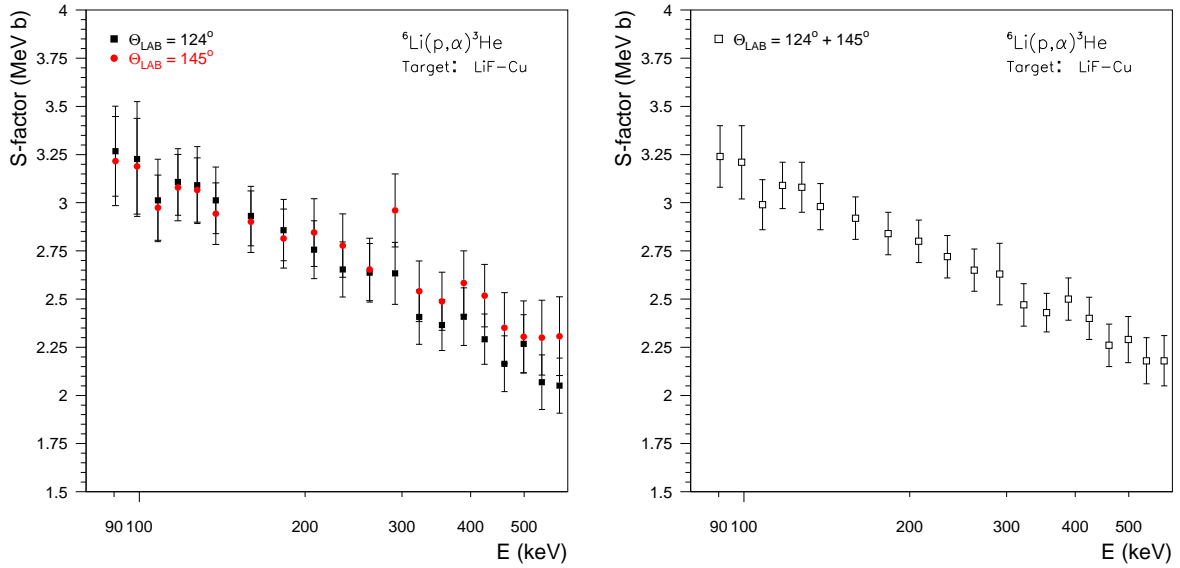


Figure 5.15: Left panel: The  $S$ -factor for the  ${}^6\text{Li}(p,\alpha){}^3\text{He}$  as a function of  ${}^6\text{Li} + p$  c.m. energy, measured for the LiF-Cu target at  $124^\circ$  (black squares) and  $145^\circ$  (red circles). Right panel: Averaged  $S(E)$  values obtained from the two Si detectors (see text for details). The value of  $S(E = 291.4 \text{ keV}, \theta_{\text{lab}} = 145^\circ)$  was not considered in the average process.

${}^6\text{Li}(p,\alpha){}^3\text{He}$					
$E$	$S(E)$	$\delta S(E)$	$E$	$S(E)$	$\delta S(E)$
(keV)	(MeV b)	(MeV b)	(keV)	(MeV b)	(MeV b)
90.5	3.24	0.16	262.0	2.65	0.11
99.0	3.21	0.19	291.4	2.63	0.16
108.1	2.99	0.13	322.3	2.47	0.11
117.5	3.09	0.12	354.7	2.43	0.10
127.4	3.08	0.13	388.5	2.50	0.11
137.7	2.98	0.12	423.8	2.40	0.11
159.5	2.92	0.11	460.6	2.26	0.11
182.8	2.84	0.11	498.9	2.29	0.12
207.7	2.80	0.11	538.7	2.18	0.12
234.1	2.72	0.11	579.9	2.18	0.13

Table 5.4:  $S$ -factor data for the  ${}^6\text{Li}(p,\alpha){}^3\text{He}$  reaction. The quoted uncertainties correspond to one standard deviation.

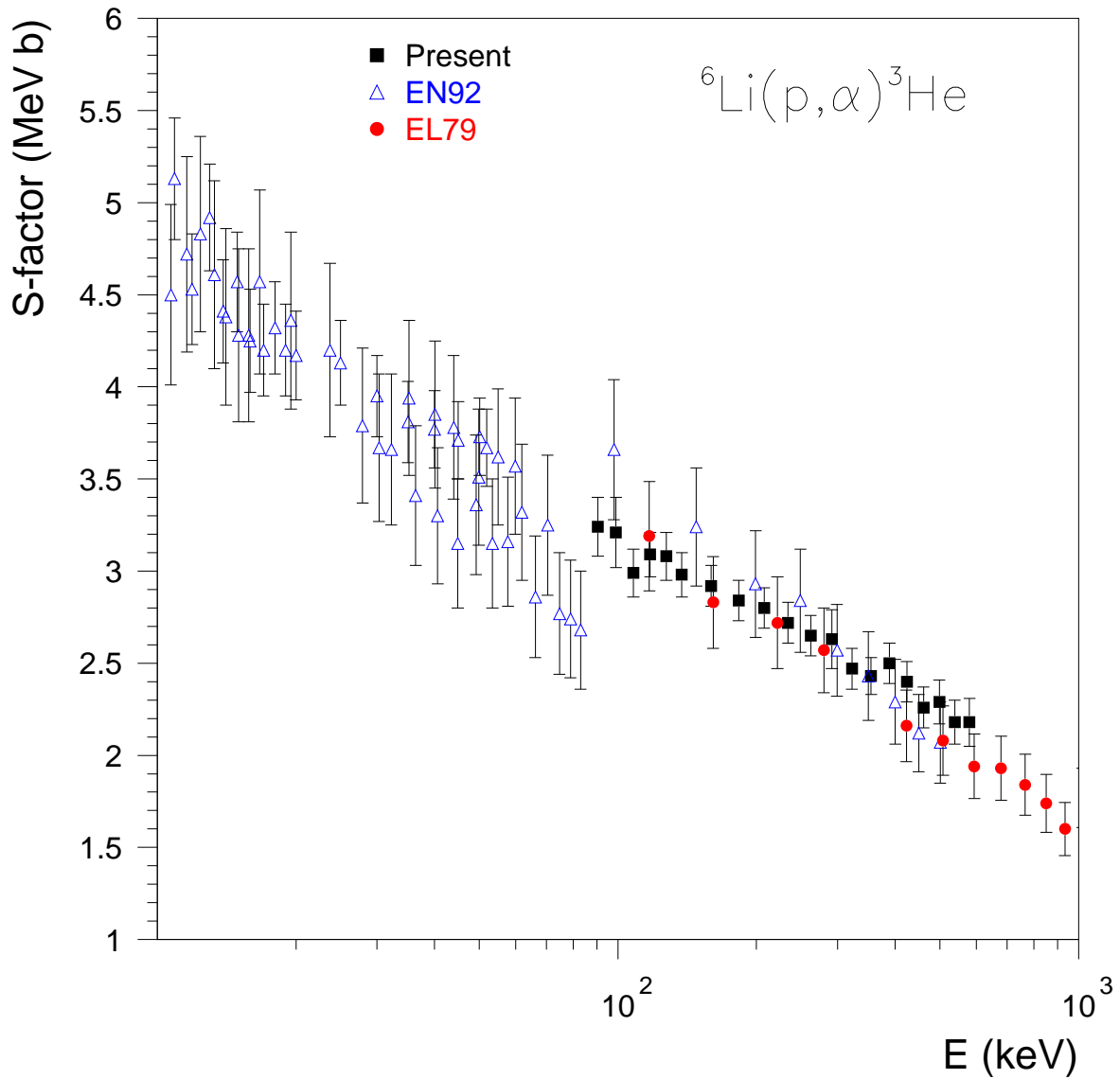


Figure 5.16: The  $S$ -factor for the  ${}^6\text{Li}(p, \alpha){}^3\text{He}$  as a function of  ${}^6\text{Li} + p$  c.m. energy. The experimental points are from the present work (black squares) and from Elwyn *et al.* [68] (red circles) and Engstler *et al.* [50] (blue triangles).

In order to reproduce the energy dependence of the astrophysical  $S$ -factor, the data points of tables 5.3 and 5.4 were  $\chi^2$  fitted with polynomial functions.

Concerning the  ${}^7\text{Li}(p,\alpha){}^4\text{He}$  reaction, it was assumed a third-order polynomial energy dependence for the  $S$ -factor

$$S(E) = S_b(E) = a + bE + cE^2 + dE^3, \quad (5.53)$$

with  $a$ ,  $b$ ,  $c$  and  $d$  as free parameters. Three different energy regions were considered, and the fit results are listed in table 5.5 and plotted in figs. 5.17, 5.18 and 5.19. From these results we conclude that the three fits are statistically equivalent, but the best-fit parameter values are sensitive to the fitted energy interval. As a consequence, we get different extrapolations to the low energy region:  $a = S_b(0)$  shows a 7% variation between different fits. These values are all within the broad range of values published in literature, though (see table 3.2). Due to its lack of physical meaning, polynomial fits, which are often used in literature, show problems for the  ${}^7\text{Li}(p,\alpha){}^4\text{He}$  reaction and are not very appropriate for accurate extrapolations. A more reliable extrapolation would require using the  $R$ -matrix approach or an hybrid-model approach (see Chap. 6).

Coefficient	89.7 < $E$ < 1740.3 (keV)	89.7 < $E$ < 902.2 (keV)	89.7 < $E$ < 714.4 (keV)
$a$ (keV b)	$63.6 \pm 1.8$	$59.7 \pm 1.3$	$59.4 \pm 1.5$
$b$ (b)	$(1.02 \pm 0.11) \times 10^{-1}$	$(1.38 \pm 0.08) \times 10^{-1}$	$(1.41 \pm 0.10) \times 10^{-1}$
$c$ (keV $^{-1}$ b)	$(-1.31 \pm 0.18) \times 10^{-4}$	$(-2.18 \pm 0.17) \times 10^{-4}$	$(-2.23 \pm 0.25) \times 10^{-4}$
$d$ (keV $^{-2}$ b)	$(9.12 \pm 0.84) \times 10^{-8}$	$(1.51 \pm 0.14) \times 10^{-7}$	$(1.53 \pm 0.26) \times 10^{-7}$
$\chi^2$	0.28	0.27	0.29

Table 5.5: Polynomial expansion  $S(E) = a + bE + cE^2 + dE^3$  fitted to the  ${}^7\text{Li}(p,\alpha){}^4\text{He}$  reaction  $S$ -factor for three different energy regions. The quoted uncertainties correspond to one standard deviation.

For the analysis that follows, we will adopt for  $S_b(E)$  the results obtained in the fit between 89.7 and 902.2 keV, since it has the wider fitted energy interval with stabilized best fit parameters.

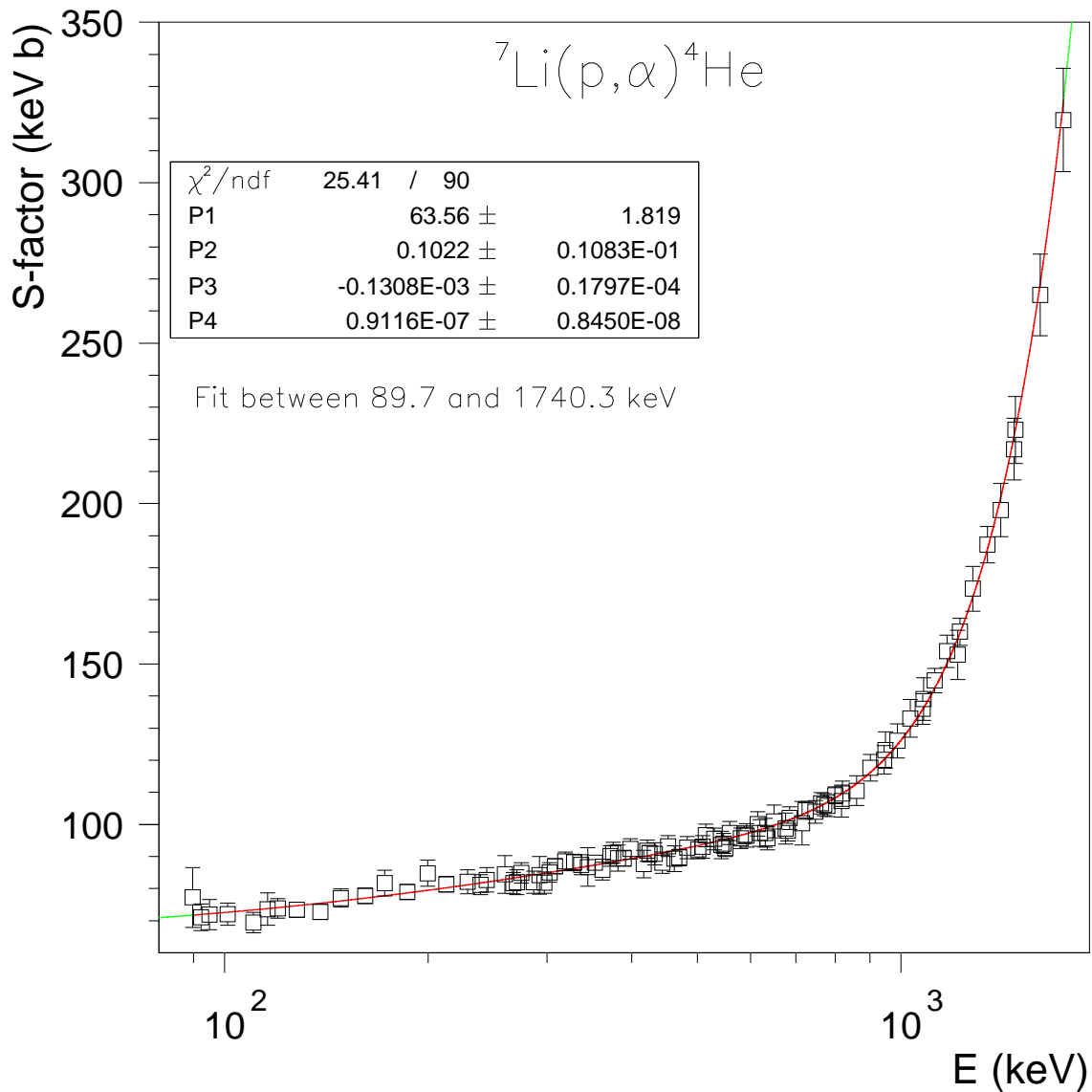


Figure 5.17: The  $S(E)$ -factor data for the  ${}^7\text{Li}(p, \alpha){}^4\text{He}$  reaction. The solid curve is a fit with a 3rd-order polynomial function (eq. 5.53). The red portion of the curve defines the fitted energy region ( $E$  between 89.7 and 1740.3 keV – full energy range), and the green portions correspond to the extrapolated curve. P1, P2, P3 and P4 correspond respectively to parameters  $a$ ,  $b$ ,  $c$  and  $d$  of eq. 5.53.

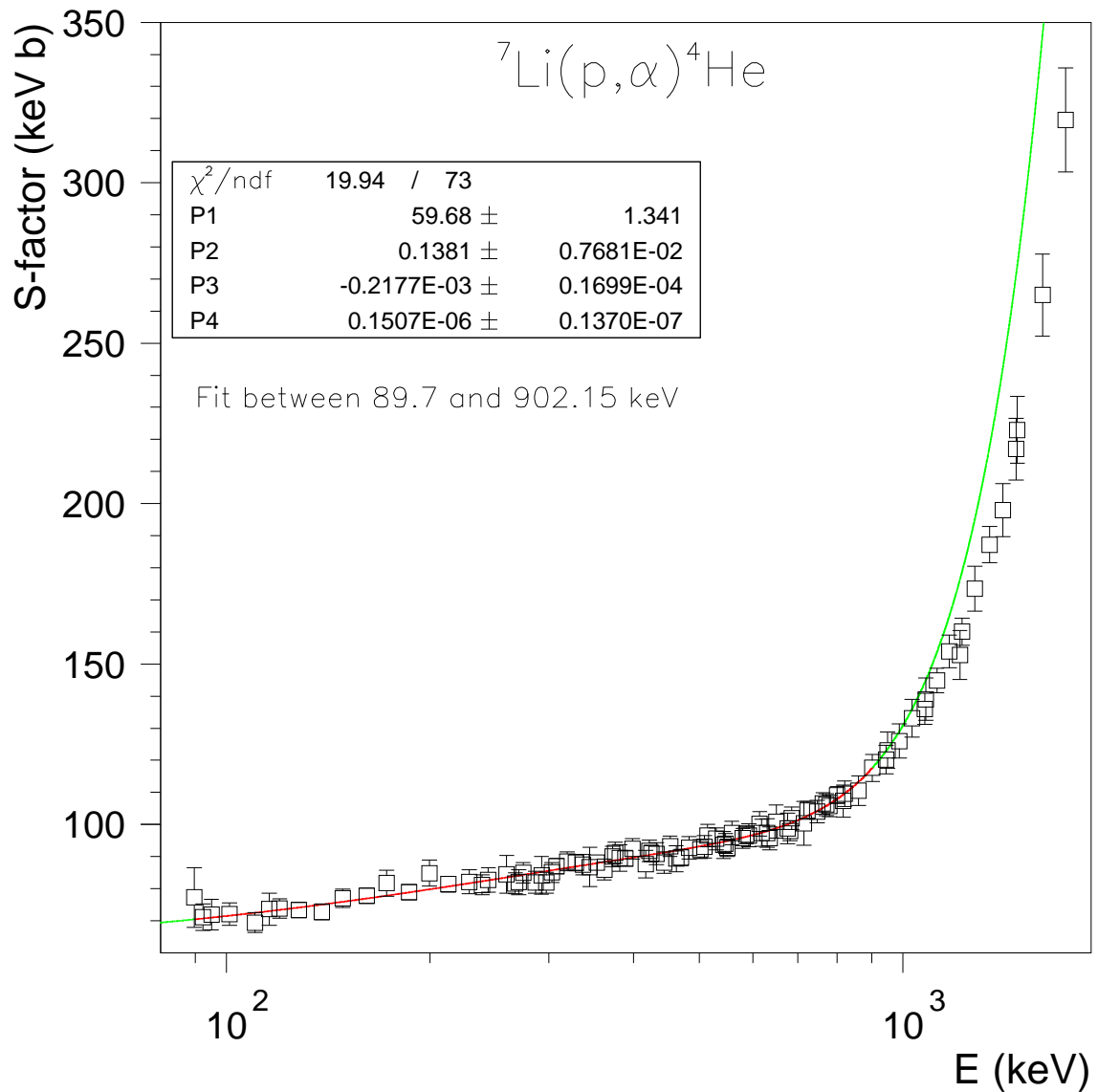


Figure 5.18: The  $S(E)$ -factor data for the  ${}^7\text{Li}(p, \alpha){}^4\text{He}$  reaction. The solid curve is a fit with a 3rd-order polynomial function (eq. 5.53). The red portion of the curve defines the fitted energy region ( $E$  between 89.7 and 902.2 keV), and the green portions correspond to the extrapolated curve. P1, P2, P3 and P4 correspond respectively to parameters  $a$ ,  $b$ ,  $c$  and  $d$  of eq. 5.53.

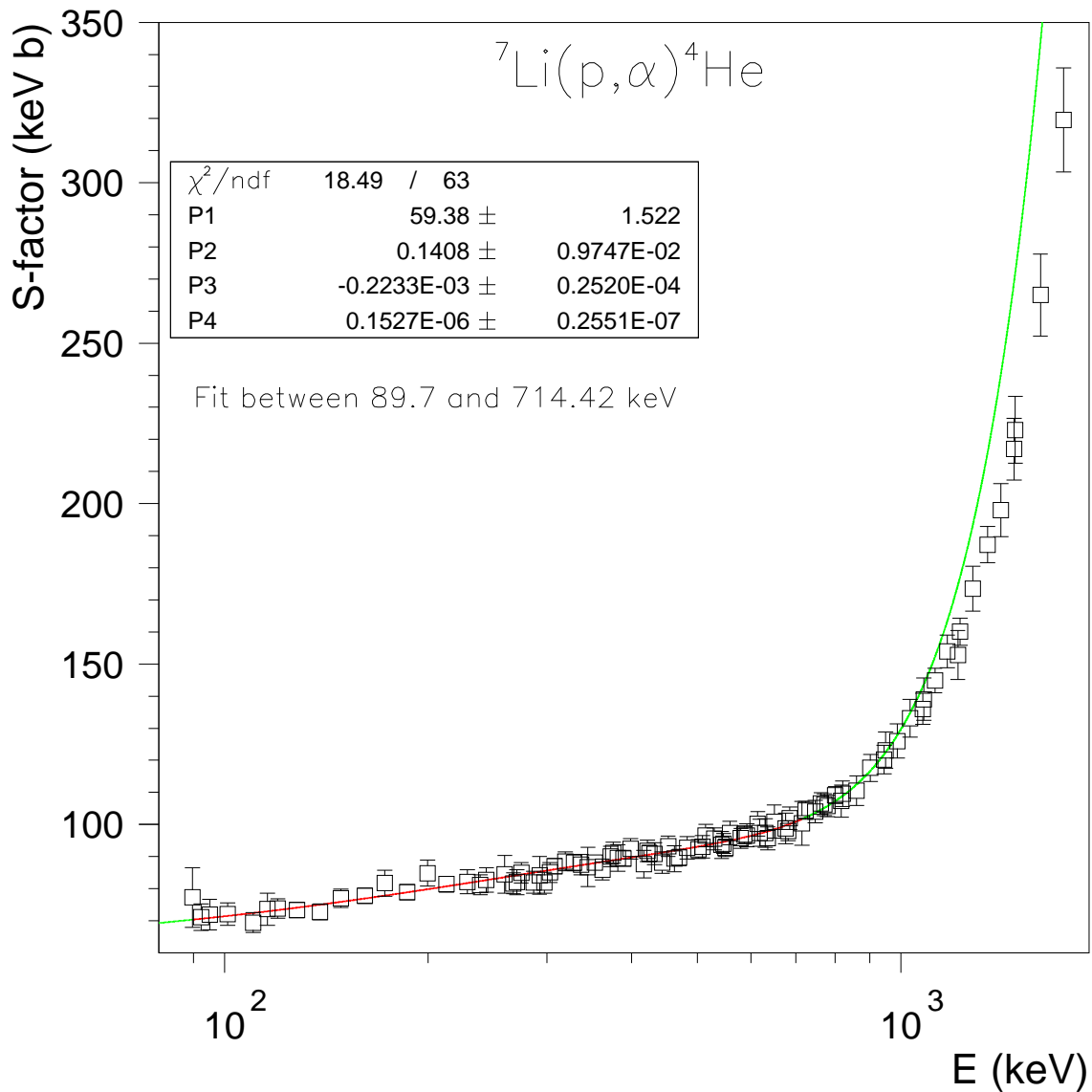


Figure 5.19: The  $S(E)$ -factor data for the  ${}^7\text{Li}(p, \alpha){}^4\text{He}$  reaction. The solid curve is a fit with a 3rd-order polynomial function (eq. 5.53). The red portion of the curve defines the fitted energy region ( $E$  between 89.7 and 714.4 keV), and the green portions correspond to the extrapolated curve. P1, P2, P3 and P4 correspond respectively to parameters  $a$ ,  $b$ ,  $c$  and  $d$  of eq. 5.53.

For the  ${}^6\text{Li}(p,\alpha){}^3\text{He}$  reaction, it was again assumed a polynomial energy dependence for the  $S$ -factor, defined by eq. 5.53. Two fits were performed, one considering only present work data and the other considering also Elwyn *et al.* (1979) data [68]. The fit results are listed in table 5.6 and plotted in figs. 5.20 and 5.21. From these results we conclude that the two fits are statistically equivalent. With the exception of parameter  $a = S_b(0)$ , the best-fit parameter values are very different in the two fits. However, the two curves, extrapolated to low energies, are very similar: 2.5% difference for  $E = 0$  keV. These values are all within the broad range of values published in literature (see table 3.3). For the analysis that follows, we will adopt the results of the combined fit, Present work plus EL79 data, since it uses more data points, a wider energy interval and the best fit parameters have smaller uncertainties. However, as in the  ${}^7\text{Li}(p,\alpha){}^4\text{He}$  case, caution must be applied when interpreting the extrapolations of the polynomial fits.

Coefficient	Present	Present + EL79
$a$ (MeV b)	$3.62 \pm 0.10$	$3.52 \pm 0.08$
$b$ (b)	$(-5.61 \pm 0.79) \times 10^{-3}$	$(-4.42 \pm 0.55) \times 10^{-3}$
$c$ (MeV $^{-1}$ b)	$(0.88 \pm 0.24) \times 10^{-5}$	$(0.49 \pm 0.12) \times 10^{-5}$
$d$ (MeV $^{-2}$ b)	$(-0.60 \pm 0.29) \times 10^{-8}$	$(-0.26 \pm 0.09) \times 10^{-8}$
$\chi^2$	0.18	0.23

Table 5.6: Polynomial expansion  $S(E) = a + bE + cE^2 + dE^3$  fitted to the  ${}^6\text{Li}(p,\alpha){}^3\text{He}$  reaction  $S$ -factor considering only present work data and considering also Elwyn *et al.* (1979) [68] data. The quoted uncertainties correspond to one standard deviation.

From the study at high energy of the  $S$ -factor corresponding to the  ${}^7\text{Li}(p,\alpha){}^4\text{He}$  and  ${}^6\text{Li}(p,\alpha){}^3\text{He}$  reactions, here described, we conclude that the smaller quoted uncertainties obtained in this work allows to define more accurately the bare  $S$ -factor. However, as our data are compatible within error bars with previous published data there are no significant astrophysical consequences drawn from this high energy study, e.g., primordial nucleosynthesis remains essentially unchanged: in Chapter 1 it was shown that the variation of  ${}^7\text{Li}(p,\alpha){}^4\text{He}$  cross section by two standard deviations would correspond to a change of around 9% in  ${}^7\text{Li}$  abundance. This means that the factor 3 discrepancy between SBBN+WMAP predictions and observations could only be removed by decreasing by  $\approx 20$  standard deviations the  ${}^7\text{Li}(p,\alpha){}^4\text{He}$  cross section at relevant

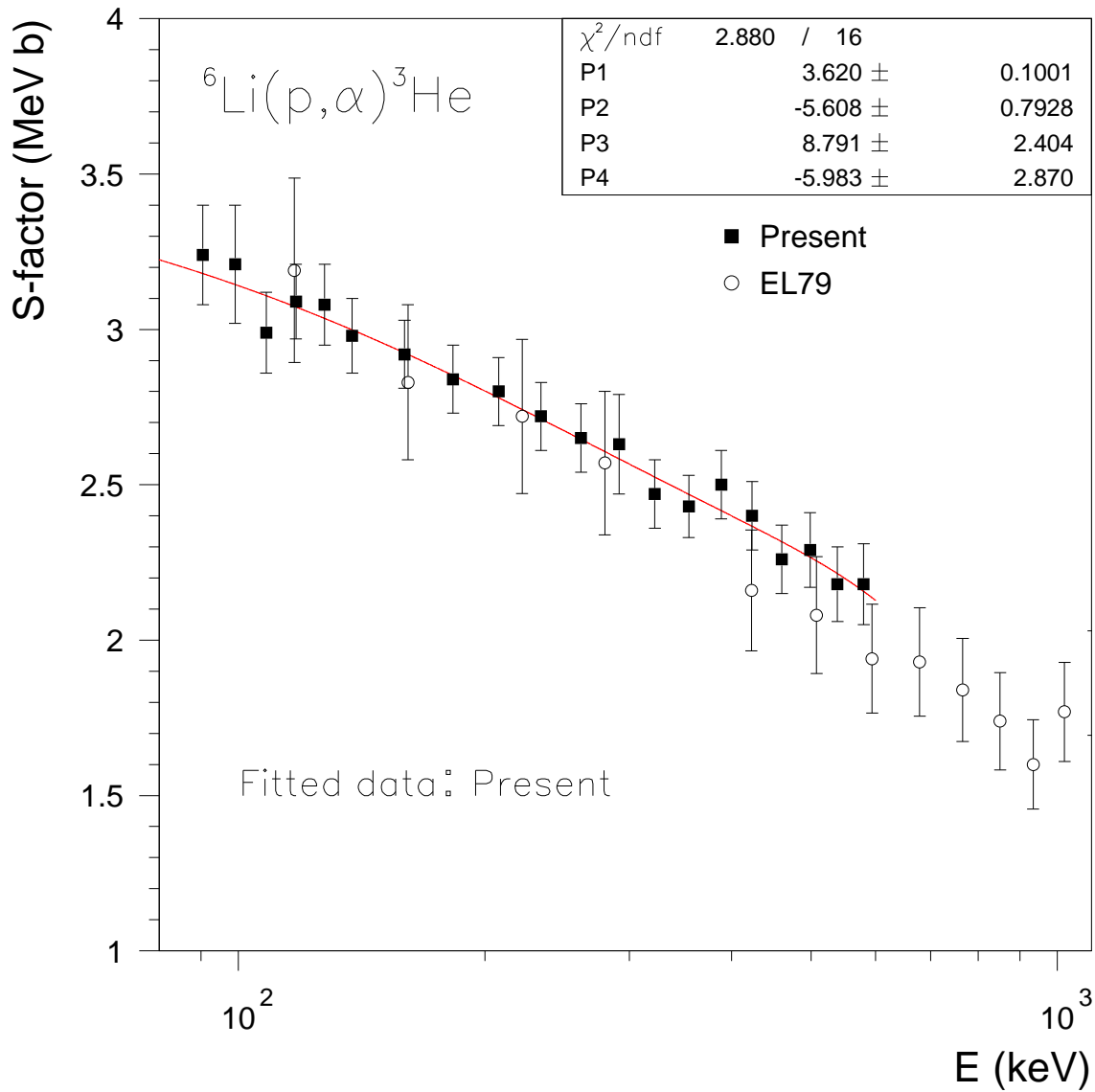


Figure 5.20: The  $S(E)$ -factor data for the  ${}^6\text{Li}(p, \alpha){}^3\text{He}$  reaction. The solid curve is a fit with a 3rd-order polynomial function (eq. 5.53) to data from present work (black squares). P1, P2, P3 and P4 correspond respectively to parameters  $a$ ,  $b$ ,  $c$  and  $d$  of eq. 5.53.

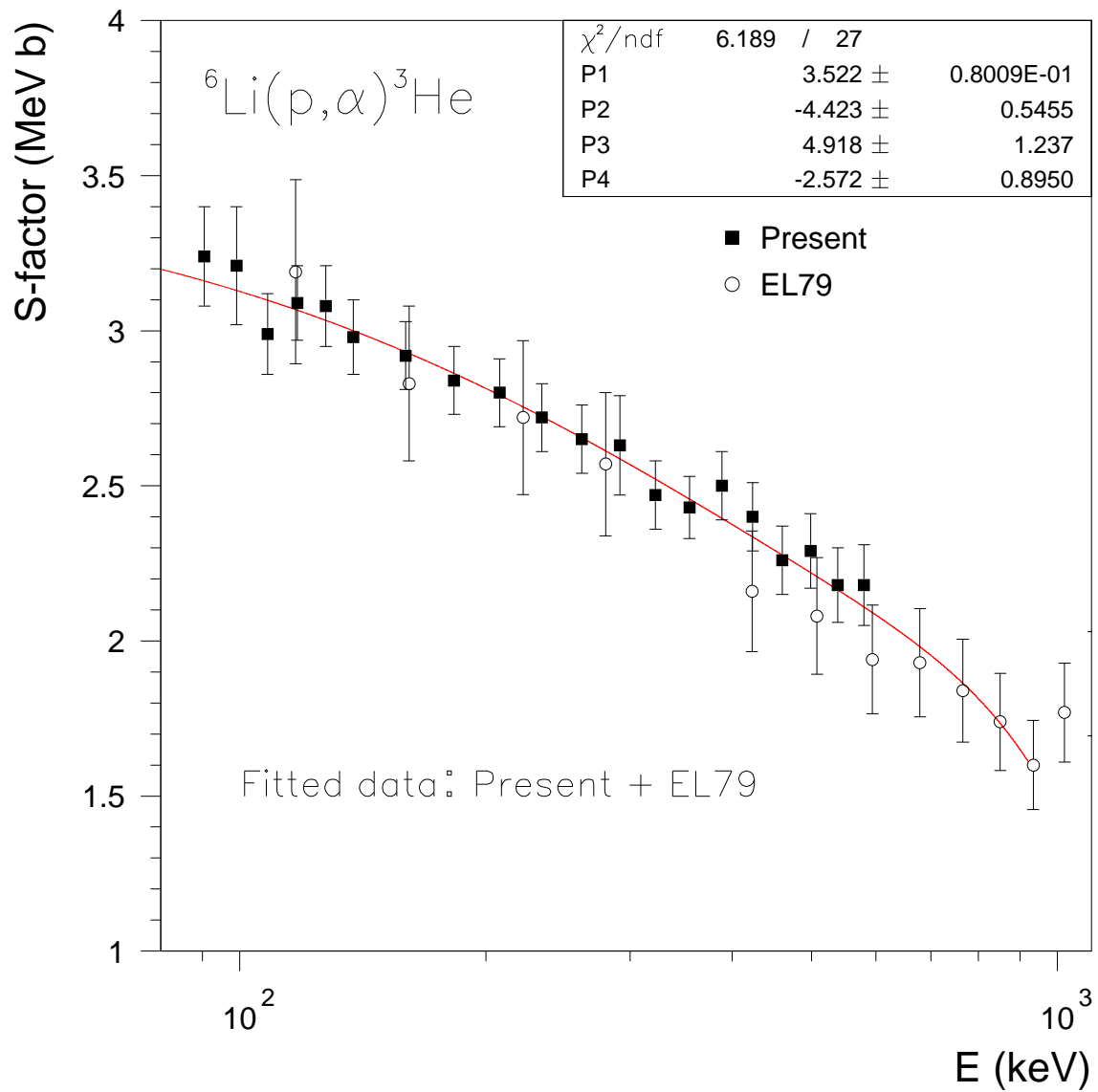


Figure 5.21: The  $S(E)$ -factor data for the  ${}^6\text{Li}(p, \alpha){}^3\text{He}$  reaction. The solid curve is a fit with a 3rd-order polynomial function (eq. 5.53) to data from present work (black squares) plus Elwyn *et al.* (1979) [68] data (open circles). P1, P2, P3 and P4 correspond respectively to parameters  $a$ ,  $b$ ,  $c$  and  $d$  of eq. 5.53.

energies ( $E < 100$  keV). From the high energy  $S(E)$  data, such drop is not feasible. This will be confirmed by the analysis of our low energy data, as described below.

## 5.2.2 Differential method – $U_e$

The extracted values of  $S(E)$  using the differential method, for the  $\text{Li}_2\text{WO}_4$  insulator, Li metal and  $\text{Pd}_{94.1\%}\text{Li}_{5.9\%}$  targets and corresponding uncertainties are listed in tables 5.7 and 5.8 for the  ${}^7\text{Li}(p,\alpha){}^4\text{He}$  and  ${}^6\text{Li}(p,\alpha){}^3\text{He}$  reactions, respectively.

For energies below 90 keV electron screening effects are no longer negligible and, as such, the  $S(E)$  data must be fitted with eq. 2.24:

$$\begin{aligned} S(E) &= C S_b(E) \frac{E}{E + U_e} \exp\left(\pi \eta(E) \frac{U_e}{E}\right) = \\ &= C S_b(E) \frac{E}{E + U_e} \exp\left[15.63 Z_{\text{Li}} Z_p \left(\frac{\mu}{E}\right)^{1/2} \frac{U_e}{E}\right], \end{aligned} \quad (5.54)$$

with  $C$  (a charge normalization factor) and  $U_e$  as free parameters, and where  $S_b(E)$  was defined in the previous section for both lithium reactions.

The fits results for the three targets are plotted in fig. 5.22 for the  ${}^7\text{Li}(p,\alpha){}^4\text{He}$  reaction, and fig. 5.23 for the  ${}^6\text{Li}(p,\alpha){}^3\text{He}$  reaction. The numerical values of the fits are listed in table 5.9.

In the next section we will show that the Debye model, which was successfully applied to the D(d,p)T reaction in metallic environments, can explain quite satisfactorily our data.

For the sake of clarity, the  $U_e$  values obtained from the fits to our  $S$ -factor data will be written as  $U_e^{exp}$ , and the  $U_e$  values calculated by the Debye model will be written as  $U_e^{th}$ .

Li <sub>2</sub> WO <sub>4</sub>			Li metal			Pd <sub>94.1%</sub> Li <sub>5.9%</sub>		
<i>E</i>	<i>S</i> ( <i>E</i> )	$\delta S$ ( <i>E</i> )	<i>E</i>	<i>S</i> ( <i>E</i> )	$\delta S$ ( <i>E</i> )	<i>E</i>	<i>S</i> ( <i>E</i> )	$\delta S$ ( <i>E</i> )
(keV)	(keV b)	(keV b)	(keV)	(keV b)	(keV b)	(keV)	(keV b)	(keV b)
29.0	64.2	2.0	24.7	81.3	4.1	32.0	130.7	5.6
33.2	66.1	2.6	28.9	83.4	1.2	40.4	110.4	6.1
40.6	65.6	1.0	33.2	81.1	1.3	49.0	104.7	4.8
49.0	66.4	1.2	40.6	73.8	0.7	57.5	97.5	4.8
57.6	67.3	0.9	49.1	73.4	0.5	66.0	86.1	6.6
66.1	69.4	1.6	57.6	73.9	0.6	74.6	78.3	6.5
74.7	68.4	1.4	66.2	72.8	0.4	83.3	74.6	4.2
			74.8	72.4	0.5			
			83.4	74.3	0.9			

Table 5.7: *S*-factor data for the  ${}^7\text{Li}(p,\alpha){}^4\text{He}$  reaction measured for *E* below 90 keV with the targets: Li<sub>2</sub>WO<sub>4</sub> insulator, Li metal and Pd<sub>94.1%</sub>Li<sub>5.9%</sub>. The quoted uncertainties correspond to one standard deviation.

Li <sub>2</sub> WO <sub>4</sub>			Li metal			Pd <sub>94.1%</sub> Li <sub>5.9%</sub>		
<i>E</i>	<i>S</i> ( <i>E</i> )	$\delta S$ ( <i>E</i> )	<i>E</i>	<i>S</i> ( <i>E</i> )	$\delta S$ ( <i>E</i> )	<i>E</i>	<i>S</i> ( <i>E</i> )	$\delta S$ ( <i>E</i> )
(keV)	(MeV b)	(MeV b)	(keV)	(MeV b)	(MeV b)	(keV)	(MeV b)	(MeV b)
28.3	3.58	0.08	24.2	5.06	0.14	31.3	7.45	0.23
32.5	3.69	0.10	28.3	4.64	0.11	39.6	6.00	0.21
39.8	3.52	0.10	32.5	4.61	0.09	47.9	5.13	0.15
48.0	3.45	0.05	39.7	4.02	0.04	56.3	4.81	0.18
56.4	3.34	0.05	48.0	3.81	0.03	64.6	3.98	0.22
64.8	3.32	0.06	56.4	3.69	0.02	73.1	3.51	0.29
73.2	3.26	0.04	64.8	3.50	0.04	81.6	3.61	0.22
			73.2	3.41	0.05			
			81.7	3.42	0.09			

Table 5.8: *S*-factor data for the  ${}^6\text{Li}(p,\alpha){}^3\text{He}$  reaction measured for *E* below 90 keV with the targets: Li<sub>2</sub>WO<sub>4</sub> insulator, Li metal and Pd<sub>94.1%</sub>Li<sub>5.9%</sub>. The quoted uncertainties correspond to one standard deviation.

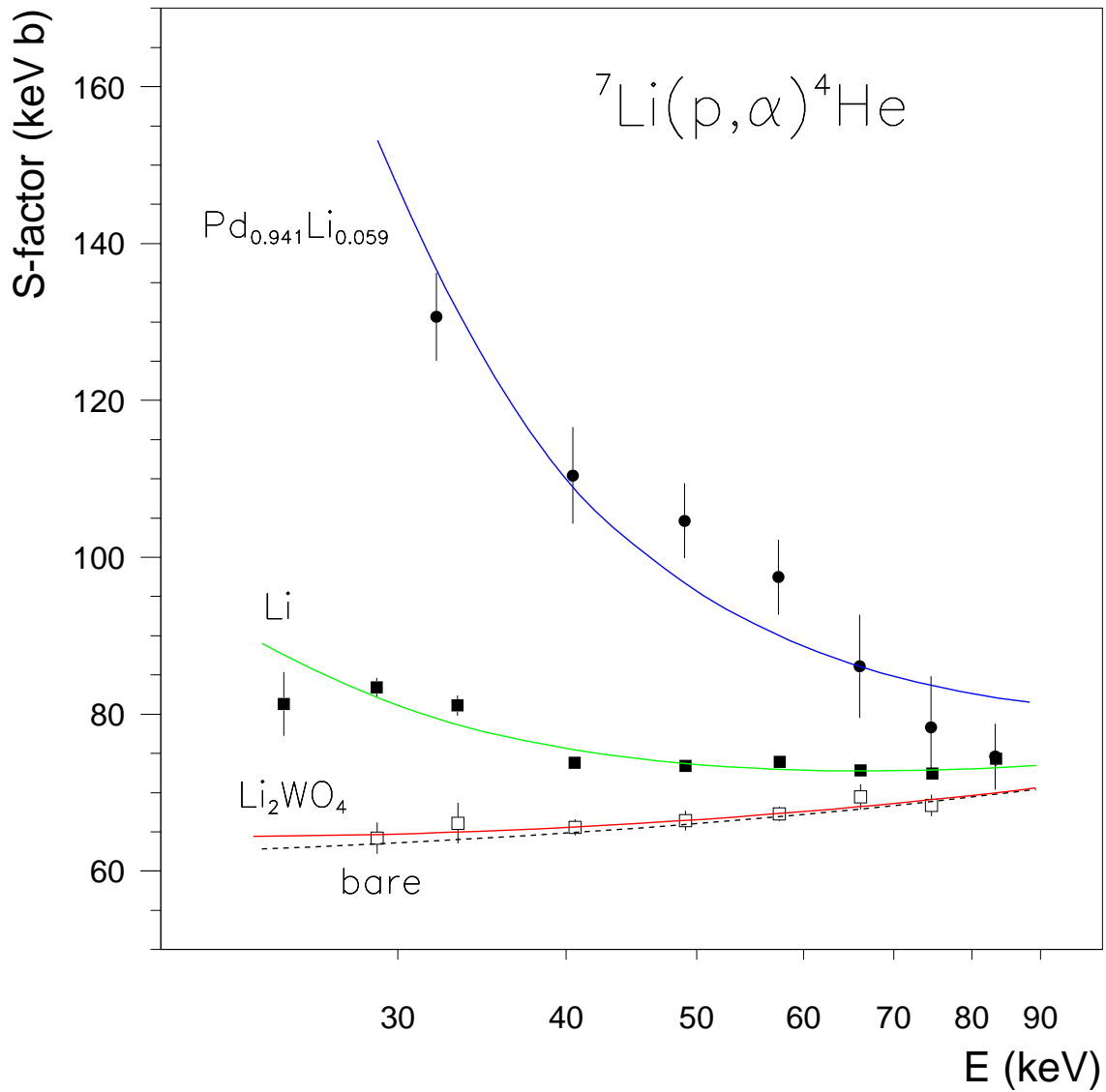


Figure 5.22: The  $S(E)$ -factor data of  ${}^7\text{Li}(p, \alpha){}^4\text{He}$  for different environments:  $\text{Li}_2\text{WO}_4$  insulator,  $\text{Li}$  metal, and  $\text{Pd}_{94.1\%}\text{Li}_{5.9\%}$  alloy. The solid curves through the data points include the bare  $S(E)$  factor (dotted curve) and the electron screening with the  $U_e$  values given in the text.

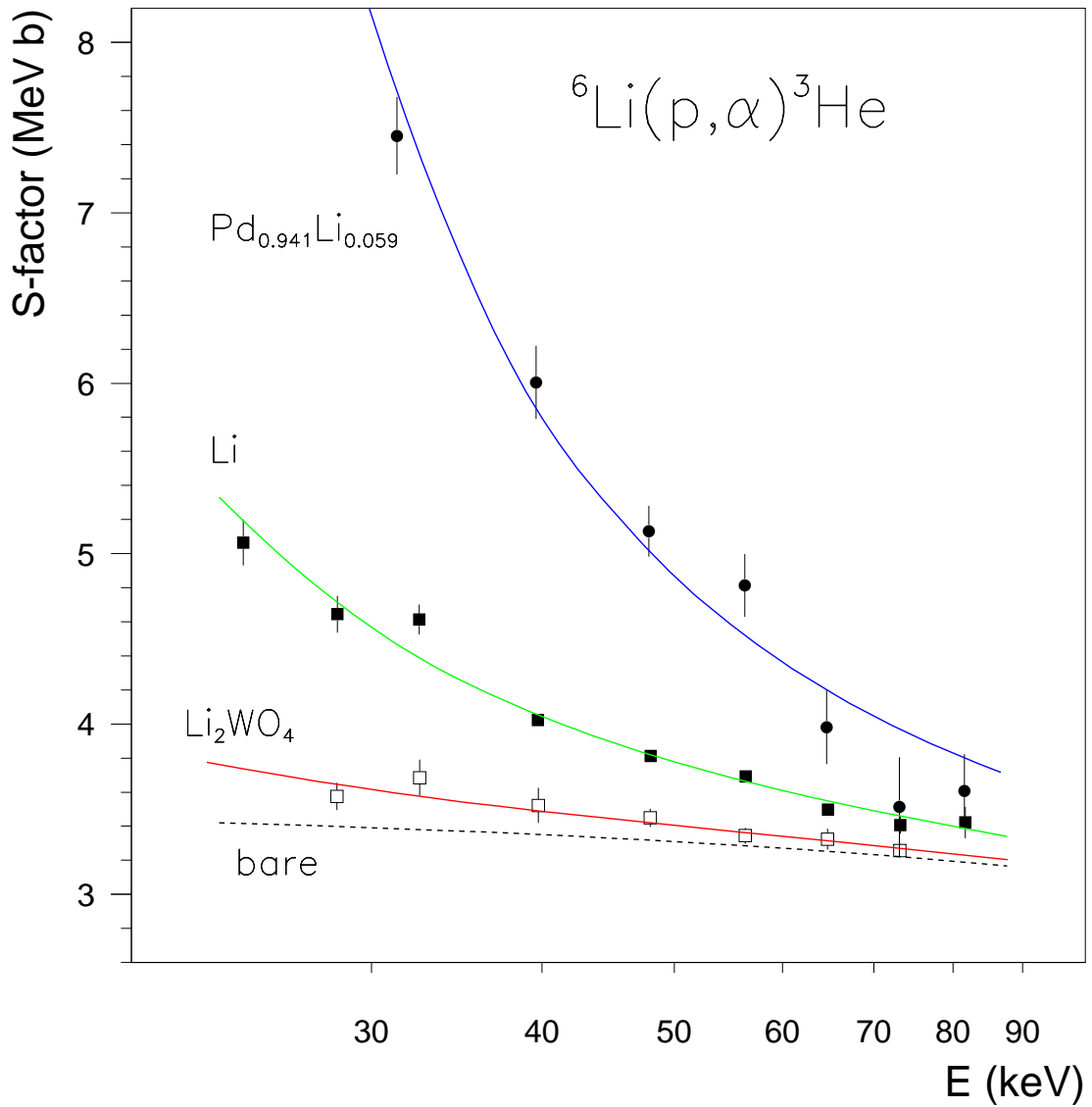


Figure 5.23: The  $S(E)$ -factor data of  ${}^6\text{Li}(p, \alpha){}^3\text{He}$  for different environments:  $\text{Li}_2\text{WO}_4$  insulator, Li metal, and  $\text{Pd}_{94.1\%}\text{Li}_{5.9\%}$  alloy. The solid curves through the data points include the bare  $S(E)$  factor (dotted curve) and the electron screening with the  $U_e$  values given in the text.

Target	${}^7\text{Li}(p,\alpha){}^4\text{He}$		${}^6\text{Li}(p,\alpha){}^3\text{He}$	
	$U_e$ (eV)	$\chi^2$	$U_e$ (eV)	$\chi^2$
$\text{Li}_2\text{WO}_4$	$78 \pm 151$	0.2	$273 \pm 111$	0.5
Li metal	$1031 \pm 59$	2.6	$1276 \pm 71$	1.9
$\text{Pd}_{94.1\%}\text{Li}_{5.9\%}$	$3528 \pm 332$	2.0	$3714 \pm 185$	1.7

Table 5.9:  ${}^7\text{Li}(p,\alpha){}^4\text{He}$  and  ${}^6\text{Li}(p,\alpha){}^3\text{He}$   $U_e$  values obtained from the  $\chi^2$  fits to the  $S$ -factor data for  $E$  below 90 keV with the targets:  $\text{Li}_2\text{WO}_4$  insulator, Li metal and  $\text{Pd}_{94.1\%}\text{Li}_{5.9\%}$ . The quoted uncertainties correspond to one standard deviation.

### 5.3 Debye shielding

The Debye length in a medium appears in the calculation of the effective potential energy of a fixed charged particle surrounded by other charged particles. This problem was first considered in 1923 by Debye and Hückel [85]. They demonstrated that the potential energy of an ion in a strong electrolyte is effectively screened by the cloud of particles surrounding it. The effective force range of the ion is therefore confined within a certain characteristic length, which is determined by the charge density and temperature of the medium. In 1954, Salpeter [86] derived an identical mechanism to show that in the plasma core of low density stars, nuclear fusion rates are enhanced by the free electrons electrostatic shielding. The argument used by Debye and Hückel, and Salpeter is now applied to metallic environments by computing the small variations of conduction (quasi-free) electron density in an infinite metal. In the interest of simplicity, the following assumptions are made: (1) the quasi-free conduction electrons are in a Maxwell-Boltzmann distribution at a temperature  $T_e$ . The conduction band energy levels of metals are very close together and, at room temperature, the electrons thermal energy is larger than the energy gap between levels and as such the conduction band may be considered as a broad single energy level. This assumption is in agreement with the Drude model of electrical conduction, developed in the 1900s to explain the transport properties of electrons in materials (especially metals). The Drude model is the application of kinetic theory to electrons in a solid. It assumes that a material contains immobile positive ions and an “electron gas” of classical, non-interacting electrons of average density  $n_{e0}$ , whose motion is damped by a frictional force, due to collisions with the ions; (2)  $|q_e \phi| \ll k_B T_e$ , where  $q_e$  is the electron charge,  $\phi$  is the

Coulomb potential in a given region of space, and  $k_B$  is the Boltzmann constant; (3) the nuclear reaction occurs between an atom of atomic number  $Z_1$  and a fully ionized atom with atomic number  $Z_2$ ; and (4) the microscopic variations of potential arising from the discrete nature of electrons surrounding the nuclei may be neglected.

The conduction electron density,  $n_e$ , varies from point to point according to the Maxwell-Boltzmann distribution:

$$n_e = n_{e0} \exp\left(-\frac{q_e \phi}{k_B T_e}\right), \quad (5.55)$$

where  $n_{e0}$  is the conduction electrons average density. Using assumption (2), we get for eq. 5.55

$$n_e \approx n_{e0} \left(1 - \frac{q_e \phi}{k_B T_e}\right). \quad (5.56)$$

The mean potential is taken as zero. The conduction electrons tend to congregate in regions of high potential, *i.e.*, near nuclei.

Poisson's equation must also be satisfied, so that

$$-\epsilon_0 \nabla^2 \phi = q_e (n_e - n_{e0}), \quad (5.57)$$

since  $n_e - n_{e0}$  is the difference in density that leads to a net charge. Replacing eq. 5.56 into eq. 5.57 we get

$$\nabla^2 \phi - \phi/R_D^2 = 0, \quad (5.58)$$

where,

$$R_D = \sqrt{\frac{\epsilon_0 k_B T_e}{n_{e0} q_e^2}}, \quad (5.59)$$

or,

$$R_D = 7.45 \times 10^3 \sqrt{\frac{k_B T_e}{e n_{e0}}} = 69 \sqrt{\frac{T_e}{\rho_a n_{eff}}} \quad (\text{m}), \quad (5.60)$$

where  $\rho_a$  is the atomic density in atoms/m<sup>3</sup>, and  $n_{eff}$  is the number of conduction electrons per metallic atom. The quantity  $R_D$  is called the Debye radius (or length) for the metallic conduction electrons, and is a function only of the conduction electrons parameters.

The solution of eq. 5.58, with the boundary condition that  $\phi$  vanishes at infinity, is

$$\phi(r) = \frac{1}{4\pi\epsilon_0} \frac{Z_1 e}{r} \exp\left(-\frac{r}{R_D}\right). \quad (5.61)$$

Thus, electrostatic disturbances in the metal are shielded by the conduction electrons in a distance of the order of  $R_D$ . The screened Coulomb potential energy of two nuclei of atomic numbers  $Z_1$  and  $Z_2$ , is then

$$V(r) = \frac{1}{4\pi\epsilon_0} \frac{Z_1 Z_2 e^2}{r} \exp\left(-\frac{r}{R_D}\right). \quad (5.62)$$

Expanding the exponential term in a Mac-Laurin series, and keeping only the first two terms of the series, we have for eq. 5.62

$$V(r) \approx \frac{1}{4\pi\epsilon_0} \frac{Z_1 Z_2 e^2}{r} - \frac{1}{4\pi\epsilon_0} \frac{Z_1 Z_2 e^2}{R_D}, \quad (5.63)$$

which is the Coulomb potential energy minus a potential energy drop, called Debye energy,  $U_D$

$$U_D = \frac{1}{4\pi\epsilon_0} \frac{Z_1 Z_2 e^2}{R_D}. \quad (5.64)$$

Besides the potential drop coming from the metallic conduction electrons, we also must include the screening from the bound electrons orbiting the nucleus of atomic number  $Z_1$ . This effect has already been explained in section 2.3 of Chapter 2, where it was introduced the definition of electron screening potential, and its limiting values: the sudden,  $U_e^{sud} = 134$  eV, and the adiabatic  $U_e^{ad} = 186$  eV limits, generically called here as the bound electron screening potential energy,  $U_e^{bound}$ . From the superposition principle for electric fields, the different contributions must “add”, so we get for eq. 5.63

$$V(r) = \frac{1}{4\pi\epsilon_0} \frac{Z_1 Z_2 e^2}{r} - U_D - U_e^{bound}. \quad (5.65)$$

$U_e^{th} = U_D + U_e^{bound}$  corresponds to the energy transfer from the electronic cloud to the incoming projectile, *i.e.*, the tunneling through a shielded Coulomb barrier at projectile energy  $E$  is equivalent to that of bare nuclei at energy  $E_{eff} = E + U_e^{th}$ .

Setting  $n_{eff}$  equal to the number of conduction electrons derived from the Hall coefficient  $n_{eff}(\text{Hall})$  (eq. 2.34) we are able to compare the Debye model with our experimental values for  $U_e$ . The values of  $n_{eff}(\text{Hall})$  can be found in literature, *e.g.*, [54].

### 5.3.1 Electron screening in the $\text{Li}_2\text{WO}_4$ insulator

The  $U_e^{exp}$  values obtained for the  $\text{Li}_2\text{WO}_4$  insulator are (recall from table 5.9):

$$\begin{aligned} {}^7\text{Li}(p, \alpha){}^4\text{He} &: U_e^{exp} = 78 \pm 151 \text{ eV} \\ {}^6\text{Li}(p, \alpha){}^3\text{He} &: U_e^{exp} = 273 \pm 111 \text{ eV} \end{aligned} \quad (5.66)$$

which are compatible within errors and are in agreement with previous works (see Chap. 3) and the bound electron screening potential. So, for this environment there is no evidence of Debye shielding, as expected for an insulator. The good agreement with previous works for the  ${}^7\text{Li}(p,\alpha){}^4\text{He}$   $S_b(E)$ , here verified, confirms that a reduction of  $\approx 20$  standard deviations in this energy range, required to cancel the discrepancy between SBBN+WMAP predictions and observations is completely ruled out.

As the bounded electron screening is predicted to be isotope independent, and since there is a systematic difference of  $\approx 200$  eV between  ${}^7\text{Li}$  and  ${}^6\text{Li}$   $U_e^{exp}$  values, we believe that this difference results from the polynomial function parametrizations used to extrapolate the bare  $S$ -factor. As already explained, polynomial extrapolations should be considered with caution. However, if we consider, for the Li metal and the  $\text{PdLi}_x$  alloys, that  $U_e^{th}$  value is the sum

$$U_e^{th} = U_D + U_e^{exp,Li2WO4} , \quad (5.67)$$

instead of  $U_e^{th} = U_D + U_e^{bound}$ , we will cancel the effect of the  $S_b(E)$  parametrizations in the determination of  $U_D$ . In this equation,  $U_e^{exp,Li2WO4}$  refers to the values of eq. 5.66 for each of the lithium reactions.

### 5.3.2 Electron screening in the Li metal

The  $U_e^{exp}$  values obtained for the Li metal are (recall from table 5.9):

$$\begin{aligned} {}^7\text{Li}(p,\alpha){}^4\text{He} & : \quad U_e^{exp} = 1031 \pm 59 \text{ eV} \\ {}^6\text{Li}(p,\alpha){}^3\text{He} & : \quad U_e^{exp} = 1276 \pm 71 \text{ eV} \end{aligned} \quad (5.68)$$

For this target at  $T_e = 293$  K, we have

$$\begin{aligned} n_{eff}^{\text{Li}} & = n_{eff}^{\text{Li}}(\text{Hall}) = 0.8 \pm 0.2 \\ \rho_a(\text{Li}) & = 4.63 \times 10^{28} \text{ at/m}^3 . \end{aligned} \quad (5.69)$$

Applying these values to eqs. 5.60 and 5.64 we get

$$R_D = 6.1 \times 10^{-12} \text{ m} \Rightarrow U_D = 710 \pm 177 \text{ eV} , \quad (5.70)$$

The predicted electron screening potential energy is then

$$\begin{aligned} {}^7\text{Li}(p,\alpha){}^4\text{He} & : \quad U_e^{th} = U_D + U_e^{exp,Li2WO4} \Rightarrow U_e^{th} = 788 \pm 177 \text{ eV} \\ {}^6\text{Li}(p,\alpha){}^3\text{He} & : \quad U_e^{th} = U_D + U_e^{exp,Li2WO4} \Rightarrow U_e^{th} = 983 \pm 177 \text{ eV} , \end{aligned} \quad (5.71)$$

where the quoted uncertainties are related to the 25% uncertainty in  $n_{eff}^{Li}$ (Hall). The  $U_e^{th}$  values are smaller than the experimental values even though they are almost compatible within errors.

A possible cause for this difference is that one or more variables that enter eq. 5.60 have a wrong value:  $T_e$  was considered to be 293 K. A 20 K drop in temperature only increases  $U_D$  by 3.6%. As this target is a bulk sample, the value of  $\rho_a$  should be correct. Finally, if we consider a higher value for  $n_{eff}^{Li}$  of  $1.5 \pm 0.3$ , we have,

$$R_D = 4.5 \times 10^{-12} \text{ m} \Rightarrow U_D = 972 \pm 243 \text{ eV} , \quad (5.72)$$

with a corresponding

$$\begin{aligned} {}^7\text{Li}(p, \alpha){}^4\text{He} & : \quad U_e^{th} = U_D + U_e^{exp, Li2WO4} \Rightarrow U_e^{th} = 1050 \pm 243 \text{ eV} \\ {}^6\text{Li}(p, \alpha){}^3\text{He} & : \quad U_e^{th} = U_D + U_e^{exp, Li2WO4} \Rightarrow U_e^{th} = 1245 \pm 243 \text{ eV} , \end{aligned} \quad (5.73)$$

which are in perfect agreement with the experimental values for both  ${}^7\text{Li}$  and  ${}^6\text{Li}$ . However, this increase in  $n_{eff}^{Li}$  by a factor  $\approx 2$  means a shift of more than three standard deviations from the original value.

### 5.3.3 Electron screening in the PdLi<sub>x</sub> alloys

The  $U_e^{exp}$  values obtained for the Pd<sub>94.1%</sub>Li<sub>5.9%</sub> are (recall from table 5.9):

$$\begin{aligned} {}^7\text{Li}(p, \alpha){}^4\text{He} & : \quad U_e^{exp} = 3528 \pm 332 \text{ eV} \\ {}^6\text{Li}(p, \alpha){}^3\text{He} & : \quad U_e^{exp} = 3714 \pm 185 \text{ eV} \end{aligned} \quad (5.74)$$

For this target at  $T_e = 293 \text{ K}$ , we have

$$\begin{aligned} n_{eff}^{Pd} & = n_{eff}^{Pd}(\text{Hall}) = 6.3 \pm 1.2 \\ \rho_a(\text{Pd}) & = 6.80 \times 10^{28} \text{ at/m}^3 . \end{aligned} \quad (5.75)$$

Applying these values to eqs. 5.60 and 5.64 we get

$$R_D = 1.8 \times 10^{-12} \text{ m} \Rightarrow U_D = 2414 \pm 460 \text{ eV} , \quad (5.76)$$

The predicted electron screening potential energy is then

$$\begin{aligned} {}^7\text{Li}(p, \alpha){}^4\text{He} & : \quad U_e^{th} = U_D + U_e^{exp, Li2WO4} \Rightarrow U_e^{th} = 2492 \pm 460 \text{ eV} \\ {}^6\text{Li}(p, \alpha){}^3\text{He} & : \quad U_e^{th} = U_D + U_e^{exp, Li2WO4} \Rightarrow U_e^{th} = 2687 \pm 470 \text{ eV} , \end{aligned} \quad (5.77)$$

where the quoted uncertainty is related to the 19% uncertainty in  $n_{eff}(\text{Pd})$ . Here again, the  $U_e^{th}$  value is smaller than the experimental one, and a good agreement is obtained if we consider a two times higher value for  $n_{eff}^{\text{Pd}}$  of  $12.8 \pm 2.4$ . In this case we have,

$$R_D = 1.3 \times 10^{-12} \text{ m} \Rightarrow U_D = 3441 \pm 654 \text{ eV} , \quad (5.78)$$

with a corresponding

$$\begin{aligned} {}^7\text{Li}(p, \alpha)^4\text{He} & : \quad U_e^{th} = U_D + U_e^{exp, Li2WO4} \Rightarrow U_e^{th} = 3519 \pm 654 \text{ eV} \\ {}^6\text{Li}(p, \alpha)^3\text{He} & : \quad U_e^{th} = U_D + U_e^{exp, Li2WO4} \Rightarrow U_e^{th} = 3714 \pm 654 \text{ eV} . \end{aligned} \quad (5.79)$$

Two PdLi<sub>x</sub> alloys were studied. For the alloy PdLi<sub>0.016%</sub> we find  $U_e^{exp} = 3834 \pm 651 \text{ eV}$  ( $\chi^2 = 2.23$ ), consistent with the above value for Pd<sub>94.1%</sub>Li<sub>5.9%</sub>, as shown in fig. 5.24 for the  ${}^7\text{Li}(p, \alpha)^4\text{He}$  reaction (there is no data for the  ${}^6\text{Li}(p, \alpha)^3\text{He}$  reaction with this target, because due to the very low counting rate, the  ${}^3\text{He}$  peak in the particle spectrum was contaminated with electronic noise). This result indicates that the metallic character of Pd remained essentially unchanged by the small Li content. The extracted values of  $S(E)$  using the differential method, for the PdLi<sub>0.016%</sub> targets and corresponding uncertainties are listed in table 5.10.

So, for both the Li metal and PdLi<sub>x</sub> targets we need to increase  $U_D$  by a factor  $\approx \sqrt{2} = 1.41$  in order to get a match between the Debye model and experimental data. This factor indeed appears if we consider in the Debye model a volume distribution of the conduction electrons around the nucleus, instead of being all concentrated in the Debye radius, as claimed by Bencze [46] in his static atomic-physics model (see section 2.3.1): by considering an electron cloud spread with uniform density in a spherical volume shell, the corresponding screening potential energy increases by a factor 3/2. In this case, we have a corrected Debye energy

$$U_D = \frac{3}{2} \frac{1}{4\pi\epsilon_0} \frac{Z_1 Z_2 e^2}{R_D} , \quad (5.80)$$

with  $R_D$  still given by eq. 5.60. This factor is controversial, though. For instance, applying Bencze's model to stellar or primordial plasmas implies the presence of the 3/2 factor in the  $U_e$  value for these scenarios (defined by eq. 2.29). However, Bahcall *et al.* (2000) [87] showed using different approaches that this factor does not exist.

Looking back to the D(d,p)T reaction data for metals [54]–[55], we verify that the values of  $n_{eff}$  and  $n_{eff}(\text{Hall})$  for several metals also show large discrepancies, but without any pattern,

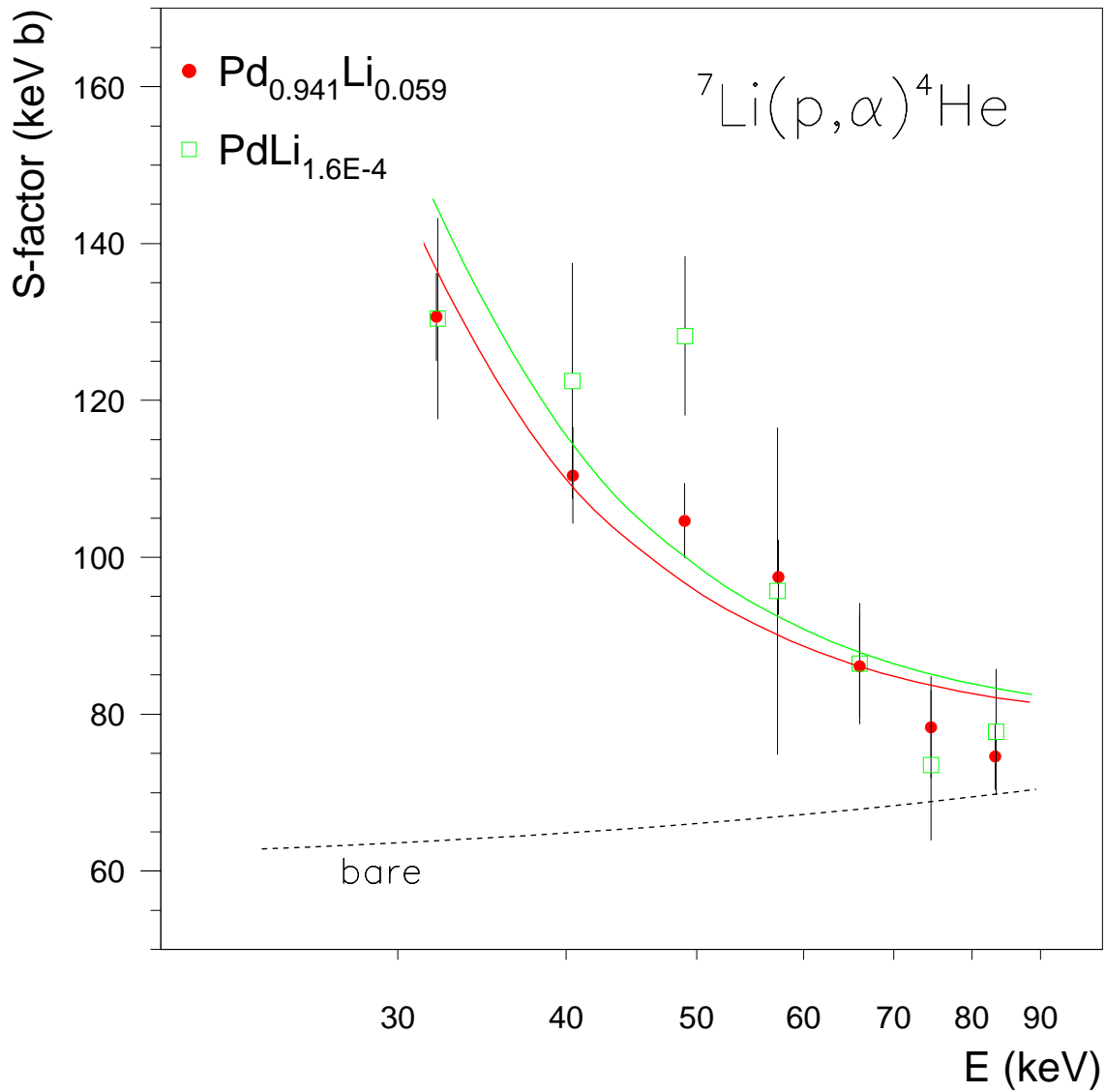


Figure 5.24: The  $S(E)$ -factor data of  ${}^7\text{Li}(p, \alpha){}^4\text{He}$  for the two  $\text{PdLi}_x$  alloys studied. The solid curves through the data points include the bare  $S(E)$  factor (dotted curve) and the electron screening with the  $U_e$  values given in the text.

$E$	$S(E)$	$\delta S(E)$
(keV)	(MeV b)	(MeV b)
32.1	130.5	12.8
40.4	122.5	15.0
49.0	128.2	10.2
57.4	95.7	20.8
66.0	86.5	7.7
74.6	73.5	9.6
83.4	77.8	8.0

Table 5.10:  $S$ -factor data for the  ${}^7\text{Li}(p,\alpha){}^4\text{He}$  reaction measured for  $E$  below 90 keV with the  $\text{PdLi}_{0.016\%}$  target. The quoted uncertainties correspond to one standard deviation.

*i.e.*, either with  $n_{eff} > n_{eff}(\text{Hall})$  or  $n_{eff} < n_{eff}(\text{Hall})$ . This random behaviour may indicate that for several metals  $n_{eff}(\text{Hall})$  is not correct, and should be remeasured, or that the assumption  $n_{eff} = n_{eff}(\text{Hall})$  is not correct.

From the Li metal and  $\text{PdLi}_x$  alloys results we conclude that the present data for the electron screening in the  ${}^7\text{Li}(p,\alpha){}^4\text{He}$  and  ${}^6\text{Li}(p,\alpha){}^3\text{He}$  reactions give a consistent picture [88] as these two environments exhibit an additional acceleration mechanism which can be explained by the Debye shielding model applied to the conduction electrons in metals, even though a perfect agreement is only obtained by considering a  $n_{eff}$  value higher than the values derived from the Hall coefficient measurements. In comparison to the data in the  $\text{D}(d,p)\text{T}$  reaction for metals [54]– [55], the screening potential energy scales with the charge  $Z_t$  of the target nucleus, as expected from the Debye model. Also, the isotopic independence of this model, *i.e.*, the same  $U_D$  for  ${}^7\text{Li}$  and  ${}^6\text{Li}$  nuclides, was verified.

Previous studies of the reactions  ${}^9\text{Be}(p,\alpha){}^6\text{Li}$  and  ${}^9\text{Be}(p,d){}^8\text{Be}$  using a metallic Be target led to a high screening potential energy  $U_e = 900 \pm 50$  eV [89], which was not understood at the time, *i.e.*, in 1997, but which is now explained by the Debye model.

Recent measurements of the electron screening in  ${}^{50}\text{V}(p,n){}^{50}\text{Cr}$  and  ${}^{176}\text{Lu}(p,n){}^{176}\text{Hf}$  [90] have also shown that the Debye model occurs across the Periodic Table and is not restricted to reactions among light nuclides. The two reactions with neutrons in the exit channel demonstrate

furthermore that the electron screening is an effect in the entrance channel of the reaction and is not influenced by the ejectiles of the exit channel.

There is another prediction of the Debye model concerning radioactive decay of nuclides in a metallic environment. In general, for the  $\alpha$ -decay and  $\beta^+$ -decay the model predicts a shorter half-life due to the acceleration mechanism of the Debye electrons for these positively charged particles, while for  $\beta^-$ -decay and electron capture process the model predicts a correspondingly longer half-life. Very recently, it has been observed in metallic environments cooled to  $T = 12$  K a longer half-life of the electron capture by  ${}^7\text{Be}$  [91], and a shorter half-life for the  ${}^{22}\text{Na}$   $\beta^+$ -decay [92]. Both results are consistent but lower than the predictions of the Debye model.

The ability of the Debye model to explain (and predict) the high  $U_e$  values observed in metallic environments is very important for stellar and BBN calculations, since we can reproduce all experimental data with the same  $S_b(E)$ . This is the same  $S_b(E)$  which is then used to determine the reaction rates of interest for astrophysics.

Besides, a good understanding of laboratory electron screening may eventually also help to improve the corresponding understanding of electron screening in stellar plasmas.

Clearly, an improved theory is highly desirable to explain why the simple Debye model appears to work so well. Without such a theory, one may consider the Debye model as a powerful parametrization of the data.

# Chapter 6

## The ${}^7\text{Li}(p,p){}^7\text{Li}$ reaction

Elastic scattering of protons by  ${}^7\text{Li}$  does not directly present an astrophysical interest but is important to describe the entrance channel of the  ${}^7\text{Li}(p,\alpha){}^4\text{He}$  reaction. This chapter describes the procedure and calculations used to obtain the  ${}^7\text{Li}(p,p){}^7\text{Li}$  differential cross section at  $\theta_{\text{lab}} = 162^\circ$ . These data were fitted by a theoretical group using an optical potential +  $R$ -matrix hybrid model, the motivation being the presence of both direct and resonant mechanism contributions to scattering.

### 6.1 Experimental setup

The  ${}^7\text{Li}(p,p){}^7\text{Li}$  reaction differential cross section was measured at the Van de Graaff 2.5 MeV accelerator at ITN, Sacavém, in the energy range  $E_{\text{lab}} = 419.7$  to  $1021.8$  keV, in a total of 45 energy points, using a thin lithium fluorine film vacuum-evaporated over a thin Ag film. The details of the experimental setup are described in section 4.1.1. The lithium fluorine target was analysed by RBS, using the procedures described in section 4.2.1, yielding a 1:1 stoichiometric ratio for Li:F and 1:0.918 ratio for Li:Ag. The LiF film was measured to be  $\Delta_{\text{lab}} = 6.0$  keV thick for  $E_{\text{lab}} = 1.03$  MeV protons, which corresponds to  $1.43 \times 10^{18}$  at/cm<sup>2</sup> or  $31.0$   $\mu\text{g}/\text{cm}^2$ . The target stability was verified by measuring the stoichiometric ratios with alpha-particles before and after the proton measurements.

## 6.2 Analysis and results

The elastically scattered protons from the  ${}^7\text{Li}$  and Ag nuclei are observed in the Si detector concurrently. From the ratio of observed counts in the two peaks, we get an expression for the  ${}^7\text{Li}(\text{p,p}){}^7\text{Li}$  differential cross section which is independent of both the collected charge,  $N_p$ , and the Si detector solid angle,  $\Omega_{\text{lab}}$ , and depends only on the differential cross section of protons scattered from Ag nuclei (which, for the energy interval studied is purely Coulombian):

$$\begin{aligned} \frac{N_{7\text{Li}}(E_{\text{lab}}, \theta_{\text{lab}})}{N_{\text{Ag}}(E_{\text{lab}}, \theta_{\text{lab}})} &= \frac{N_p N_{7\text{Li}} \frac{d\sigma_{el}^{7\text{Li}}(E_{\text{lab}}, \theta_{\text{lab}})}{d\Omega_{\text{lab}}} \Omega_{\text{lab}}}{N_p N_{\text{Ag}} \frac{d\sigma_{\text{Ruth}}^{\text{Ag}}(E_{\text{lab}} - \Delta_{\text{lab}}, \theta_{\text{lab}})}{d\Omega_{\text{lab}}} \Omega_{\text{lab}}} = \frac{N_{7\text{Li}} \frac{d_{el}^{7\text{Li}}\sigma(E_{\text{lab}}, \theta_{\text{lab}})}{d\Omega_{\text{lab}}}}{N_{\text{Ag}} \frac{d\sigma_{\text{Ruth}}^{\text{Ag}}(E_{\text{lab}} - \Delta_{\text{lab}}, \theta_{\text{lab}})}{d\Omega_{\text{lab}}}} \Rightarrow \\ &\Rightarrow \frac{d\sigma_{el}^{7\text{Li}}(E_{\text{lab}}, \theta_{\text{lab}})}{d\Omega_{\text{lab}}} = \frac{N_{7\text{Li}}(E_{\text{lab}}, \theta_{\text{lab}})}{N_{\text{Ag}}(E_{\text{lab}}, \theta_{\text{lab}})} \frac{d\sigma_{\text{Ruth}}^{\text{Ag}}(E_{\text{lab}} - \Delta_{\text{lab}}, \theta_{\text{lab}})}{d\Omega_{\text{lab}}} \frac{1}{r}, \end{aligned} \quad (6.1)$$

where  $N_{7\text{Li}}$  and  $N_{\text{Ag}}$  are the  ${}^7\text{Li}$  and Ag areal densities,  $r$  is the ratio

$$r = \frac{N_{7\text{Li}}}{N_{\text{Ag}}} = 0.918, \quad (6.2)$$

and  $d\sigma_{\text{Ruth}}^{\text{Ag}}(E_{\text{lab}} - \Delta_{\text{lab}}, \theta_{\text{lab}})/d\Omega_{\text{lab}}$  is the differential Rutherford cross section of protons scattered from Ag nuclei (eq. 4.9), and is calculated for  $E_{\text{lab}} - \Delta_{\text{lab}}$  which corresponds to the proton beam energy that enters the Ag layer after crossing the LiF film.

The elastic cross section is usually expressed as a ratio to the corresponding Rutherford cross section:

$$\frac{\frac{d\sigma_{el}^{7\text{Li}}(E_{\text{lab}}, \theta_{\text{lab}})}{d\Omega_{\text{lab}}}}{\frac{d\sigma_{\text{Ruth}}^{7\text{Li}}(E_{\text{lab}}, \theta_{\text{lab}})}{d\Omega_{\text{lab}}}} = \frac{N_{7\text{Li}}(E_{\text{lab}}, \theta_{\text{lab}})}{N_{\text{Ag}}(E_{\text{lab}}, \theta_{\text{lab}})} \frac{\frac{d\sigma_{\text{Ruth}}^{\text{Ag}}(E_{\text{lab}} - \Delta_{\text{lab}}, \theta_{\text{lab}})}{d\Omega_{\text{lab}}}}{\frac{d\sigma_{\text{Ruth}}^{7\text{Li}}(E_{\text{lab}}, \theta_{\text{lab}})}{d\Omega_{\text{lab}}}} \frac{1}{r}. \quad (6.3)$$

$N_{7\text{Li}}(E_{\text{lab}}, \theta_{\text{lab}})$  and  $N_{\text{Ag}}(E_{\text{lab}}, \theta_{\text{lab}})$  are calculated by  $\chi^2$  fitting the  ${}^7\text{Li}$  and Ag peaks observed in the backscattering spectra respectively with a gaussian with a low energy lorentzian tail, and one gaussian plus one gaussian with a low energy lorentzian tail, as exemplified in figs. 6.1 and 6.2. The continuum produced by the plural scattering events of protons on silver atoms were  $\chi^2$  fitted with two exponentials and included in the statistics of  $N_{\text{Ag}}(E_{\text{lab}}, \theta_{\text{lab}})$ . The presence in the spectra of the  ${}^6\text{Li}$  and C peaks near the  ${}^7\text{Li}$  peak, required that these two peaks were also fitted, alongside with the  ${}^7\text{Li}$  peak. The carbon peak was fitted with a gaussian with a low energy lorentzian tail, while the  ${}^6\text{Li}$  peak was fitted with a gaussian whose width,  $w$  was fixed by the  ${}^7\text{Li}$  width (one of the fitting parameters) according to

$$w_{6\text{Li}} = \frac{k_{6\text{Li}} + \cos^{-1} \theta_{\text{lab}}}{k_{7\text{Li}} + \cos^{-1} \theta_{\text{lab}}} w_{7\text{Li}}, \quad (6.4)$$

where  $k_{6\text{Li}}$  and  $k_{7\text{Li}}$  are the kinematical factors [73] of  ${}^6\text{Li}$  and  ${}^7\text{Li}$  respectively.

The  ${}^6\text{Li}$  and  ${}^7\text{Li}$  peaks are always fitted simultaneously except for energies below 455 keV where the  ${}^6\text{Li}$  peak is no longer visible and, as such, not considered in the fits.

For energies above 600 keV the  ${}^7\text{Li}$  and C peaks are well separated and are fitted independently, with the C peak fitted prior to  ${}^7\text{Li}$ . Lower energies require a simultaneous fit.

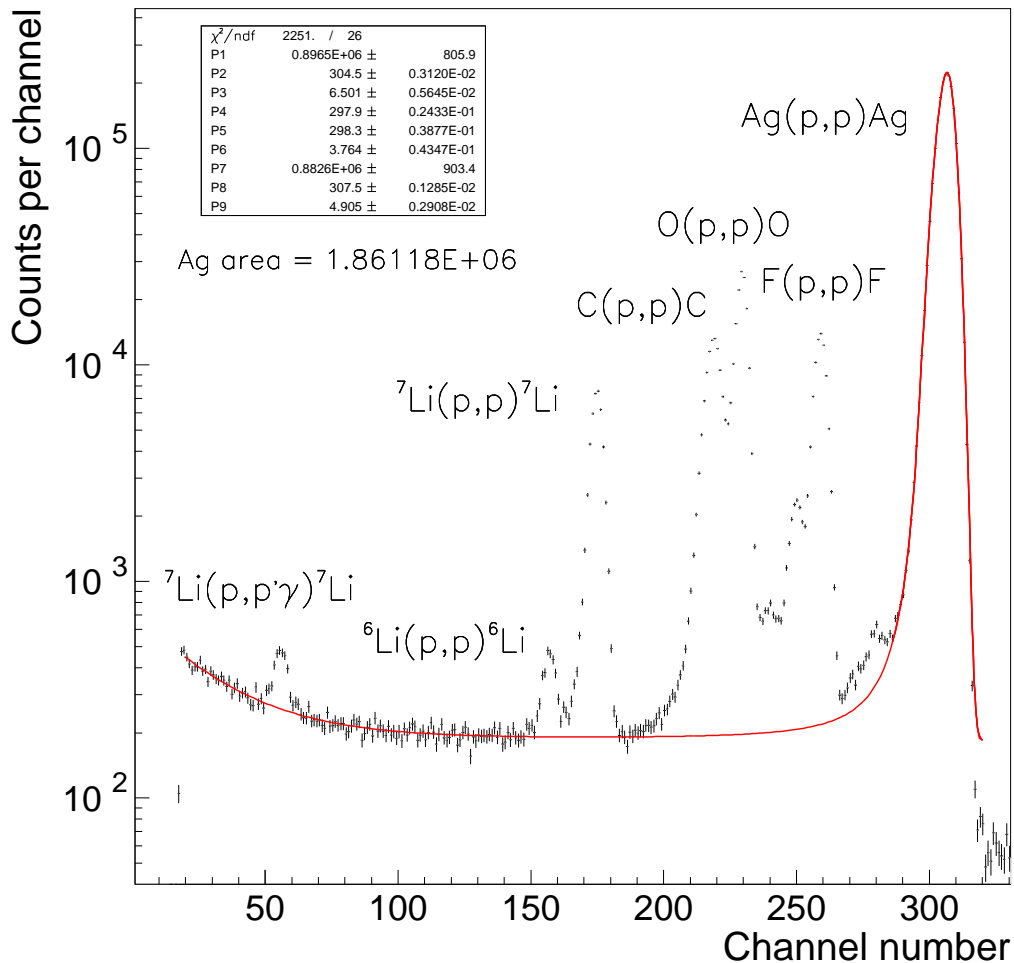


Figure 6.1: The 1021.8 keV  $\text{H}^+$  backscattering spectrum of the LiF-Ag target measured at  $\theta_{\text{lab}} = 162^\circ$ . The red curve shows a  $\chi^2$  fit to the Ag peak with a gaussian plus a gaussian with a low energy lorentzian tail, and a two exponential fit to the continuum produced by the plural scattering events of protons on silver atoms.

Cross section ratios obtained in this work are presented in fig. 6.3. The excitation function is dominated by the 440 and 1030 keV resonances. The first resonance corresponds to the

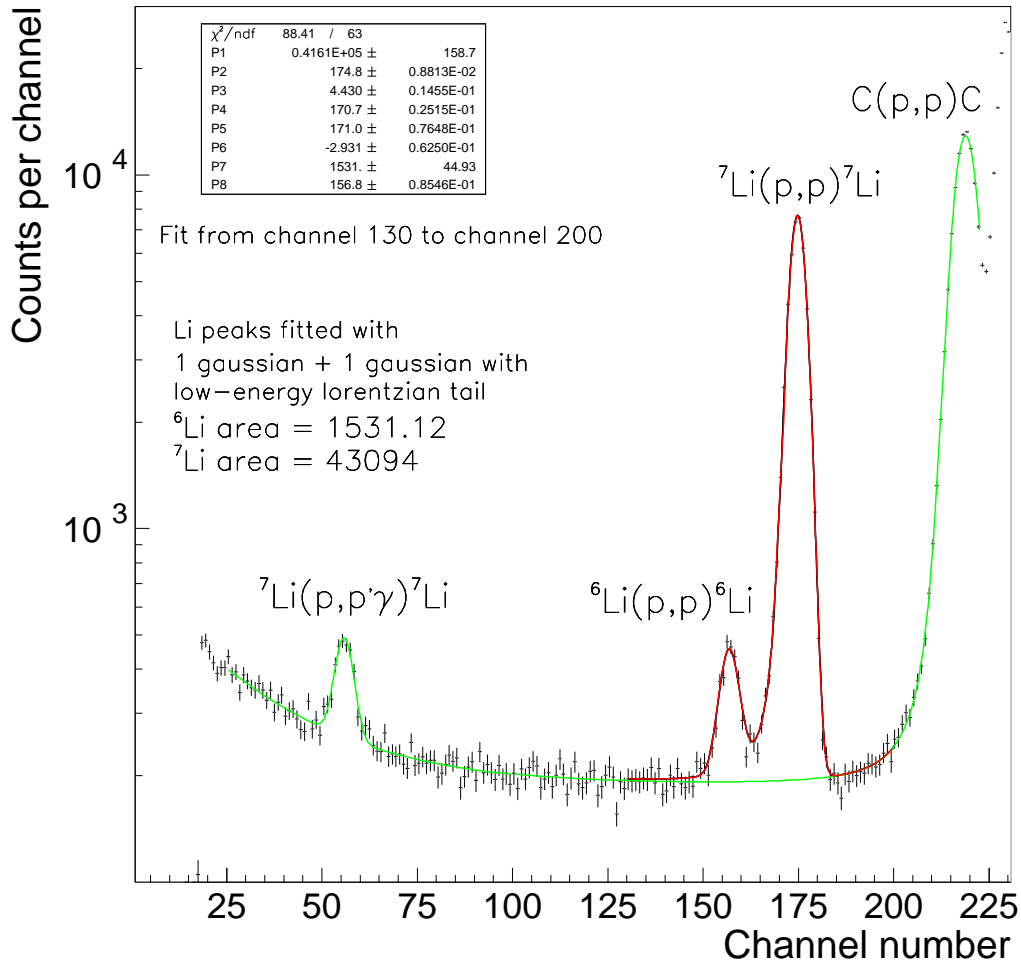


Figure 6.2: Zoom of the 1021.8 keV  $\text{H}^+$  backscattering spectrum of the LiF-Ag target measured at  $\theta_{\text{lab}} = 162^\circ$ . The red curve shows a  $\chi^2$  simultaneous fit to the  ${}^6\text{Li}$  and  ${}^7\text{Li}$  peaks. The  ${}^6\text{Li}$  peak was fitted with a gaussian shape and the  ${}^7\text{Li}$  peak was fitted with a gaussian plus a gaussian with a low energy lorentzian tail. The lithium fits were done on top of the continuum and the carbon peak (green curve), fitted with two exponentials and a gaussian with a low energy lorentzian tail, respectively. See text for details.

${}^8\text{Be}$   $1^+$  state at 17.64 MeV (see fig. 3.2), and the second resonance, only partially measured, corresponds to the broad  ${}^8\text{Be}$   $1^+$  state at 18.15 MeV ( $\Gamma_{cm} = 138$  keV). The quoted uncertainties correspond to one standard deviation, and are associated to uncertainties in the determination of the ratio  $r$ , and in the parametrizations used to fit the Ag continuum (2 exponentials) and the Li and C peaks (gaussians with low energy lorentzian tails). Another source of uncertainty appears when one compares the measured cross section ratios with theoretical calculations or other measurements, due to the influence of the target thickness on the measured yields. Off-resonance or on-resonances with large widths when compared with the target energy thickness, the effect of the target thickness on the measurements may be taken into account using an effective energy  $E_{eff} = E_{lab} - \Delta_{lab}/2$ , for each value of the incident energy. For resonances with widths smaller or of the order of the target thickness, the measured yield results from the integration of the nuclear reaction cross section over the target thickness. Assuming a small solid angle of particle detection we have

$$\begin{aligned} N_{7\text{Li}}(E_{lab}, \theta_{lab}) &= N_p \frac{N_{7\text{Li}}}{x} \Omega_{lab} \int_0^x \frac{d\sigma_{el}^{7\text{Li}}(E, \theta_{lab})}{d\Omega_{lab}} dx \\ &= \frac{N_p N_{7\text{Li}}}{x \epsilon(E_{lab})} \Omega_{lab} \int_{E_{lab}-\Delta_{lab}}^{E_{lab}} \frac{d\sigma_{el}^{7\text{Li}}(E, \theta_{lab})}{d\Omega_{lab}} dE \\ &= \frac{N_p N_{7\text{Li}}}{\Delta_{lab}} \Omega_{lab} \int_{E_{lab}-\Delta_{lab}}^{E_{lab}} \frac{d\sigma_{el}^{7\text{Li}}(E, \theta_{lab})}{d\Omega_{lab}} dE, \end{aligned} \quad (6.5)$$

where  $x$  is the target thickness and  $\epsilon(E_{lab})$  is the stopping power cross section at incident energy.

According to Spyrou *et al.* [93], the beam energy distribution,  $\Delta_b = 1.0$  keV, and the energy straggling of protons inside the target (Bohr's formula [93]) may be described by a single gaussian function,  $g(E_{lab}, E, x')$ , where  $E$  and  $x'$  are the variables of energy and depth:

$$g(E_{lab}, E, x') = B \exp \left[ -\frac{(E_{lab} - E - \epsilon(E_{lab}) x')^2}{0.36 \Gamma_t} \right]. \quad (6.6)$$

$B$  is the normalization constant and  $\Gamma_t$  is the total FWHM of the energy spreading:

$$\Gamma_t = \left( \Delta_b^2 + 0.86 z^2 \frac{\bar{Z}}{\bar{A}} x' \right)^{1/2}, \quad (6.7)$$

where  $x'$  is in units of  $\mu\text{g}/\text{cm}^2$ ,  $\bar{Z}$  and  $\bar{A}$  are the average atomic number and weight, and  $z$  is the atomic number of the projectile.

In order to take into account these effects, eq. 6.5 modifies to

$$N_{7\text{Li}}(E_{lab}, \theta_{lab}) = N_p \frac{N_{7\text{Li}}}{x} \Omega_{lab} \int_0^x \int_0^\infty \frac{d\sigma_{el}^{7\text{Li}}(E, \theta_{lab})}{d\Omega_{lab}} g(E_{lab}, E, x') dE dx'. \quad (6.8)$$

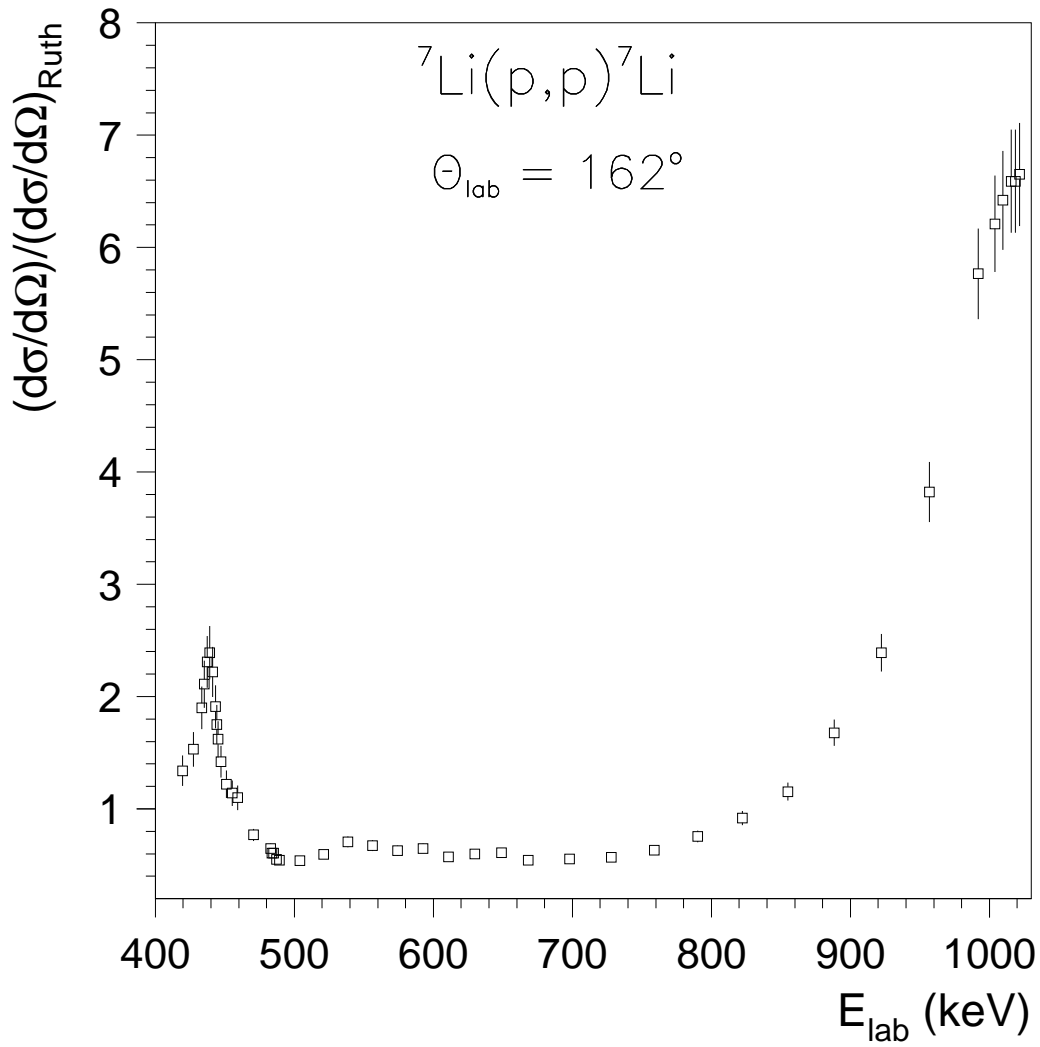


Figure 6.3: Cross section of the reaction  ${}^7\text{Li}(p,p){}^7\text{Li}$  normalised to Rutherford cross section. The scattering angle measured in the laboratory frame is  $162^\circ$ .

The double integral of eq. 6.8 was calculated numerically by implementing a FORTRAN program (listed in Appendix C) which included routines from the CERNLIB package [82], and with the following parametrization for the cross section

$$\left[ \frac{d\sigma_{el}^{7\text{Li}}(E, \theta_{\text{lab}})}{d\Omega_{\text{lab}}} \right] / \left[ \frac{d\sigma_{Ruth}^{7\text{Li}}(E, \theta_{\text{lab}})}{d\Omega_{\text{lab}}} \right] = \sigma_0 f(E), \quad (6.9)$$

where

$$f(E) = 1 + \frac{a\Gamma^2 + 2b\Gamma(E - E_r)}{\Gamma^2 + 4(E - E_r)^2}. \quad (6.10)$$

Taking for  $\Gamma$  the value of 12.2 keV, eq. 6.8 was  $\chi^2$  fitted (with the same Fortran program) to the experimental values of the 440 keV resonance, and obtained, for this resonance, the theoretical or true cross section function as defined above, with:

$$\begin{aligned} a &= 1.1 \pm 0.2 \\ b &= -0.40 \pm 0.09 \\ \sigma_0 &= 1.12 \pm 0.06 \\ \chi^2 &= 0.80. \end{aligned} \quad (6.11)$$

In table 6.1 we provide, for the energy range 419.7–1021.8 keV, values of the elastic cross section normalised to the Rutherford cross section, corrected for target thickness effects.

The fig. 6.3 shows that the two resonances lie on a background, which provides evidence for a direct mechanism contribution. Therefore, as direct mechanisms are properly described using optical potentials and resonant mechanisms using  $R$ -matrix theory, a hybrid model which combines the two in a consistent manner was used to fit our data. Also the elastic excitation function at  $\theta_{\text{lab}} = 90^\circ$  and total inelastic cross section data were fitted, by the hybrid model. This work was the subject of Rui Bento's master thesis [94] where it was shown that the hybrid model fits well the experimental data, even though the values obtained for the energies and widths of some resonances were considerably different from the reference values. As these discrepancies show up for all data sets, the problem indicates that the hybrid model still needs tuning. It would be very interesting to apply this model to the  ${}^7\text{Li}(\text{p},\alpha){}^4\text{He}$  reaction, and compare with it with  $R$ -matrix results and polynomial extrapolations.

$E_{\text{lab}}$ (keV)	$d\sigma/d\Omega$	$\delta(d\sigma/d\Omega)$	$E_{\text{lab}}$ (keV)	$d\sigma/d\Omega$	$\delta(d\sigma/d\Omega)$
419.7	1.34	0.13	556.2	0.67	0.05
427.4	1.53	0.15	574.2	0.63	0.04
433.3	1.90	0.19	592.4	0.65	0.04
435.3	2.11	0.21	611.0	0.57	0.04
437.2	2.31	0.23	629.8	0.60	0.04
439.2	2.39	0.24	648.9	0.61	0.04
441.2	2.22	0.22	668.2	0.54	0.04
443.2	1.91	0.19	697.8	0.55	0.04
444.2	1.75	0.18	728.0	0.57	0.04
445.2	1.62	0.16	758.8	0.63	0.04
447.2	1.42	0.14	790.3	0.75	0.05
451.2	1.22	0.12	822.4	0.92	0.06
455.2	1.14	0.11	855.0	1.15	0.08
459.2	1.10	0.11	888.4	1.68	0.12
470.5	0.77	0.05	922.3	2.39	0.17
482.9	0.65	0.04	956.9	3.82	0.27
484.0	0.61	0.04	992.0	5.76	0.40
485.0	0.60	0.04	1003.9	6.22	0.44
487.1	0.55	0.04	1009.9	6.42	0.45
489.2	0.54	0.04	1015.8	6.60	0.46
504.0	0.54	0.04	1018.8	6.59	0.46
521.1	0.59	0.04	1021.8	6.65	0.47
538.5	0.70	0.05			

Table 6.1: Differential cross section of elastic scattering of protons by  ${}^7\text{Li}$  normalized to rutherford cross section values. The scattering angle is  $\theta_{\text{lab}} = 162^\circ$ . The quoted uncertainties correspond to one standard deviation.

# Chapter 7

## Conclusions

The  ${}^7\text{Li}(p,\alpha){}^4\text{He}$  and  ${}^6\text{Li}(p,\alpha){}^3\text{He}$  astrophysical  $S$ -factors, were measured concurrently using seven and four targets, respectively.

The  ${}^7\text{Li}(p,\alpha){}^4\text{He}$  bare component of  $S(E)$  was measured from  $E = 89.7$  to  $1740.3$  keV using two LiF targets of different thicknesses and one  ${}^7\text{Li}$  implanted in Al target. The three  $S_b(E)$  data sets obtained are in excellent agreement in the overlapping energy regions, producing a final set that is in very good agreement with previous works for  $E > 400$  keV. Below this energy, a small systematic discrepancy is observed but within error bars.

The  ${}^6\text{Li}(p,\alpha){}^3\text{He}$   $S_b(E)$  was measured at  $E = 90.5$  to  $579.9$  keV using one LiF target, and the results are in very good agreement with previous works.

The smaller quoted uncertainties obtained in this work for both lithium reactions allows to define more accurately the bare  $S$ -factor, including its extrapolation to lower energies. These extrapolations were done using polynomial functions, an approach often used in literature. Even though these parametrizations fit very well  $S_b(E)$ , they lack physical meaning and its results should be taken with caution when doing extrapolations to low energy. A more reliable extrapolation would require doing a  $R$ -matrix fit or a hybrid model fit to the high energy part of the  $S$ -factor. Nevertheless, since the present data for the bare  $S$ -factor shows no significant variations for both reactions, as compared to previous works, the astrophysical consequences, *e.g.*, for primordial nucleosynthesis, remain essentially unchanged.

A new measurement of the  ${}^7\text{Li}(p,\alpha){}^4\text{He}$  angular distributions was done. The calculated  $A_2(E)$  coefficient is in good agreement with previous works. For energies above  $\approx 1100$  keV,

the  $A_4(E)$  coefficient is not zero, so proton partial waves with  $\ell_i = 3$  ( $f$  waves), in addition to  $p$  waves, should also be taken into account for the theoretical description of the entrance channel of this reaction.

The present data for the electron screening in the  ${}^7\text{Li}(p,\alpha){}^4\text{He}$  and  ${}^6\text{Li}(p,\alpha){}^3\text{He}$  reactions for different environments give a consistent picture. As expected, for the  $\text{Li}_2\text{WO}_4$  insulator the  $U_e^{exp}$  values obtained are compatible with the sudden–adiabatic limits range calculated from atomic-physics models. The Li metal and  $\text{PdLi}_x$  alloys exhibit an additional acceleration mechanism due to the quasi-free metallic electrons at the Debye radius: (i) in comparison to the data in the  $\text{D}(d,p)\text{T}$  reaction for metals, the screening potential energy scales with the charge  $Z_t$  of the target nucleus, as expected from the Debye model; (ii) the isotopic independence of this model, *i.e.*, the same  $U_D$  for  ${}^7\text{Li}$  and  ${}^6\text{Li}$  nuclides, was verified.

Previous and more recent experimental data confirm the Debye model showing that it is not restricted to reactions among light nuclides, it is an effect in the entrance channel of the reaction, and that it changes the half-lives of radioactive nuclides.

The ability of the Debye model to explain (and predict) the high  $U_e$  values observed in metallic environments is very important for stellar evolution and BBN models since, by showing that laboratory measurements are well understood, we can rely on the cross sections input parameters for these models.

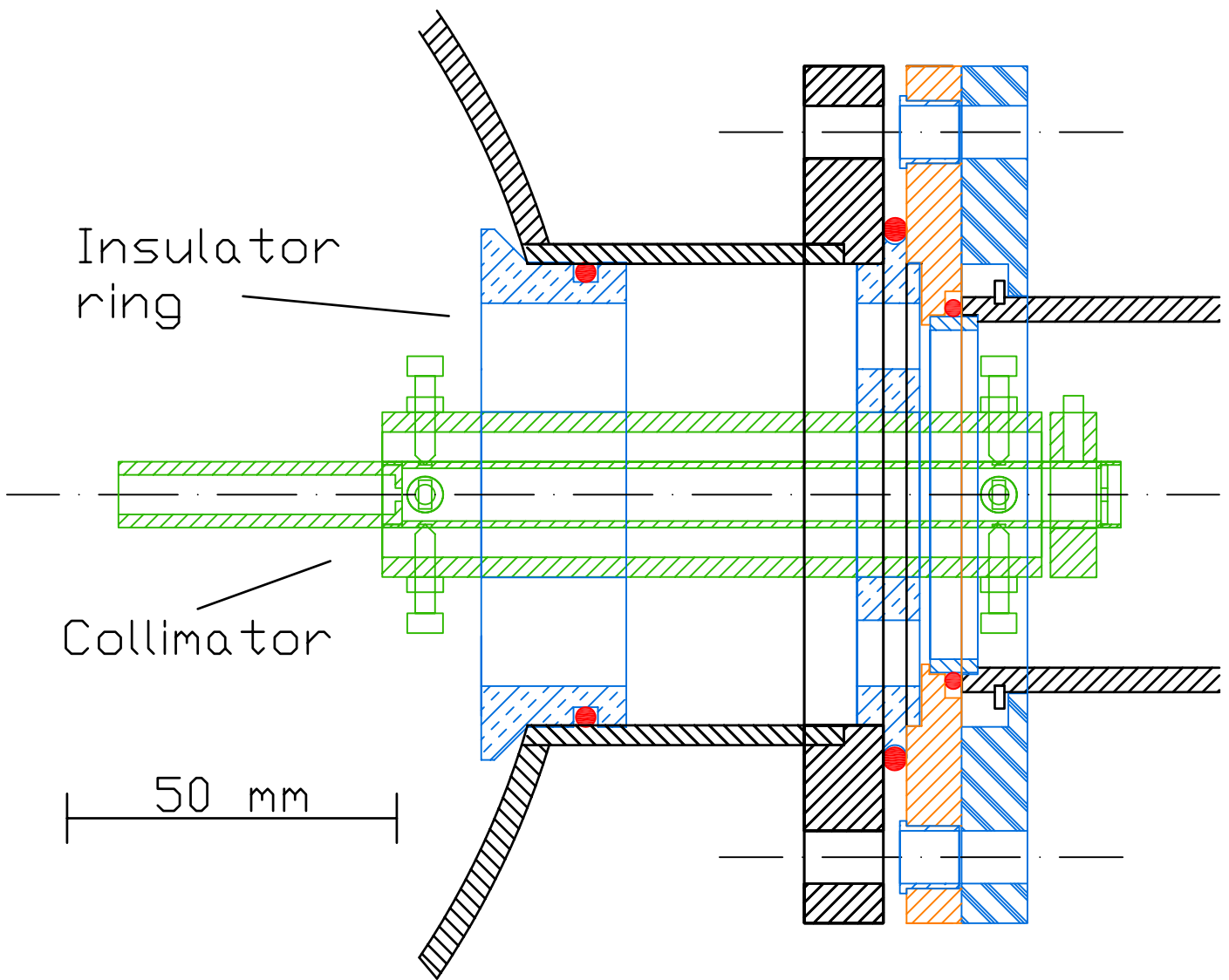
Clearly, an improved theory is highly desirable to explain why the simple Debye model appears to work so well. Without such a theory, one may consider the Debye model as a powerful parametrization of the data.

The  ${}^7\text{Li}(p,p){}^7\text{Li}$  differential cross section was measured from  $E_{\text{lab}} = 419.7$  to  $1021.8$  keV using one LiF target. A hybrid model that uses a combination of optical potentials to describe direct mechanisms and  $R$ -matrix theory to describe resonances, was used to adjust our data, alongside with other data sets from  ${}^7\text{Li}$  elastic and inelastic scattering. The hybrid model fits well experimental data but the values obtained for the resonance energies and widths don't match the reference values, which seems to indicate that the theoretical model still needs some tuning. It would be very interesting to apply this model to the  ${}^7\text{Li}(p,\alpha){}^4\text{He}$  reaction, and compare with it with  $R$ -matrix results, and polynomial extrapolations.

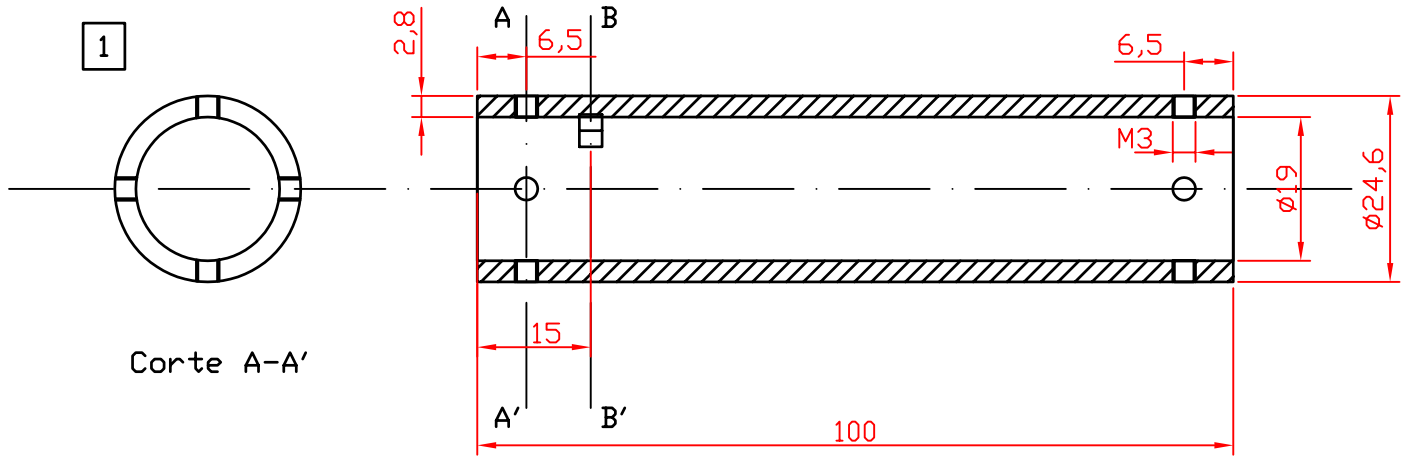
# **Appendix A**

## **ITN target chamber blueprints**

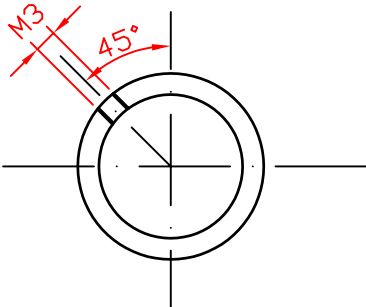




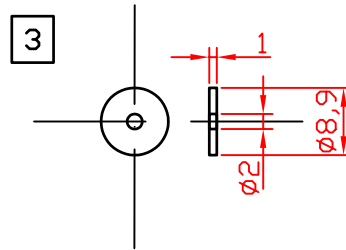
1	Collimador		AISI 304	3				
1	Tubo dos colimadores		AISI 304	2				
1	Tubo de suporte		AISI 304	1				
Nº	DESIGNAÇÃO	Nº DA NORMA Nº DO DESENHO	MATERIAL	Nº REF	PRODUTO SEMI ACABADO Nº DO MOLDE Nº DA MATRIZ	PESO	OBSERVAÇÕES	
Projectou	João Cruz		Câmara PIGE/PIXE/NRA			ITN / CFNUL / FCT-UNL		
Desenhou	João Cruz							COLLIMS9.DWG
Copiou								
Verificou								
Escala 1/1		SISTEMA DE COLIMAÇÃO DO FEIXE						
Tolerância ± 0,1								



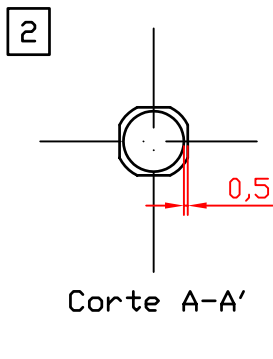
Corte A-A'



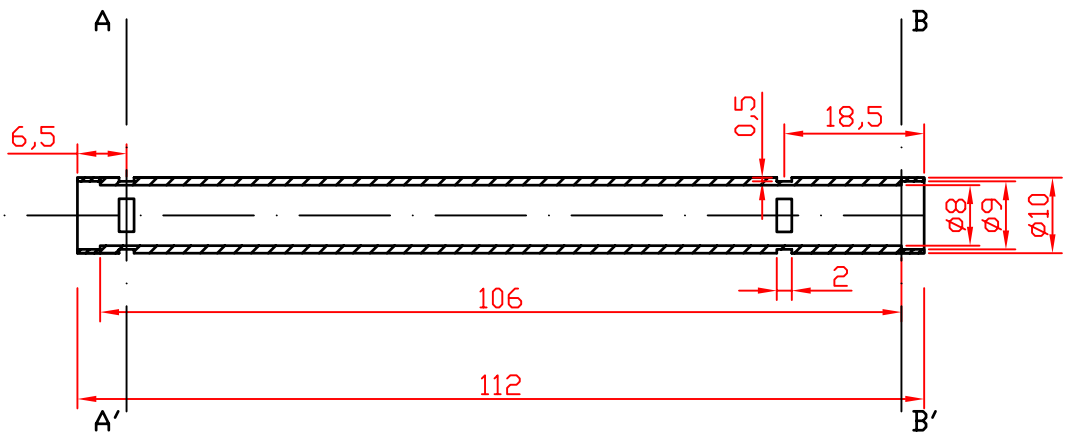
Corte B-B'



3

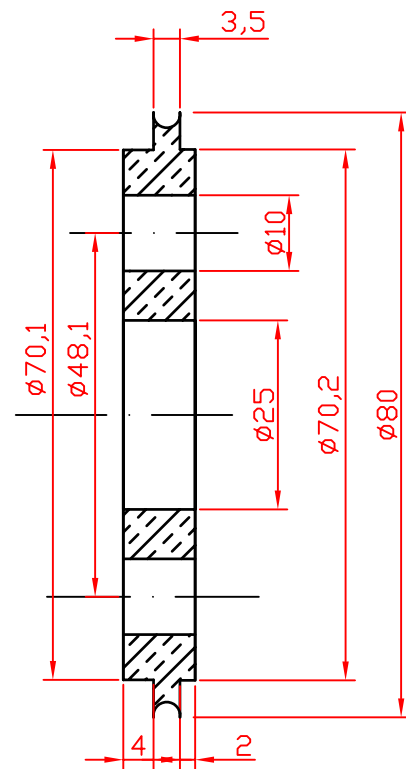
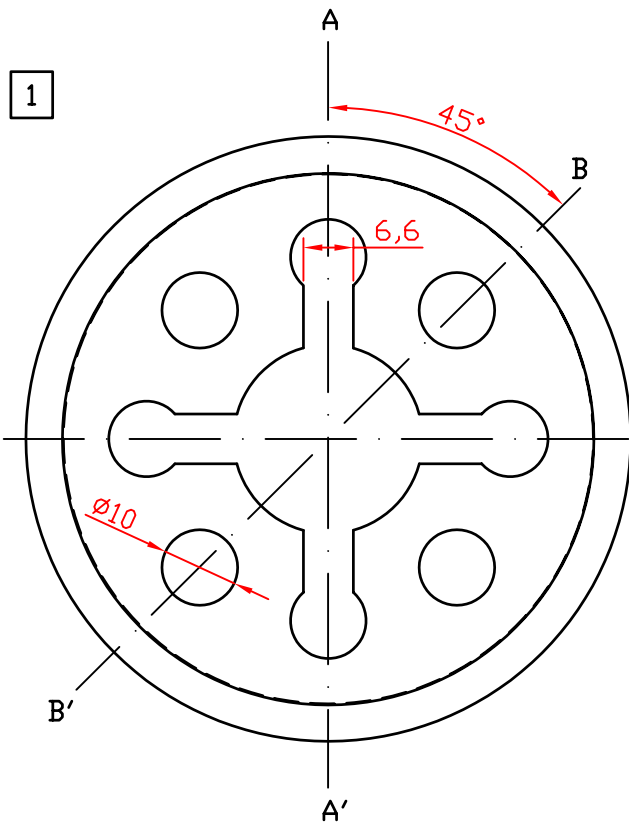


Corte A-A'

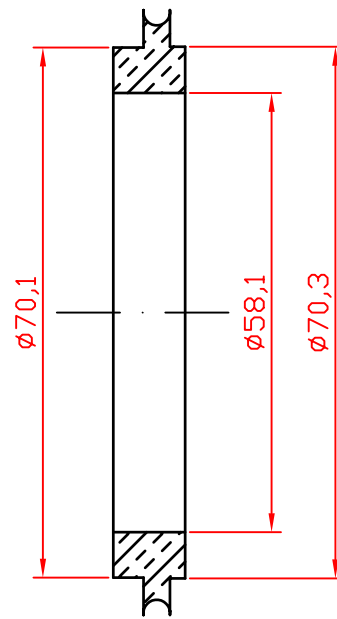
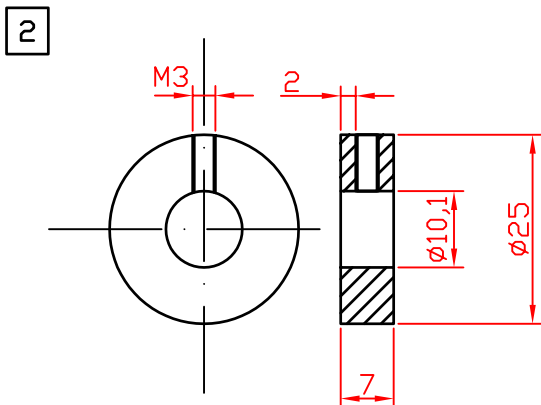


Corte B-B'

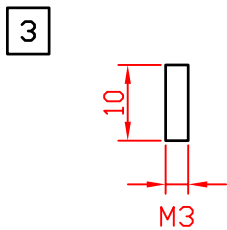
1	Collimador		AISI 304	3				
1	Tubo dos colimadores		AISI 304	2				
1	Tubo de suporte		AISI 304	1				
Nº	DESIGNAÇÃO	Nº DA NORMA Nº DO DESENHO	MATERIAL	Nº REF	PRODUTO SEMI ACABADO Nº DO MOLDE Nº DA MATRIZ	PESO	OBSERVAÇÕES	
Projectou	João Cruz		<p>Câmara PIGE/PIXE/NRA</p>			<p>ITN / CFNUL / FCT-UNL</p>		
Desenhou	João Cruz							<p>COLLIMS9P1.DWG</p>
Coplou								
Verificou								
Escala 1/1		<p>SISTEMA DE COLIMAÇÃO DO FEIXE</p>						
Tolerância ± 0,1								



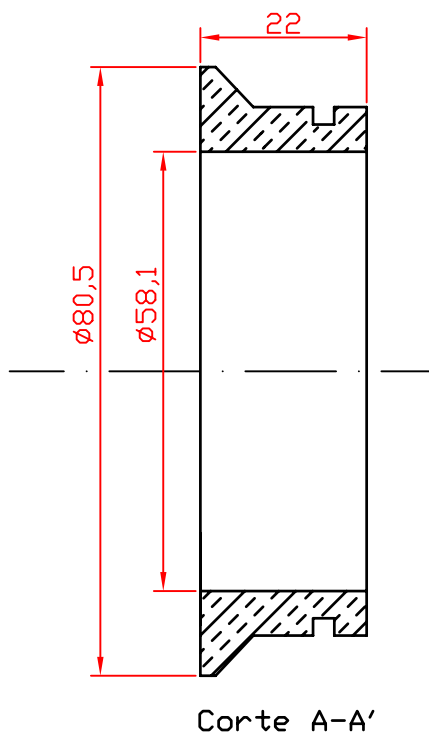
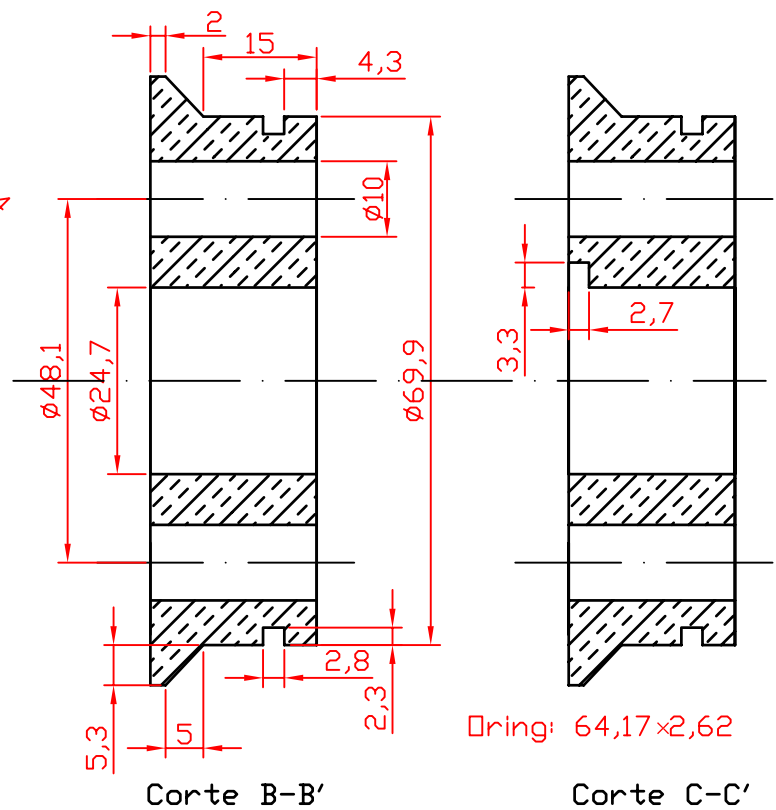
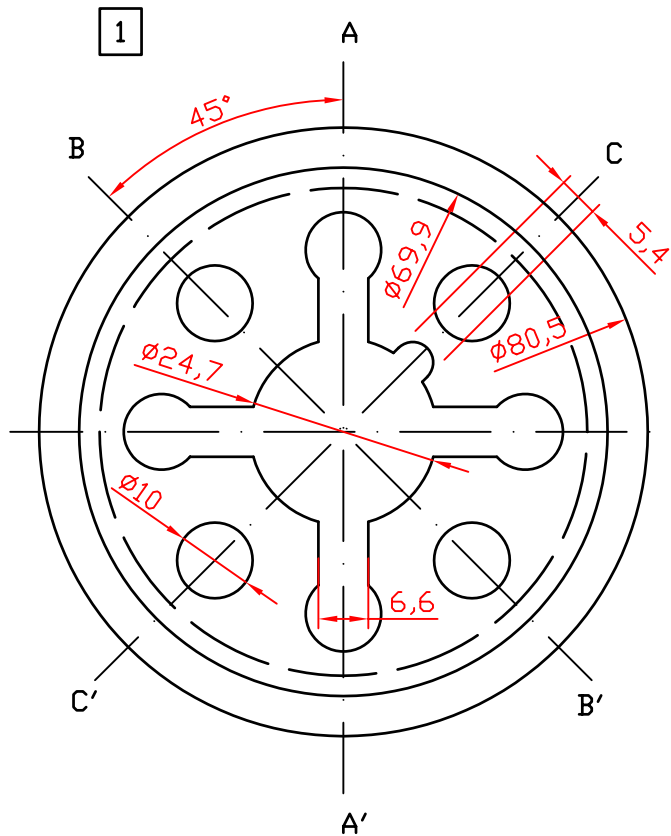
Corte B-B'



Corte A-A'

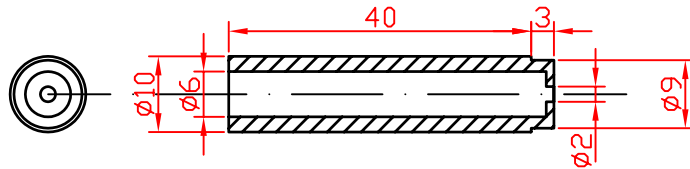


1	Perne		AISI 304	3			
1	Beam stopper		AISI 304	2			
1	Suporte do oring		ACRÍLICO	1			
Nº	DESIGNAÇÃO	Nº DA NORMA Nº DO DESENHO	MATERIAL	Nº REF	PRODUTO SEMI ACABADO Nº DO MOLDE Nº DA MATRIZ	PESO	OBSERVAÇÕES
Projectou	João Cruz	<p>Câmara PIGE/PIXE/NRA</p>				ITN / CFNUL / FCT-UNL	
Desenhou	João Cruz					COLLIMS9P2.DWG	
Coplou							
Verificou							
Escala 1/1		SISTEMA DE COLIMAÇÃO DO FEIXE					
Tolerância ± 0,1							

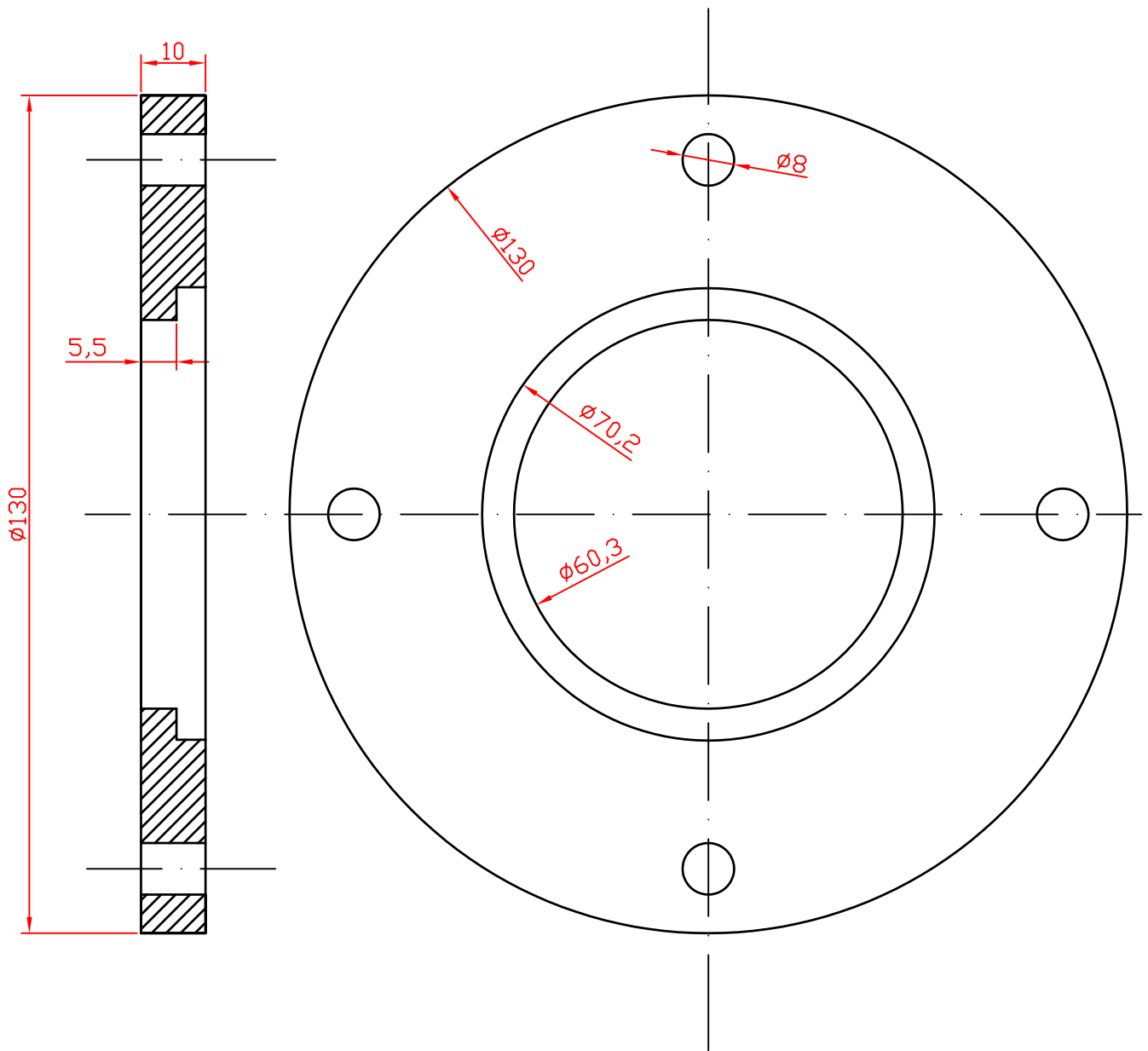


1	Suporte		Polipropileno	1					
Nº	DESIGNAÇÃO		Nº DA NORMA Nº DO DESENHO	MATERIAL	Nº REF	PRODUTO SEMI ACABADO Nº DO MOLDE Nº DA MATRIZ	PESO OBSERVAÇÕES		
Projectou	João Cruz		Câmara PIGE/PIXE/NRA			ITN / CFNUL / FCT-UNL			
Desenhou	João Cruz					COLLIMS9P3.DWG			
Coplou									
Verificou									
Escala 1/1			SISTEMA DE COLIMAÇÃO DO FEIXE						
Tolerância $\pm 0,1$									

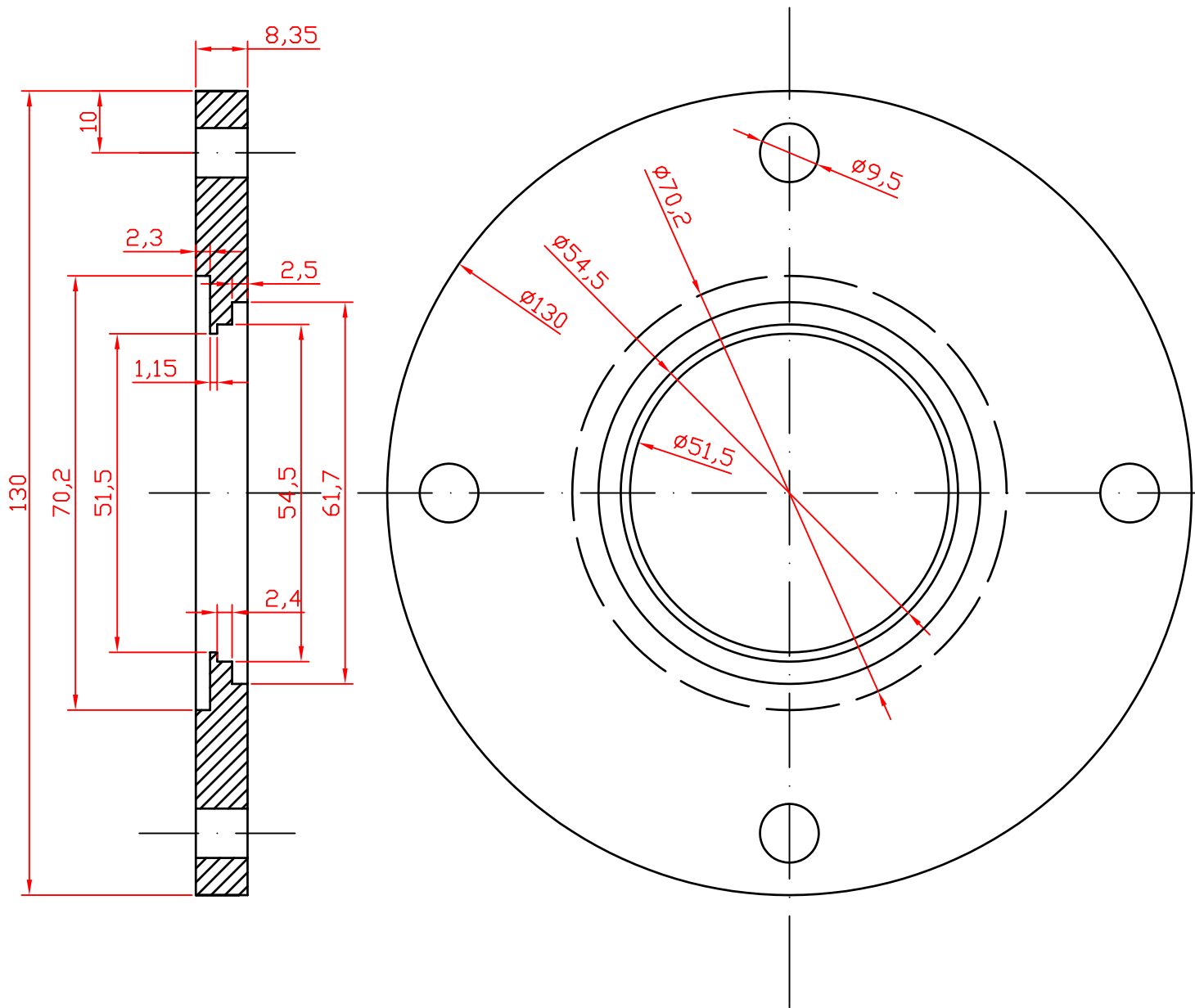
1



1	Extensómetro com colimador		AISI 304	1											
Nº	DESIGNAÇÃO	Nº DA NORMA Nº DO DESENHO	MATERIAL	Nº REF	PRODUTO SEMI ACABADO Nº DO MOLDE Nº DA MATRIZ	PESO	OBSERVAÇÕES								
Projectou	João Cruz		<p>Câmara PIGE/PIXE/NRA</p>			<p>ITN / CFNUL / FCT-UNL</p>									
Desenhou	João Cruz							<p>COLLIMS9P4.DWG</p>							
Coplou															
Verificou															
Escala 1/1		<p>SISTEMA DE COLIMAÇÃO DO FEIXE</p>			<table border="1" style="width: 100%; height: 20px;"> <tr> <td></td><td></td><td></td><td></td><td></td><td></td><td></td><td></td> </tr> </table>										
Tolerância $\pm 0,1$															



1	Flange isolante		PVC	1					
Nº	DESIGNAÇÃO	Nº DA NORMA Nº DO DESENHO	MATERIAL	Nº REF	PRODUTO SEMI ACABADO Nº DO MOLDE Nº DA MATRIZ	PESO	OBSERVAÇÕES		
Projectou	João Cruz		Câmara PIGE/PIXE/NRA			ITN / CFNUL / FCT-UNL			
Desenhou	João Cruz							SHIELDING2A.DWG	
Copiou									
Verificou									
Escala 1/1		Flange isolante para tubo de entrada na câmara							
Tolerância ± 0,1									

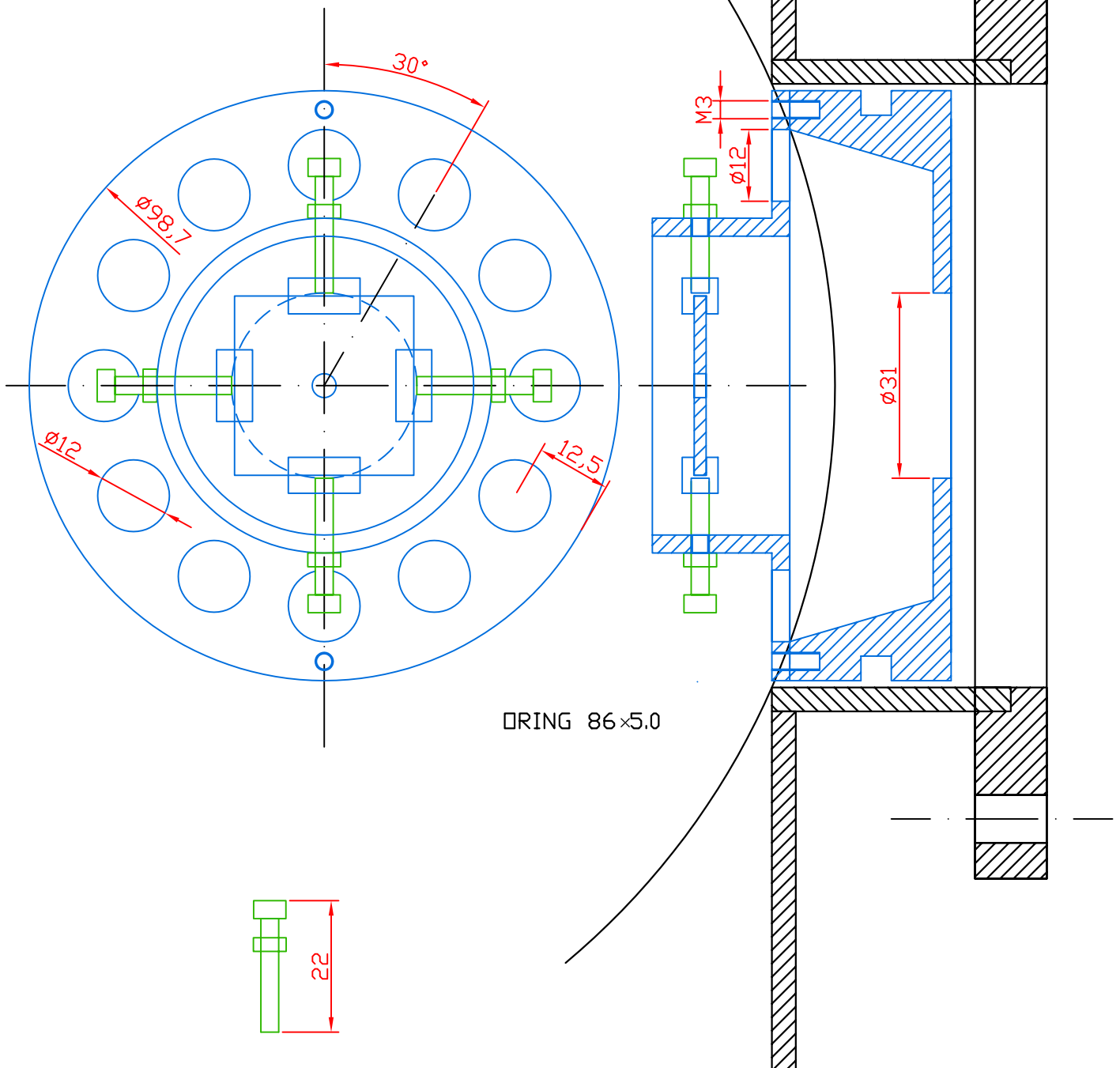


1	Flange isolante		Alumínio	1						
Nº	DESIGNAÇÃO	Nº DA NORMA Nº DO DESENHO	MATERIAL	Nº REF	PRODUTO SEMI ACABADO Nº DO MOLDE Nº DA MATRIZ	PESO	OBSERVAÇÕES			
Projectou	João Cruz		<p>Câmara PIGE/PIXE/NRA</p>				ITN / CFNUL / FCT-UNL			
Desenhou	João Cruz						SHIELDING2B_V2.DWG			
Coplou										
Verificou										
Escala 1/1		Flange isolante para tubo de entrada na câmara								
Tolerância ± 0,1										

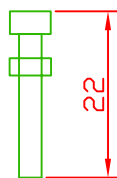
Top view

ISO 100

Front view



ORING 86x5.0



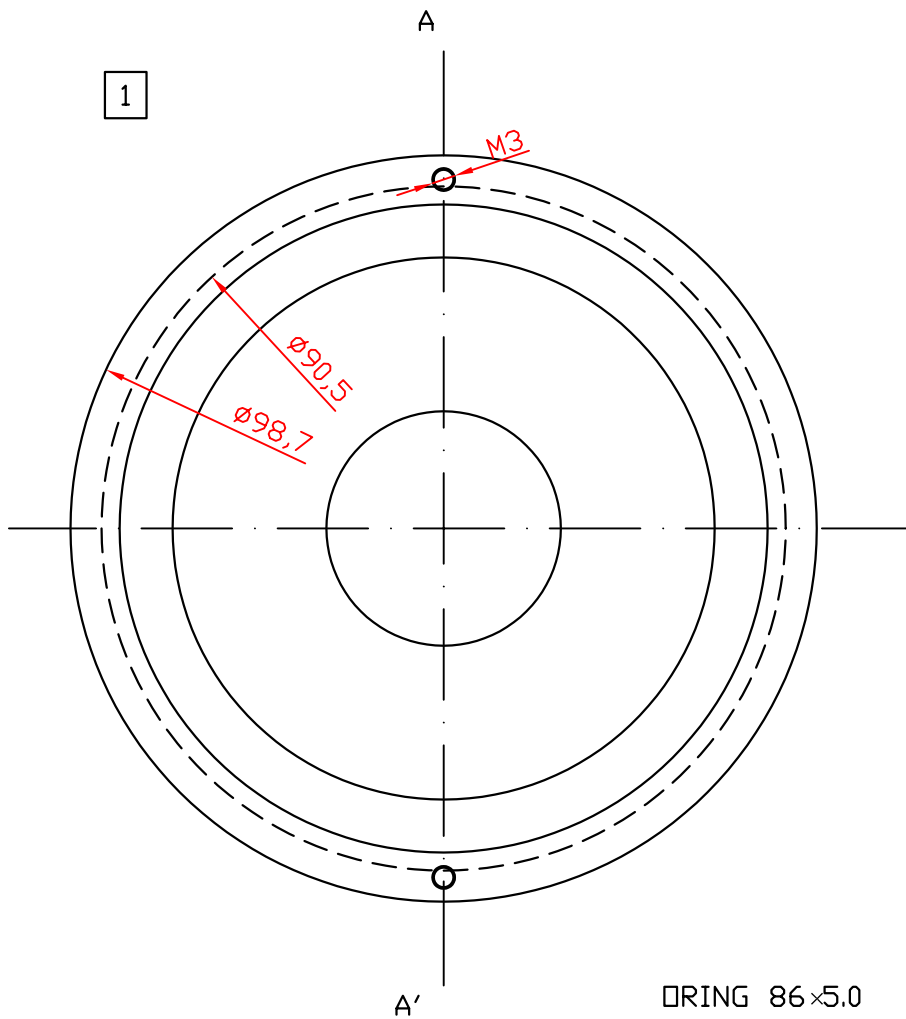
Projectou	João Cruz	
Desenhou	João Cruz	
Coplou		
Verificou		
Escala 1/1		
Tolerância ± 0,1		

Câmara  
PIGE/PIXE/NRA

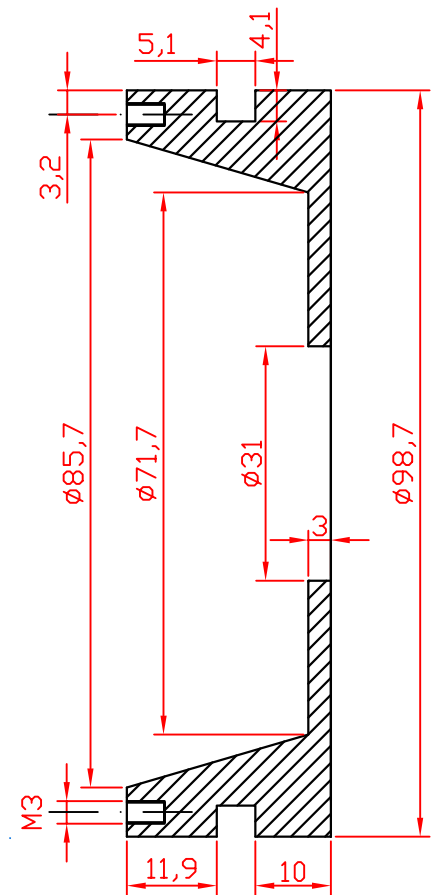
ITN / CFNUL / FCT-UNL

BEAM\_STOPPER\_b.DWG

BEAM STOPPER

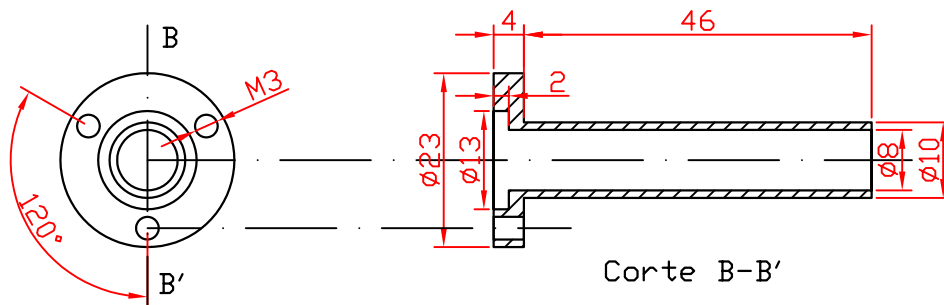



ORING 86x5.0



Corte A-A'

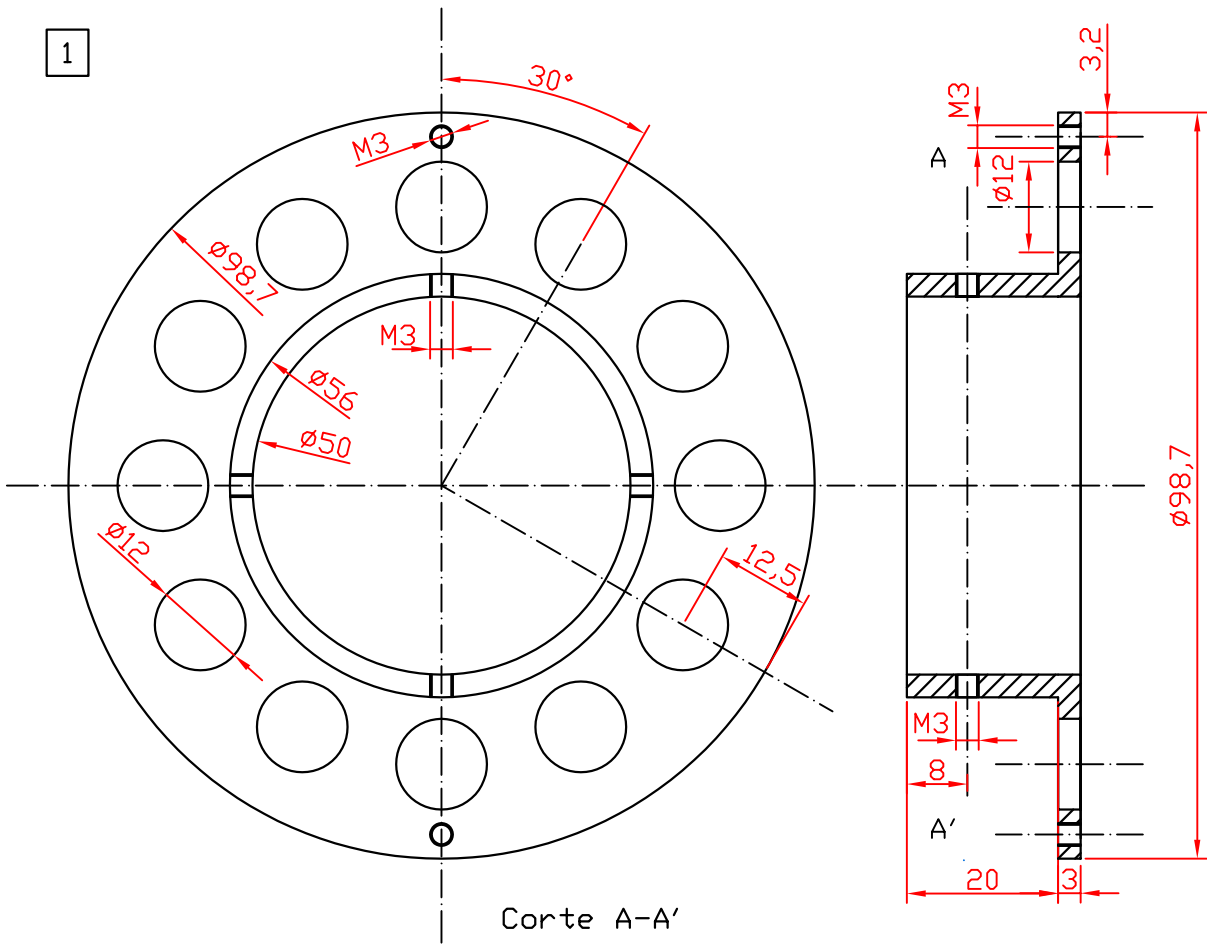
2



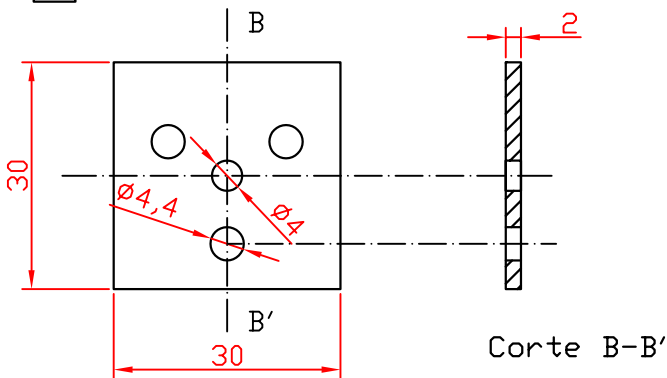
Corte B-B'

1	Extensómetro		AISI 304	2					
1	Peça de encaixe à flange		AISI 304	1					
Nº	DESIGNAÇÃO	Nº DA NORMA Nº DO DESENHO	MATERIAL	Nº REF	PRODUTO SEMI ACABADO Nº DO MOLDE Nº DA MATRIZ	PESO	OBSERVAÇÕES		
Projectou	João Cruz		<p>Câmara PIGE/PIXE/NRA</p>				ITN / CFNUL / FCT-UNL		
Desenhou	João Cruz						BEAM_STOPPER_bP1.DWG		
Coplou									
Verificou									
Escala 1/1		BEAM STOPPER							
Tolerância $\pm 0,1$									

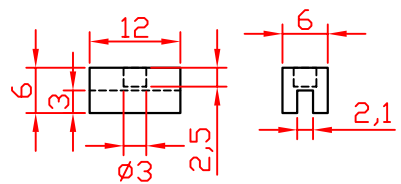
1



2



3



4	Suporte		AISI 304	3				
1	Beam stopper		AISI 304	2				
1	Peça suporte beam stopper		AISI 304	1				
Nº	DESIGNAÇÃO	Nº DA NORMA Nº DO DESENHO	MATERIAL	Nº REF	PRODUTO SEMI ACABADO Nº DO MOLDE Nº DA MATRIZ	PESO	OBSERVAÇÕES	
Projectou	João Cruz		Câmara PIGE/PIXE/NRA				ITN / CFNUL / FCT-UNL  BEAM_STOPPER_bP2.DWG	
Desenhou	João Cruz							
Coplou								
Verificou								
Escala 1/1		BEAM STOPPER						
Tolerância ± 0,1								

## **Appendix B**

### **${}^7\text{Li}(\text{p},\alpha){}^4\text{He}$ angular distributions tables**

$E = 1740$ keV			$E = 1609$ keV			$E = 1477$ keV		
$\cos^2 \theta$	$W(E, \theta)$	$\delta W(E, \theta)$	$\cos^2 \theta$	$W(E, \theta)$	$\delta W(E, \theta)$	$\cos^2 \theta$	$W(E, \theta)$	$\delta W(E, \theta)$
	(rel.units)	(rel.units)		(rel.units)	(rel.units)		(rel.units)	(rel.units)
0.001	47.00	0.80	0.001	38.51	0.89	0.001	30.41	0.61
0.034	47.64	0.77	0.032	37.64	1.36	0.031	30.76	0.61
0.127	51.12	0.56	0.125	40.44	0.49	0.122	33.46	0.45
0.258	55.60	0.71	0.255	45.75	0.53	0.252	36.75	0.47
0.412	60.23	0.85	0.409	49.54	0.59	0.406	42.31	0.51
0.485	62.36	1.33	0.482	51.56	1.32	0.479	43.65	0.72
0.573	64.13	0.63	0.570	54.20	0.57	0.568	45.55	0.53
0.643	66.81	0.89	0.641	56.21	0.88	0.638	47.76	0.75
0.724	68.00	0.64	0.722	57.93	0.53	0.720	49.37	0.55
0.798	69.95	0.93	0.796	60.21	1.30	0.795	50.50	1.46
0.857	69.11	0.77	0.856	59.14	0.86	0.855	51.25	0.80
0.907	70.52	0.94	0.906	59.96	0.87	0.905	52.73	0.81
0.947	70.34	1.35	0.947	60.06	0.71	0.946	52.82	0.81

Table B.1: Angular distributions,  $W(E, \theta)$ , of the  ${}^4\text{He}$  particles for the  ${}^7\text{Li}(p,\alpha){}^4\text{He}$  reaction at  $E = 1740$ , 1609 and 1477 keV. The quoted uncertainties are only statistical.

$E = 1345$ keV			$E = 1214$ keV			$E = 1081$ keV		
$\cos^2 \theta$	$W(E, \theta)$	$\delta W(E, \theta)$	$\cos^2 \theta$	$W(E, \theta)$	$\delta W(E, \theta)$	$\cos^2 \theta$	$W(E, \theta)$	$\delta W(E, \theta)$
	(rel.units)	(rel.units)		(rel.units)	(rel.units)		(rel.units)	(rel.units)
0.001	24.03	0.38	0.009	18.98	0.51	0.001	15.96	0.56
0.029	23.35	0.60	0.028	19.53	0.62	0.027	14.79	0.54
0.120	26.38	0.42	0.121	21.10	1.08	0.109	17.27	0.41
0.248	30.02	0.40	0.182	22.80	0.56	0.241	20.16	0.82
0.402	34.66	0.46	0.244	24.71	0.57	0.395	24.92	0.80
0.475	35.89	0.90	0.326	26.33	1.57	0.558	27.19	0.52
0.564	39.43	0.60	0.406	28.20	0.83	0.713	32.04	0.71
0.636	40.66	0.57	0.487	30.40	0.92	0.851	35.68	0.84
0.718	41.74	0.46	0.561	32.70	0.80	0.945	35.64	0.60
0.793	45.21	0.87	0.648	32.60	0.55			
0.853	46.22	0.76	0.722	35.13	1.35			
0.905	45.34	1.09	0.852	37.96	0.87			
0.946	46.42	1.02	0.945	38.98	0.90			

Table B.2: Angular distributions,  $W(E, \theta)$ , of the  ${}^4\text{He}$  particles for the  ${}^7\text{Li}(p,\alpha){}^4\text{He}$  reaction at  $E = 1345$ , 1214 and 1081 keV. The quoted uncertainties are only statistical.

$E = 949$ keV			$E = 817$ keV			$E = 685$ keV		
$\cos^2 \theta$	$W(E, \theta)$	$\delta W(E, \theta)$	$\cos^2 \theta$	$W(E, \theta)$	$\delta W(E, \theta)$	$\cos^2 \theta$	$W(E, \theta)$	$\delta W(E, \theta)$
	(rel.units)	(rel.units)		(rel.units)	(rel.units)		(rel.units)	(rel.units)
0.001	12.46	0.49	0.001	11.16	0.46	0.001	9.08	0.30
0.025	12.18	0.49	0.023	10.76	0.45	0.021	9.66	0.30
0.106	14.40	0.38	0.102	11.45	0.33	0.097	10.15	0.38
0.237	17.38	0.48	0.232	14.22	0.71	0.226	12.57	0.25
0.390	20.78	0.45	0.386	17.18	0.41	0.379	14.06	0.36
0.554	24.19	0.40	0.550	20.30	0.44	0.544	17.27	0.59
0.710	28.09	0.69	0.707	22.63	0.57	0.703	19.33	0.44
0.849	30.28	0.55	0.847	25.67	0.71	0.845	22.12	0.47
0.944	31.97	0.96	0.943	26.93	0.52	0.942	23.07	0.46

Table B.3: Angular distributions,  $W(E, \theta)$ , of the  ${}^4\text{He}$  particles for the  ${}^7\text{Li}(p,\alpha){}^4\text{He}$  reaction at  $E = 949$ , 817 and 685 keV. The quoted uncertainties are only statistical.

$E = 551$ keV			$E = 418$ keV			$E = 274$ keV		
$\cos^2 \theta$	$W(E, \theta)$	$\delta W(E, \theta)$	$\cos^2 \theta$	$W(E, \theta)$	$\delta W(E, \theta)$	$\cos^2 \theta$	$W(E, \theta)$	$\delta W(E, \theta)$
	(rel.units)	(rel.units)		(rel.units)	(rel.units)		(rel.units)	(rel.units)
0.001	8.04	0.19	0.002	6.45	0.25	0.003	3.98	0.24
0.019	7.99	0.31	0.017	6.17	0.24	0.014	3.84	0.17
0.093	8.25	0.14	0.088	6.35	0.17	0.083	4.00	0.08
0.221	10.02	0.18	0.215	7.43	0.19	0.207	4.08	0.08
0.374	11.24	0.22	0.367	8.23	0.39	0.359	4.44	0.08
0.539	13.35	0.27	0.534	9.03	0.21	0.526	4.96	0.09
0.699	14.66	0.22	0.695	9.82	0.18	0.690	5.06	0.09
0.843	16.12	0.40	0.840	11.21	0.33	0.837	5.66	0.14
0.941	17.40	0.53	0.940	11.57	0.24	0.939	5.81	0.14

Table B.4: Angular distributions,  $W(E, \theta)$ , of the  ${}^4\text{He}$  particles for the  ${}^7\text{Li}(p,\alpha){}^4\text{He}$  reaction at  $E = 551$ , 418 and 274 keV. The quoted uncertainties are only statistical.

$E = 150$ keV			$E = 80$ keV		
$\cos^2 \theta$	$W(E, \theta)$	$\delta W(E, \theta)$	$\cos^2 \theta$	$W(E, \theta)$	$\delta W(E, \theta)$
	(rel.units)	(rel.units)		(rel.units)	(rel.units)
0.004	1.020	0.040	0.006	0.074	0.006
0.012	1.060	0.040	0.009	0.081	0.004
0.077	0.970	0.030	0.072	0.079	0.004
0.199	1.070	0.030	0.198	0.078	0.003
0.350	1.100	0.030	0.342	0.081	0.004
0.518	1.110	0.030	0.502	0.080	0.006
0.683	1.150	0.030	0.678	0.084	0.003
0.833	1.220	0.050	0.830	0.081	0.007
0.938	1.270	0.050	0.937	0.077	0.006

Table B.5: Angular distributions of the  ${}^4\text{He}$  particles for the  ${}^7\text{Li}(p,\alpha){}^4\text{He}$  reaction at  $E = 150$  and  $80$  keV. The quoted uncertainties are only statistical.

$E$ (keV)	$A_2(E)$	$A_4(E)$	$\chi^2$
1740	$0.321 \pm 0.009$	$-0.060 \pm 0.012$	0.44
1609	$0.382 \pm 0.011$	$-0.069 \pm 0.013$	1.27
1477	$0.438 \pm 0.009$	$-0.051 \pm 0.011$	0.66
1345	$0.533 \pm 0.011$	$-0.028 \pm 0.015$	1.60
1214	$0.559 \pm 0.018$	$-0.035 \pm 0.023$	0.71
1081	$0.669 \pm 0.019$	0	2.22
949	$0.736 \pm 0.020$	0	0.33
817	$0.724 \pm 0.022$	0	1.09
685	$0.702 \pm 0.019$	0	1.02
551	$0.604 \pm 0.012$	0	1.68
418	$0.473 \pm 0.017$	0	1.15
274	$0.314 \pm 0.019$	0	1.63
150	$0.149 \pm 0.025$	0	1.00
80	$0.036 \pm 0.045$	0	0.41

Table B.6:  $A_2(E)$  and  $A_4(E)$  coefficients values obtained from  $\chi^2$  fits to the angular distributions of the  ${}^4\text{He}$  particles for the  ${}^7\text{Li}(p,\alpha){}^4\text{He}$  reaction. The quoted uncertainties correspond to one standard deviation.

## **Appendix C**

### **FORTRAN programs**



Jan 25, 07 3:03	xs519-125.f	Page 4/8
c	<pre> parameter(pi=3.14159d0) common/datavct/ecm(kpoints),yield(kpoints),eyield(kpoints) external fdat lff=29 open(lff,file='xs519-125.txt',status='old') do i=1,kpoints   read(lff,*) edum,rfrac(i) enddo close(lff) lfout=30 open(lfout,file='xs519-125.txt',status='unknown') mli=7.016d0 mh=1.008d0 sangle=3.751d-3*1.05 pcharge=1.602d-19 conv=1.0d24 c-----ys gives the ratio between Yield and S(E) ----- eps=i.d-10 do j=1,kpoints   ys=0.d0   ehig=ecm(j)   do i=1,nlay     if (ehigh.lt.150) write(*,*) 'Ecm bef=',ehigh     call stopping(ehigh,i,sp,deltae)     if (deltae.gt.ehigh) then       deltae=ehigh       write(*,*) 'layer=',i     endif     elow=ehigh-deltae     ys=ys+dgauss(fdat,elow,ehigh,eps)/sp     if (elow.le.0.) goto 10   enddo   c---Also tried dquad from CERLIB to make the numerical integration.---   c---There is no difference between dgauss and dquad.-----   ehig=elow enddo c---Compute effective energy----- 10 ehig=ecm(j)   eeff=ehigh   f1=dgauss(fdat,elow,ehigh,eps)   f2=dgauss(fdat,eeff,ehigh,eps)   f3=f1-2.*f2   write(*,*) f1,f2,f3   if (f3.gt.1.d-10) then     eeff=eeff-.01     goto 20   endif c---Compute K factor-----   elab=eeff*(mli+mh)/mli   call kfactor(elab,c2cm,kk)   write(*,*) 'Elab, kk =',elab,kk c---Compute W(E,theta)-----   call wfactor(eeff,c2cm,ww,dwda2sq) c---Compute S-factor-----   sfact=1.01*4.*pi*yield(j)*Id6*pcharge*conv/(2.d0*sangle*kk*ww*ys)   dsdy2=(sfact/yeild(j))**2   esfact=dsqrt(dsdy2*eyield(j)**2+(0.06*sfact)**2)   &amp;+((1.d0-rfrac(j))*sfact)**2+dwda2sq*(sfact/ww)**2   dum=dsqrt(dwda2sq)*(sfact/ww)/esfact </pre>	

Jan 25, 07 3:03	xs519-125.f	Page 3/8
c	<pre> pc3(1)=1.69860e1 pc3(2)=-3.57315e-2 pc3(3)=4.33747e-5 pc3(4)=-2.60225e-8 pc3(5)=6.01429e-12 c-----(.le. 2000 keV)----- pc4(1)=7.65502 pc4(2)=-3.87513e-3 pc4(3)=7.32867e-7 c---Layers thickness (in 10^15 at/cm^2): tlay ---- c---atomic fraction of li per layer: flj ----- c---atomic fraction of Al per layer: fal ----- c---atomic fraction of O per layer: fo ----- c---Total number of layers = 14 ----- c---open(30,file='s7li04-v2.txt',status='old') do i=1,nlay   read(30,*) tlay(i),fc(i),fo(i),flj(i),fal(i) enddo close(30) c---fim subroutine initpar----- return end c--- c---subroutine initdat(nhistro,icut) c--- c---Read input file. c--- parameter(kpoints=32) common/datavct/ecm(kpoints),yield(kpoints),eyield(kpoints) common/quest/iquest(100) call holelet(0) c--- open(30,file='7li519-125.txt',status='old') do i=1,kpoints   read(30,*) ecm(i),yield(i),eyield(i) enddo close(30) c--- write(*,*) return end c---fim subroutine initdat----- c--- subroutine calculo c--- Calculate the S-factor by the integral method. c--- parameter(nlay=14) parameter(kpoints=32) real*8 ys,fdat,ehigh,elow,eps,sp,deltae real*8 sangle,pcharge,conv,kk,ww,sfact,esfact,dsdy2 real*8 mli,mh,elab,pi,eeff,f1,f2,f3,c2cm,dwda2sq real*8 edum,rfrac(kpoints) integer nlayi </pre>	



```

Jan 25, 07 3:03          xs519-125.f          Page 8/8
c-----fim subroutine stopping -----
end

c-----function fdat(ecm)-----
real*8 ecm,arg,zh,zii,mh,mli,reducma
parameter(zh=1.d0,zii=3.d0)
mli=7.016d0
mh=1.008d0
reducma=mli*mh/(mli+mh)
arg=-31.29d0*zh*zii*dsqrt(reducma/ecm)
fdat=exp(arg)/ecm
return
end
    
```

```

Jan 25, 07 3:03          xs519-125.f          Page 7/8
c-----
cpcab=ebonds+ecore
epbragg=(14.03d0+15.44d0)/2.d0
fac=ff*epcab/epbragg
if (fac.lt.1.d0) fac=1.d0
c-----
c      stpoi=.95*stpci
c      stpci=.95*stpoi
c      stpoi=1.05*stpci
c      stpci=1.05*stpoi
c-----
deltaej=fac*160.0*(0.5*stpoi+0.5*stpci)/1.d3
elab=elab-deltaej
ecm=elab*mli/(mli+mh)
c-----
if (elab.le.100.d0) then
  stpi=plii(1)+plii(2)*elab+plii(3)*elab**2+plii(4)*elab**3+
  &plii(5)*elab**4+plii(6)*elab**5
  stpal=pal1(1)+pal1(2)*elab+pal1(3)*elab**2+pal1(4)*elab**3+
  &pal1(5)*elab**4+pal1(6)*elab**5
  stpo=poi(1)+poi(2)*elab+poi(3)*elab**2+poi(4)*elab**3+
  &poi(5)*elab**4+poi(6)*elab**5
  stpc=pci(1)+pci(2)*elab+pci(3)*elab**2+pci(4)*elab**3+
  &pci(5)*elab**4+pci(6)*elab**5
else if (elab.lt.300.d0) then
  stpi=plii(1)+plii(2)*elab+plii(3)*elab**2+plii(4)*elab**3+
  &plii(5)*elab**4+plii(6)*elab**5+plii(7)*elab**6
  stpal=pal2(1)+pal2(2)*elab+pal2(3)*elab**2+pal2(4)*elab**3+
  &pal2(5)*elab**4+pal2(6)*elab**5+pal2(7)*elab**6
  stpo=poi(1)+poi(2)*elab+poi(3)*elab**2+poi(4)*elab**3+
  &poi(5)*elab**4+poi(6)*elab**5
  stpc=pci(1)+pci(2)*elab+pci(3)*elab**2+pci(4)*elab**3+
  &pci(5)*elab**4+pci(6)*elab**5
else if (elab.lt.1300.d0) then
  stpi=plii(1)+plii(2)*elab+plii(3)*elab**2+plii(4)*elab**3+
  &plii(5)*elab**4+plii(6)*elab**5+plii(7)*elab**6
  stpal=pal2(1)+pal2(2)*elab+pal2(3)*elab**2+pal2(4)*elab**3+
  &pal2(5)*elab**4+pal2(6)*elab**5+pal2(7)*elab**6
  stpo=poi(1)+poi(2)*elab+poi(3)*elab**2+poi(4)*elab**3+
  &poi(5)*elab**4+poi(6)*elab**5
  stpc=pci(1)+pci(2)*elab+pci(3)*elab**2+pci(4)*elab**3+
  &pci(5)*elab**4+pci(6)*elab**5
else if (elab.le.2100.d0) then
  stpi=plii(1)+plii(2)*elab+plii(3)*elab**2
  stpal=pal3(1)+pal3(2)*elab+pal3(3)*elab**2
  stpo=poi(1)+poi(2)*elab+poi(3)*elab**2
  stpc=pci(1)+pci(2)*elab+pci(3)*elab**2
endif
c-----
c      stpli=.95*stplii
c      stpal=.95*stpal
c      stpo=.95*stpo
c      stpc=.95*stpc
c      stpli=1.05*stplii
c      stpal=1.05*stpal
c      stpo=1.05*stpo
c      stpc=1.05*stpc
c-----
stp=(stpli+fal(ilay)/fli(ilay)*stpal+fo(ilay)/fli(ilay)*stpo+
&fc(ilay)/fli(ilay)*stpc)*1.d-3*1.d-15*mli/(mli+mh)
deltaes=(fli(ilay)*stpi+fai(ilay)*stpal+fo(ilay)*stpo+
&fc(ilay)*stpc)*tlay(ilay)*1d-3*mli/(mli+mh)
return
    
```



Jan 25, 07 3:09	xs6lifu-125.f	Page 4/7
	<pre> call stopping(ehigh,i,sp,deltae) if (deltae.gt.ehigh) then   deltae=ehigh endif elow=ehigh-deltae dintsp=dintsp+dgauss(fdat,elow,ehigh,eps)/sp if (elow.le.0.) goto 10 c---Also tried dquad from CERNLIB to make the numerical integration.--- c---There is no difference between dgauss and dquad.----- ehigh=elow enddo c---Compute effective energy----- 10  ehigh=ecm(j)     eeff=ehigh     f1=dgauss(fdat,elow,ehigh,eps)     f2=dgauss(fdat,eeff,ehigh,eps)     f3=f1-2.*f2     write(*,*) f1,f2,f3     if (f3.gt.1.d-10) then       eeff=eeff-.01       goto 20     endif c---Compute K factor-----     elab=eeff*(mli+mh)/mli     call kfactor(elab,c2cm,kk) c---Compute W(E,theta)-----     call wfactor(eeff,c2cm,ww,dwdalsq) c---Compute S-factor-----     sfact=1.17*1.01*4.*pi*conv*     &amp;ys/dintsp/(sangle*kk*ww)**2     dsdy2=(sfact/yeild(j))**2     esfact=dsqrt(dsdy2*eyield(j)**2+(0.05*sfact)**2)     &amp;+((1.d0-rfrac(j))*sfact)**2+dwdalsq*(sfact/ww)**2 c---Express in Mev-b-----     sfact=sfact/1.d3     esfact=esfact/1.d3 c-----     write(*,*) eeff,sfact,esfact     write(lfout,*) eeff,sfact,esfact enddo close(lfout) return -----fim subroutine calculo ----- end  subroutine wfactor(eeff,c2cm,ww,dwdalsq) c c  Compute W(E,theta) c----- real*8 eeff,c2cm,ww real*8 al,pl,a2,p2 real*8 dalgp(3),ealp(3),dalsq,dwdalsq al=-1.4911d-1+2.24d-3*eeff-2.1034d-6*eeff**2 a2=-2.9d-2-2.6d-4*eeff c----- pl=-dsqrt(c2cm) p2=(3.*c2cm-1.)/2. ww=1.d0+al*pl+a2*p2 c---Compute associated error----- dalgp(1)=1.d0 </pre>	

Jan 25, 07 3:09	xs6lifu-125.f	Page 3/7
	<pre> parameter(kpoints=20) common/datavct(ecm(kpoints),yield(kpoints),eyield(kpoints)) common/quest/iquest(100) call hdelet(0) open(30,file='6lifu-125.txt',status='old') do i=1,kpoints   read(30,*) ecm(i),yield(i),eyield(i) enddo close(30) c----- write(*,*) return end fim subroutine initdat----- end subroutine calculo c c  Calculate the S-factor by the integral method. c----- parameter(nlay=1) parameter(kpoints=20) common/datavct/ecm(kpoints),yield(kpoints),eyield(kpoints) real*8 ys,fdat,ehigh,elow,eps,sp,deltae real*8 sangle,pcharge,conv,kk,ww,sfact,esfact,dsdy2 real*8 mli,mh,elab,pl,f1,f2,f3,eeff real*8 arg,zh,zli,reducma,dintsp,c2cm real*8 edum,rfrac(kpoints),dwdalsq parameter(zh=1.d0,zli=3.d0) parameter(pi=3.14159d0) external fdat c----- lff=29 open(lff,file='xs6lifu-125err.txt',status='old') do i=1,kpoints   read(lff,*) edum,rfrac(i) enddo close(lff) c----- lfout=20 open(lfout,file='xs6lifu-125.txt',status='unknown') mli=6.015121d0 mh=1.008d0 c---CUIDADO: Ang. solidos para LiF e 7Li impl. em Al sao diferentes----- sangle=3.65d-3*1.05 pcharge=1.602d-19 conv=1.0d24 c-----ys gives the ratio N_alpha / N_p ----- eps=1.d-10 reducma=mli*mh/(mli+mh) do j=1,kpoints   dintsp=0.d0   ehigh=ecm(j)   ys=yield(j)*1d6*pcharge   do i=1,nlay </pre>	

xs6lifu-125.f

Thursday January 25, 2007

2/4

```

Jan 25, 07 3:09          xs6lifcu-125.f          Page 6/7
common/layers/tlay(nlay)
mli=6.015121d0
mh=1.008d0
rnf=0.48
rn7li=0.48*.9258
rn6li=0.48*.0742
rnc=0.04
elab=ecm*(mli+mh)/mli
c-----
if (elab.le.100.d0) then
  stpli=pli(1)+pli(2)*elab+pli(3)*elab**2+pli(4)*elab**3+
  &pli(5)*elab**4+pli(6)*elab**5
  stpfpf1(1)+pf1(2)*elab+pf1(3)*elab**2+pf1(4)*elab**3+
  &pf1(5)*elab**4+pf1(6)*elab**5
  stpc=pc1(1)+pc1(2)*elab+pc1(3)*elab**2+pc1(4)*elab**3+
  &pc1(5)*elab**4+pc1(6)*elab**5
else if (elab.lt.300.d0) then
  stpli=pli2(1)+pli2(2)*elab+pli2(3)*elab**2+pli2(4)*elab**3+
  &pli2(5)*elab**4+pli2(6)*elab**5+pli2(7)*elab**6
  stpfpf2(1)+pf2(2)*elab+pf2(3)*elab**2+pf2(4)*elab**3+
  &pf2(5)*elab**4
  stpc=pc2(1)+pc2(2)*elab+pc2(3)*elab**2+pc2(4)*elab**3+
  &pc2(5)*elab**4
else if (elab.lt.1300.d0) then
  stpli=pli2(1)+pli2(2)*elab+pli2(3)*elab**2+pli2(4)*elab**3+
  &pli2(5)*elab**4+pli2(6)*elab**5+pli2(7)*elab**6
  stpfpf3(1)+pf3(2)*elab+pf3(3)*elab**2+pf3(4)*elab**3+
  &pf3(5)*elab**4
  stpc=pc3(1)+pc3(2)*elab+pc3(3)*elab**2+pc3(4)*elab**3+
  &pc3(5)*elab**4
else if (elab.le.2100.d0) then
  stpli=pli3(1)+pli3(2)*elab+pli3(3)*elab**2
  stpfpf4(1)+pf4(2)*elab+pf4(3)*elab**2
  stpc=pc4(1)+pc4(2)*elab+pc4(3)*elab**2
endif
c-----
c      stpli=.95*stpli
c      stpfc=.95*stpfc
c      stpc=.95*stpc
c      stpli=1.05*stpli
c      stpfc=1.05*stpfc
c      stpc=1.05*stpc
c-----
stp=(stpli+rnf/rn6li*stp+rn7li/rn6li*stpli+rnc/rn6li*stpc)*
&i.d-3*I.d-15*mli/(mli+mh)
deltae=(rn7li*stpli+rnf*stp+rn6li*stpli+rnc*stpc)*
&tlay(ilay)*id-3*mli/(mli+mh)
return
c-----fim subroutine stopping -----
end

c-----function fdat(ecm)-----
c-----Compute integrand function -----
c-----
real*8 ecm,arg,zh,zii,mh,mli,reducma
parameter(zh=1.d0,zii=3.d0)

```

```

Jan 25, 07 3:09          xs6lifcu-125.f          Page 5/7
daldp(2)=eeff
daldp(3)=eeff**2
ealp(1)=3.171d-3
ealp(2)=3.889e-5
ealp(3)=8.160d-8
dalsq=0.d0
do i=1,3
  dalsq=dalsq+(daldp(i)*ealp(i))**2
enddo
dwdalsq=pl**2*dalsq
return
c-----fim subroutine wfactor-----
end

subroutine kfactor(elab,c2cm,kk)
c-----
c      Compute K factor .
c-----
real*8 elab,c2cm,kk
real*8 m1,m2,m3,m4,theta,pi,qvalue,et
real*8 dum,aa,bb,cc,dd,e3et
parameter(pi=3.14159d0)
m1=1.007825d0
m2=6.015121d0
m3=3.016029d0
m4=4.002603d0
theta=124.d0
theta=theta*pi/180.d0
qvalue=(m1+m2-m3-m4)*.931.502d0
et=elab/1.d3+qvalue
dum=(m1+m2)*(m3+m4)
aa=m1*m4/dum*elab/1.d3/et
bb=m1*m3/dum*elab/1.d3/et
cc=m2*m3/dum*(1.d0+m1/m2*qvalue/et)
dd=m2*m4/dum*(1.d0+m1/m2*qvalue/et)
e3et=bb*(acos(theta)+dsqrt(dd/bb-dsin(theta)**2))**2
c2cm=1.d0-e3et/dd*(dsin(theta))**2
kk=e3et/(dsqrt(aa*cc)*dsqrt(dd/bb-dsin(theta)**2))
return
c-----fim subroutine kfactor-----
end

subroutine stopping(ecm,ilay,stp,deltae)
c-----
c-----Compute effective stopping power -----
c-----
real*8 ecm,stp,stpli,stpc,stp,deltae
real*8 elab,mli,mh
integer ilay
parameter (n7=7,n6=6,n5=5,n3=3,nlay=1)
common/sp,pli(n6),pli2(n7),pli3(n3),
&pf1(n6),pf2(n5),pf3(n5),pf4(n3),
&pc1(n6),pc2(n5),pc3(n5),pc4(n3)

```

Jan 25, 07 3:09	xs6lifcu-125.f	Page 7/7
<pre>mli=6.015121d0 mb=1.008d0 reducma=mli*mb/(mli+mb) arg=-31.29d0*zh*zli*dsgt(reducma/ecm) fdat=dexp(arg)/ecm return end</pre>		

xs6lifcu-125.f

Thursday January 25, 2007



```

Jan 25, 07 2:45          fitnuc.f          Page 3/5
C-----
      lfout=2
      enddo
C---fim subroutine imprimir-----
      return
      end

C-----
      subroutine ffdat (nhisto,icut)
C      Fit cross section data.
C-----
      parameter (nbin=100,xmin=3.0,xmax=8.0)
      parameter (npar=3)          !Fit dos dados
      common/ppar/par (npar),step (npar),pmin (npar),pmax (npar),
      &sig (npar),chi2
      common/nparam/npara
      common/quest/quest (100)
      parameter (kpoints=13)
      common/fivct/x2fit (kpoints),v2fit (kpoints),ev2fit (kpoints)

      real xdados (kpoints),ydados (kpoints)
      external fdat
C-----
      Parameters to fit:
      par (1) = a
      par (2) = b
      par (3) = sigma_0
C-----
      par (1)=5.
      par (2)=1.7
      par (3)=2.26
      pmin (1)=-1.0e+10
      pmax (1)=0.0
      pmin (2)=-1.0e+10
      pmax (2)=1.0e+10
      pmin (3)=-1.0e+10
      pmax (3)=1.0e+10
      do i=1,npar
         step (i)=0.0001
      enddo
      npts=kpoints
      write (*,*)
C-----
      write (*,*) 'First fit begins'
      call hfiv (npts,1,1,x2fit,v2fit,ev2fit,fdat,'vr',npara,
      &par (1),step (1),pmin (1),pmax (1),sig (1),chi2)
      write (*,*)
C-----
      write (*,*) 'Second fit begins'
      call hfiv (npts,1,1,x2fit,v2fit,ev2fit,fdat,'vr',npara,
      &par (1),step (1),pmin (1),pmax (1),sig (1),chi2)
C-----
      do i=1,kpoints
         xdados (i)=x2fit (i)
         ydados (i)=v2fit (i)
      enddo
      call hhook1 (nhisto,'dados',kpoints,xdados (1),xdados (kpoints),0.)
      call hbarx (nhisto)
      call hpak (nhisto,v2fit)

```

Thursday January 25, 2007

```

Jan 25, 07 2:45          fitnuc.f          Page 4/5
C-----
      call hpake (nhisto,ev2fit)
      call hbfun1 (10*nhisto,'fdat',kpoints,x2fit (1),x2fit (kpoints),fdat)
C-----
      call hput (nhisto,'fimuc.rz','u')
      call hput (10*nhisto,'fnuc.rz','u')
      return
      end

C-----
      function fdat (xx)
C-----
      real*8 x (2),eproton,dgmlt2,a2,b2,thick,er
      external fsub2
      parameter (thick=31.0d0)
      parameter (er=440.0d0)
      parameter (npar=3)          !Fit dos dados
      common/ppar/par (npar),step (npar),pmin (npar),pmax (npar),
      &sig (npar),chi2
      common/energia/eproton
      eproton=dble (xx)
C-----
      a2 = extremo de integracao inferior em energia
      b2 = extremo de integracao superior em energia
      a2=er-2.d2
      b2=er+2.d2
      fdat=par (3)+par (3)*sngl (dgmlt2 (fsub2,a2,b2,40,8,x)/thick)
      return
      end

C-----
      subroutine fsub2 (m,u2,f2,x)
      external fsub1
      real*8 u2,f2,x
      integer m
      dimension u2 (*),f2 (*),x (2)
      real*8 c2,d2,er,taur,dgmlt1,thick
      real*8 par1,par2,dum
      parameter (er=440.0d0,taur=12.2d0)
      parameter (thick=31.0d0)
      parameter (npar=3)          !Fit dos dados
      common/ppar/par (npar),step (npar),pmin (npar),pmax (npar),
      &sig (npar),chi2
C-----
      c2 = extremo de integracao inferior em espessura
      d2 = extremo de integracao superior em espessura
      c2=0.d0
      d2=thick
      par1=dble (par (1))
      par2=dble (par (2))
      do l=1,m
         x (2)=u2 (l)
         dum=2.d0*(x (2)-er)/taur
         f2 (l)=(par1+par2*dum)/(1.d0-dum**2)*dgmlt1 (fsub1,c2,d2,40,8,x)
      enddo
      return
      end

```

fitnuc.f

2/3

```

c-----fsubl-----
      subroutine fsub1(m,ul,fl,x)
      real*8 pi,ul,fl,x
      integer m
      dimension ul(*),fl(*),x(2)
      parameter (pi=3.14159d0)
      real*8 taut,deltab2,zprot2,ztgt,atgt,bigb
      real*8 epton,tep_1,tep,avogadro
      parameter(avogadro=6.023d23)
      common/energia/eproton
      deltab2=1.d0
      zprot2=1.d0
      ztgt=6.d0
      atgt=12.9697d0
      tep=3.40058d-1
      do l=1,m
         x(l)=ul(l)
         taut=dsqrt(deltab2+8.6d-1*zprot2*ztgt/atgt*x(1))
         bigb=1.d0/dsqrt(3.6d-1*pi*taut)
         fl(l)=bigb*exp(-(eproton-x(2)-tep*x(1))**2/(3.6d-1*taut))
      enddo
      return
      end

```

## **Appendix D**

**Tables for  ${}^7\text{Li}(p,\alpha){}^4\text{He}$  and  ${}^6\text{Li}(p,\alpha){}^3\text{He}$**

***S*-factor values calculated by the integral  
method**

Target: ${}^7\text{Li}$ implanted in Al								
$\theta_{\text{lab}} = 124^\circ$			$\theta_{\text{lab}} = 145^\circ$			$\theta_{\text{lab}} = 124^\circ + 145^\circ$		
$E$ (keV)	$S(E)$ (keV b)	$\delta S(E)$ (keV b)	$E$ (keV)	$S(E)$ (keV b)	$\delta S(E)$ (keV b)	$E$ (keV)	$S(E)$ (keV b)	$\delta S(E)$ (keV b)
89.7	77.37	12.67	89.7	77.09	13.61	89.7	77.23	9.28
95.1	75.10	6.95	95.1	68.74	6.46	95.1	71.92	4.73
115.8	72.65	7.82	115.8	74.55	6.60	115.8	73.60	5.04
125.8	74.02	5.37	125.8	68.57	4.99	125.8	71.29	3.66
136.5	71.63	5.06	136.5	70.08	6.43	136.5	70.85	3.98
147.9	74.52	5.70	147.9	77.52	6.35	147.9	76.02	4.24
149.5	78.24	5.46	149.5	77.89	5.43	149.5	78.07	3.85
160.0	78.17	5.93	160.0	77.13	5.66	160.0	77.65	4.10
172.7	80.94	5.41	172.7	82.42	5.93	172.7	81.68	4.00
185.9	81.17	5.50	185.9	77.45	5.91	185.9	79.31	4.03
199.7	85.47	5.52	199.7	84.15	6.05	199.7	84.81	4.08
214.0	80.29	5.10	214.0	81.52	5.34	214.0	80.90	3.69
228.8	80.96	5.19	228.8	83.28	5.35	228.8	82.12	3.73
244.0	82.78	5.57	244.0	82.72	5.27	244.0	82.75	3.83
259.7	84.45	5.91	259.7	78.74	5.54	259.7	84.45	5.91
273.6	84.68	5.35	273.6	85.06	5.39	273.6	84.87	3.80
275.9	84.93	5.96	275.9	78.51	5.55	275.9	84.93	5.96
292.4	84.17	5.84	292.4	77.15	5.38	292.4	84.17	5.84
309.4	90.22	6.26	309.4	82.01	5.73	309.4	86.12	4.22
318.8	88.34	6.22	318.8	85.68	6.67	318.8	87.01	4.55
344.7	86.76	6.07	344.7	77.59	5.46	344.7	86.76	6.07
352.5	88.64	5.78	352.5	87.68	5.67	352.5	88.16	4.05
381.7	89.60	5.71	381.7	89.46	5.94	381.7	89.53	4.12
387.6	89.43	5.73	387.6	88.78	5.69	387.6	89.11	4.04
417.0	88.22	6.77	417.0	87.09	5.51	417.0	87.65	4.27
424.3	87.20	5.74	424.3	91.87	5.87	424.3	89.54	4.10
462.4	87.58	5.60	462.4	91.07	5.81	462.4	89.33	4.03
502.1	92.74	5.93	502.1	93.06	5.95	502.1	92.90	4.20
543.3	95.75	6.16	543.3	91.50	5.89	543.3	93.63	4.26
551.3	91.22	5.77	551.3	94.76	5.92	551.3	92.99	4.13
586.0	94.86	6.08	586.0	97.90	6.40	586.0	96.38	4.41
630.1	96.55	6.37	630.1	98.20	6.27	630.1	97.37	4.47
675.6	97.76	7.26	675.6	99.74	6.43	675.6	98.75	4.81
684.6	96.64	6.31	684.6	103.54	6.74	684.6	100.09	4.61
722.6	100.08	6.42	722.6	103.28	6.64	722.6	101.68	4.61
746.7	99.22	6.36	746.7	101.66	6.54	746.7	100.44	4.56
772.1	102.02	6.52	772.1	103.42	6.65	772.1	102.72	4.66
817.1	106.17	6.85	817.1	108.42	7.18	817.1	107.30	4.96
949.4	119.82	7.65	949.4	126.49	8.43	949.4	123.15	5.67
1081.4	137.49	9.37	1081.4	140.63	9.40	1081.4	139.06	6.64
1214.3	151.47	10.14	1214.3	154.26	11.62	1214.3	152.86	7.64
1345.3	180.82	11.16	1345.3	186.63	12.79	1345.3	183.72	8.41
1477.1	218.63	13.48	1477.1	227.32	16.58	1477.1	222.98	10.46
1608.7	254.88	15.79	1608.7	275.18	21.78	1608.7	265.03	12.78
1740.3	309.11	19.45	1740.3	330.02	29.01	1740.3	319.57	16.15

Table D.1:  ${}^7\text{Li}(p,\alpha){}^4\text{He}$   $S$ -factor measured with the  ${}^7\text{Li}$  implanted in Al target. The quoted uncertainties correspond to one standard deviation.

Target: LiF-Ag								
$\theta_{\text{lab}} = 124^\circ$			$\theta_{\text{lab}} = 145^\circ$			$\theta_{\text{lab}} = 124^\circ + 145^\circ$		
$E$ (keV)	$S(E)$ (keV b)	$\delta S(E)$ (keV b)	$E$ (keV)	$S(E)$ (keV b)	$\delta S(E)$ (keV b)	$E$ (keV)	$S(E)$ (keV b)	$\delta S(E)$ (keV b)
270.6	83.16	6.53	270.6	80.83	4.74	270.6	82.00	3.84
286.5	81.52	5.67	286.5	82.44	4.36	286.5	81.98	3.46
302.8	82.54	4.23	302.8	87.57	4.46	302.8	85.05	3.07
306.5	87.53	4.12	306.5	88.07	4.15	306.5	87.80	2.92
319.6	88.62	5.19	319.6	91.42	5.40	319.6	90.02	3.74
328.8	88.30	5.16	328.8	90.65	4.25	328.8	89.48	3.28
336.7	83.74	4.34	336.7	91.16	4.59	336.7	87.45	3.16
351.8	86.66	4.56	351.8	89.06	4.61	351.8	87.86	3.24
354.3	86.54	3.94	354.3	89.90	4.11	354.3	88.22	2.84
372.4	89.11	4.50	372.4	91.08	4.49	372.4	90.10	3.18
375.6	91.27	4.68	375.6	91.09	4.58	375.6	91.18	3.27
390.8	87.90	4.36	390.8	91.71	4.47	390.8	89.81	3.12
400.2	95.04	5.18	400.2	96.16	5.09	400.2	95.60	3.63
421.9	93.01	5.04	421.9	90.65	4.48	421.9	91.83	3.35
425.5	91.75	5.31	425.5	92.98	4.26	425.5	92.37	3.32
444.0	88.21	4.77	444.0	88.04	4.63	444.0	88.13	3.32
453.0	89.98	4.16	453.0	96.45	4.43	453.0	93.22	3.24
470.6	87.21	4.56	470.6	89.16	6.54	470.6	88.19	3.74
483.4	93.57	5.02	483.4	91.97	4.84	483.4	92.77	3.48
501.8	91.59	4.68	501.8	91.64	8.63	501.8	91.61	4.11
514.8	93.29	5.24	514.8	99.91	4.67	514.8	96.60	3.49
530.0	93.27	4.78	530.0	97.76	4.86	530.0	95.51	3.41
547.1	91.43	4.29	547.1	96.68	4.50	547.1	94.06	3.11
558.9	95.72	5.13	558.9	98.98	5.14	558.9	97.35	3.63
580.5	95.65	4.45	580.5	95.72	4.44	580.5	95.69	3.14
588.5	94.78	5.05	588.5	99.69	5.14	588.5	97.23	3.60
614.6	98.13	5.34	614.6	102.22	5.36	614.6	100.17	3.78
618.9	93.21	4.92	618.9	101.55	5.16	618.9	97.38	4.17
649.9	95.79	4.28	649.9	106.01	4.74	649.9	100.90	5.11
681.9	92.82	4.85	681.9	104.04	5.21	681.9	98.43	5.61
685.9	98.52	4.57	685.9	109.24	5.04	685.9	103.88	5.36
714.4	93.58	4.85	714.4	107.13	5.33	714.4	100.36	6.77
723.0	104.25	4.85	723.0	109.98	5.11	723.1	107.11	3.52
747.8	102.95	5.19	747.8	112.04	5.54	747.8	107.49	4.55
762.3	103.53	4.50	762.3	109.59	4.95	762.4	106.56	3.33
769.6	109.95	7.66	769.6	109.27	5.58	769.6	109.61	4.51
779.3	102.88	4.39	779.3	108.78	5.15	779.3	105.83	3.34
800.3	106.50	5.11	800.3	111.78	5.34	800.3	109.14	2.64
820.3	108.91	5.59	820.3	110.32	5.60	820.3	109.61	3.95
860.7	105.91	4.59	860.7	115.14	5.13	860.8	110.52	4.61
902.2	113.97	6.21	902.2	121.27	5.59	902.2	117.62	4.16
944.5	118.04	6.45	944.5	122.36	6.09	944.5	120.20	4.43
988.0	124.93	7.64	988.0	127.12	7.38	988.0	126.03	5.31
1032.4	127.19	6.06	1032.4	138.98	7.45	1032.4	133.08	5.90
1077.7	131.85	5.93	1077.7	140.12	8.33	1077.7	135.99	4.83
1124.1	138.59	6.80	1124.1	145.87	7.14	1124.1	142.23	4.92
1171.5	151.91	6.75	1171.5	156.05	7.66	1171.5	153.98	5.06
1225.0	158.64	7.76	1225.0	164.87	8.19	1225.0	161.75	5.63

Table D.2:  ${}^7\text{Li}(p,\alpha){}^4\text{He}$   $S$ -factor measured with the LiF-Ag target. The quoted uncertainties correspond to one standard deviation.

Target: LiF-Cu								
$\theta_{\text{lab}} = 124^\circ$			$\theta_{\text{lab}} = 145^\circ$			$\theta_{\text{lab}} = 124^\circ + 145^\circ$		
$E$	$S(E)$	$\delta S(E)$	$E$	$S(E)$	$\delta S(E)$	$E$	$S(E)$	$\delta S(E)$
(keV)	(keV b)	(keV b)	(keV)	(keV b)	(keV b)	(keV)	(keV b)	(keV b)
92.4	71.42	5.80	92.4	70.67	5.92	92.4	71.05	4.14
101.1	70.80	5.02	101.1	73.29	4.75	101.1	72.05	3.45
110.3	70.66	4.16	110.3	68.19	4.74	110.3	69.43	3.13
120.0	74.58	4.23	120.0	73.12	4.27	120.0	73.85	3.00
130.0	76.01	4.65	130.0	74.97	4.19	130.1	75.49	3.11
140.6	74.67	4.10	140.6	74.65	4.48	140.6	74.66	3.02
162.8	78.07	4.32	162.8	77.74	4.33	162.8	77.91	3.06
186.7	79.64	4.35	186.7	77.51	4.12	186.7	78.58	2.99
212.1	82.80	4.90	212.1	80.89	4.28	212.1	81.84	3.22
239.0	81.66	4.47	239.0	80.67	4.33	239.0	81.17	3.11
267.5	82.77	4.75	267.5	80.58	4.61	267.5	81.67	3.31
297.4	84.14	4.89	297.4	79.54	4.40	297.4	81.84	3.27
329.0	88.63	5.76	329.0	85.06	5.87	329.1	86.85	4.11
362.1	87.16	4.70	362.1	84.64	4.51	362.1	85.90	3.25
396.6	89.08	4.76	396.6	89.30	4.82	396.6	89.19	3.39
432.7	89.91	4.78	432.7	91.80	4.94	432.7	90.86	3.44
470.3	92.21	4.98	470.3	90.28	4.80	470.3	91.24	3.45
509.3	93.50	4.93	509.3	92.51	5.05	509.3	93.00	3.53
549.9	92.51	5.24	549.9	92.36	4.99	549.9	92.44	3.62
592.0	96.19	5.05	592.0	96.98	5.13	592.0	96.58	3.60
635.6	96.90	5.12	635.6	94.53	5.03	635.6	95.71	3.59
680.7	98.14	5.45	680.7	97.22	5.31	680.8	97.68	3.81
1121.9	147.72	8.09	1121.9	147.26	8.51	1121.9	147.49	5.86
1222.2	163.22	8.88	1222.2	153.59	9.10	1222.2	158.41	6.35
1278.4	179.87	9.65	1278.4	167.06	10.00	1278.4	173.47	6.95
1341.3	189.10	10.42	1341.3	192.29	11.31	1341.3	190.69	7.66
1405.7	189.96	10.45	1405.7	206.08	13.51	1405.7	198.02	8.26
1471.7	207.85	12.20	1471.7	226.13	15.71	1471.7	216.99	9.63

Table D.3:  ${}^7\text{Li}(p,\alpha){}^4\text{He}$   $S$ -factor measured with the LiF-Cu target. The quoted uncertainties correspond to one standard deviation.

Target: LiF-Cu								
$\theta_{\text{lab}} = 124^\circ$			$\theta_{\text{lab}} = 145^\circ$			$\theta_{\text{lab}} = 124^\circ + 145^\circ$		
$E$ (keV)	$S(E)$ (MeV b)	$\delta S(E)$ (MeV b)	$E$ (keV)	$S(E)$ (MeV b)	$\delta S(E)$ (MeV b)	$E$ (keV)	$S(E)$ (MeV b)	$\delta S(E)$ (MeV b)
90.5	3.27	0.23	90.5	3.22	0.23	90.5	3.24	0.16
99.0	3.23	0.30	99.0	3.19	0.25	99.0	3.21	0.19
108.1	3.01	0.21	108.1	2.97	0.17	108.1	2.99	0.13
117.5	3.11	0.17	117.5	3.08	0.17	117.5	3.09	0.12
127.4	3.09	0.20	127.4	3.07	0.17	127.4	3.08	0.13
137.7	3.01	0.17	137.7	2.94	0.16	137.7	2.98	0.12
159.5	2.93	0.15	159.5	2.90	0.16	159.5	2.92	0.11
182.8	2.86	0.16	182.8	2.81	0.15	182.8	2.84	0.11
207.7	2.76	0.15	207.7	2.85	0.18	207.7	2.80	0.11
234.1	2.65	0.14	234.1	2.78	0.16	234.1	2.72	0.11
262.1	2.64	0.15	262.1	2.65	0.16	262.1	2.65	0.11
291.4	2.63	0.16	291.4	2.96	0.19	291.4	2.63	0.16
322.3	2.41	0.14	322.3	2.54	0.16	322.3	2.47	0.11
354.7	2.37	0.13	354.7	2.49	0.15	354.7	2.43	0.10
388.5	2.41	0.15	388.5	2.58	0.17	388.5	2.50	0.11
423.8	2.29	0.13	423.8	2.52	0.16	423.8	2.40	0.11
460.6	2.16	0.14	460.6	2.35	0.18	460.6	2.26	0.11
498.9	2.27	0.15	498.9	2.30	0.19	498.9	2.29	0.12
538.7	2.07	0.14	538.7	2.30	0.19	538.7	2.18	0.12
579.9	2.05	0.14	579.9	2.31	0.20	579.9	2.18	0.13

Table D.4:  ${}^6\text{Li}(p,\alpha){}^3\text{He}$   $S$ -factor measured with the LiF-Cu target. The quoted uncertainties correspond to one standard deviation.



# Bibliography

- [1] URL of NASA probe WMAP: <http://map.gsfc.nasa.gov>.
- [2] Alpher, R.H., Bethe, H.A., and Gamow, G., *Phys. Rev.* 73 (1948) 803
- [3] Penzias, A. A., Wilson, R. W., *ApJ* 142 (1965) 419
- [4] Spergel, D. N., Verde, L., Peiris, H. V. *et al.* , *Astrophys. J.* 148 (2003) 175
- [5] Coc, A., Vangioni-Flam, E., Descouvemont, P., Adahchour, A., and Angulo, C., *ApJ* 600 (2004) 544 (ArXiv:astro-ph/0309480)
- [6] Cyburt, R.H., *Phys. Rev. D*70 (2004) 023505 (ArXiv:astro-ph/0401091)
- [7] Serpico, P.D., Esposito, S., Iocco, F., Mangano, G., Miele, G., and Pisanti, O., *JCAP* 12 (2004) 10S
- [8] Izotov, Y.I., Chaffee, F.H., Foltz, C.B., Green, R.F., Guseva, N.G., and Thuan, T.H., *ApJ* 527 (1999) 757
- [9] Luridiana, V., *et al.* , *ApJ* 592 (2003) 846
- [10] Izotov, Y.I., and Thuan, T.H., ArXiv:astro-ph/0310421 (2003)
- [11] Crighton, N.H.M., Webb, J.K., Ortiz-Gil, A., and Fernández-Soto, A., ArXiv:astro-ph/0403512 (2004)
- [12] Spite, F. and Spite, M., *A&A* 115 (1982) 357
- [13] Maurice, E., Spite F., and Spite M., *A&A* 132 (1984) 278

- [14] Ryan, S.G., Norris, J.E., and Beers, T.C., ApJ 523 (1999) 654
- [15] Thorburn, J.A., ApJ 421 (1994) 318
- [16] Ryan, S.G., Beers, T.C., Olive, K.A., Fields, B.D., and Norris, J.E., ApJ 530 (2000) L57
- [17] Bonifacio, P., *et al.*, IAU Joint Discussion 15 (2003) 39
- [18] Melendez, J., and Ramirez, I., ArXiv:astro-ph/0409383 (2004)
- [19] Charbonnel, C., and Primas, F., ArXiv:astro-ph/0505247 (2005)
- [20] Asplund, M., Lambert, D.L., Nissen, P.E., Primas, F., Smith, V.V., ArXiv:astro-ph/0510636 (2005)
- [21] Smith, V.V., Lambert, D.L., and Nissen, P.E., ApJ 408 (1993) 262
- [22] Hobbs, L.M., and Thorburn, J.A., ApJ 428 (1994) L25
- [23] Hobbs, L.M., and Thorburn, J.A., ApJ 491 (1997) 772
- [24] Smith, V.V., Lambert, D.L., and Nissen, P.E., ApJ 506 (1998) 405
- [25] Cayrel, R., Spite, M., Spite, F., Vangioni-Flam, E., Cassé, M., and Audouze, J., A&A 343 (1999) 923
- [26] Nissen, P.E., Asplund, M., Hill, V., and D'Odorico, S., A&A 357 (2000) L49
- [27] Asplund, M., Carlsson, M., and Botnen, A.V., ArXiv:astro-ph/0302406 (2003)
- [28] Lambert, D.L., ArXiv:astro-ph/0410418 (2004)
- [29] Pinsonneault, M. H., Walker, T. P., Steigman, G., and Narayanan, V. K., ApJ 527 (1999) 180
- [30] Pinsonneault, M. H., Steigman, G., Walker, T. P., and Narayanan, V. K., ApJ 574 (2002) 398
- [31] Richard, O., Michaud, G., and Richer, J., ApJ 580 (2002) 1100
- [32] Richard, O., Michaud, G., and Richer, J., ApJ 619 (2005) 538

- 
- [33] Talon, S., and Charbonnel, C., A&A 418 (2004) 1051
- [34] Charbonnel, C., and Talon, S., Science 309 (2005) 2189
- [35] Vauclair, S., and Charbonnel, C., A&A 295 (1995) 715
- [36] Reeves, H., Fowler, W.A., and Hoyle, F., Nature 226 (1970) 727
- [37] Rolfs, C. and Rodney, W.S., *Cauldrons in the Cosmos*, The University of Chicago Press, 1988
- [38] Mercer, D.J., *et al.* , Phys. Rev. C 63 (2001) 065805
- [39] Prantzos, N., astro-ph/0510122 (2006)
- [40] Ramaty, R., Scully, S., Lingenfelter, R., and Kozlovsky, B., ApJ 534 (2000) 747
- [41] Smith, M.S., Kawano, L.H. and Malaney, R.A., Astrophys. J. S.85 (1993) 219
- [42] Nollett, K.M. and Burles, S., Phys. Rev.D61 (2000) 123505
- [43] Angulo, C., *et al.* , ApJ 630 (2005) L105 (ArXiv:astro-ph/0508454)
- [44] Cohen-Tannoudji, C., Diu, B., and Laloë, F., *Quantum Mechanics*, Wiley Interscience, 1977
- [45] Assenbaum, H.J., Langanke, K., Rolfs, C., Z. Phys. A 327 (1987) 461
- [46] Bencze, G., Nuc.Phys. A492 (1989) 459
- [47] Bracci, L., Fiorentini, G., Melezhik, V.S., Mezzorani, G., and Quarati, P., Nuc.Phys. A513 (1990) 316
- [48] Greife, U., Gorris, F., Junker, M., Rolfs, C., and Zahnow, D., Z.Phys. A351 (1995) 107
- [49] Engstler, S., Krauss, A., Nelder, K., Rolfs, C., Schröder, U., and Langanke, K., Phys. Lett. B200 (1988) 2179
- [50] Engstler, S., Raimann, G., Angulo, C., Greife, U., Rolfs, C., Schröder, U., Somorjai, E., and Kirch, B., Z.Phys. A342 (1992) 471

- [51] Angulo, C., *et al.*, Z.Phys. A345 (1993) 231
- [52] Yuki, H., Kasagi, J., Lipson, A.G., Ohtsuki, T., Baba, T., Noda, T., Lyakhov, B.F., and Aami, B.F., JETP Lett. 68 (1998) 823
- [53] Czerski, K., Hulke, A., Biller, A., Heide, P., Hoeft, M., and Ruprecht, G., Europhys. Lett. 54 (2001) 449
- [54] Raiola, F., Ph.D. thesis, Bochum 2005
- [55] Raiola, F. *et al.*, J. Phys. G31 (2005) 1141
- [56] Hurd, C.M., *The Hall effect in Metals and Alloys*, Plenum Press (1972)
- [57] Landolt-Börnstein (Berlin: Springer) 1959, Band II, 161
- [58] Descouvemont, P., Adahchour, A., Angulo, C., Coc, A., and Vangioni-Flam, E., astro-ph/0407101 (2004)
- [59] Spinka, H., Tombrello, T.A., and Winkler, H., Nucl. Phys. A164 (1971) 1
- [60] Rolfs, C., Kavanagh, R.W., Nucl. Phys. A455 (1986) 179
- [61] Lattuada, M., Pizzone, R.G., Typel, S., Figuera, P., Miljanic, D., Musumarra, A., Pellegriti, M.G., Rolfs, C., Spitaleri, C., and Wolter, H.H., Ap. J. 562 (2001) 1076
- [62] Barker, F.C., Nuc. Phy. A707 (2002) 277
- [63] Cassagnou, Y., Jeronymo, J.M.F., Mani, G.S., Sadeghi, A., and Forsyth, P.D., Nucl. Phys. 33 (1962) 449; 41 (1963) 176
- [64] Fiedler O., and Kunze, P., Nucl. Phys. A 96 (1967) 513
- [65] Kasagi, J., J. Phys. Soc. Jpn. 71 (2002) 2881; Kasagi, J., J. Phys. Soc. Jpn. 73 (2004) 608
- [66] Marion, J.B., Weber, G., Mozer, F.S., Phys. Rev. 104 (1956) 1402
- [67] Gemeinhardt, W., Kamke, D., von Rhöneck, C., Z. Phys. 197 (1966) 58
- [68] Elwyn, A.J., *et al.*, Phys. Rev. C20 (1979) 1984

- 
- [69] Shinozuka, T., Tanaka, Y., Sugiyama, K., Nucl. Phys. A326 (1979) 47
- [70] Szabo, J., *et al.*, Nucl. Data for Science and Technology. Böckhoff, K.H. (ed.), p. 956. Brussels: ECSC 1983; and Szabo, J., private communication
- [71] Kwon, J.U., Kim, J.C., Sung, B.M., Nucl. Phys. A493 (1989) 112
- [72] Tumino, A., Phys. Rev. C67 (2003) 065803
- [73] Joseph R. Tesmer, Michael Nastasi (Edts), Handbook of Modern Ion Beam Materials Analysis, MRS (1995)
- [74] URL of Genplot: <http://www.genplot.com>
- [75] Mateus, R., Jesus, A.P., Ribeiro, J.P., NIMB 229 (2005) 302
- [76] Massalski, T. B., Binary Alloys Phase Diagrams, American Society for Metals (1986)
- [77] Villars, P. & Calvert, L. D., Pearson's Handbook of Crystallographic Data for intermetallic phases, 2<sup>nd</sup> Edt., ASM international (1996)
- [78] James, F., MINUIT – Function minimization and error analysis – Reference Manual, CERN, URL: <http://asdoc.web.cern.ch/wwwasdoc>
- [79] URL of SRIM: [www.srim.org](http://www.srim.org)
- [80] Ryssel, H., Ruge, J., Ion implantation, Vol. I, John Wiley & Sons (1986)
- [81] Teodoro, O.M.N.D., Ph.D. thesis, Lisboa 1998
- [82] URL of CERNLIB: <http://cernlib.web.cern.ch/cernlib>
- [83] Ziegler, J.F., and Manoyan, J.M., Nucl. Instrum. Meth. B35 (1988) 215
- [84] Harmon, J.F., Phys. Rev. C8 (1973) 106
- [85] Debye, P., Hückel, E., Phys. Z. 24 (1923) 185
- [86] Salpeter, E., Aust. J. Phys. 7 (1954) 373
- [87] Bahcall, J., *et al.*, ArXiv:astro-ph/0010055

- [88] Cruz, J., *et al.* , Phys. Lett. B624 (2005) 181
- [89] Zahnow, D., *et al.* , Z. Phys. A 359 (1997) 211
- [90] Kettner, K.U, *et al.* , J. Phys. G 32 (2006) 489
- [91] Wang, B., *et al.* , Eur. Phys. J. A 28 (2006) 375
- [92] Limata, B., *et al.* , Eur. Phys. J. A 28 (2006) 251
- [93] Spyrou K., Chronidou, C., Harissopulos, S., Kossionides, S., Paredellis, T., Z. Phys. A 357 (1997) 283
- [94] Bento, R., master thesis, Lisboa 2005